# Chemical vapor deposited graphene for quantum Hall resistance standards

## Inauguraldissertation

zur
Erlangung der Würde eines Doktors der Philosophie
vorgelegt der
Philosophisch-Naturwissenschaftlichen Fakultät
der Universität Basel

von

**Kishan Thodkar**
**aus Bangalore, Indien**

Basel, 2017

Genehmigt von der Philosophisch-Naturwissenschaftlichen Fakultät
auf Antrag von

Prof. Dr. Christian Schönenberger
Prof. Dr. Michel Calame
Dr. Franz Ahlers

Basel, den 17. Oktober 2017

Prof. Dr. Martin Spiess
Dekan

*'Dedicated to my parents, sister and family.'*

# List of abbreviations

| | |
|---|---|
| LO (A) | longitudinal optical (acoustic) |
| TO (A) | transverse optical (acoustic) |
| EPC | electron-phonon coupling |
| LL | Landau level |
| DOS | density of states |
| QHE | quantum Hall effect |
| QHR | quantized Hall resistance |
| QMT | quantum metrology triangle |
| CVD | chemical vapor deposition |
| SLG | single layer graphene |
| hBN | hexagonal boron nitride |
| PMMA | Poly(methyl methacrylate) |
| APS | Ammonium persulfate $(NH_4)_2S_2O_8$ |
| XPS | X-ray photoelectron spectroscopy |
| LEEM | low-energy electron microscopy |
| FET | field effect transistor |
| NMP | N-Methyl-2-pyrrolidone |
| HMDS | Hexamethyldisilazane |
| TLM | transfer length method |
| S(M)D | single (multi) domain |
| S(L)G | small (large) grain |
| CCC | cryogenic current comparator |
| WL | weak localization |

# Contents

# 1

# Introduction

*"The mind of man has perplexed itself with many hard questions. Is space infinite, and in what sense? Is the material world infinite in extent, and are all places within that extent equally full of matter? Do atoms exist or is matter infinitely divisible?"*

James Clerk Maxwell[1]

Our present day lives finds itself in sync along the lines of this famous quote by James Clerk Maxwell. Maxwell points out to the perplexity of the human brain, its desire to question the myriad things surrounding us in our day to day lives. Being born in the twentieth century, it's quite challenging to not come across perplexing answers mankind has found for several questions such as: the mobile phone, television, computers, the Internet, antibiotics and many more. Consumer electronics for example has made incredible progress. Taking one particular example, the first fully transistorized computer TRADIC in 1954 to IBM's POWER9 series scheduled to be available in 2017, a noticeable change between them is the reduced size of the various building blocks of electronic circuits [1, 2]. The 'transistor' is one of the smallest building blocks of a computer. The POWER9 series processor will be manufactured using a 14 nanometer FinFET process and will consist of up-to eight billion transistors [2].

[1] "The Theory of Molecules', lecture to the British Association at Bradford. In The Popular Science Monthly (1874) vol. 4, 277.

A ponderous question would be, why shrink the transistor and other building blocks? In the consumer electronics industry, one of the mantra for innovation is higher device performance and less power consumption. Present day microprocessors have been successful in delivering this and follow the trend of doubling of the number of transistors in a microprocessor every two years, called Moore's law. Advances in both material science and manufacturing technologies have been pivotal in making this a reality. Since, present day transistors start to reach the dimension of a few nanometer, many challenges of such miniaturization needs to be addressed. Such as reducing the power consumption, minimizing the leakage current, improving reliability and cost effectiveness. It is relevant to think about the next steps, isn't it?

Welcome the era of two-dimensional, one-dimensional and even zero-dimensional materials. Some of the famous 2D, 1D & 0D materials are: Graphene, $MoS_2$, hexagonal Boron Nitride (hBN), Phosphorene, Stanene, Silicene, Germanene, carbon nanotubes, nanowires, buckyballs and many more. Graphene is touted as the material of the $21^{st}$ century for its interesting combination of both electronic, optical and mechanical properties and several promising application possibilities. It was successfully isolated during a Friday night experiment by Andre Geim and Kostya Novoselov at University of Manchester in 2004. Graphene's discovery opened doors for a family of several other two dimensional materials. A staggering amount of up-to **700** 2D materials also referred to as **'zoo of 2D materials'** has been predicted to be stable and can be synthesized.

Although single layer graphene might not be useful to develop a transistor due to the absence of a band gap, several other applications are foreseen. Some of them are: quantum resistance metrology, transparent conducting electrodes, optoelectronics, Hall effect sensors, conductive ink, spintronics, UV lens, infrared light detector, sensors (pressure, NEMS, molecular adsorption). It was soon realized that large scale graphene production techniques are necessary for industrial scale graphene based applications. Three prominent techniques for large scale graphene production have been developed: 1) epitaxial growth 2) chemical vapor deposition (CVD) and 3) liquid phase exfoliation (LPE). With a growing industrial interest, various aspects such as material synthesis, quality and characterization need to be addressed to facilitate its commercialization.

In this PhD project, we address the different aspects in the development of CVD graphene based quantum Hall resistance standards (QHR) for metrological applications. An interesting application of graphene is its use in developing quantum

Hall resistance standards (QHR). Resistors are one of the most widely used passive components in electrical circuits, a precise and reliable resistance standard is thus vital for the appropriate calibration and reproducibility of various electronic systems during manufacturing. Standard wire-wound resistors suffer from degradation and at best offer an uncertainty of few parts per million (ppm). The quantized Hall resistance plateaus were recognized to serve as the ultimate reference for resistance standards. The quantized Hall resistances is defined in terms of Planck constant ***h*** and electron charge ***e*** and are independent of sample dimensions. These advantages along with the universality and robustness of the quantum Hall effect offers an unparalleled advantage over passive resistor standards.

Graphene offers a unique advantage in realization of a convenient resistance standard, operating at easier measurement conditions. Low dissipation QHE in CVD graphene has been elusive due to several reasons. The various aspects considered within this project involve the synthesis of large area CVD graphene films on copper foil and its thorough characterization using electrical transport, Raman spectroscopy, X-ray photoelectron spectroscopy and low-energy-electron microscopy. The outline of this work is as follows.

In **chapter 2**, a brief background into graphene's properties is described. This is followed with the basic introduction on classical Hall effect and integer quantum Hall effect in graphene. The need for quantum Hall resistance standards (QHR) is presented with a particular focus on the advantage of CVD graphene based QHR. A few details about the cost of graphene production and its application in Hall sensing is presented.

In **chapter 3**, CVD of graphene on copper foils is discussed and various growth recipes demonstrating the control over the size of graphene grains and growth dynamics are presented. Crystallinity of a material defines the purity and ultimately influences its performance. In CVD graphene, the grain boundaries in the film introduce charge scattering and limit the material's performance. However, the occurrence of the grain boundaries can be controlled by altering the growth conditions. It is desirable to have CVD graphene films with large grain size or a uniform mono-crystalline film. These details along with the graphene transfer techniques onto $SiO_2$/Si substrate are presented. The limitation of PMMA-assisted transfer and the prime cause behind the presence of polymer residues is highlighted.

A thorough characterization of graphene is necessary to understand its limitations and easier integration of new 2D materials with existing CMOS technology. In **chapter 4**, we describe three distinct tools used to characterize graphene films

and correlate the observations. First, we performed large area Raman mapping of graphene to study residual doping and intrinsic strain in as-transferred graphene film. This study highlights the detrimental influence of polymer transfer and describes techniques to correlate graphene's Raman G peak positions with net charge density. This is helpful in the understanding of residual doping in the graphene film. PMMA-residues are also characterized using Raman spectroscopy to help distinguish between graphene and residues.

Further, low-energy-electron microscopy (LEEM) was used to study defects/grain boundaries in ultra-clean CVD graphene films. Details about the film crystallinity can be accessed using LEEM. To obtain an elemental understanding of the PMMA-residues, X-ray photoelectron spectroscopy (XPS) was performed. A clear difference between freshly spin-coated PMMA and PMMA-residues after transfer was observed, linking the observation from Raman analysis of residues. During the XPS study we found traces of copper in as-transferred graphene film, suggesting that the nano-particulates observed along the grains/wrinkles in the LEEM study could be residual copper.

In **chapter 5**, a study of electrical response of graphene films and the role of graphene-metal contact interface is discussed. Two techniques utilized to fabricate Hall bar structures are described. A new protocol using stencil lithography used to minimize residues and fasten the fabrication process is presented. The prime cause behind the doping of graphene films was studied and two techniques to overcome doping in as-transferred graphene films were developed namely: 1) thermal annealing and 2) solvent treatment. The effects of the two distinct procedures were also identified through systematic experimental procedure. Electrical transport of clean and p-doped CVD graphene field-effect transistors (FET) are also presented. Two techniques to characterize contact resistance $R_c$: 1) transfer length method (TLM) and 2) direct measurement technique based on QHE of CVD graphene FETs are also discussed.

In **chapter 6**, we compare single domain graphene and polycrystalline graphene film using Raman spectroscopy and electrical characterization to study the difference between the two films. Interestingly, although the crystallinity of the films are different, the influence of polymer transfer is similar in both the graphene films as observed in the Raman analysis. However, a large difference in the charge mobility was observed. Single domain graphene sample had a higher field effect mobility in comparison to multi domain graphene sample. This can arise due to the increased charge scattering at the grain boundaries in the polycrystalline graphene films.

Further, the two-dimensionality of graphene makes it highly sensitive to adsorbates. These adsorbates can be polymer residues from transfer, ambient contaminants, charged molecules and so-on. Some of the adsorbates introduce residual doping in graphene. In **chapter 7**, a study identifying the mechanism leading to the reduction of doping is discussed in detail. By exposing the graphene films to solvent molecules with a strong binding affinity, ambient adsorbates can be replaced with solvent molecules. Molecular binding calculations were performed to support the experimental findings and identify the main mechanism leading to reduction in doping.

In **chapter 8**, we show the first demonstration of low longitudinal resistance in our CVD graphene films and high precision resistance quantization of CVD graphene on $SiO_2$ substrate. A comparison of graphene films with small grain and large grain is performed to study the influence of grain size on the electrical transport. It was observed that the graphene films with larger grains is desirable to develop high-quality CVD graphene based QHR. The observation of high precision resistance quantization of within $\pm 30$ parts in $10^9$ for a range of charge densities highlights the need for high quality of graphene films for developing QHR standards. Some of the limitations encountered in CVD graphene based QHRs are also discussed and possible solutions are also presented.

The conclusion and outlook of this work is discussed in **chapter 9** and the detailed supplementary measurements supporting the observations detailed in the main chapters in presented in appendices A - E.

# 2

# Background: Graphene's properties and quantum resistance standard applications

## 2.1. Band structure of graphene

Graphene is one of the most widely studied material of the present times due to its impressive electronic and mechanical properties [3–5]. Graphene was isolated in 2004 by Andre Geim and Kostya Novoselov, for which they were awarded the Nobel prize in physics in 2010. It is the first 2-dimensional material to be successfully isolated. Graphene consists of $sp^2$ hybridized carbon-carbon bonds (one s-orbital and two p-orbitals), which form a network of $\sigma$-bonds and determine graphene's unique mechanical properties. The distance between the adjacent carbon atoms is a=1.42 Å. The remaining $p_z$ orbital points perpendicular to graphene plane. The electrons from the $\pi$-bond are responsible for the electronic properties of graphene. Each of the carbon atom from the lattice contributes one electron to the $\pi$-band, which is half filled for pristine graphene [6]. A pictorial representation of a graphene ribbon is shown in fig. 2.1 -a.

The honeycomb-like arrangement of the carbon atoms (2.1) leads to a a triangular Bravais lattice with a two atom basis as shown in fig. 2.1 -b. The primitive unit cell is shaded in grey with carbon atoms A and B [7, 8]. The lattice vectors are given by:

$$\boldsymbol{a_1} = \frac{a}{2}\left(3e_x, \sqrt{3}e_y\right), \quad \boldsymbol{a_2} = \frac{a}{2}\left(3e_x, -\sqrt{3}e_y\right). \tag{2.1}$$

where $a$ = 1.42 Å, *i.e.*, the $C-C$ bond length. The Brillouin zone is hexagonal in the reciprocal lattice, as shown in fig. 2.1 -c and is given by:

$$\boldsymbol{b_1} = \frac{2\pi}{3a}\,(k_x, \sqrt{3}k_y)\,, \quad \boldsymbol{b_2} = \frac{2\pi}{3a}\,(k_x, -\sqrt{3}k_y). \tag{2.2}$$

The six corners of the Brillouin zone can be represented as two distinct but energetically degenerate points given by:

$$K = \left(\frac{2\pi}{3a}, \frac{2\pi}{3\sqrt{3}a}\right)\,, \quad K' = \left(\frac{2\pi}{3a}, \frac{2\pi}{-3\sqrt{3}a}\right) \tag{2.3}$$

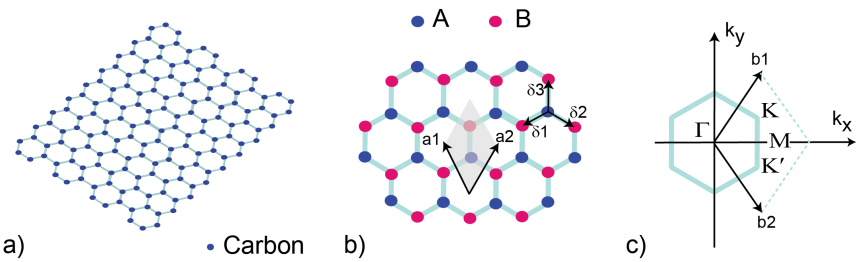


**Figure 2.1:** a) Graphene lattice representation with carbon atoms arranged in hexagonal lattice. b) Graphene lattice representation in real-space with the unit cell (shaded grey region) and its basis vector a1 and a2. The two colours depict the carbon atoms from distinct sublattices. c) The first Brillouin zone of the reciprocal lattice with the base vectors b1 and b2.

The three nearest neighbour vectors ($\delta_{1-3}$) are given by:

$$\delta_1 = \frac{a}{2}\,(1, \sqrt{3}), \quad \delta_2 = \frac{a}{2}\,(1, -\sqrt{3}), \quad \delta_3 = a\,(1, 0). \tag{2.4}$$

Using the tight-binding Hamiltonian for electrons and considering both nearest and next-nearest neighbor hopping, the Hamiltonian has the form [7, 8]:

$$H = -t \sum_{\langle i,\, j\rangle,\, \sigma} (a^{\dagger}_{\sigma,i} b_{\sigma,j} + H.c.) - t' \sum_{\langle\langle i,\, j\rangle\rangle,\, \sigma} (a^{\dagger}_{\sigma,i} a_{\sigma,j} + b^{\dagger}_{\sigma,i} b_{\sigma,j} + H.c.), \tag{2.5}$$

where $a_{i,\sigma}$ annihilates an electron and $a^{\dagger}_{i,j}$ creates an electron with spin $\sigma$ on sublattice A, t is the nearest neighbor hopping energy (t = $\approx 2.7eV$) and t' is the next nearest neighbor hopping energy. The energy bands are derived from 2.5 and is given by:

$$E_{\pm}(k) = \pm t\sqrt{3 + f(k)} - t'f(k) \tag{2.6}$$

where

$$f(k) = 2cos(\sqrt{3}k_y a) + 4cos(\frac{\sqrt{3}}{2}k_y a)cos(\frac{3}{2}k_x a). \tag{2.7}$$

The plus sign in equation 2.6 signifies the upper band ($\pi^*$), while the negative sign signifies the lower band ($\pi$). From fig. 2.2, we can observe that the energy spectrum is symmetric around zero energy for t'=0. For finite values of t', the electron-hole asymmetry is broken and the $\pi$ and $\pi^*$ bands become asymmetric. This second term in Eq. 2.6 is called the 'trigonal warping' term. The complete band structure of graphene is shown in fig. 2.2 -a and a zoom-in of the band structure around the K and K' points is shown in fig. 2.2 b with both t and t' terms [7, 8]. The energy dispersion in the vicinity of the Dirac points can be obtained by combining Eq. 2.6 and Eq. 2.3 as k=K+q ($|K| \gg |a|$) and is given by:

$$E_{\pm}(q) \approx \pm \hbar v_f \, |q| \tag{2.8}$$

where $q$ is the momentum measured relative to the Dirac points and $v_f$ is the fermi velocity ($v_f = 3ta/2$), with a value of $v_f \simeq$1x10$^6$ m/s, which was first obtained by Wallace in 1947 [9]. One of the most interesting aspects of graphene's energy dispersion is it's energy-momentum relationship with the valence and conductions band at $q = 0$. At this point, the dispersion relationship is linear and the conduction and valence band touch at the so-called the "Dirac' points". The region close to the Dirac point is referred to as the "Dirac cone". This makes graphene a zero band-gap semiconductor with a linear energy dispersion for both type of charge carriers. The Dirac points touching at K and K' points in momentum space can be seen in fig. 2.2b, gives rise to a valley degeneracy with $g_v = 2$ [7, 8].

The energy dispersion of graphene resembles that of massless relativistic particles which are described by the Dirac equation. A direct consequence of the latter is that the cyclotron mass depends on the square root of electronic density, given by [7, 8]:

$$m^* = \frac{1}{2\pi}\Big[\frac{\delta A(E)}{\delta E}\Big]_{E=E_f} \tag{2.9}$$

where A(E) is the k-space area, given by:

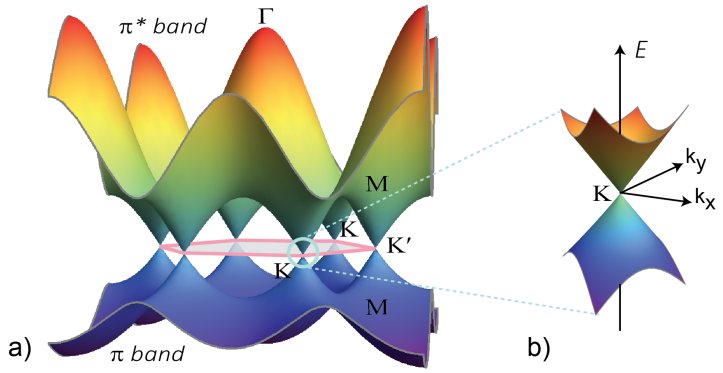


**Figure 2.2:** a) Electronic dispersion of single layer graphene lattice and b) Band structure in the close vicinity of the K and K' points.

$$A(E) = \pi\, q\, (E)^2 = \pi \frac{E^2}{v_f^2}. \tag{2.10}$$

The electronic density is related to the Fermi momentum $k_f$ via $k_f^2/\pi$ = n, and leads to:

$$m^* = \frac{\sqrt{\pi n}}{v_f}. \tag{2.11}$$

Furthermore, the density of states of graphene can be derived using Eq. 2.5; and close to the Dirac points the dispersion is approximated equation using Eq. 2.8:

$$D(E) = \frac{4E}{2\pi(\hbar v_f)^2}. \tag{2.12}$$

where the factor four accounts for the spin and valley degeneracy. Although at the Dirac point the charge density is expected to be zero, a residual charge density is typically observed experimentally due to doping, thermal broadening, disorder and defects in the graphene film. Nevertheless, a region with low electron and hole density can be observed, which is termed as the 'charge neutrality point' (CNP). The transition from electron to hole transport takes place smoothly, and can for instance be achieved using an external 'gate', allowing for tuning of the charge carrier density, given by [10]:

$$n = \frac{C_g(V_g - V_{off})}{e}. \tag{2.13}$$

where $C_g$ is the gate capacitance per unit area (F/cm$^2$), $V_g$ the gate voltage (V),

$V_{off}$ an offset of the CNP due to chemical doping and $e$ the elementary charge. In case of pristine graphene, $V_{off}$ can be ignored due to the absence of residual doping. The field effect mobility can be estimated by [10]:

$$\mu = \frac{1}{C_g}\frac{\delta\sigma}{\delta V_g}. \tag{2.14}$$

where $\sigma$ is defined by:

$$\sigma = \frac{I\,L}{V_{SD}W}. \tag{2.15}$$

where $V_{SD}$ is the bias potential and L & W the dimensions of the graphene sample.

### 2.1.1. Phonon dispersion in graphene

In this section the phonons in graphene are discussed briefly which is helpful in understanding the different Raman modes of graphene in the upcoming chapters. The phonon dispersion of graphene is shown in fig. 2.3. The graphene unit cell has two atoms (2.1), which leads to six phonon branches, three acoustic (A) and three optical phonons (O). Four of the phonon branches are in-plane (two acoustic and two optical) while the other two are out-of-plane phonon branches. Depending on the direction of the zone-center mode, the modes are known as transverse (T) or longitudinal (L) [11–14].

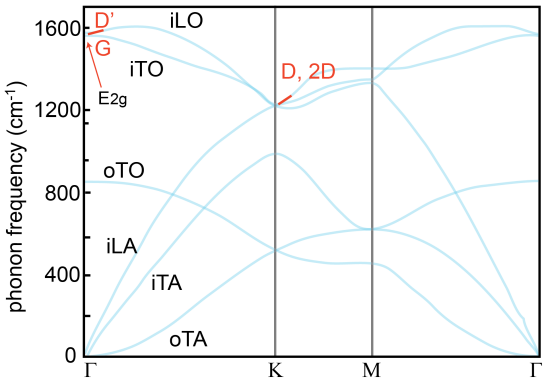


**Figure 2.3:** Phonon dispersion of graphene. Some of the prominent phonons (D, G and 2D) in graphene are highlighted with the $\Gamma$, $K$ and $M$ symmetry points are shown. Redrawn with permission from Venezuela et al [15].

At the Brillouin zone center $\Gamma$ there are: $A_{2u}$+$B_{2g}$+$E_{1u}$+$E_{2g}$ modes. The $E_{2g}$ mode is the only Raman active mode. There is one degenerate in-plane optical

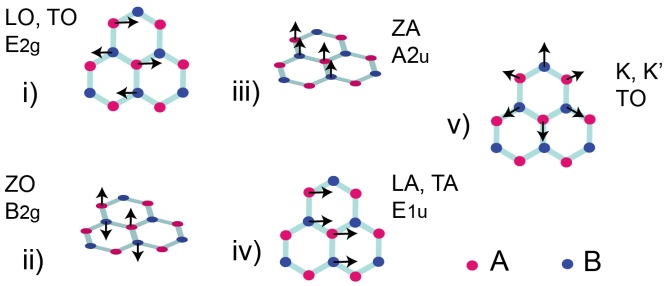


**Figure 2.4:** Representation of phonon vibration contributing to major Raman bands in graphene (i-v). iTO and iLO phonons leading to the G band vibrations at the Γ-point and D-band vibrations from the iTO phonon at the K-point. The movement of the lattice is described using the black arrows.

mode $E_{2g}$ and one out-of-plane optical mode $B_{2g}$. The $E_{2g}$ phonon at the Γ point corresponds to the origin of G-band in graphene. The D-peak originates due to the breathing mode of the six-atom rings (2.4) and is activated by the presence of defects in the graphene lattice [11, 12, 16]. The various phonon modes are represented in fig. 2.4 i-v. The LO and TO phonon modes at the Γ point are degenerate and represent the $E_{2g}$ group. The out-of-plane movement of the sublattice A, B is represented by the ZO phonon belonging to the $B_{2g}$ group. In the case of ZA ($A_{2u}$), LA and TA ($E_{1u}$) phonons both the sublattice move synchronously and are infrared active.

The iLO (in-plane longitudinal optical) and iTO phonons are mainly responsible for the Ramans bands of graphene, which are energetically dispersive at the Γ and $K$ points (2.3). The phonon energy softening at these points is called as the Kohn anomaly [17]. During this process, the phonon creates a virtual electron-hole pair which recombines and creates another phonon, as a result of which the phonon lifetime and energy are lowered. The Kohn anomaly lead to strong electron-phonon coupling (EPC) around these two points [17]. The degree of phonon energy renormalization is determined by the electron-phonon coupling strength [11, 12, 16, 18]. Further details about the Raman bands in graphene is discussed in chapter 4.

## 2.2. Classical Hall effect

The Hall effect was discovered by Edwin Hall in 1879 during his doctoral work at John Hopkins University, Maryland, USA [19]. The principle of Hall effect is

extensively used in magnetic field sensors. The applications range from automotive industry, telecommunications and consumer electronics [20].

The principle of Hall effect is as follow: when a current $I$ (applied bias current) flows through a conductor in presence of a large magnetic field $B$, a voltage $V_H$ (Hall voltage) is developed transverse to the direction of the applied current $I$. The Hall effect principle is detailed in fig. 2.5, with $I$ being the applied current and $V_H$ is the Hall voltage [19].

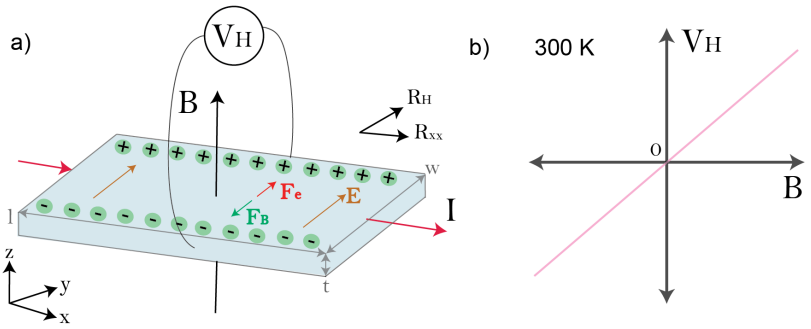


**Figure 2.5:** Representation of the Hall effect in a conductor. The application of a magnetic field perpendicular do the conductor results in the Hall voltage $V_H$ transverse to the current flow $I$. b) Typical representation of Hall voltage response to varying magnetic fields under ambient conditions in thin film conductors.

This Hall voltage $V_H$, was found to be dependent on the applied current $I$ and the magnetic field $B$ i.e.:

$$V_H \propto I, B \tag{2.16}$$

The observation of this effect was explained by the taking into account of the Lorentz force $F_B$ *i.e.* a charged particle moving in a magnetic field experiences a force given by:

$$F_B = e(\vec{v} \times \vec{B}) \tag{2.17}$$

where $e$ is the charge of an electron, $v$ the electron velocity (or electron drift velocity $v_d$) and $B$ the magnetic field. In fig. 2.5 we observe that, as a result of the Lorentz force $F_B$, the electrons accumulate along one side of the conductor. This process results in a charge imbalance, which in turn creates an electric field $E$. The electrostatic force due electric field $E$ is given by:

$$F_e = \frac{e\, V_H}{w} \tag{2.18}$$

where $e$ is the electron charge, $V_H$ is the voltage difference developed across the sample i.e. the Hall voltage and $w$ the width of the Hall bar. In the equilibrium state, we have:

$$\frac{e\,V_H}{w} = e\,\nu_d\,B \tag{2.19}$$

The current $I$ flowing through the conductor is then given by:

$$I = N\,e\,\nu_d\,A \tag{2.20}$$

where $N$ being the electron density, $\nu_d$ the electron drift velocity and A is the cross section of the conductor ($A = w\,d$, $d$ is the sample thickness). Using the equations 2.19 and 2.20, the Hall voltage is given by:

$$V_H = \frac{I\,B}{N\,e\,d} \tag{2.21}$$

For thin samples, the electron density is defined by the planar density and the 2D electron density per unit area is given by $n = N\,d$, the Hall voltage is then given by:

$$V_H = \frac{I\,B}{n\,e} \tag{2.22}$$

The Hall resistance $R_H$ is given by $R_H = V_H/I$ i.e.:

$$R_H = \frac{B}{n\,e} \tag{2.23}$$

It is important to note that the Hall resistance $R_H$ is only dependent on the magnetic field $B$ and the charge density $n$, while being independent of physical parameters such as conductor dimensions. The longitudinal resistance $R_{xx}$ measured along the direction of the current flow is unaffected by the magnetic field and is given by:

$$R_{xx} = \frac{V_{xx}}{I} \tag{2.24}$$

### 2.2.1. Classical Hall effect in graphene

A typical graphene device in Hall bar configuration is shown in fig. 2.6 a. The Hall bar geometry allows to measure both Hall resistance ($R_{xy}$) and longitudinal resistance ($R_{xx}$). The device consists of patterned graphene film in a standard Hall bar geometry on top of a 300 nm thermal grown silicon dioxide and bulk p-doped

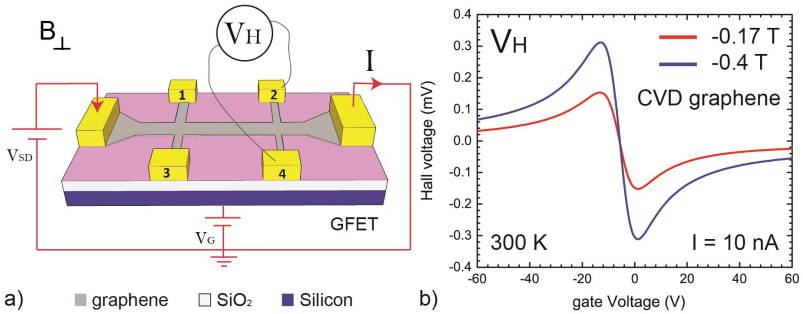


**Figure 2.6:** a) Representation of a graphene Hall bar device. The Hall voltage is measured transverse to the direction of the current flow either between 1-3 or 2-4. b) The Hall voltage response $V_H$ of a typical graphene Hall bar device. The bipolar Hall voltage response shows the transition from electron to holes as majority charge carriers.

silicon substrate. This geometry constitutes a typical graphene-field effect transistor, and using this configuration, the charges in graphene can be modulated by applying a potential on the bulk silicon ($V_G$). In this case the silicon substrate acts as a back gate (2.6). The current $I$ is passed between the current contacts also called the '*source*' and the '*drain*' contacts and the Hall voltage can be measured either between the $1-3$ or $2-4$ contacts. In fig. 2.6b we can observe the Hall effect response of such a graphene device at room temperature for two magnetic field values. One of the interesting features of the response is the bipolar Hall voltage behavior. This change in sign of the Hall voltage is due to the transition in majority charge carriers from electrons to holes. This change is observed as the gate voltage is tuned from negative to positive values [21, 22].

### 2.2.2. Applications of Hall effect sensors

The Hall effect sensor market is actively growing and the market value is expected to be around 2 billion USD by 2020 with a growth rate of 8.5%. The automotive industries are among the largest consumers of sensors based on Hall effect and consumer electronics on second place. Some of the key advancements in the Hall sensor technology is the sensing element, *i.e.* the conductor material. The advancement in the material science has been pivotal in producing highly sensitive Hall effect sensors. Some of the commonly used materials for producing Hall effect sensors are: Silicon (Si), GaAs and InAs. New and upcoming materials such as single layer graphene have been shown to provide even higher magnetic field sensitivity when compared to existing materials. Ultrahigh charge mobilities, low

charge densities in these materials play an important role in improving the Hall sensitivity. Sensing the Hall voltage lies in the core of several applications based on the principle of Hall effect. This is used in applications such as: position, rotational speed, fluid flow, current and pressure sensing, smartphones and global positioning systems [21, 22].

## 2.3. Quantum Hall effect

In 1980, Klaus von Klitzing was performing an experiment similar to Edwin Hall. However, the conditions of the experiment were different i.e. low temperature and in the 2D limit. During the experiment with silicon-based samples, Klaus von Klitzing discovered that the Hall conductivity was exactly quantized. This discovery earned Klaus von Klitzing the Noble prize in Physics in 1985. In the quantum Hall effect, at well defined magnetic fields the Hall resistance plateaus were observed together with a vanishing longitudinal resistance [23, 24]. The resistance quantization was found to be:

$$R_H = \frac{1}{n}\frac{h}{e^2} \tag{2.25}$$

where, $n$ is an integer value, $h$ the Plank's constant and $e$ the electron charge. This type of resistance quantization and the zero resistance value of $R_{xx}$ can be explained using a two-dimensional system with Landau levels.

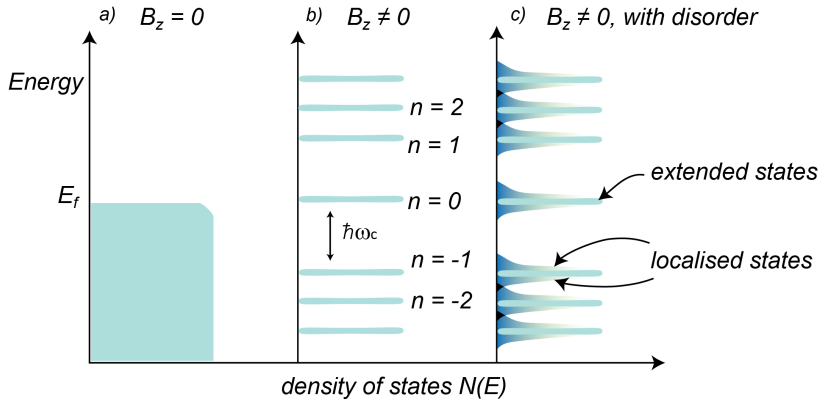


**Figure 2.7:** Representation of density of states versus energy in a) $B_z$=0 b) $B_z \neq 0$ and c) $B_z \neq 0$ in presence of disorder.

In the presence of a high magnetic field perpendicular to the sample plane, the

density of states (DOS) collapses onto quantized orbits, which are separated by well defined gaps. These states are called extended states [23, 24]. Such discrete states are called the Landau levels, named after the Soviet physicist Lev Landau himself [25]. The scenario when the magnetic field $B_z$=0 is shown in fig. 2.7a, where DOS is a constant function of energy. In the presence of magnetic field $B_z \neq 0$, the quantization of DOS into $\delta$-functions is depicted in fig. 2.7b (in case of zero disorder). By considering the Schrödinger equation for a single electron in a 2D system in the presence of a magnetic field, the Landau level (LL) energy is given by:

$$E_N = (N + 1/2)\hbar\omega_c \tag{2.26}$$

where N=0,1,2,.. is the LL index and the cyclotron frequency is given by:

$$\omega_c = \frac{eB}{m^*} \tag{2.27}$$

where $B$ is the magnetic field and $m^*$ the effective mass. In fig. 2.7c, a broadening of the $\delta$-functions in the presence of disorder, as is the case in real samples is depicted. The states due to the presence of disorder are called localised states. The LL degeneracy or the number of LL states per unit area is given by:

$$n_B = \frac{eB}{h} \tag{2.28}$$

With the increase in the magnetic field, the spacing between the LLs increases *i.e.*, it requires more electrons to fill each of the LL. The LLs are filled sequentially upto the Fermi level. At low magnetic fields and low temperatures, a large number of LLs is filled and upon increase of the magnetic field, the LL degeneracy increases, resulting in fewer LL being occupied. At sufficiently large magnetic fields, only the lowest LL is occupied. Between these two scenarios, there are special cases which contain an integer number of LLs that are exactly filled, given by:

$$B_\nu = \frac{1}{\nu}\frac{nh}{e} \tag{2.29}$$

where $\nu = \frac{n}{n_B}$ is called the filling fraction. This filling fraction provides the ratio of number of electrons to the number of available states per LL. Using 2.28, the filling fraction can be written as:

$$\nu = \frac{n}{n_B} = n\frac{h}{eB} = n\frac{\phi_o}{B} = n2\pi l_B^2 \tag{2.30}$$

where $\phi_o = h/e$ is the flux quantum and $2\pi l_B^2$ is the area of a Landau level and $l_B = \sqrt{\hbar/eB}$. At the exact filling factors, all the lower LLs are completely filled while being separated by the cyclotron energy gap of $\Delta = \hbar\omega_c$. Since there are no states between the quantized states, there is no scattering, provided that $k_B T < \Delta$. This leads to a dissipation-less transport and hence the resistance $R_{xx}$ is zero. From the classical Hall effect equation we know that $R_H = B/ne$. By substituting Eq. 2.29, we obtain:

$$R_H = \frac{1}{\nu}\frac{h}{e^2} \tag{2.31}$$

By considering transport in terms of conductance, from Drude model, the conductivity is given by:

$$\sigma = \frac{ne^2\tau}{m^*} \tag{2.32}$$

where the conductivity defines the relation between the current density ($J$) and the electric field ($E$), $e$ is the electron charge, $n$ the charge density, $m^*$ the effective mass and $\tau$ the charge scattering lifetime.

At zero magnetic field, the conductivity is isotropic and given by: $\sigma = 1/\rho$. In the presence of a magnetic field however, the conductivity is anisotropic and is given by a 2D tensor relation:

$$\sigma = \begin{pmatrix} \sigma_{xx} & \sigma_H \\ -\sigma_H & \sigma_{xx} \end{pmatrix}$$

The resistivity tensor can be written as:

$$\rho = \frac{1}{\sigma_{xx}^2 + \sigma_H^2} \begin{pmatrix} \sigma_{xx} & -\sigma_H \\ \sigma_H & \sigma_{xx} \end{pmatrix}$$

From the above mentioned resistivity relation, the conductivities of the QHE state can be written as:

$$\sigma_{xx} = 0, \quad \sigma_H = \nu\frac{e^2}{h} \tag{2.33}$$

The vanishing longitudinal resistance in QHE regime can also be understood from the point of view of conductivities *i.e.* at exact filling the Fermi level lies in the gap between LLs, where the DOS is zero. The condition of exact filling factors, however is only possible at unique magnetic field values [23, 24, 26, 27].

### 2.3.1. Integer quantum Hall effect in graphene

In fig. 2.8 we can see the representation of graphene's band structure in the absence (2.8 a) and in the presence of a magnetic field (2.8 b). By solving the Dirac equation for a perpendicular magnetic field, the LL energy states for graphene can be written as:

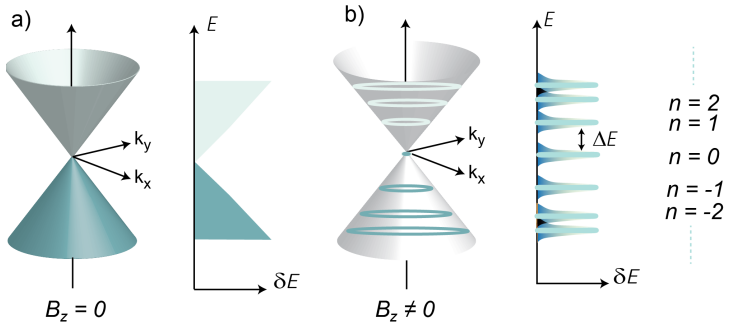


**Figure 2.8:** a) Representation of single layer graphene's band structure in the absence of magnetic field and b) in presence of a magnetic field.

$$E_N = sgn(n)\sqrt{2e\hbar v_F^2|n|B} \tag{2.34}$$

From Eq. 2.34 one can notice that for the first two LLs, the energy gap is large. This is one of the main reasons behind the possibility of observing the Quantum Hall effect in graphene, even at room temperature [28]. The integer $n$ represents electron-like (n>0) or a hole-like (n<0) LL indices [7, 8, 10].

The appearance of n=0 LL at the Dirac point is an indication of a special electron-hole degenerate LL due to the band structure of graphene. The Hall conductivity can be written as:

$$\sigma_H = \frac{4e^2}{h}(N + 1/2) = \pm 2, \pm 6, \pm 10, ... \frac{e^2}{h} \tag{2.35}$$

The first values of $\pm 2$ belong to the zero energy LLs which consist of both electrons and holes, whose value is $\approx$12.957 $k\Omega$. In fig. 2.9 we can observe such

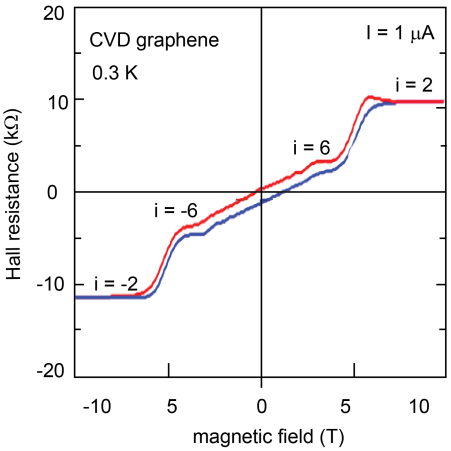


**Figure 2.9:** Hall resistance versus Magnetic field of a CVD graphene sample at 0.3K, gate voltage = 8V. The red and blue curves are measured across two different pairs of voltage contacts.

a resistance quantization in a CVD graphene sample. The $R_H$ plateau i=2 can be seen to be quantized around 12.906 k$\Omega$, with the onset of the plateau i=6 also being present [5, 29, 30].

## 2.4. Quantum Hall resistance standard: Motivation

Soon after the discovery of the quantum Hall effect, the idea of a stable resistance standard was also coined. This gathered immense interest from the metrology community, as in the case of a quantum Hall resistance (QHR) standard, the resistance is only given by fundamental constants such as electron charge $e$ and Plank's constant $h$ [31]:

$$R_H = \frac{h}{e^2} \tag{2.36}$$

Such a QHR standard, has several advantages over a passive wire wound resistor standard, whose resistance is defined by:

$$R = \frac{\rho L}{A} \tag{2.37}$$

where $\rho$ is the material resistivity, $L$ is the length of the resistor and $A$ is the cross section area. These type of wire-wound resistance standards are bound to be

temperature, humidity, air pressure sensitive which cause their resistance values to drift in time [32]. Due to these prime limiting factors, there has been an astounding interest to replace them with a more robust resistance standard that is independent of sample dimension and that offers greater precision and repeatability *i.e.* the QHR standards [32, 33]. This allowed for the definition of a new international resistance standard for electrical resistance called the Klitzing constant ($R_{K-90}$) and given by:

$$R_{K-90} = \frac{h}{e^2} = 25812.807557(18)\Omega \tag{2.38}$$

$$\frac{R_{K-90}}{2} = \frac{h}{2e^2} = 12906.403778\Omega \tag{2.39}$$

### 2.4.1. QHR requirements

There are several stringent requirements to be met by a QHR in-order to be established as an international electrical resistance standard. These requirements stem from the rigorous measurement demands set by the metrology institutes. Some of the prime requirements are: i) a high source current ($I_{SD} > \mu A$) ii) sub-Ohmic contacts to the two-dimensional electron gas (2DEG) iii) ease of operational conditions iv) repeatability v) high accuracy of resistance quantization.

A high value of source current ($I_{SD}$) is desired, as this improves the measurement signal quality ($V_{xx}$) i.e. better signal-to-noise ratio. In the QHE regime, given that $R_{xx}$ drops to zero *i.e.*, for instance 0.1 m$\Omega$, with a bias current $I_{SD}$= 1$\mu A$, the voltage measured is $V_{xx} = I_{SD}R_{xx} = 0.1\ nV$. Such measurements are much easier to perform if the QHR can handle higher bias current (tens of $\mu A$) in the QHE regime without dissipation, thereby increasing the magnitude of $V_{xx}$. Moreover, the contacts of the Hall bar device must be Ohmic and the contact resistance $R_c$ must be below $1\Omega$. If the $R_c$ is high, this can affect the resistance quantization. The quantization accuracy is of prime importance in realizing a good QHR and a deviation accuracy of few parts per billion or higher is required [33].

### 2.4.2. Advantages of a graphene based QHR

The QHE in graphene is defined by Landau levels at energies described by 2.34 i.e. $\pm\nu_F\sqrt{2\hbar neB}$. Interestingly, the energy spacing between the first two LLs is $\Delta E^{01}(B)$ = 36 $\sqrt{B[T]}$ meV, which is much higher than the widely used 2DEG based on Gallium Arsenide (GaAs, 1.7B[T] meV) [34–37]. Moreover, in graphene,

the plateau $\nu = 2$ Hall resistance plateau of value $R_K/2$ can even be observed at room temperature [28].

This opens up the possibility of QHR operating under relaxed conditions *i.e.* higher temperature and lower magnetic fields. The latter is not possible to achieve in GaAs based QHR due to the smaller energy gap (1.7B[T] meV). The comparison of the energy spacing in graphene ($\nu = 2$) and GaAs with respect to magnetic field is shown in fig. 2.10. For instance, at 12T, $\Delta E^{01}_{graphene}/\Delta E_{GaAs} \approx 6.1$ i.e. at 12 T the energy level spacing between the first two LLs is 6.1 times larger in graphene. This type of QHR operating under relaxed conditions brings forth the opportunity to disseminate these standards from the national metrology institutes to industrial calibration facilities. The latter is due to the ease in realization of a cryo-free table-top systems operating in liquid-nitrogen temperature which can offer up-to $< 6T$ [38].

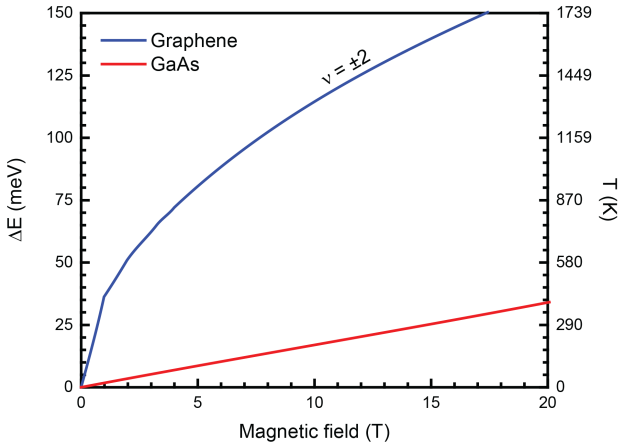


**Figure 2.10:** Plot of energy level spacing of $\Delta E^{01}_{graphene}$, $\Delta E_{GaAs}$ versus magnetic field (T).

## 2.5. CVD graphene based QHR

Several techniques can be used to produce high quality graphene. In this work, we have used chemical vapor deposition (CVD) technique to produce high quality graphene films. The main advantages of CVD technique over another widely used technique i.e. the epitaxially grown graphene are i) the CVD grown graphene can be transferred onto several substrates of choice, ii) charge carrier density tuning via bulk back gate and iii) lower cost of production (substrate). A brief

comparison of CVD graphene with other techniques in terms of quality versus price can be found in 2.11. Graphene film quality can be quantified using various characterization techniques such as: Raman spectroscopy, electrical transport and electron microscopy. Using these tools it is possible to measure the charge carrier mobility, defect density, mechanical strength, film uniformity and so-on. We can observe that CVD graphene offers better quality for a relatively lower cost of production [39]. Using the CVD technique it is possible to produce high-quality graphene samples, which is advantageous for the development of a robust and reproducible QHR.

Many studies have been performed to test the potential of graphene as a QHR and compared the operational parameters with the well-established GaAs QHR [33]. In epitaxially grown graphene on SiC (Silicon carbide) samples an unprecedented accuracy of $10^{-9}$ quantization of $R_{K-90/2}$ has been achieved by several groups. The measurement conditions of the SiC samples were: i) magnetic field range of 10-19T and ii) source current of tens of $\mu A$. In an exfoliated graphene on $SiO_2$ sample, the $R_H$ value was measured with an experimental uncertainty of 15x$10^{-6}$. It was found that high contact resistances limited the possibility of obtaining a better quantization [36, 40].

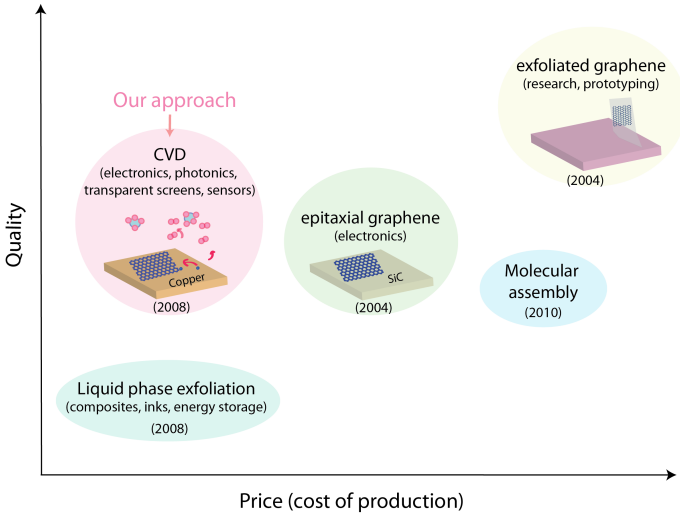


**Figure 2.11:** Brief comparison of various graphene production techniques with their respective quality and price of production. Our approach i.e. CVD of graphene has the potential in offering better quality material for a relatively lower cost of production. Adapted with permission from Novoselov et al. [39].

Another study on exfoliated graphene on GaAs substrate performed by the PTB group in a 30x150 $\mu m^2$ Hall bars revealed an uncertainty of -5.1$\pm$6.3x10$^{-9}$ at 60 mK and 18T [41]. However, due to the limitation in the size of the exfolaited graphene flakes, mass production of such samples is challenging. Interestingly, in large area CVD graphene film based QHR studies, the best uncertainty result achieved so far is $\sim 10^{-2}$ at 1.7K with a residual longitudinal resistance of $\sim$500 $\Omega$ [42]. The differences in the uncertainties observed in different graphene samples allows the possibility to further understand the limitations in realizing state-of-the-art graphene based QHR.

### 2.5.1. This work

In our study with CVD graphene, an unprecedented quantization accuracy of within $\approx$ **30 parts in 10$^9$** for a range of gate voltages has been observed in CVD graphene Hall bars fabricated on $SiO_2$ substrates for the first time, as of the writing of this thesis (0.3 K, $I_{SD} = 5\ \mu$ A, 12 T). During this study, it has been observed that the quality of the graphene films are highly important and play a vital role in the development of ultra-low longitudinal resistance in the QH regime. The CVD growth technique and further characterization and measurement studies are detailed in the upcoming chapters. See table 2.1 for comparison of various uncertainty measurements of graphene based QHR studies performed by different NMIs.

| NMI | Type of graphene | Uncertainty |
|---|---|---|
| HFM lab Nijmegen | exfoliated (2008) | 15 ppm (350 mK, 3 $\mu$A, 14 T) [43] |
| NPL, UK & Chalmers | epitaxial (2010) | 0.5 ppb (4 K, 10 $\mu$A, 5T)[38] |
| NIST USA | CVDG on $SiO_2$ (2011) | 10 ppt* (1.7 K, 14 T) [42] |
| PTB, Germany | exf. on GaAs (2012) | -5.1 ppb (60 mK, 10 $\mu$A, 18 T) [41] |
| LNE, France | epitaxial (2016) | 0.01 ppb (1.3K, 50$\mu$A, 5 T)[44] |
| **This work** | CVDG on $SiO_2$ | $<$ 30 ppb (0.3 K, 5 $\mu$A, 12 T) |

**Table 2.1:** Collection of various high precision measurements of graphene based QHR performed by different NMIs on different type of graphene samples. *ppt: parts per thousand.

### 2.5.2. Brief insight into costs of graphene production

Graphene is at the forefront of being one of the first 2D material to be integrated into real life applications. One of the easiest ways to mass produce graphene is via liquid phase exfoliation process (LPE). Using the LPE technique micro to nano meter scale graphene platelets can be produced. Such graphene platelets can be combined with other materials and can be used to produce composite materials that offer superior mechanical properties. One of the widely talked about applications of such graphene platelets is the large-area transparent, flexible and conductive layers/screens for touch screen and display applications. This application of graphene is seen as a replacement for the presently existent ITO (Indium Tin oxide) based applications. A brief cost comparison of graphene and ITO production is made in 2.2 [45].

| **material** | **cost (production)** |
|---|---|
| graphite | 1.50 - 2.00 $ /kg |
| Indium (solid form) | 650 $ /kg |
| Indium Tin oxide | 800 $ /kg |
| graphene nano-platelets (surface area: 500-1000 $m^2/g$) | 220 $\sim$ 300 $ /kg |

**Table 2.2:** Cost comparison of graphene and Indium Tin oxide (ITO). Note: The graphene nano-platelets are specified using the term 'surface-area' coverage.

# 3

# Chemical vapor deposition of graphene and transfer

## 3.1. Abstract

Graphene can be produced in several ways. Depending on the application and graphene quality requirements, the route towards large scale graphene production can be charted further. The various techniques available to produce graphene are: i) mechanical exfoliation ii) chemical vapor deposition (CVD) iii) epitaxial graphene iv) plasma enhanced CVD (PECVD) and v) liquid phase exfoliation (LPE). Out of all the fore mentioned techniques, chemical vapor deposition and epitaxial growth of graphene are widely considered to mass produce high-quality single layer graphene films with excellent electrical and mechanical properties. In this chapter, CVD of graphene on copper substrate and its transfer onto $SiO_2$/Si substrate is discussed. Transfer techniques studied and developed during this thesis are detailed along with their respective advantages and limitations.

## 3.2. Chemical vapor deposition of graphene

One of the most widely used techniques in the semiconductor industry to produce high quality materials is the 'chemical vapor deposition' (CVD) technique. In a typical CVD process, the target substrate is exposed to volatile precursors that chemically react and decompose to form the desired deposit. Several materials namely: $SiO_2$, SiC, $Si_3N_4$, graphene, carbon nanotubes, various high-k materials and many more can be produced using the CVD process.

CVD of graphene has been on the rise since 2008 [46–48]. It is being considered as one of the prime methods to mass produce high quality CVD graphene with electrical and mechanical properties comparable to that of exfoliated graphene [49, 50]. CVD graphene offers several advantages compared to other graphene production techniques as highlighted in fig. 2.11, such as: i) possibility to transfer graphene onto other substrates ii) relatively lower cost of production iii) re-usability of growth substrate. CVD graphene now can be produced even on roll-to-roll (30 inch & 100 m) basis, which can be useful to produce next generation flexible displays [51, 52].

### 3.2.1. Growth chamber and dynamics

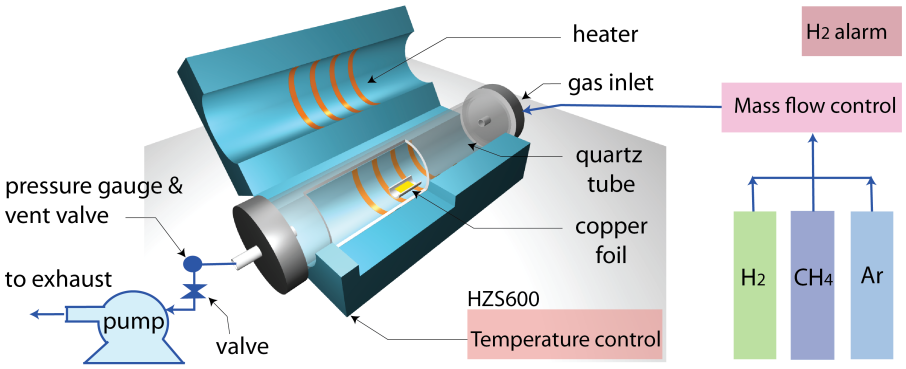


**Figure 3.1:** Graphene chemical vapor deposition system design. The prime building blocks of the system are: i) quartz tube ii) oven iii) gas flow control system iv) pressure gauge v) vacuum pump and vi) hydrogen gas alarm unit.

The detailed design of our hot-wall CVD chamber is shown in fig. 3.1. The CVD chamber primarily consists of a quartz tube, hot-wall oven and gas inlet/outlet connections. A scroll pump and a flow valve is used to modulate the pressure

inside the growth chamber and the gas flow is set using appropriate mass flow controllers. The temperature of growth condition is set and modulated using the Carbolite HZS600 oven itself.

The gas precursors used during the graphene CVD process are: hydrogen ($H_2$), argon (Ar) and methane ($CH_4$). Methane gas acts as the carbon source during the graphene growth. Various other types of carbon sources, in gaseous and solid phase can be used as growth precursors, such as: acetylene, ethylene and polymer films [47]. Methane gas is most preferred for the graphene growth due to its low pyrolysis rate and low formation of bi and multi layer graphene films in comparison to other gas precursors such as acetylene ($C_2H_2$) [47, 53].

Several metals can be used for CVD graphene synthesis such as: Cu, Co, Ni, Rh, Ir, Pt, Fe, Ru [54]. Copper is used as the growth substrate during graphene CVD process. The advantages of using copper as the growth substrate are: i) low carbon solubility ii) low cost iii) weak-coupling of as-grown CVD graphene and copper substrate and iv) ease of copper substrate handling (etching, transfer) [55]. The fore mentioned advantages make copper a prime choice for graphene CVD.

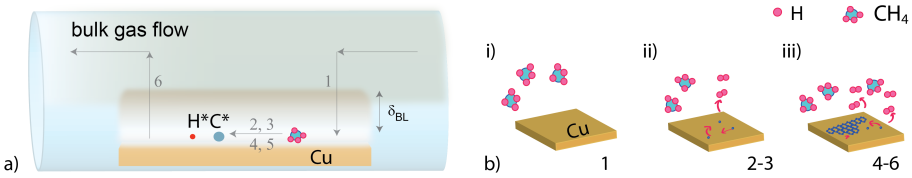


**Figure 3.2:** a) Side view of the growth chamber (a) and on copper substrate (b) demonstrating the various processes including adsorption (i), diffusion (ii) and desorption of active species (iii) during graphene growth.

During the CVD process, the reaction temperature, pressure, growth substrate, growth precursors and gas flow conditions are pivotal in determining the reaction byproduct. In fig. 3.2 a and b, we can see the typical processes taking place on copper substrate during the graphene CVD process. At the appropriate growth temperature and pressure, the carbon species reach the copper substrate diffusing through the "boundary layer" ($\delta_{BL}$). The boundary layer on the growth substrate is described in fig. 3.2 is a result of the pressure, gas flow (density) conditions inside the growth chamber. These carbonaceous species get adsorbed on the copper surface (fig. 3.2 a-2) and decompose to form active carbon species (fig. 3.2 a-3). These active carbon species diffuse on the surface of catalyst i.e. copper surface forming the graphene lattice fig. 3.2 a-4. The inactive species and the reaction

byproducts are desorbed from the surface via the boundary layer and are swept away with the bulk gas flow (fig. 3.2 a-5, 6) [56]. Another view describing all the processes taking place on copper surface is detailed in fig. 3.2 b i-iii.

The growth processes can be briefly classified into two regimes, which is dependent on either the growth dynamics occur in the boundary layer or closer to the substrate surface. The two regimes are namely: i) mass transport region and ii) surface reaction region [56]. Two type of fluxes can co-exist in these conditions:

$$F_m = h_g(C_g - C_s) \tag{3.1}$$

$$F_s = K_s C_s \tag{3.2}$$

where $F_m$ is the flux of the active species through the boundary layer and $F_s$ is the flux of the active species consumed on the copper surface, $K_s$ is the surface reaction constant, $C_g$ is the concentration of gas in the bulk flow, $C_s$ is the concentration of active species and $h_g$ is the mass transport coefficient. Considering the CVD conditions of our system i.e high temperature (1000 °C) and pressure (>1 mbar), the growth in our case is performed in the mass transport dominated regime i.e. wherein $K_s \gg h_g$. By operating under lower pressures or UHV conditions one can transition into surface reaction dominated growth regime, where $h_g \gg K_s$ [56]. All the CVD graphene growth presented in the next section were performed under mass-transport dominated regime.

### 3.2.2. Growth recipe

In 3.3, a typical CVD graphene growth recipe is described. The various stages of the graphene CVD process are: i) pre-annealing of copper substrate ii) growth phase and iii) cooling of the chamber. The copper foils used for the CVD growth are commercially bought and require thorough cleaning prior to the growth. The copper foils are first cleaned in acetic acid to remove organic impurities and copper oxide from its surface. This cleaning step is followed by the pre-anneal of the copper foils in the oven which is maintained at the growth temperature (1000°C). The copper foils used during the CVD process are polycrystalline with difference crystalline configuration. However, during the pre-annealing, the crystallinity of the copper foils can change to certain preferred orientations (111 or 100). Further growth details can be found in section B. Moreover, the commercial copper surface is not flat over large areas and consist of several corrugations on the surface. Such corrugation

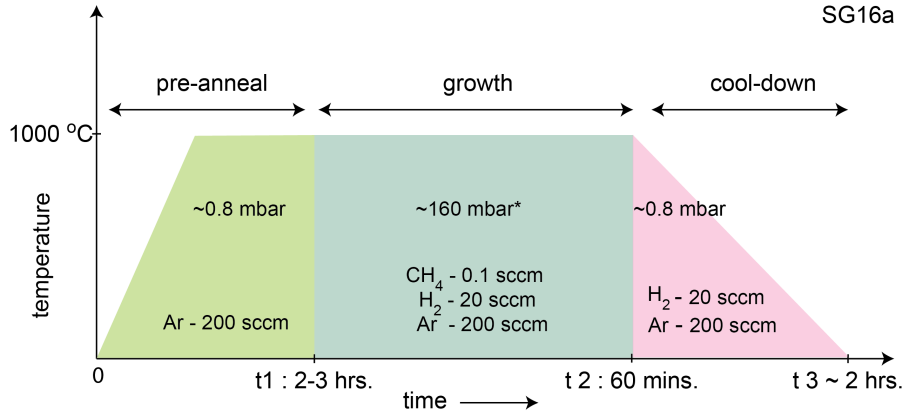


**Figure 3.3:** Description of CVD graphene growth recipe SG16a.∗ The pressure was tuned using a gas valve.

are a result of copper pressing procedure during manufacturing. A typical AFM scan of the copper foil prior to growth can be found in the appendix C.6.

The CVD graphene growth phase is initiated with the inflow of methane and hydrogen gas. The methane gas acts as the carbon precursor during the growth. The hydrogen gas however, plays a dual role during the CVD growth. It has been studied that $H_2$ helps in: i) maintaining the size and morphology of the graphene domains and ii) activate surface bound carbon species which form the monolayer graphene film [57, 58]. After the appropriate growth time, which is dependent on the methane gas concentration, the oven is cooled to room temperature in argon and hydrogen gas flow. It is important to maintain the as-grown CVD graphene film on copper in a non-oxidative environment until the oven temperature is $<350^{\circ}$C to prevent oxidation and eventual damage of the graphene film.

The conditions mentioned in the growth recipe described in fig. 3.3 is part of the recipe 'SG16a' (SG: slow growth). Since the growth time was observed to be longer for growing graphene films with larger individual domains/grains, the recipes were coined with the acronym 'SG' (slow growth). Several growth recipes were formulated and tested during this work. A brief table consisting of selected recipes out of more than 100 odd attempts are listed in fig. 3.4. As mentioned earlier in the chapter, various parameters influence the graphene growth such as: temperature, pressure and gas concentration. Out of the three options, precursor gas flow conditions was one of the main parameter tweaked to grow CVD graphene films with large individual grains ($>100$ $\mu$m).

| flow rate (sccm) | SG11 1000 °C | SG12 1000 °C | SG16 1000 °C | RG1 1000 °C | SG30 1000 °C | SG40 1020 °C | SG55* 1065 °C |
|---|---|---|---|---|---|---|---|
| pre-anneal (sccm) | $H_2$ 500 | $H_2$ 500 | Ar 100 | Ar 200 | Ar 200 | Ar 200 $H_2$ 5 | Ar 200 |
| Ar<br>$CH_4$<br>$H_2$ | 200<br>0.04<br>100 | 200<br>0.04<br>100 | 200<br>0.04<br>20 | 200<br>1.5<br>20 | 30<br>0.006<br>10 | 30<br>0.006<br>5 | 60<br>0.012<br>20 |
| PA$^{\alpha}$<br>$G_\tau$<br>$G_\chi$ | 3 hr<br>6 hr<br>~5 mbar | 3 hr<br>3 hr<br>~100 mbar | 1 hr<br>6 hr<br>~150 mbar | 2 hr<br>5 min.<br>~1 mbar | 0.5 hr<br>6 hr<br>~200 mbar | 0.5 hr<br>4 hr<br>~0.7 mbar | 12 hr<br>2 hr<br>~200 mbar |
| comments | ~ 20 μm grains | ~ 20 μm grains | ~ 200 μm grains | ~10-20 μm grains | no nucleation | square shaped grains | ~1000 μm grains |

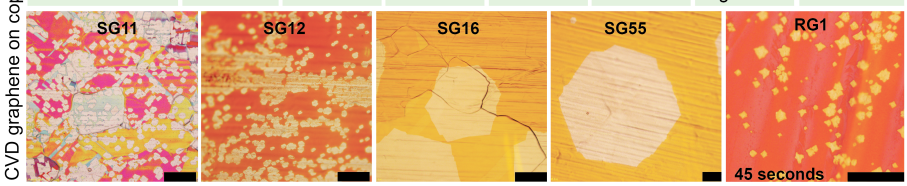


$^{\alpha}$PA: pre-anneal, $G_\tau$: growth time, $G_\chi$: growth pressure

*Copper foil electro-polished

**Figure 3.4:** Various growth recipes developed during this thesis. Optical images of as-grown CVD graphene on copper are shown below. From SG11 to SG55 it can noticed the gradual increase in the individual CVD graphene domain, scale bar: 100 $\mu$m. The foils were heated at 200 °C to oxidize the regions of Cu without graphene.

In our early recipe 'RG1', the individual graphene grains were few tens of micrometers large [59]. Given that our devices are few hundreds of micrometers in size, having a graphene film with micrometer-sized grains induces increased charge carrier scattering at the grain boundaries and lowers the charge carrier mobility of the graphene transistor. In-order to improve the charge carrier transport and field effect mobility of the graphene films, growing graphene films with large grain size is of utmost importance.

We were able to grow uniform graphene films with large individual grains by primarily controlling the hydrogen to methane concentration during the growth phase, i.e. given by:

$$\frac{C_{H_2}}{C_{CH_4}} \tag{3.3}$$

Higher the hydrogen gas concentration and lower the methane concentration,

the higher is the possibility of growing larger graphene grains [60–62]. In fig. 3.4 we can see that in SG16 the $C_{H_2}/C_{CH_4}$ is ∼500 and for RG1 the $C_{H_2}/C_{CH_4}$ is ∼13.33. This shows that the presence of higher hydrogen gas concentration during the growth phase has a direct influence on activating the surface bound active carbon species which form the graphene lattice. In growth trials with higher $C_{H_2}/C_{CH_4}$ ratio $\gg$1500, no graphene nucleation was observed (see: SG30 3.4). However, the nucleation density ($N_D$) of the graphene grains must also be controlled to facilitate the growth of individual graphene domains. In the RG1, since the methane concentration is high, the $N_D$ of graphene grains is much higher when compared to SG16. To further reduce the $N_D$, the copper foils were electropolished in diluted hydrophosphoric acid ($H_3PO_4$). In fig. 3.4 SG55, the graphene growth was performed on electropolished copper foils at 1065 °C. Millimeter scale single crystal CVD graphene grains were grown using this technique. After electropolishing of the copper foils, the surface of the foils are smoother and consist of lower defective sites, thus reducing the $N_D$ significantly and aiding the growth of large graphene grains as in SG55 [63, 64].

Furthermore, few other attempts were made towards obtaining flatter copper foils. Copper thin film (2 $\mu$m) were thermally deposited on three inch $SiO_2$/Si wafer. SEM imaging showed that the as-deposited films were nanocrystalline and the domain size can be increased by thermal annealing of the thin films. However, even after thermal annealing the copper surface was not found to be flat over large areas (∼100 $\mu$m) and deep trenches were noticed at the regions were individual domains coalesce. Please refer to appendix C.8 for the images of copper thin films evaporated on wafer and SEM images.

### 3.2.3. Influence of pressure on shape of CVD graphene grain

In fig. 3.5, the influence of pressure during the growth phase on the shape of the graphene grains is shown. In 3.5 a we can see that the graphene grains are unevenly shaped while in 3.5 b we can observe evenly shaped hexagonal graphene grains. In the case of 3.5 b, the chamber pressure was increased using the valve (see: fig. 3.1) which consequently leads to an increase in the partial pressure of $H_2$ due to the pressure build-up. The boundary layer ($\delta_{BL}$) thickness is inversely proportional to the growth pressure i.e. at high pressure the $\delta_{BL}$ thickness is lower compared to low pressure conditions [56, 65]. When the growth pressure is ∼100 times larger, due to lower desorption rate of the active carbon species,

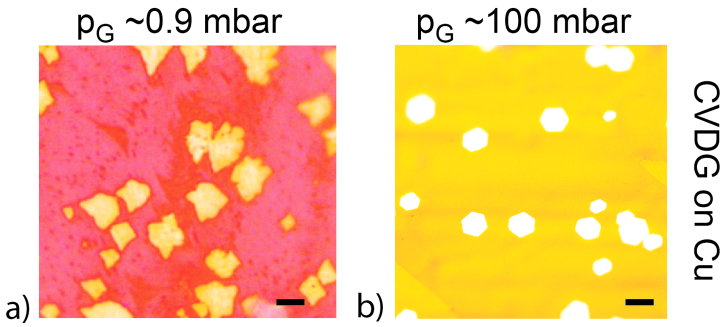


**Figure 3.5:** Influence of pressure on shape of CVD graphene grain, scale bar: 20 $\mu$m. $P_G$: growth pressure.

the graphene grains tend to form an evenly hexagonal shape as in the case of 3.5 b. Such evenly shaped hexagonal graphene grains can easily be observed under atmospheric-pressure CVD (APCVD) conditions [65]. Moreover, under LPCVD (low-pressure CVD) conditions, the copper desorption rate and the successive desorption rate of active surface bound carbon species are both higher, this can lead to unevenly shaped graphene grains shapes (4, 6-lobed structures, see: 3.6 b-c).

## 3.3. Transfer of large area CVD graphene

After the CVD growth of graphene films on copper substrate, its transfer onto suitable substrates is required. In this section various transfer procedures developed and tested during the thesis are discussed. Various limitations and advantages of the transfer processes are also briefly discussed.

### 3.3.1. PMMA assisted transfer

During the copper etching process, the graphene film needs to be supported, without which the graphene film rolls-up due to surface tension of the copper etchant solution (APS: ammonium persulphate). To circumvent this issue, the graphene film is supported by a thin polymer layer. One of the most commonly used procedures is the PMMA (poly-methyl methacrylate) assisted transfer process [46]. This is also the most simple and robust technique for large area CVD graphene transfer. Partially due to its ease of use and its common availability in standard cleanroom, PMMA is among the most favoured polymer for the transfer.

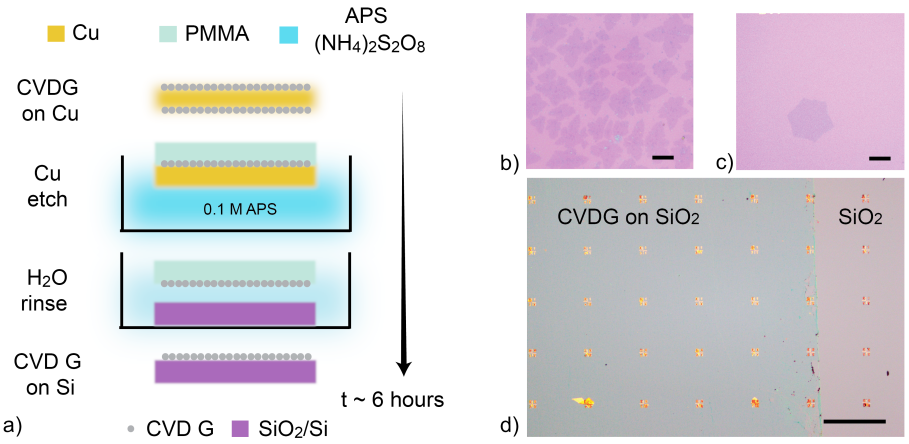


**Figure 3.6:** a) Description of PMMA assisted transfer process of CVD graphene onto $SiO_2$/Si substrates. b, c) Optical microscopy images of individual CVD graphene grains on $SiO_2$/Si substrate, scale bar 20 $\mu$m.. d) Optical microscopy image of uniform CVD graphene film transferred onto $SiO_2$/Si substrate, scale bar 200 $\mu$m.

The PMMA-assisted CVD graphene transfer process is described in fig. 3.6. During the transfer process, the top side of copper foil with CVD graphene was spin coated with 300 nm thick 50K (molecular weight) PMMA layer. The graphene layer on the bottom side of the copper foil is removed using oxygen plasma, to expose the copper foil to APS solution. After the completion of copper etching the CVD graphene/PMMA stack is rinsed in DI water and transferred onto 300 nm $SiO_2$/Si substrate. This is followed by dissolution of PMMA film in solvents. The results of the PMMA-assisted transfer process is shown in fig. 3.6 b-d, demonstrating the possibility to successfully transfer both individual CVD graphene grains and large area CVD graphene film. In fig. 3.7 millimeter scale single crystalline CVD graphene grains transferred onto $SiO_2$/Si substrate is shown. This shows the robust capability of transferring large area CVD graphene films and grains using this transfer process [66].

Some of the main limitations of the PMMA-assisted transfer process are: i) PMMA residues on CVD graphene ii) the growth substrate is etched away during the transfer process iii) time consuming transfer process. While the etch time can be reduced by increasing the copper etchant concentration, options i and ii are unavoidable. More details about the influence of APS on PMMA during the CVD graphene transfer is detailed in the next section. For AFM characterization of CVD graphene film refer to appendix C.7. Wrinkles, folds and polymer residues from the

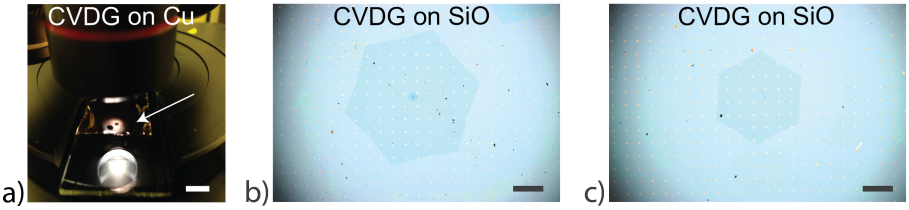


**Figure 3.7:** a) Millimeter scale single crystalline CVD graphene grains on copper is directly visible under the microscope illumination. b, c) Optical microscopy images of millimeter scale single crystalline CVD graphene transferred onto $SiO_2$/Si substrate, scale bar 500 $\mu$m.

transfer can be noticed in C.7.

### 3.3.2. Influence of APS on PMMA during CVD graphene transfer

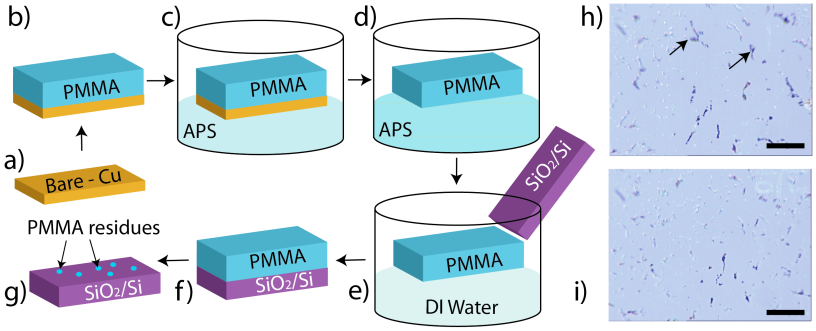


**Figure 3.8:** Standard polymer assisted wet transfer test of PMMA on bare-copper foil without graphene. a) bare copper foil b) spin coat of thin (500 nm) PMMA film on bare-copper foil c) etching of bare-Cu/PMMA stack in ammonium persulphate (APS) solution (0.1M) at t=0 d) PMMA film exposed to APS after completion of copper etching at t=t1. Time t1 depends on the strength of the etching solution and typically ranges from several minutes to hours, depending on the etchant concentration. e) rinse of PMMA film in DI water f) transfer of the PMMA film onto $SiO_2$/Si substrate g) PMMA residues on substrate after the removal of PMMA film. h-j) optical images of PMMA residues leftover from the transfer process after the bulk removal of PMMA removal. Selected polymer residues are as marked using the black circles and arrows, scale bar: 20 $\mu$m.

To better understand the cause of PMMA residues on CVD graphene after the transfer process, a control experiment with only bare copper foil and PMMA layer was devised. This helps in better understanding the influence of APS solution directly on PMMA. Such a procedure is described in fig. 3.8.

PMMA layer is spun on bare copper foil and undergoes the transfer process detailed in section fig. 3.3.1. After the transfer of PMMA film onto $SiO_2$/Si substrate, large residues of PMMA were found to be present on the substrate even after rigorous solvent exposure over long durations. In fig. 3.8 h-i the PMMA residues from transfer is shown. Our hypothesis is that the PMMA layer undergoes slight oxidation during the APS exposure, which gives rise to PMMA-residues that cannot be dissolved in solvents. Further detailed characterization of these PMMA-residues can be found under section 4.4.3 and 4.2.6.

## 3.4. Other transfer techniques

In this section all the other transfer techniques tried and developed during the thesis are discussed. The techniques are namely: i) Electrochemical transfer ii) Palladium assisted peeling of CVD graphene and iii) Metal film assisted transfer. Some of the prominent shortcomings of these transfer techniques that limited device fabrication in CVD graphene films transferred using these techniques are also discussed below.

### 3.4.1. Electrochemical transfer

One of the alternate approach for a faster transfer of large area CVD graphene onto selected substrate while preserving the growth substrate is the 'electrochemical transfer' or also known as the "bubbling" transfer [60, 67].

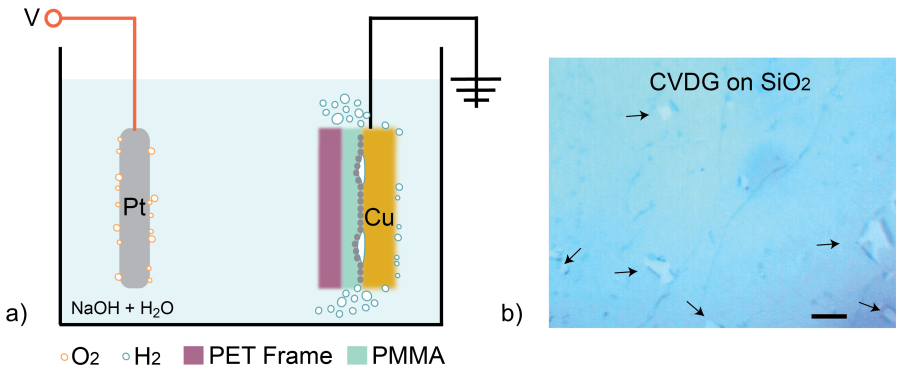


**Figure 3.9:** Electrochemical transfer process of large area CVD graphene films. a) Illustration of the electrochemical cell with Platinum (anode) and PMMA/graphene/copper (cathode) electrodes b) optical image of transferred graphene film using the electrochemical transfer process, scale bar: 20 $\mu$m. The arrows depict the holes formed during the transfer process.

This transfer process works on the principle of electrolysis. A basic description of such an electrochemical transfer approach is shown in fig. 3.9 a. The PMMA/CVD graphene/copper stack acts as the cathode while the platinum film acts as the anode of the electrolytic cell. When a current is applied and maintained at a constant level, hydrogen ($H_2$) bubbles generated during the process at the cathode, intercalate between the graphene/copper interface. Overtime, the intercalation of $H_2$ between the graphene/copper interface increases during the electrolysis process, the PMMA/CVD graphene film is eventually released from the copper surface. For better stability, PMMA/CVD graphene stack can be further supported with a PET (polyethylene teraphthalate) frame. Depending on the bias applied and the concentration of the electrolyte, the typical transfer time can range between 30 seconds to several minutes [60, 67].

Although this transfer process is relatively faster and offers re-usability of the growth substrate, one of the major limiting factor is the holes in the CVD graphene films after transfer (fig. 3.9 b). These holes can possibly occur during the electrolysis process, during which a rupture of a micro-scale $H_2$ bubble in close proximity to graphene is imminent and unavoidable.

### 3.4.2. Palladium assisted peeling of CVD graphene

Another large area transfer technique developed during this work is the 'palladium assisted peeling' of CVD graphene films. This procedure is described in detail in fig. 3.10.

In 3.10 a we show an optical image of thermal deposited palladium (Pd) layer (80 nm) directly on top of CVD graphene on copper. Since the adhesion of graphene to palladium is stronger than graphene to copper, the entire CVD graphene film can be peeled from the copper growth substrate. A tape or a polymer layer on top of palladium/graphene/copper stack can be useful during the peeling process. In fig. 3.10 b an optical image of CVD G on palladium film is shown. In-order to check the uniformity of the peeling process, the copper foil was maintained at 200 °C for a minute. During this heating step, the regions of copper foil not covered by graphene is oxidized. In fig. 3.10 c we can see that the entire copper film is oxidized during the heating step, this shows that the entire graphene film has been transferred onto palladium layer during the peeling.

This type of metal assisted peeling process can be extremely useful to form ultra-clean metal-graphene interfaces devoid of polymer contaminants. However,

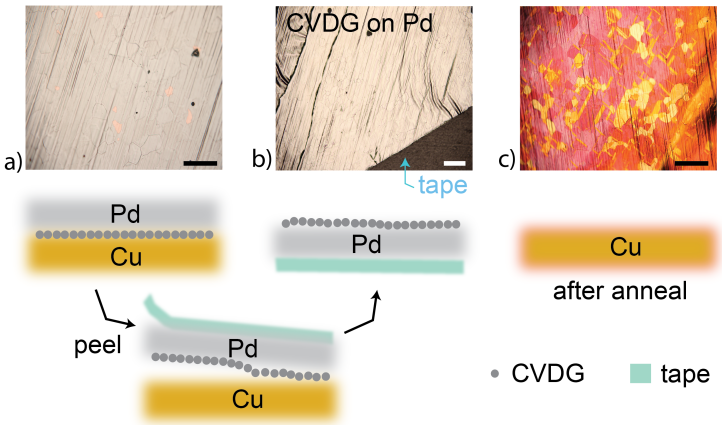


**Figure 3.10:** Palladium thin film assisted peeling of large area CVD graphene film. Optical image of a) palladium thin film deposited on as-grown CVD graphene on copper b) after the peeling of Pd/CVD graphene from the copper substrate c) oxidized copper foil after a brief hot plate anneal at 200 °C, scale bar: 200 $\mu$m.

transferring tape/Pd/CVDG stack onto $SiO_2$/Si substrate was found to be challenging and limited the usage of this transfer process. This type of a clean transfer process can be however useful for alternative device structures such as a vertical graphene-field effect transistor(VGFET).

### 3.4.3. Metal film assisted CVD graphene transfer

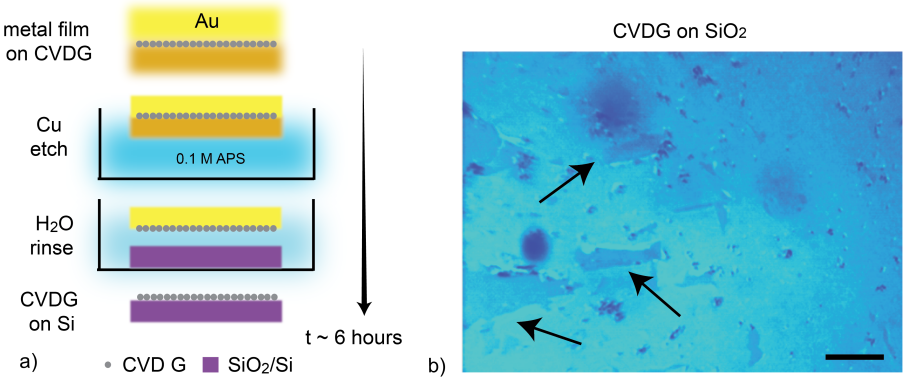


**Figure 3.11:** Thin gold film assisted large area CVD graphene transfer process b) optical microscopy image of CVD graphene transferred onto $SiO_2$/Si substrate using the transfer process, scale bar 10 $\mu$m. The arrows point to the holes formed during the transfer process.

Another approach to avoid direct polymer contact with CVD graphene was achieved by considering a sacrificial metal layer i.e. such as a thin gold (or aluminum) film (60 nm) [68, 69]. The metal film assisted transfer process is detailed in 3.11 a. The transfer procedure is similar to 3.3.1 with the only difference being that the polymer film is replaced by thermal deposited gold film (deposited after CVD graphene growth). In fig. 3.11 b we can see an optical image of CVD graphene transferred onto $SiO_2$/Si substrate using this approach. Numerous holes were observed in the graphene film after the transfer which limited the use this approach for larger graphene devices.

## 3.5. Conclusion

In summary, by reducing the methane concentration and with appropriate hydrogen to methane ratio, we demonstrated CVD graphene films with individual graphene grains ranging from micro to millimetre scale. By altering the growth pressure we were able to tune the shape of graphene grains from four-lobed structure ($<$0.1 mabar) to hexagonal shape at higher pressure ($>$100 mbar). Several transfer techniques were tested and developed during this work. We find that PMMA-assisted transfer technique offers the best possibility to transfer large-area graphene films onto $SiO_2$ substrate with minimal damage and high yield. During the rest of the work PMMA-assisted transfer technique was considered for device fabrication.

# 4

# Characterization of CVD graphene

## 4.1. Abstract

In this chapter, different techniques utilized to characterize our as-grown and as-transferred CVD graphene on copper and $SiO_2$/Si substrates are discussed. The characterization techniques considered during this work are namely: i) Raman spectroscopy ii) low-energy electron microscopy (LEEM) and iii) X-ray photoelectron spectroscopy (XPS). These techniques are extremely useful to both characterize graphene's properties and also the contaminants on graphene films.

## 4.2. Raman characterization of CVD graphene

### 4.2.1. Introduction

Raman spectroscopy is an indisputable non-invasive tool to characterize graphene [12, 13]. Using this technique it is possible to identify: number of layers ($N_L$), doping, strain, wrinkles/folds, defect density in the graphene film. In bi-layer graphene films it has also been used to identify the type of stacking. In this work, large-area Raman mapping is used to characterize number of layers, residual doping and strain in as-transferred CVD graphene on $SiO_2$/Si substrates [13].

Some of the prominent Raman scattering processes in single layer graphene

namely the G, 2D and D band are pictorially represented in fig. 4.1 [11, 12]. The G band (1580 $cm^{-1}$) is an in-plane $sp^2$ C-C stretching mode and is associated with a first order intra-valley scattering process. An incident photon resonantly excites an electron-hole pair (e-h) in graphene which is scattered by either an iTO or an iLO phonon, see fig. 2.1.1 for further details. This is followed by the recombination of electron-hole pair and a subsequent emission of a photon which is red-shifted by the phonon energy, as represented in figure 4.1 [11, 16].

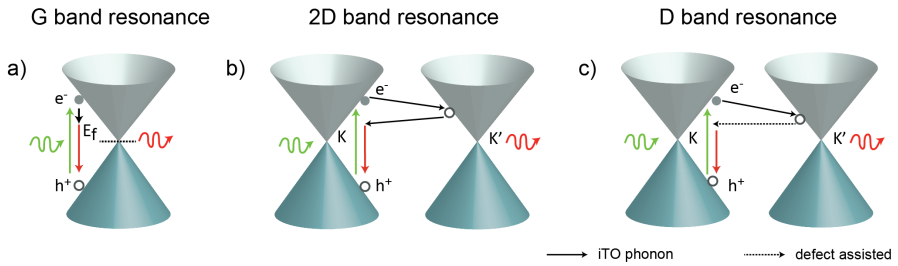


**Figure 4.1:** Main Raman scattering processes in graphene. a) first-order G-band process b) second-order double resonant 2D-band c) defect-assisted second-order double resonant D-band.

The 2D band (2675 cm $^{-1}$) originates from an in-plane breathing-like mode of the carbon rings. It is the strongest peak in graphene occurring due to second-order inter-valley scattering process involving two iTO phonons. The double resonant process is described in fig. 4.1 wherein an electron-hole pair generated due to an incident photon at the K point is inelastically scattered by an iTO phonon at the $K^{'}$ point [70]. In-order to conserve the energy and momentum, the electron scatters back to K point and recombines with the hole. Since the momentum conservation is satisfied by the two phonons with opposite wave vectors, no defects are required for the activation of the 2D band [11, 13, 16].

The D-band resonance (1350 $cm^{-1}$) is a disorder-induced inter-valley scattering process involving an iTO phonon and a defect for its activation4.1 [11, 13, 16]. Lattice vacancy, $sp^3$ type of defects, grain boundaries, edges in the graphene can give rise to the D peak. In fact, the D and the 2D band are second order processes but have a similar intensity as the one-phonon G mode, due to i) G mode is a non-resonant process, ii) D and 2D are double resonant processes. Also note that the G-mode intensity can be increased by tuning $E_F$ to $\sim E_{laser}/2$ [71, 72].

### 4.2.2. Raman spectra of graphene

Some of the prominent Raman peaks observed in a perfect single layer graphene (pink), multi-layered graphene (green) and defective graphene (blue) are shown in fig. 4.2. In SLG spectra (pink) we can notice that the intensity ratio of 2D to G i.e. $I_{2D/G} >> 1$, which is a clear indication of a single layer graphene while in the MLG (multi-layer graphene) spectra (green) the G peak intensity is much higher than the 2D peak intensity. However, care must be taken while considering the 2D/G intensity ratio as it has been shown to be sensitive to the oxide thickness of the underlying substrate due to optical interference effects and doping. Moreover, the shape of the 2D peak is also a good indicator of graphene layer thickness. A single Lorentzian peak fit of the 2D peak is an indication of SLG. While a D peak

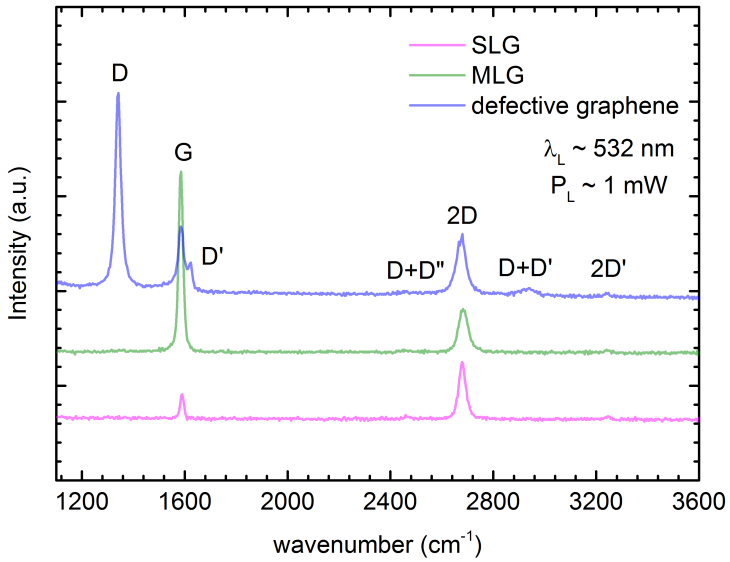


**Figure 4.2:** Prominent graphene Raman spectras of single layer graphene (pink), multi-layer graphene (green) and defective graphene (blue) are shown in 4.2.

is absent in the SLG and MLG spectra, its presence is clearly noticeable in the defective graphene spectra (blue), along with other peaks such as D'and D+D'. The D' peak is mainly observed in samples exposed to harsh conditions such as ion bombardment. Defects in SLG graphene film in our case were introduced on purpose by exposing the graphene film to a short (2 min.) UV-Ozone treatment. The presence of D+D" is a combination of D and D" peaks, the D" peak is assigned to a weak peak belonging to the longitudinal acoustic branch phonon occurring

at $\sim$1100 cm$^{-1}$ in defected samples.The absence of a D peak in the SLG and MLG spectra is indicative of minimal or absence of defects in the graphene film and is a signature of safe growth conditions. Weak signature of 2D' (overtone of D' peak) is also observable in all the samples. Similar to the case of 2D peak, the momentum conservation is satisfied by two phonons and does not require defects for the activation of 2D' peak. The 2D' peak is similar to the 2D peak but occurs due to intra-valley scattering process [11, 13, 16].

### 4.2.3. Large area scan of CVD graphene film

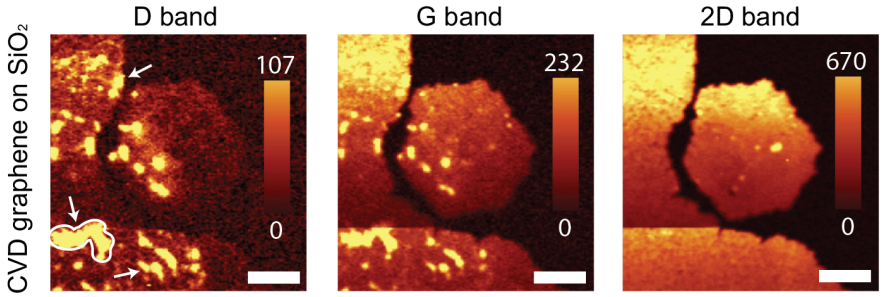


**Figure 4.3:** Large area Raman mapping of D, G and 2D band intensities of as-transferred CVD graphene film on $SiO_2$ substrate. The polymer residues from transfer are highlighted in white contour and arrows, scale bar: 10 $\mu$m.

The Raman spectra shown in fig. 4.2 is descriptive of local properties of the graphene film. Analyzing the regional variation of spectra provides more detailed information about graphene's properties over large areas. Such large area scans are very helpful in studying regional variations in: doping, strain, number of layers and defects in graphene. One such large area Raman mapping (50 $\mu$m x 50 $\mu$m) of as-transferred CVD graphene on $SiO_2$ substrate is shown in fig. 4.3. These maps were made by filtering the three prominent bands i.e. D (1250 - 1450 cm$^{-1}$), G (1500 - 1700 cm$^{-1}$) and 2D (2575 - 2800 cm$^{-1}$) from the spectra. The dimension of the map i.e. size(X) by size (Y): 150 x 150 spectras and each spectra consists of 1024 points. The respective intensities are shown in the color bar. We can see that the $I_{2D/G}$ is uniformly $>>$ 1 throughout the map which is a clear indication of uniform single layer graphene film. Since CVD graphene films are prone to PMMA-residues from wet transfer, these residues can be clearly observed in such large area maps. A closer Raman inspection of such residues is discussed in fig. 4.6. The PMMA-residues are highlighted using white arrows. Interestingly the

residues give rise to peaks mainly in D and G band region but minimal signature in the 2D band region. In these large area scans no D' peaks were observed.

### 4.2.4. G and 2D peak dependency on charge carrier density

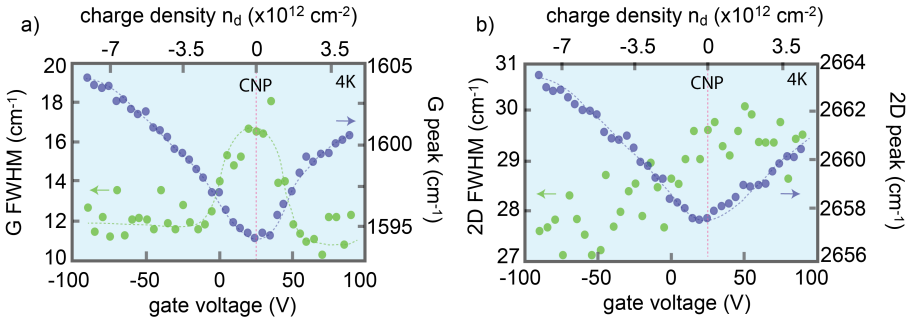


**Figure 4.4:** a, b) G and 2D peak frequency (blue) $\omega_{G,2D}$, FWHM (green) $\tau_{G,2D}$ vs. gate voltage (V) and charge density (x$10^{12}$ cm$^{-2}$) (top x-axis). The charge neutrality point (CNP) is marked using red dotted lines. These measurements were performed at 4K. Dotted lines are the guide to the eyes.

One of graphene's unique electronic property is the capability to tune the charge carrier density from holes to electrons with transition across its charge neutrality point. This charge carrier tunability is accessible by changing the bias voltage to the gate terminal of a graphene field effect transistor (GFET, 2.6). In fig. 4.4 we show the dependency of G/2D peak frequency $\omega_{G,2D}$ and G/2D peak FWHM $\tau_{G,2D}$ on charge carrier density. A clear dependency of both and G and 2D peak frequency and FWHM can be observed on charge carrier density. A stronger response of G peak ($\omega_G$ and $\tau_G$) is observed in response to change in charge carrier density when compared to 2D peak response, due to the strong electron-phonon coupling at $\tau$ point [10, 18, 73, 74].The measurements shown in 4.4 were performed together with Jonas Roch (Nanophotonics group, Univ. of Basel). The charge density to gate voltage relation can be found in appendix fig. C.1 - C.3 [59].

The 2D peak frequency $\omega_{2D}$ is observed to change by $\sim$6 cm$^{-1}$, while extremely minimal changes are observed in $\tau_{2D}$ for a gate sweep of $\pm$100V. In the case of G peak response, $\omega_G$ changes up-to 10cm$^{-1}$ and a clear dependency on its FWHM is also observed within the gate sweep of $\pm$100V. The physical understanding of the $\omega_G$ response to doping is such that the addition of electrons to the anti-bonding orbitals leads to phonon softening and removal of electrons leads to phonon stiffening [18].

This response of G peak frequency $\omega_G$ to a change in charge density can be used to characterize the residual doping in graphene films i.e. by knowing $\omega_G$ the charge density can be estimated (assuming no strain variations). It is estimated that a shift of 0.6 $cm^{-1}$ related to a $\Delta$n charge density of 2.4x$10^{11}$ $cm^{-2}$ [73].

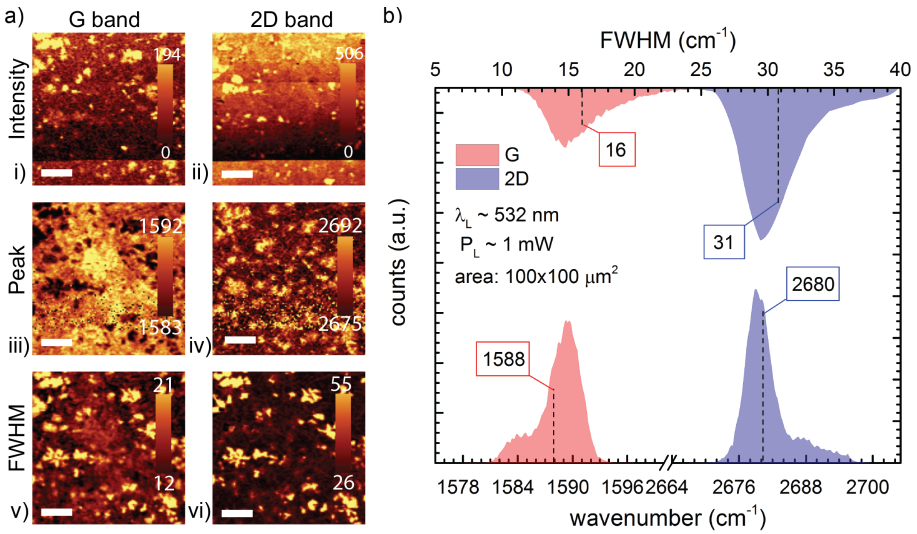


**Figure 4.5:** Large area Raman mapping of G, 2D bands of as-transferred CVD graphene film i-ii) Intensity iii-iv) peak position v-vi) FWHM and b) histogram of G, 2D peak position and FWHM (top axis) of maps shown in iii-vi. The average of the histogram is marked in black dotted lines, scale bar: 20 $\mu$m.

A large area Raman map of CVD graphene film is shown in fig. 4.5. In fig. 4.5 i-ii the G and 2D band intensities are shown. By performing single Lorentzian peak fit to both G and 2D peaks, the peak position (fig. 4.5 iii-iv) and FWHM (fig. 4.5 v-vi) maps can be extracted. Subsequently, the histogram of peak position and FWHM maps are depicted in fig. 4.5 b and their averages are highlighted using dotted lines. From the histograms the average of $\omega_G$, $\tau_G$ is $\sim$1588 $cm^{-1}$, 16 $cm^{-1}$, by comparing this value to fig. 4.4 a, this value is indicative of slight p-doping in CVD graphene. Moreover, the broadness of the histograms is an indication of charge carrier inhomogeneity in the graphene film. The causes of such doping, type of doping (n or p type) and inhomogeneity will be discussed in further detail in the upcoming chapters.

### 4.2.5. Residual strain in as-transferred CVD graphene on $SiO_2$ substrate

The phonon softening or stiffening of graphene's Raman peaks can also be achieved by applying mechanical strain to the graphene film [75]. Strain can be of uni-axial, bi-axial or a combination of both types. The response of G, 2D peaks are different depending on the type of strain. It has been observed that the G peak splits into $G^+$ and $G^-$ for a uni-axial strain of $> 0.4\%$ and splitting of 2D peaks has been observed for higher uni-axial strain of $> 3\%$. It has been observed that the wet transfer of CVD graphene onto $SiO_2$ substrate leads to compressive strain in the film [76].

Nanometer scale strain fluctuations have also been observed in exfoliated graphene samples directly transferred onto $SiO_2$/Si substrate [77]. A G peak shift ranging from -57 $\pm$ 2 $cm^{-1}$ /% to -62 $\pm$ 3 $cm^{-1}$ /% has been found in the case of biaxial compressive strain in graphene films [78–81]. Assuming $\omega G_{exf.}$ of $\sim$ 1582-1585 $cm^{-1}$ for an unstrained graphene sample [59, 82], from fig. 4.5 the $\omega G_{CVD}$ peak average is around 1588 $cm^{-1}$, which gives a difference $\Delta G_{CVD-exf.}$of 6 to 3 $cm^{-1}$, using which we can roughly estimate the biaxial compressive strain in our as-transferred CVD graphene films on $SiO_2$/Si substrates to be around $\approx 0.1\%$ [59].

### 4.2.6. Raman characterization of polymer residues

Raman spectroscopy was also used to characterize PMMA residues from the wet transfer process. The PMMA residues were isolated using the technique detailed in fig. 3.8, chapter 3. The complete Raman characterization of PMMA residues is detailed in fig. 4.6. The Raman signatures of the PMMA residues can be clearly observed in fig. 4.6 d. Clearly, the PMMA residues have a stronger response in the regions of D and G band resonances of graphene. A clear difference between the spectra of freshly spun PMMA and the PMMA-residues can also be observed, oxidation of PMMA during its exposure to APS solution could explain the difference in Raman spectra. Another peak arising around 470 $cm^{-1}$ was also observed in certain spectra of PMMA residues. The latter is, however, absent in freshly spun PMMA Raman spectra. The occurrence of the peak at 470 $cm^{-1}$ can be due to the presence of deformed C-C skeletal structures of the PMMA molecule [83].

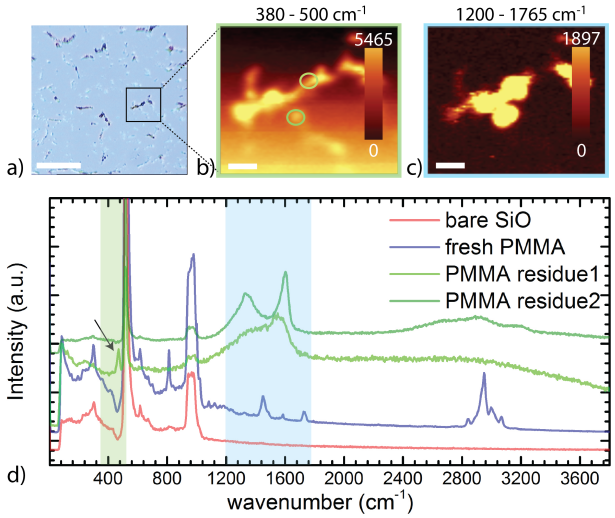


**Figure 4.6:** Characterization of PMMA residues from wet transfer process. a) Optical image of PMMA residues on $SiO_2$/Si substrate, PMMA residues were isolated using technique detailed in 3.8. b) Large are Raman map of peaks in the range of 380 - 500 $cm^{-1}$ and c) 1200 - 1765 $cm^{-1}$. d) Spectras comparing freshly spun PMMA layer (purple) and PMMA residues (Green), scale bar: 2 $\mu$m.

## 4.3. Low energy electron microscopy of CVD graphene

### 4.3.1. Introduction

Low energy electron microscopy or shortly known as 'LEEM' is one among the widely used techniques used for imaging surfaces [84]. The low-energy electrons of a few eV to tens of eV are extremely surface sensitive and any changes in the local structure or composition gives rise to change in contrast in LEEM images. Moreover, this technique can also be extended to studying biological samples such as protein imaging without radiation damage [85]. In-order to image interesting nano objects using a coherent electron beam of low-energy electrons, a highly transparent and robust substrate that is able to support nano-sized object deposition becomes vital [86]. Such substrate requirements have been met by single layer graphene due to its high transparency and mechanical stability [87].

In fig. 4.7, the LEEM in holography mode is described, which was used to characterize our free-standing CVD graphene films [88]. An ultra-sharp tungsten

tip acts as a coherent point source for low-energy electrons which is field emitted towards the graphene sample. The sample is typically 200 to 1000 nm away from the tip. The detector unit consists of a micro-channel plate (MCP), a fibre optic plate (FOP) and a charge-coupled device camera is placed at 68 mm from the tip [88]. All the LEEM characterization of our CVD graphene samples shown in this section was performed in collaboration together with Dr. Jean-Nicolas Longchamp at Prof. Dr. Hans-Werner Fink's group, University of Zürich.

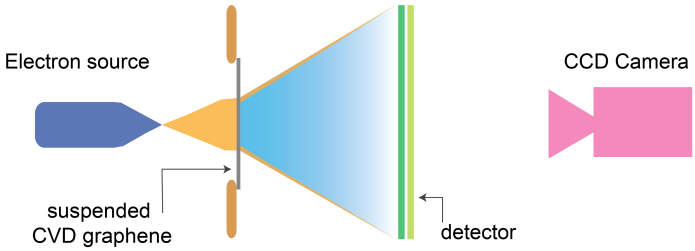


**Figure 4.7:** Illustration of the low energy electron microscopy in holography mode. The suspended graphene film is placed in-between the electron source and the detector.

### 4.3.2. Preparing ultra-clean CVD graphene surface for LEEM imaging

In order to perform LEEM imaging of graphene or use graphene as a substrate for biological sample imaging, it is necessary to fabricate hollow structures in the substrate such that the graphene film is freely suspended over the hollow domains. Trenches were etched in silicon nitride substrates to facilitate suspension of graphene. In the LEEM images to be discussed below, the region in the center denotes suspended CVD graphene i.e. the view of the CCD camera. From previous discussions in fig. 3.8, the wet transfer of CVD graphene onto $SiO_2$ substrate leads to PMMA residues even after extensive exposure to solvents. This is evident in the first LEEM images of CVD graphene samples taken using the LEEM technique shown in fig. 4.8 i. This shows that the solvent exposure does not completely remove PMMA. The PMMA residues on graphene limit the possibility of imaging biological samples on graphene.

In fig. 4.8 i) it can be seen that the image is dark with minimal transmission of low-energy electrons, this is primarily due to the scattering of low-energy electrons with PMMA-residues. In-order to circumvent this problem, it was discovered

that a platinum assisted catalytic etching of PMMA leftovers produced ultra-clean graphene surfaces [89]. This was achieved by depositing a thin film of platinum ($\sim$ 10 nm) on these substrates prior to graphene transfer and subsequently heating the sample in air at 200$^{\circ}C$ for 10 to 15 minutes. The result of this cleaning effect is shown in fig. 4.8 ii, it can be clearly observed that the transmission rate is much higher and the suspended CVD graphene is cleaner with no residues from PMMA transfer. This cleaning method has proven to be extremely useful in protein imaging on graphene surfaces [87].

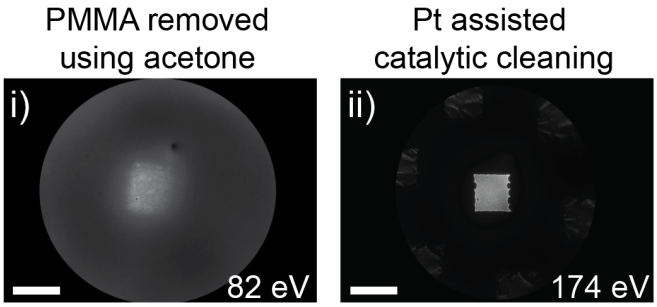


**Figure 4.8:** LEEM characterization of CVD graphene with i)PMMA removed using acetone and ii) PMMA removed using platinum catalysis technique. The region in the center denotes suspended CVD graphene. The energy of the coherent electron beam is mentioned within the images, scale bar: 500 nm.

### 4.3.3. LEEM imaging of ultra-clean CVD graphene surfaces

Ultra-clean CVD graphene surface characterization using LEEM after the Pt-assisted catalytic cleaning is shown in fig. 4.9 i-vi. The suspended CVD graphene is highlighted using the red arrow. These images contain precisely six reflections, marked using white arrows, which is a result of low-energy eletron beam interaction with suspended CVD graphene films in the middle. The number of reflections is indicative of crystallinity of the suspended graphene film. Similar reflections were also observed in several larger suspended graphene windows (iv-vi, scale: 2 $\mu$m), which is suggestive of uniform crystallinity over large scales in our CVD graphene films. The possibility of suspending ultra-clean single layer graphene over such large areas and graphene's mechanical stability and high transparency provides an ideal platform to perform low-energy electron holography measurements with biological samples [87].

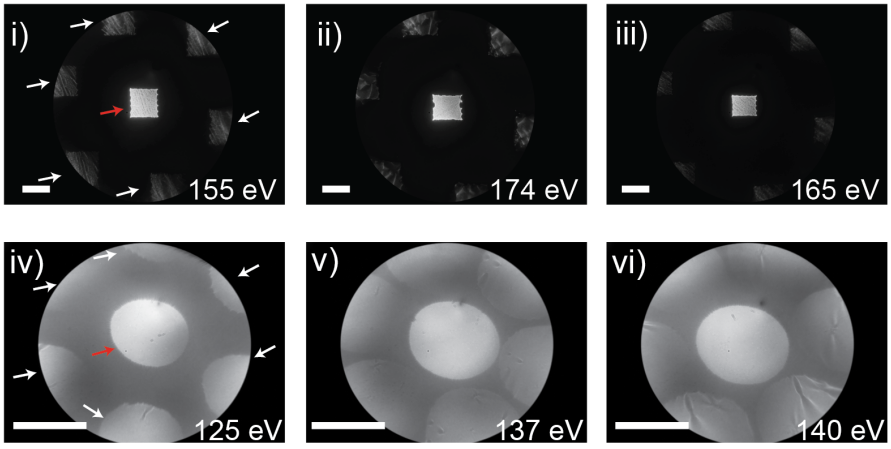


**Figure 4.9:** LEEM characterization of ultra-clean CVD graphene surfaces after Pt-assisted catalytic cleaning i-vi) The energy of the coherent electron beam is as mentioned within the image, scale bar: i-iii: 500 nm, iv-vi: 2 $\mu$m.

### 4.3.4. LEEM imaging of defects in CVD graphene and hBN

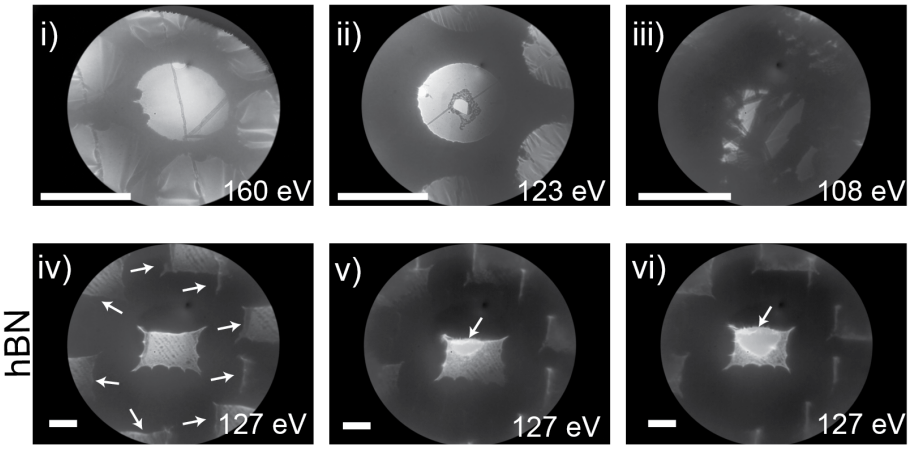


**Figure 4.10:** LEEM characterization of defects in CVD graphene surfaces after Pt-assisted catalytic cleaning i-vi) scale bar: i-iii: 2 $\mu$m, iv-vi: 500 nm.

CVD graphene films are prone to defects either during the growth process or transfer process. Characterizing such defects is of utmost importance to understand the limitations of the material. In fig. 4.10 i-iii we show some of the defects characterized in our CVD graphene films using LEEM. In fig. 4.10 i we can see a

grain boundary/nano-ribbon like-structure passing through the CVD graphene film. Increasing the kinetic energy of low-energy electrons resulted in rupture of such ribbons possibly due to heating effects, one such instance is shown in fig. 4.10 ii (rupture is visible in the centre). The heating of such ribbons can be assisted by agglomeration of adsorbates at the grain boundaries. A multi-layer wrinkle/ribbon is also depicted in fig. 4.10 iii, the decrease in intensity with increase in graphene layers can also be observed. This technique can also be used to identify the number of graphene layers ($N_L$). Commercially available mono-layer hexagonal Boron nitride (hBN) was also characterized using LEEM after catalytic cleaning. Interestingly, the number of reflections in the mono-layer hBN was observed to be more than six, marked using white arrows, which is suggestive of denser polycrystallinity of hBN within the 500 nm window when compared to our CVD graphene films. During the imaging of the hBN with a constant energy, we observed the rupture of hBN film possibly due to charging effects of the suspended hBN film fig. 4.10 v-vi.

## 4.4. X-ray photoelectron spectroscopy of PMMA

### 4.4.1. Introduction

One of the widely used techniques for determination of the chemical composition of material surfaces is the 'X-ray photoelectron spectroscopy' (XPS) also known as 'electron spectroscopy for chemical analysis' (ESCA). XPS works on the principle of the photo-electric effect wherein the material surface is irradiated with soft X-rays and the ejected core electrons i.e. photoelectrons are investigated to extract the material's surface properties [90]. The working principle of XPS: an incoming photon excites an electron in the material which is subsequently ejected from the material's surface. The ejected electron's kinetic energy is measured using a spectrometer as depicted in fig. 4.11 [90].

By knowing the energy of the incoming photon $h\nu$, the kinetic energy of the photoelectron $E_{kin}$ and the sample's work function $\phi$, the binding energy $E_B$ can be calculated by equation 4.1.

$$E_B = h\nu - \phi - E_{kin} \tag{4.1}$$

The binding energy $E_B$ of such photoelectrons is an intrinsic material property

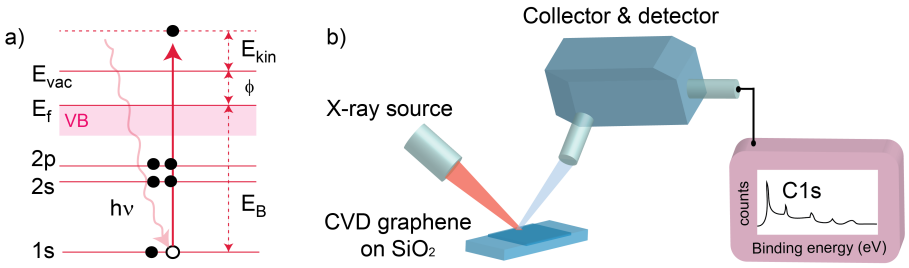


**Figure 4.11:** a) Principle of X-ray photoelectron spectroscopy technique b) schematic representation of a typical XPS setup.

and thus provides information about the chemical composition of a material's surface. Moreover, changes in binding energy of a particular element due to its chemical environment can also be measured using this technique (presence of other elements, alloys). The photoelectrons escape the material and are collected by the detector (fig. 4.11, b). Typical depth of XPS analysis is between 2 to 5 nm [91]. In-order to minimize the loss of photoelectrons, the pressure within the XPS chamber is maintained well below $10^{-11}$mbar.

The XPS characterization was performed in collaboration with Lucas Moser and Laurent Marot at the Physics department, University of Basel. The XPS measurements were performed using a VG ESCALAB 210 system equipped with a mono-chromatized Al K$\alpha$ (h$\nu$ = 1486.6ev) radiation source with the pass energy of 20 eV used for all narrow scan measurements and 100 eV pass energy for survey scans. Normal electron escape angle and a step size of 0.05 eV were used. The Gaussian broadening of the spectrometer (convolution of the spectral resolution (which itself is a convolution of the analyzer resolution and the source resolution) and thermal broadening) was calibrated as 0.55 eV for the 20 eV analyzer pass energy. The charge-up shifts of the XPS peaks were calibrated by taking the Si2p peak of $SiO_2$ ($Si^{4+}$) component to be 103.2 eV. The analysis of core level lines discussed in the following section was performed in UNIFIT 2016 [92, 93] .

### 4.4.2. XPS survey spectrum of bare $SiO_2$ substrate, fresh-PMMA and PMMA-residues

In earlier sections we saw the presence of PMMA-residues from CVD graphene transfer. In-order to characterize the chemical composition of residues from transfer we performed XPS on i) bare $SiO_2$/Si substrate ii) freshly spin coated PMMA and

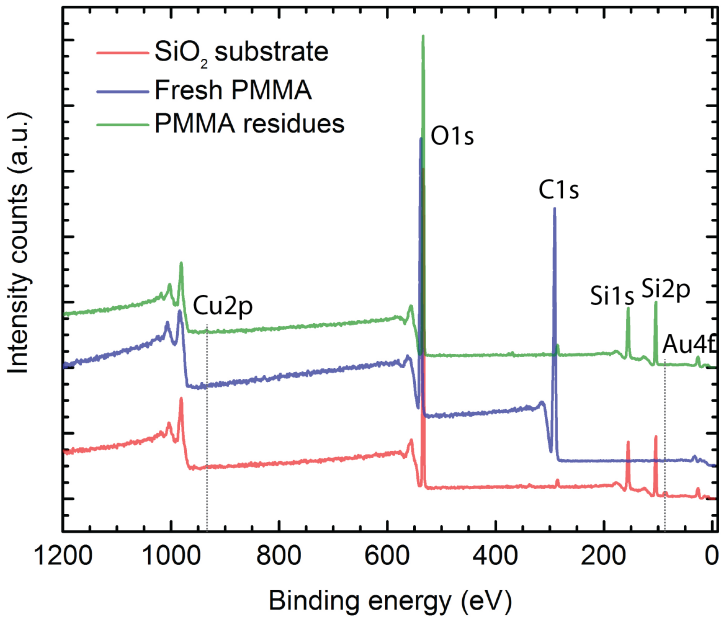


**Figure 4.12:** XPS survey spectrum of bare $SiO_2$ substrate (red), fresh PMMA (blue) and PMMA residues (green). Both the PMMA samples were on $SiO_2$ substrate. The Cu2p peak at $\sim$ 933.5 eV in the PMMA-residues survey spectrum indicates the presence of copper residues from transfer.

iii) PMMA residues from transfer. In the survey spectrum of the substrate (fig. 4.12, red) we primarily found the presence of Si1s, Si2p, O1s, as expected for $SiO_2$. Small presence of C1s was also observed, occurring possibly due to the adsorbed hydrocarbons from exposure to ambient atmosphere. An Au4f peak due to the presence of gold markers on the substrate can be seen.

To compare PMMA before and after transfer, an XPS survey was taken on freshly spin coated PMMA layer ($\sim$300 nm) on substrate. The Si1s and Si2p peaks are no longer visible due to the thickness of the PMMA layer. However, the increase in the C1s and O1s peak is indicative of PMMA presence (fig. 4.12, purple). After performing the transfer detailed in fig. 3.8 an XPS survey of the PMMA-residues was performed (fig. 4.12, green). Interestingly, we observed Si1s, Si2p, O1s, Au4f and Cu2p peaks in the PMMA-residues sample. The Cu2p peak is indicative of leftover copper residues from the wet transfer process. These copper residues along with PMMA residues are possibly the adsorbates noticed in fig. 4.10 ii during LEEM imaging.

### 4.4.3. XPS comparison of fresh-PMMA and PMMA-residues

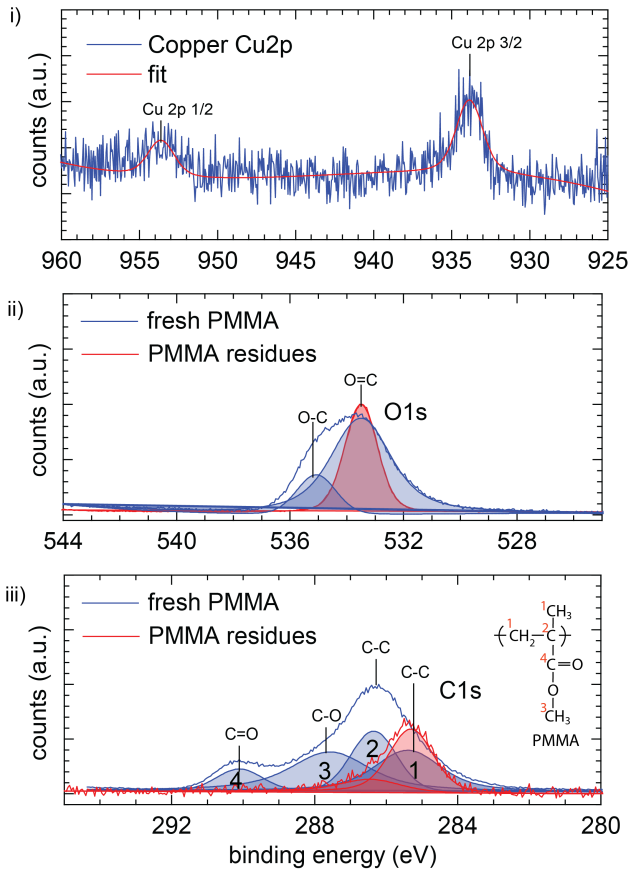


**Figure 4.13:** a) Fine scan of Cu2p peak b) C1s and O1s fine scan survey comparison of fresh-PMMA and PMMA-residue samples. Inset: chemical formula of PMMA.

In this section a closer look at the copper peak from the XPS survey scan of PMMA-residues is discussed. The fine scan of Cu2p survey spectrum found in the PMMA-residue sample occurring at ∼933.5 eV (Cu2p $\frac{3}{2}$) and at 953.5 (Cu2p $\frac{1}{2}$) is shown in the fig. 4.13 i. The clear presence of Cu2p peak indicates leftover copper atoms from wet transfer process, although the copper etching was performed overnight over several hours. The absence of Cu2p peak in all the other surveys further indicate that the copper residues found in PMMA-residue sample is a resultant of transfer process. This study also suggests that leftover copper atoms can certainly be present in as-transferred CVD graphene on $SiO_2$, as seen in fig.

7.4.

As discussed earlier, exposure of PMMA to APS (Cu etchant solution) leads to irremovable PMMA residues. This can occur possibly due to the oxidation of PMMA when in contact with APS. Comparing the XPS survey scan of fresh-PMMA with PMMA-residues, we find noticeable differences in the C1s and O1s peak shapes, fig. 4.13 ii. The respective peak fit was performed using the software UNIFIT 2016. The consequent individual peaks were identified in the C1s peak of fresh-PMMA and PMMA-residues by referring to S. Rosencrance et al [94–96]. The charge-up shifts of the fresh-PMMA XPS peaks were calibrated taking the Si2p peak of SiO2 (Si4+) component to be 103.5 eV [96].

## 4.5. Conclusion

In this chapter we presented a thorough characterization of CVD graphene using three distinct techniques i.e. i) Raman spectroscopy ii) Low-energy electron imaging of suspended CVD graphene and iii) X-ray photoelectron spectroscopy of fresh-PMMA and PMMA-residues on $SiO_2$/Si substrate. Using the large area Raman mapping, we have shown that it is possible to i) correlate G-peak position ($\omega_G$) to charge doping density of the graphene film, ii) characterize graphene layer thickness, iii) study the Raman signature of PMMA-residues, folds and iv) characterize residual strain in as-transferred CVD graphene films.

The defects in the CVD grown graphene films such as grain boundaries/ribbons were characterized using low-energy electron microscopy and remnants of transfer process were also identified. It was encouraging to note that over large areas the CVD graphene films were single layer and grain boundary-free, which is a sign of large single crystal CVD graphene grains. The chemical composition of the residues were further characterized using XPS. The XPS survey spectrum showed minimal presence of copper residues, which could be among the adsorbates visualized during LEEM imaging. The difference in the C1s and O1s peaks of fresh-PMMA and PMMA-residue highlights the oxidative influence of APS on PMMA during the wet transfer of graphene.

# 5

# Fabrication and electrical characterization of CVD graphene field effect transistors

## 5.1. Abstract

Device fabrication has been one of the pivotal part of this thesis and is also one of the crucial steps in experimental studies. Since graphene is only one atom thick, its electrical transport is easily influenced by residues or ambient adsorbents on/below the graphene film. Special emphasis towards reducing contamination during fabrication were considered during the development of the fabrication protocol. In this chapter, two procedures developed to fabricate large area CVD graphene Hall bar devices i.e.: i) electron beam lithography and ii) stencil lithography are discussed. Further, the relevant thermal annealing, solvent treatment and contact resistance characterization techniques are presented.

### 5.1.1. Route 1: Electron-beam lithography

In fig. 5.1 the standard electron beam (e-beam) assisted lithography process is described. First, a layer of e-beam sensitive resist (ZEP520) is spun on as-transferred CVD graphene on $SiO_2$ substrate (5.1 i). Second, the ZEP520 is exposed to electron beam according to the desired Hall-bar pattern (5.1 ii) and subsequent development of the exposed ZEP520 film is performed. Third, oxygen plasma is used to pattern the CVD graphene into Hall bar device structure. The

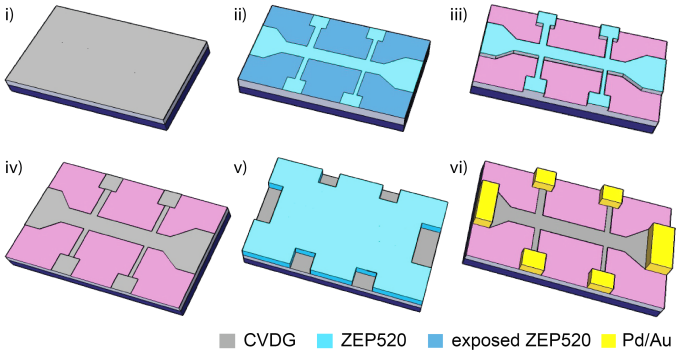


**Figure 5.1:** Electron-beam lithography description. i) as-transferred CVD graphene on $SiO_2$/Si substrate ii) ZEP520 resist after e-beam exposure iii) after graphene patterning using oxygen plasma iv) patterned graphene on substrate after removal of resist mask v) after second step of e-beam lithography, prior to metal evaporation and vi) after lift-off process.

patterned resist film acts as a protection layer on CVD graphene during the reactive ion etching process (fig. 5.1 iii, iv). Fourth, similar e-beam lithography approach is followed to fabricate metal contacts to the graphene film (fig. 5.1 v & vi). After the metal evaporation process, the metal film residing on top of the polymer film is removed during the 'lift-off' process. Only the metal film in contact with graphene remain. A layer of 5 nm palladium and 60 nm gold is used as the metal contact to graphene. Complete fabrication protocol is listed in the appendix A. In fig. 5.2a, an optical image of a typical CVD graphene Hall bar device fabricated using e-beam lithography can be seen, graphene film patterned in Hall bar pattern can be seen in fig. 5.2 b.

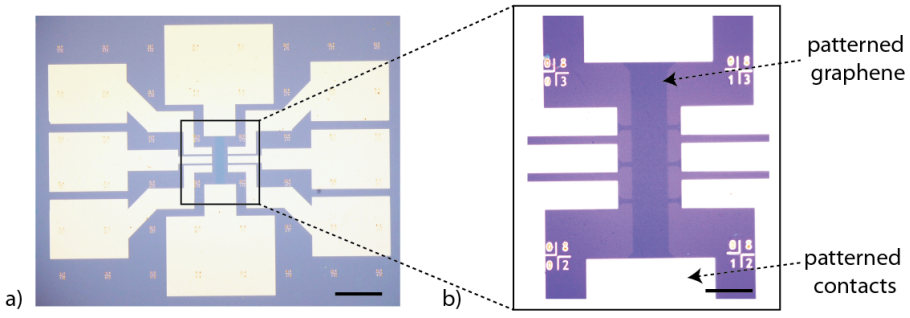


**Figure 5.2:** a) Optical image of e-beam fabricated sample and b) close-up of patterned graphene, scale bar: 200 $\mu$m (a) & 50 $\mu$m (b).

### 5.1.2. Route 2: Stencil lithography

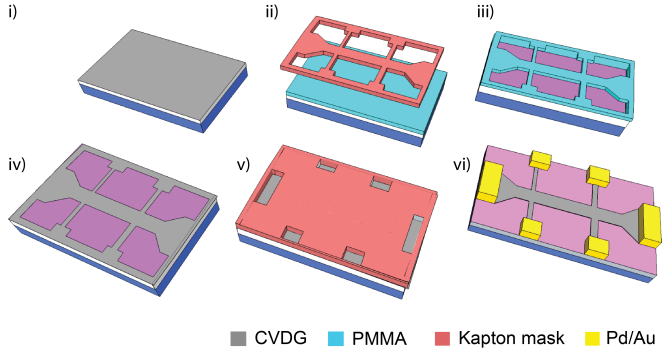


**Figure 5.3:** Stencil lithography based approach for large scale graphene Hall bar fabrication. i) as-transferred CVD graphene on $SiO_2$/Si substrate ii) alignment of patterning mask on chip iii, iv) before and after removal of PMMA etch mask iv) patterned graphene film v) alignment of contact patterning mask vi) after metal evaporation process.

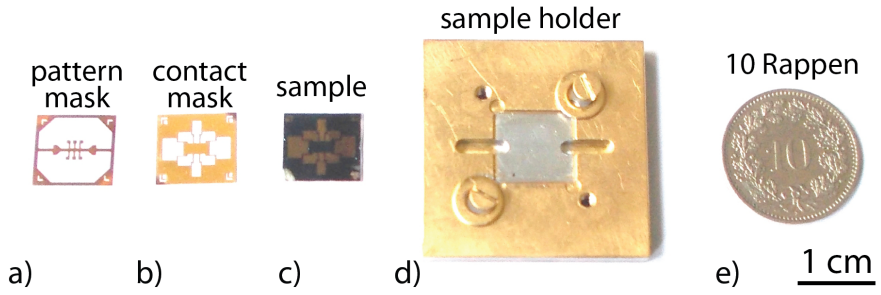


**Figure 5.4:** Optical images of stencil lithography process for graphene Hall bar fabrication. a) Graphene patterning mask b) contact patterning mask c) a typical graphene Hall bar device after fabrication. d) Metal sample holder for substrate-mask alignment and clamping e) size comparison with a 10 Rappen coin, scale bar: 1 cm.

As an alternative approach, stencil lithography was utilized to fabricate large CVD graphene Hall bar devices (L, W: 3500 $\mu$m, 500 $\mu$m). This approach brings forth the following advantages: i) requires only one routine of resist spin coating on graphene, ii) shorter fabrication time and iii) relatively cleaner fabrication procedure, due to minimal exposure to solvents and resist. Minimal exposure to contaminants and residues during fabrication can be very helpful in fabricating clean graphene devices. Moreover, since there is no e-beam exposure, the fabrication time consists of mainly stencil alignment. These stencils were produced in kapton films using

laser ablation technique by Rolf Brönnimann, Transport at Nanoscale interfaces, EMPA, Dübendorf, Zurich.

First, a thin layer of PMMA (300 nm) is spun on top of as-transferred CVD graphene on $SiO_2$/Si substrate (fig. 5.3 i). Second, the stencil mask for patterning graphene is placed on top of the PMMA/CVDG (fig. 5.3 ii), this is followed by the exposure to oxygen plasma in-order to etch the regions of PMMA/CVDG that is not covered by the stencil mask (fig. 5.3 iii). Third, the PMMA layer is dissolved in solvents (fig. 5.3 iv) and the next stencil mask for metal evaporation is placed on top the structure(fig. 5.3 v). Fourth, after the metal evaporation process, the second mask is removed (fig. 5.3 vi). In fig. 5.4 we can see the optical images of kapton foil based masks used to produce these samples, a typical Hall bar device fabricated using this technique is shown in fig. 5.4c. Detailed fabrication protocol can be found in the appendix A.

Some of the other techniques considered during this work in an attempt to obtain polymer residue-free graphene devices were: 1) hBN/graphene/hBN (full CVD) (hBN: hexagonal Boron Nitride) heterostructures and 2) use of metal etch mask during fabrication.

Hexagonal Boron Nitride (hBN) is a large bandgap semiconductor and is considered as an ideal substrate for graphene due to similar hexagonal lattice structure and insulating properties. Thanks to a bandgap of $E_g$= 5 eV, it can serve as an ideal substrate for graphene. High quality hBN/graphene/hBN heterostructures can be fabricated using exfoliation technique [49]. We fabricated heterostructures consisting of CVD grown hBN from Graphenea, the optical images of the sample can be seen in C.10. However, due to limitations (holes, crystallinity) in the quality of the multilayer hBN films an improvement in the field effect characteristics could not be observed (see: C.11).

Second, metal thin films were used to protect the graphene surface during the transfer process, see appendix C.12. Using this technique it is possible to transfer graphene films on $SiO_2$ substrates and avoid PMMA contamination of graphene films during the transfer. However, due to poor yield of the samples post lift-off process, this technique was not considered further (see: C.12). Further, some of the optical images of Hall bar sample fabrication using electron beam lithography procedure on a single domain of CVD graphene is shown C.13.

## 5.2. Graphene field effect transistor

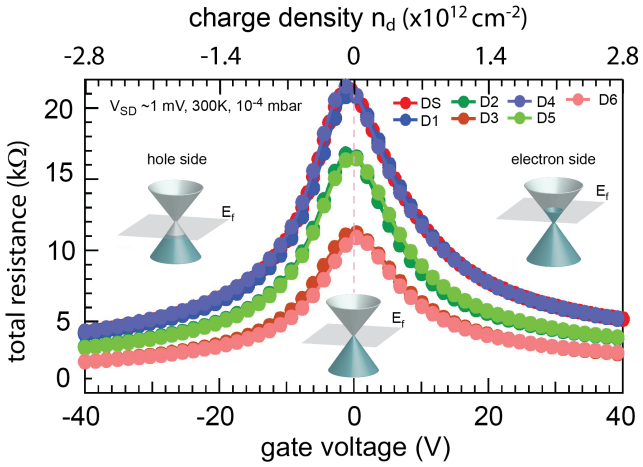


**Figure 5.5:** Total resistance as a function of gate voltage of a CVD graphene transistor, charge density $n_d$ (top x-axis) of different contact pairs of a Hall bar device. Inset: representation of graphene's band diagram in i) hole-dominated, ii) at the charge neutrality point and iii) electron-dominated regime. These electrical transport measurements were performed under low-vacuum conditions of $10^{-4}$ mbar at room temperature.

Field effect transport of a CVD graphene transistor is shown in fig. 5.5. The respective band structure in the three distinct regimes i.e.: i) hole-conduction ii) around the charge neutrality point (CNP) and iii) electron-conduction is described in the inset of fig. 5.5 [97]. As the gate voltage is changed from large negative values to positive values, a constant input bias ($V_{SD}$) is maintained between the source and drain contacts. Due to the change in gate voltage, the charge density $n_d$ of the graphene film is modulated. By measuring the change in current (I) passing through the graphene film during the gate modulation and subsequent calculation of resistance ($R_T$=$V_{SD}$/I) yields the result described in fig. 5.5, where $R_T$ denotes the total resistance of the graphene FET [97, 98]. The charge density to gate voltage relation can be found in C.1 - C.3.

We can observe a clear transition from hole to electron dominated transport in the graphene film as the gate voltage is swept from -40V to +40V. This change is clearly reflected in the increase and decrease of resistance as the gate voltage is varied from negative to positive values. The peak in the resistance constitutes the charge neutrality point of graphene. The CNP can be observed to be at zero

gate voltage. This is a signature of low residual doping in graphene films. High residual doping leads to shift of the charge neutrality point (CNP) away from zero gate voltage, either to the positive (p-type) or negative side (n-type), depending on the the type of dopants [99, 100]. The field effect transport (FET) measurements were performed on a Hall bar device with eight contacts i.e. 2 current contacts (drain, source) and three pairs of voltage contacts (titled: 1-6). The presence of CNP at zero gate voltage is suggestive of low p-doping in the graphene film over the entire device. Further, the residual impurity charge carrier density (charge traps in $SiO_2$) can be accessed from the slope of the conductance versus gate trace. Moreover, it can be noticed that the FET characteristics is symmetric on both the hole & electron side.

SG 18 Mobility ($cm^2$ / Vs)

| Chip / Sample | B4_C1 | B4_C2 | B4_C3 | B4_C4 | B4_C5 | B4_C6 | B4_C8 |
|---|---|---|---|---|---|---|---|
| A1 | 2100 | 2400 | 1378 | 700 | D | 2160 | 1600 |
| A2 | 1300 | 2300 | 2200 | D | D | D | D |
| B1 | D | 2500 | 1065 | 2274 | 1013 | D | D |
| B2 | D | 2430 | 2262 | 1700 | 2000 | 3000 | D |

D: broken device

**Figure 5.6:** Mobility chart of various samples from batch 4 (B4). The growth recipe used to produce the samples were SG18 (SG: slow growth). These devices were thermal annealed prior to electrical measurements (see:5.10) and characterized under low vacuum ($10^{-4}$ mbar).

A mobility chart of samples from different chips of batch 4 (B4), grown using recipe SG18 (SG: slow growth) is shown in 5.6. It can be noticed that the mobilities vary in the range of 1000 - 3000 $cm^2$/Vs (50% of samples with $\mu_{FET}$ >2000 $cm^2$/Vs). The broken device (D) denotes a sample damaged during fabrication (refer to: C, C.2, C.3 for mobility estimation technique).

## 5.3. Graphene FET with high residual doping

In fig. 5.7 a, b the typical field effect characteristics of CVD graphene transistors with high residual p-doping is shown. The CNP is observed to be shifted in particular to high positive gate voltages. Such a shift towards positive (negative) gate voltage

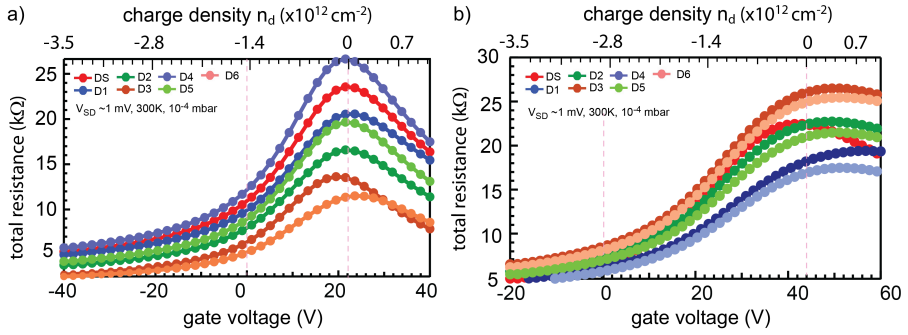


**Figure 5.7:** Total resistance as a function of gate voltage, charge density $n_d$ (top x-axis) of a highly p-doped CVD graphene transistor across different contact pair of the entire Hall bar device. These electrical transport measurements were performed under low-vacuum conditions of $10^{-4}$ mbar at room temperature.

is an indication of high residual hole-doping (electron-doping) in the CVD graphene film [99, 100]. The shift is relatively higher in fig. 5.7b when compared to fig. 5.7a, this can occur due to a higher presence of residues in sample fig. 5.7b. It can be observed that CNP is uniformly shifted to higher gate voltages across the entire device. This shows that the residual doping is present across the film and is not very localized at a specific region of the device. In our CVD graphene samples the occurrence of such p-doping in particular is commonly noticed. The causes of such p-doping are discussed in detail in the following sections.

### 5.3.1. Causes of residual doping

The prime reason behind the p-doping of graphene films is the adsorption of water, oxygen and other contaminants present in ambient conditions [99–102]. A schematic representation of as-transferred graphene film is described in fig. 5.8. While such doping can be induced during exposure to air, it can also occur due to solvent exposure during transfer and fabrication process. Since the CVD graphene transfer is performed in solution, the presence of a water layer on graphene cannot be ignored fig. 3.3.1. The electrochemical interaction between such ambient contaminants and the graphene layer has been identified as the key mechanism behind the p-doping of graphene. Such a layer of ambient contaminants act as an electron-acceptor, leading to the hole doping of graphene film. The mechanism can be described using equation 5.1 [101, 102].

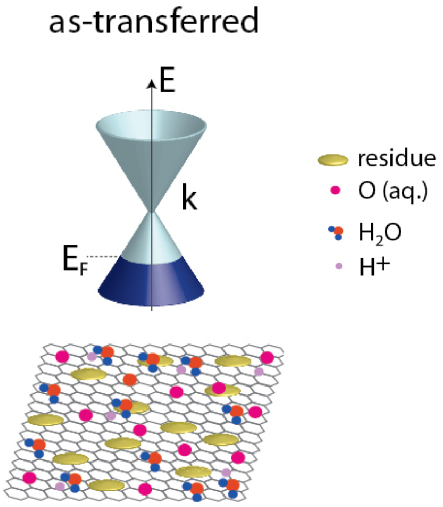


**Figure 5.8:** Schematic representation of as-transferred CVD graphene surface and the respective band diagram of p-doped graphene.

$$O_2(aq) + 4\,H^+ + 4\,e^-\,(graphene) \underset{red}{\overset{ox}{\rightleftharpoons}} 2\,H_2O \tag{5.1}$$

Given that the work function of graphene $E_G \simeq$ -4.6 eV, for a pH = 6 the electrode potential of adsorption layer (on graphene) is $E_i \sim$ -5.3 eV. The latter acts as a strong driving force to shift graphene's fermi-level well into the valence band [101, 102]. For the calculation of $E_{redox}$ values please refer to appendix C.24. It is well-known that the pH value of moisture ($E_i$) is heavily influenced by the carbon dioxide ($CO_2$) content in air. Such redox reactions necessitate the transfer of up-to 4 electrons in sequence, involving four intermediate reactions generating: superoxide anion ($O2^{\cdot -}$), hydrogen peroxide, hydroxyl radical ($\cdot OH$) [101, 102]. For further details about the graphene-redox system model, please refer to the appendix C.24.

Doping in graphene can be induced using different approaches such as intentional exposure of graphene to special solvents. However, in our case no such exposure to special chemicals was performed and the mechanism behind p-doping in our as-transferred graphene films is due to ambient contaminants, as discussed above. Further experiments to probe the adsorbed layer of contaminants are discussed in greater detail in chapter 7 .

## 5.4. Overcoming residual doping in graphene

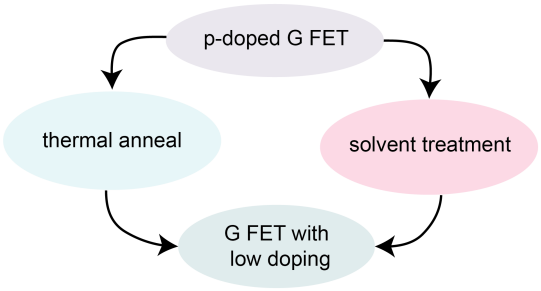


**Figure 5.9:** Two of the most widely used approaches to reduce residual doping in graphene films.

Since the adsorption of contaminants is unavoidable either due to the sample preparation procedure or during the eventual exposure of the sample to ambient conditions, removal of such unwanted residues becomes important. The residual doping in graphene films can be reduced or completely removed using certain techniques. Two such prime approaches are: i) thermal anneal and ii) solvent treatment (fig. 5.9). The details of these approaches are described below.

### 5.4.1. Thermal annealing of graphene

In the thermal annealing approach the graphene samples are heated to 150-300 $^{\circ}C$ in low pressure conditions (1 mbar to $10^{-5}$ mbar) for several hours [103, 104]. The result of such a heating procedure can be seen in the graphene field effect characteristic shown in fig. 5.10. There is a clear shift of the CNP, close to zero gate voltage after such annealing procedure (blue). Before the annealing process the CNP is at higher gate voltages, as expected in most of the freshly fabricated devices (red).

Thermally activated desorption of the ambient contaminants on graphene film during the thermal annealing process is the key reason behind the improvement of the FET characteristics of the device. These procedures can be either performed by heating the graphene sample under ultra-low/low-vacuum conditions without or with an additional carrier gas flow. Forming gas (5% $H_2$, Argon) is one of the most commonly used carrier gas during annealing. Pressure during thermal annealing was found to be one of the most important parameter. Consistent results were obtained when the samples were annealed at low pressures ($<$1 mbar).

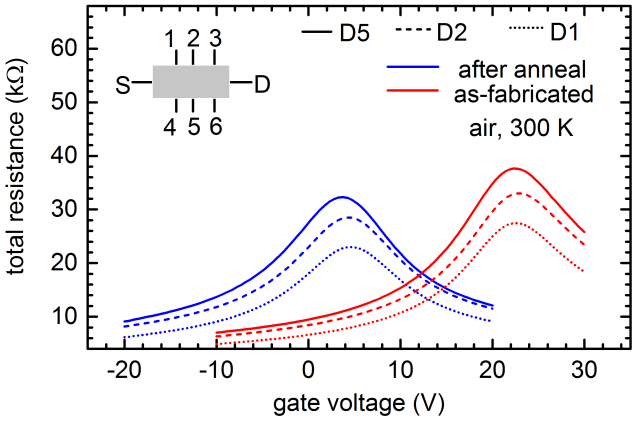


**Figure 5.10:** Total resistance as a function of gate voltage of as-fabricated and thermal annealed CVD graphene transistor. These electrical transport measurements were performed in air at room temperature, $I_{SD}$ = 1$\mu$A. The sample was annealed overnight (t≈12h).

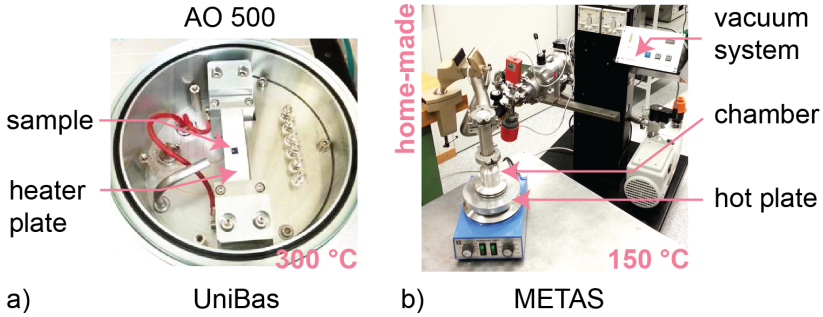


**Figure 5.11:** Two types of annealing approaches used to prepare clean CVD graphene transistors. a) Commercially available thermal annealing oven (AO 500), sample shown resting on the heater plate b) home-made thermal annealing solution at METAS consisting of a T connector (with graphene sample inside), hot-plate and vacuum system.

At our lab in Basel, a commercially available thermal annealing oven (MBE Komponenten, AO 500) was used to anneal the samples. Since the samples had to be transported to METAS in Bern, during many occasions we noticed an up-shift of the CNP after the transportation. In-order to overcome this, we devised a solution shown in fig. 5.11 b. A home-made fix consisting of a simple T-connector (with graphene sample inside), hot-plate and vacuum system were put together to anneal the samples. The result of samples annealed using fig. 5.11b approach is shown in fig. 5.10. A uniform shift of CNP is measured across different contact pairs, this shows that the such a thermal annealing procedure has a uniform impact

throughout the sample. The experimental details of sample annealing can be found in the appendix B.

### 5.4.2. Solvent treatment of graphene

Another alternate approach to reduce doping is the solvent treatment of CVD graphene films. The mechanism leading to a reduction of doping after the treatment is the replacement of ambient contaminants by the solvent molecules in some cases. This is possible due to a higher binding affinity $E_b$ of such solvent molecules to graphene i.e. in the case of NMP (N-Methyl-2-pyrrolidone) and HMDS (hexamethyldisilazane) when compared to the $E_b$ of ambient contaminants. Further experiments detailing these mechanisms are given in chapter 7 .

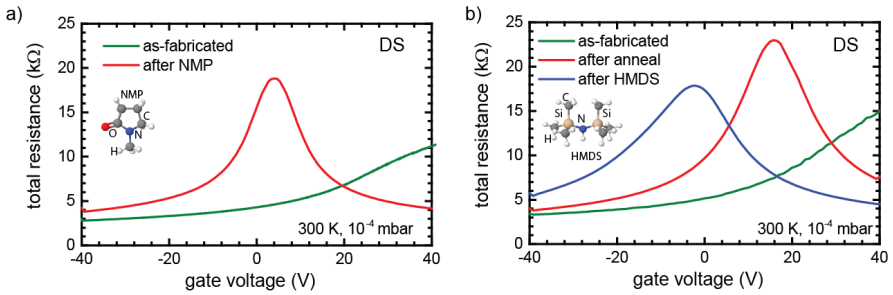


**Figure 5.12:** Total resistance as a function of gate voltage of CVD graphene transistor before and after solvent treatment. a) FET characteristics of NMP treated CVD graphene and b) HMDS treated CVD graphene device. Inset: NMP (a) and HMDS (b) molecular structure. These electrical transport measurements were performed at room temperature.

In fig. 5.12 we show the FET characteristics of as-fabricated CVD graphene before and after the solvent treatment. In fig. 5.12a the CNP in as-fabricated device is $>$+40V (green) and shifts close to zero gate voltage after exposure to NMP solution (red). Similar effect is also observed in samples treated to HMDS. Such solvent treatments can be helpful as an alternate technique to reduce doping in graphene films when thermal annealing is not preferred [105–107]. In fig. 5.12 b we can see that even after thermal annealing there is residual p-doping in graphene film (red curve), this is observed to occur in samples annealed under high annealing pressure ($>$50 mbar). However, after HMDS treatment we can observe a shift in CNP close to zero gate voltage.

A schematic understanding of the solvent treatment mechanism is shown in fig. 5.13. This type of solvent treatment of graphene films lead to replacement of

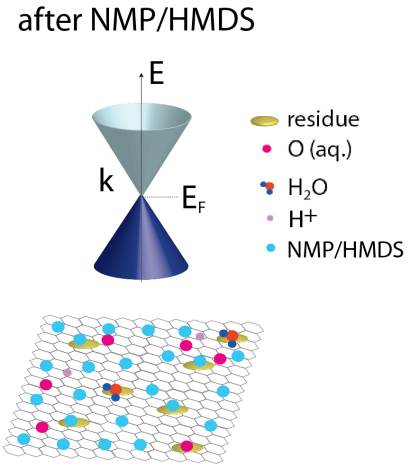


**Figure 5.13:** Schematic representation of solvent treated CVD graphene surface and the respective band diagram of solvent-treated graphene.

ambient contaminants with solvent molecules. Further experiments to study the effective surface coverage of such molecules on graphene surface is required to understand the long-term stability of these treatment procedures. The experimental details of solvent treatment can be found in the appendix B.

## 5.5. Contact and sheet resistance characterization

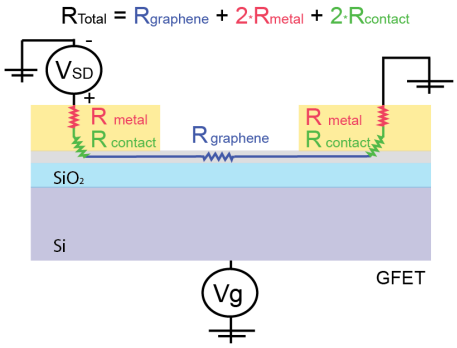


**Figure 5.14:** Schematic representation of various resistances found in a typical graphene FET.

In this section we detail our approach to characterize the contact resistance ($R_c$) of our CVD graphene FETs. Low contact resistance ($<1\Omega$) is one of the most important requirements in realizing a successful quantum Hall resistance (QHR) standard, as an imperfect contact leads to a large deviations of QHR [33]. Moreover, a high quality graphene-metal interface is of prime importance in realizing high performance graphene devices. It has been studied that high $R_c$ limits the on-current of GFETs [108, 109]. A representation of such resistances encountered in a graphene FET is shown in fig. 5.14. The total resistance is given by the sum of: i) resistance of the graphene film ($R_{graphene}$), ii) resistance of the metal contact ($R_{metal}$) and iii) contact resistance ($R_{contact}$). Typically $R_{metal}$ is much lower compared to $R_{contact}$ and can be ignored [98, 108–111]. The total resistance can be represented as ($R_s$ is the sheet resistance):

$$R_{graphene} = \frac{R_s L}{W} \tag{5.2}$$

$$R_{total} = R_{graphene} + 2R_C = \frac{R_s L}{W} + 2R_C \tag{5.3}$$

Two methods used to characterize contact resistance in our CVD graphene FETs are discussed in the following sections. First, a technique called 'transfer length method' (TLM) is used to extract $R_c$ at room temperature. Second, a more direct method of measuring $R_c$ in quantum Hall effect regime is considered.

### 5.5.1. Transfer length method

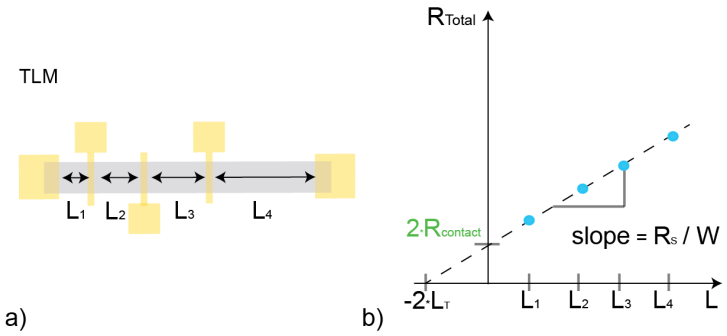


**Figure 5.15:** Transfer length method principle. a) Typical array of GFETs with increasing length $L_1$, $L_2$..$L_n$ b) TLM measurement plot with linear approximation.

The transfer length method (TLM) is a classical technique used to measure contact resistance ($R_c$) and sheet resistance ($R_s$) of a material. The principle of the TLM technique is shown in fig. 5.15. A TLM GFET array with a series of contacts of similar dimension are spaced length $L_i$ away from one another (fig. 5.15 a. The total resistance ($R_T$) is measured for each pair of adjacent contacts and is plotted as a function of length L, as shown in fig. 5.15 b. Linear approximation of the measured resistance values can then be extrapolated to extract $R_c$, $R_s$ and $L_T$ (transfer length), as shown below.

In the case of channel length L=0, from fig. 5.3, the total resistance is given by:

$$R_{total} = 2R_c \tag{5.4}$$

From the slope of the line, the sheet resistance $R_s$ can be found.

$$slope = \frac{R_s}{W} \tag{5.5}$$

Using the TLM technique, the transfer length ($L_T$) parameter can also be characterized (see: fig. 5.15). Current crowding effects have been found to explain the exponential drop in current flow (in or out) at the contact with a characteristic length scale $L_T$. The parameter $L_T$ is considered as an effective length of a contact i.e. the average distance charge carriers travel in the material before it flows into the contact.

For the optical image of the TLM device and measurement scheme refer to

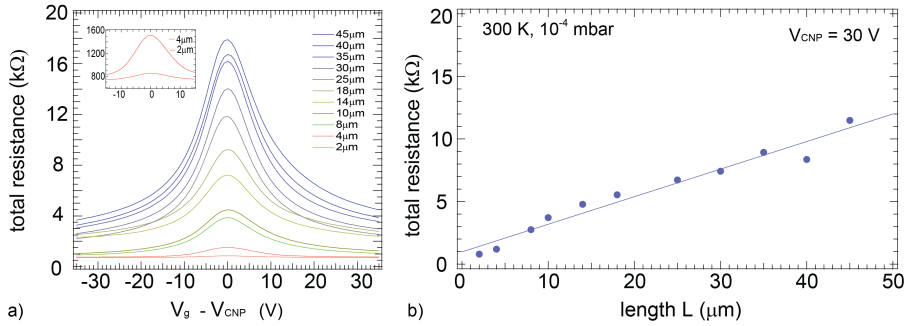


**Figure 5.16:** a) Total resistance as a function of gate voltage of CVD GFET with different channel length $L$. Inset: a zoom-in on characteristics of FETs with small channel length (2, 4$\mu$m). b) TLM plot of respective total resistance (at CNP) for different channel length of the GFETs, dotted line represents the fit. Sample width = 4$\mu$m.

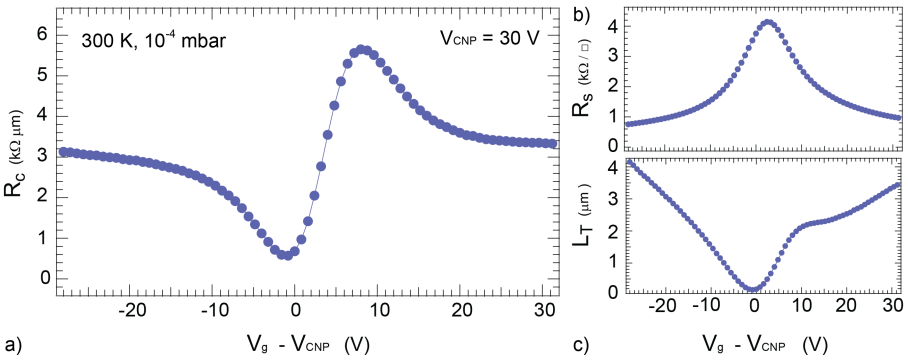


**Figure 5.17:** a-c) Contact resistance $R_c$ (a), sheet resistance $R_s$ (b) and transfer length $L_T$ (c) as a function of gate voltage of the TLM GFET array.

appendix C.9. From our measurements, we find a best value of $R_c \sim 600\ \Omega\ \mu$m, at CNP (fig. 5.17a). The contact to graphene was achieved using thermal metal evaporation process and a 5 nm palladium/ 60 nm gold was used as metal contacts. We can also notice a clear gate dependence of $R_c$, $R_s$ and $L_T$. The dependence of $R_c$ follows a dip and peak at the CNP. The feature can be understood by the transition from hole to electron dominated charge carrier transport in the graphene film. The $R_s$ is found to be 4 k$\Omega/\square$ at the CNP and is observed to decrease with increasing gate voltages. This trend can be understood due to increase in charge density away from the CNP. The $L_T$ is found to decrease at the CNP, since the charge density is minimal at the CNP, the effective length of the contact is also smaller when compared to $L_T$ at higher charge carrier density. This TLM study was

performed as a part of the master project of Oliver Braun, supervised by K. Thodkar at University of Basel.

### 5.5.2. Direct $R_c$ measurement in the QHE regime

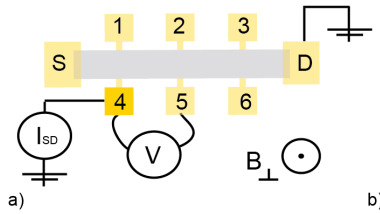


a)

b)

| sample | contact | $I_{SD}$ (mA) | Rc (Ω) B=10.6 T | Rc (Ω) B=11.6 T |
|---|---|---|---|---|
| LG2 | 4 | 1 | 7.5 | 1.4 |
| | 5 | 1 | 8.4 | 17.1 |
| | 6 | 1 | < 1 | < 1 |
| | D | 1 | < 1 | < 1 |
| | 2 | 1 | < 1 | < 1 |
| | 1 | 1 | 76.2 | 76.7 |

**Figure 5.18:** a) Representation of a direct contact resistance characterization technique in the quantum Hall regime. b) Table of $R_c$ values characterized at two magnetic fields 10.6 T & 11.6 T. The measurements were performed in QHE regime at 0.3 K.

The direct $R_c$ measurement discussed in this section is performed on a graphene Hall bar sample in the QHE regime. A voltage drop is measured across the contact to be characterized ($R_{cj}$) and the adjacent contact on the same Hall potential while a source current is applied at $R_{cj}$ and one of the current contact, as described in fig. 5.18 a. This technique can be used when the sample is well quantized i.e. when $R_{xx} \approx 0$ and thus $R_{cj}$ can be obtained directly [33].

In table fig. 5.18 b we show the $R_c$ values characterized using this technique. For contacts 6, D, 2, the $R_c$ values are well below 1 Ω, which shows that a combination of palladium-gold metal contact can form a low contact resistance junction to graphene. Such low $R_c$ values are also acceptable for QHR standards. A comparatively higher $R_c$ of 76 Ω is measured for one of the voltage contacts (Nr. 1), such high $R_c$ values are not desirable for QHR measurements. Such an abrupt increase in $R_c$ can be caused due to various reasons such as: i) residues at the graphene-metal interface or ii) contact film damage during fabrication or bonding process. Further, these values were measured for a bias current $I_{SD}$ = 1 $\mu$A, similar measurements at higher bias currents have been performed and the results are shown in appendix D.8 and D.9. The direct $R_c$ characterization shows a clear increase in $R_c$ with bias currents, this can possibly be due to heating at the graphene/Pd/Au interface occurring possibly from non-uniform Palladium islands (thickness ∼5 nm) due to the presence of polymer residues.

## 5.6. Conclusion

In this chapter two fabrication approaches were explored to batch fabricate CVD graphene transistors. Graphene field effect characteristics were presented and the source behind the doping of CVD graphene films were identified. Two key approaches i.e. i) thermal annealing and ii) solvent treatment were detailed to overcome the unwanted residual doping of the graphene films.

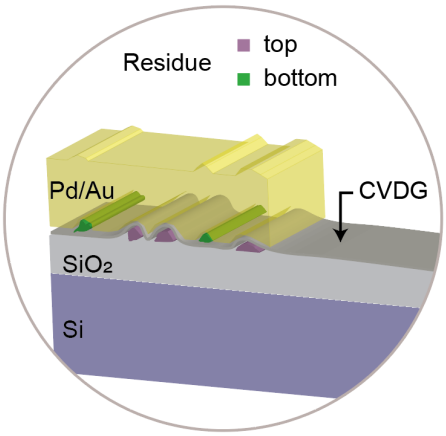


**Figure 5.19:** Schematic representation of polymer residues at the graphene-metal contact interface.

The graphene-metal interfaces were explored by following two distinct techniques i.e. i) transfer-length method (TLM) and ii) quantum Hall effect based direct $R_c$ measurement. The results of direct $R_c$ is found to be encouraging with the $R_c$ values well below 1$\Omega$, showing that it is possible to achieve good ohmic contacts in our Hall bar devices using thermal evaporation process. However, such low contact resistances were not systematically measured uniformly on the entire device. For instance on contact Nr. 1, a relatively high $R_c$ = 76.7 $\Omega$ was measured while low $R_c < 1\Omega$ was measured on other contacts. Using the TLM technique an $R_c$ of 600 $\Omega$ $\mu$m was measured, at the CNP (300K), these values are comparable with the present results in literature for palladium-gold contacts to graphene [108]. From earlier XPS and Raman studies in chapter 4, we could see the presence of PMMA-residues on as-transferred graphene, (see: appendix C.4, C.5, C.7, C.18) which can influence $R_c$ [108, 112, 113]. A study of $R_c$ characterization with varying bias currents showed that $R_c$ tends to increase with the increase in bias current, see: D.9

and D.8. The latter can be possibly due to thermal heating at the graphene/Pd/Au interface occurring possibly from non-uniform Palladium islands (thickness $\sim$5 nm) due to the presence of polymer residues.

A schematic representation of a possible scenario describing the influence of such polymer residues at the graphene-metal contact interface is shown in 5.19. The residues are marked in green (residue on top of graphene) and purple (residue on substrate/beneath graphene). The occurrence of such polymer residues on graphene films influences the reproducibility of contacts with low $R_c$ values. Such influence of residues on $R_c$ and $R_c$ variations within the sample is a well known limitation and has also been observed in other systems such as carbon nanotube transistors and Silicon Carbide based QHRs [112, 114]. Moreover, further contact resistance characterization in samples fabricated using alternative techniques with increasing bias currents is helpful in studying the effect of residues at the graphene-metal contact interface on $R_c$ values.

An alternative technique to contact CVD graphene can be to perform thermal evaporation of palladium contacts directly on as-grown graphene on copper. This step can be useful in minimizing the presence of polymer residues at the graphene-metal contact interface. In conclusion, using our approach (transfer and fabrication) although low $R_c$ values can be achieved on certain contact pairs, reproducible contacts with low $R_c$ was not possible. The latter can be due to the well known influence of residues in the graphene-metal interface. In chapter 8 we will see that although $R_c$ values differ within the sample, high precision resistance quantization in CVD graphene samples can be achieved.

# 6

# Comparing single and multi domain CVD graphene

**Abstract**

We systematically investigate the impact of granularity in CVD graphene films by performing Raman mapping and electrical characterization of single (SD) and multi domain (MD) graphene. In order to elucidate the quality of the graphene film, we study its regional variations using largearea Raman mapping and compare the G and 2D peak positions of as-transferred chemical vapor deposited (CVD) graphene on $SiO_2$ substrate. We find a similar upshift in wavenumber in both SD and MD graphene in comparison to freshly exfoliated graphene. In our case, doping could play the dominant role behind the observation of such upshifts rather than the influence due to strain. Interestingly, the impact of the polymer-assisted wet transfer process is the same in both the CVD graphene types. The electrical characterization shows that SD graphene exhibits a substantially higher (a factor 5) field-effect mobility when compared to MD graphene. We attribute the low sheet resistance and mobility enhancement to a decrease in charge carrier scattering thanks to a reduction of the number of grain boundaries and defects in SD graphene. This chapter has been published in reference [59].

## 6.1. Introduction

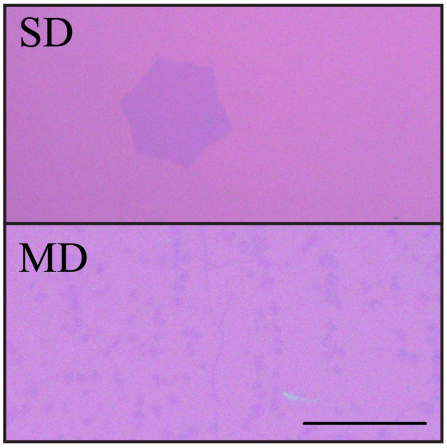


**Figure 6.1:** Illustration: Optical images of single and multi domain CVD graphene, scale bar: 50 $\mu$m.

Large-scale production of CVD graphene requires characteristics such as high mobility, low doping and low sheet resistance to be maintained uniformly over large areas. In this study, we performed a comparative systematic quality study of individual CVD graphene crystals (single domain) and uniformly grown CVD graphene films (multi domain). We rely on large-area Raman mapping and its histogram to study the regional variations in the graphene film instead of single Raman spectra to elucidate the quality of the graphene films with regard to doping, number of layers and strain in the CVD grown graphene film. We subjected SD and MD CVD graphene to the same polymer assisted wet transfer/ substrate preparation procedure and performed large-area Raman intensity mapping and electrical transport characterization.

The average peak position of G and 2D bands of as transferred CVD graphene is then compared with a freshly exfoliated graphene flake which is free of polymeric residues. Two different growth conditions were used for the SD and MD graphene growth. We achieved the growth of SD graphene by considering low carbon flow rate and stopping the CVD growth prior to the formation of a uniform single graphene layer. MD graphene samples with a uniform coverage of single layer graphene were obtained by having a higher carbon flow rate and the growth process was stopped after the coalescence of individual graphene domains (see: fig. 6.2).

We found a similar upshift in wavenumbers of the G and 2D peak positions in both CVD graphene types when compared to a freshly exfoliated single layer graphene flake. In addition, the electrical transport characteristics show five times higher field effect mobility and lower sheet resistance for the SD type when compared to MD type, with graphene's Dirac peak close to zero back-gate voltage in both types.

## 6.2. Optical images of single and multi domain CVD graphene

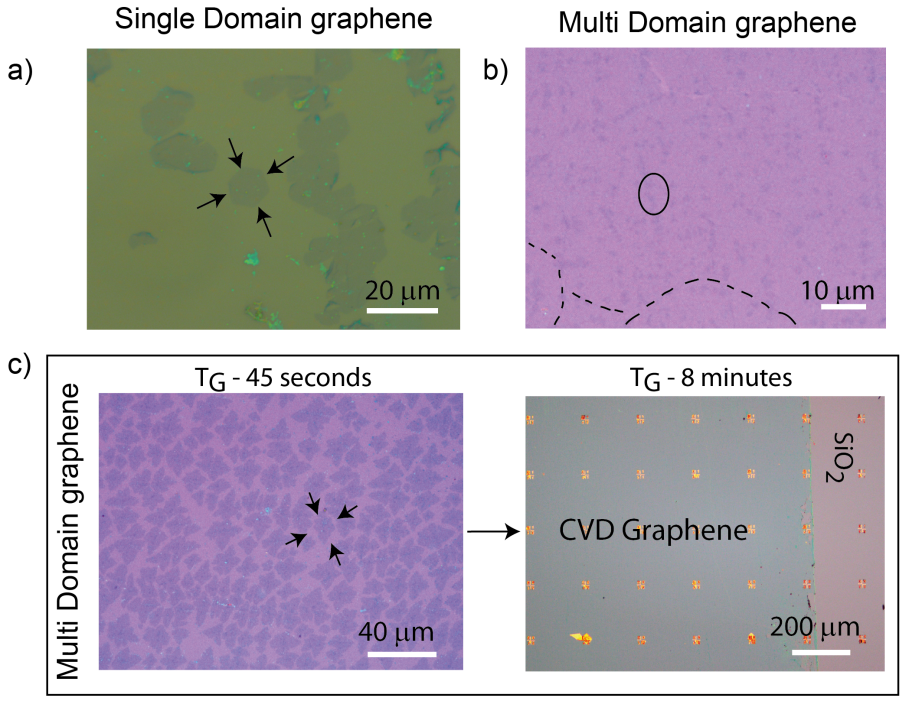


**Figure 6.2:** (a) Optical image of SD graphene on $SiO_2$. An individual graphene grain is indicated using black arrows. (b) Optical image of MD graphene on $SiO_2$ substrate. A bi-layer graphene flake is marked by circle and wrinkles are marked by dotted lines. (c) Optical images of MD graphene transferred on $SiO_2$ substrate at growth time $T_G$ of 45 seconds and 8 minutes.

CVD graphene was grown on polycrystalline copper foil using low pressure CVD technique in a hot wall CVD reactor at a temperature of 1000 °C .The film

was then transferred onto a 300 nm thick $SiO_2$/Si substrates using a wet etching technique (see: fig. 3.3.1) [66]. Optical images of SD and MD graphene transferred on $SiO_2$/Si substrate are shown in figure 1a, b. In figure 1c we can see a high density of individual graphene grains at growth times $T_G \sim 45$ s, and at $T_G \sim 8$ min where the SD graphene grains start to coalesce thus forming a uniform sheet of MD graphene.

Prior to the film growth, the copper foil undergoes a high temperature annealing at 1000 $^\circ$ C under an argon (Ar) gas flow. To initiate the CVD of graphene, methane ($CH_4$) and hydrogen ($H_2$) gas are introduced into the CVD chamber for a certain period of time of 6 hours for SD graphene and 15 minutes for MD graphene. A low carbon supply is required to assist the growth of single graphene grains at a reduced nucleation density [56, 60, 115–117]. In this work, the methane flow rate for SD graphene was kept at 0.04 sccm; while for the MD growth, the $CH_4$ flow was 2.5 sccm. After the growth, the chamber was cooled down to ambient temperature in an Ar/$H_2$ flow (see: B for growth details).

## 6.3. Raman characterization of single and multi domain CVD graphene

We performed large area confocal Raman spectroscopy ($\lambda_L \sim 532$ nm, $P_L \sim 2$ mW) of SD and MD graphene transferred onto a 300 nm $SiO_2$/Si substrate to characterize the quality of CVD graphene. Raman spectroscopy has turned out to be the most effective non-invasive tool to characterize doping, strain, edges, number of layers, stacking of layers and defects in graphene [12]. The G and 2D peaks are the two prominent Raman peaks which can be observed around 1585 cm $^{-1}$ and 2674 cm$^{-1}$ for exfoliated graphene flakes on Si/$SiO_2$ substrate (see: fig. C.21) [12, 118] (see: C for Raman characterization details). The G and 2D peak positions and their FWHM help gathering information related to doping and strain. Defects in graphene can be characterized by studying the variations of the D peak within the graphene flake. This peak, which occurs around 1345 cm$^{-1}$, is the result of defect assisted inter-valley scattering processes [13, 119, 120].

Disorder in graphene (bond disorder, defects) can also be characterized by the measurement of the intensity ratios of the D and G peaks [121]. Studying regional variations in the graphene film is of utmost importance to elucidate the true quality of the graphene film. Hence we rely on large area Raman mapping instead of

single Raman spectra from different regions for characterizing parameters such as doping, thickness of the graphene film and strain. In fig. 6.3 a-c and g-i we show large area Raman intensity maps for the D, G and 2D bands and their peak position histograms (fig. 6.3 d-f, j-l) for SD and MD graphene samples. We observe nearly hexagonal graphene grains for SD graphene growth conditions as seen in fig. 6.2 and fig. 6.3 a. The G peak position can be used to estimate the charge carrier concentration in the graphene sheet, which can be tuned by electrically modulating graphene's Fermi level using a back-gate voltage. It has been observed that the G peak position shifts to larger wavenumbers for both electron and hole doping [73, 122]. The average peak positions for the G and 2D bands for the SD sample are 1589 $cm^{-1}$ and 2684 $cm^{-1}$ respectively. They are up-shifted by 4 $cm^{-1}$ and 10 $cm^{-1}$ when compared to the values observed for freshly exfoliated graphene samples on $SiO_2$/Si substrate.

In fig. 6.3 g-i and j-l we can see the large area scan and histogram of peak positions for MD graphene. The average G and the 2D peaks positions are located at 1590 $cm^{-1}$ and 2684 $cm^{-1}$ [73]. When compared to SD graphene, we observe an upshift of 1 $cm^{-1}$ for G band; which shows a slightly higher p-doping for the MD sample. The type of doping can be verified by the direction of the Dirac peak shift (see: fig. 6.4, $V_{CNP} > 0$ V denotes p-doping. We also observe more features in the D and G band large area scans of MD graphene (marked in fig. 6.3 g-i). The bright lines in the D and G band scans can result from wrinkles and folds in the copper foil, which can occur during the graphene transfer (see: fig. 6.2, fig. C.4).

Moreover, the upshift in wavenumbers observed in both CVD graphene types (as compared to a freshly exfoliated graphene sample where $G_{exf}$ 1585 $cm^{-1}$ and $2D_{exf}$ 2674 $cm^{-1}$) is of similar magnitude, which suggests that the impact of the polymeric residues from the transfer process of CVD graphene is the same, although SD and MD graphene types were grown under different conditions. The observed upshift of the G, 2D peak position is due to the high p-doping induced due to exposure to water and PMMA leftovers during the transfer process, which is absent in a freshly exfoliated graphene flake. High p-doping (n-doping) of graphene can result in stiffening (softening) of the G peak phonons and cause an upshift in wavenumbers. The polymeric residues and wrinkles from the transfer result in a pronounced D peak as seen in the regional D band intensity scan where they appear as bright spots and lines (see: fig. 6.3 g).

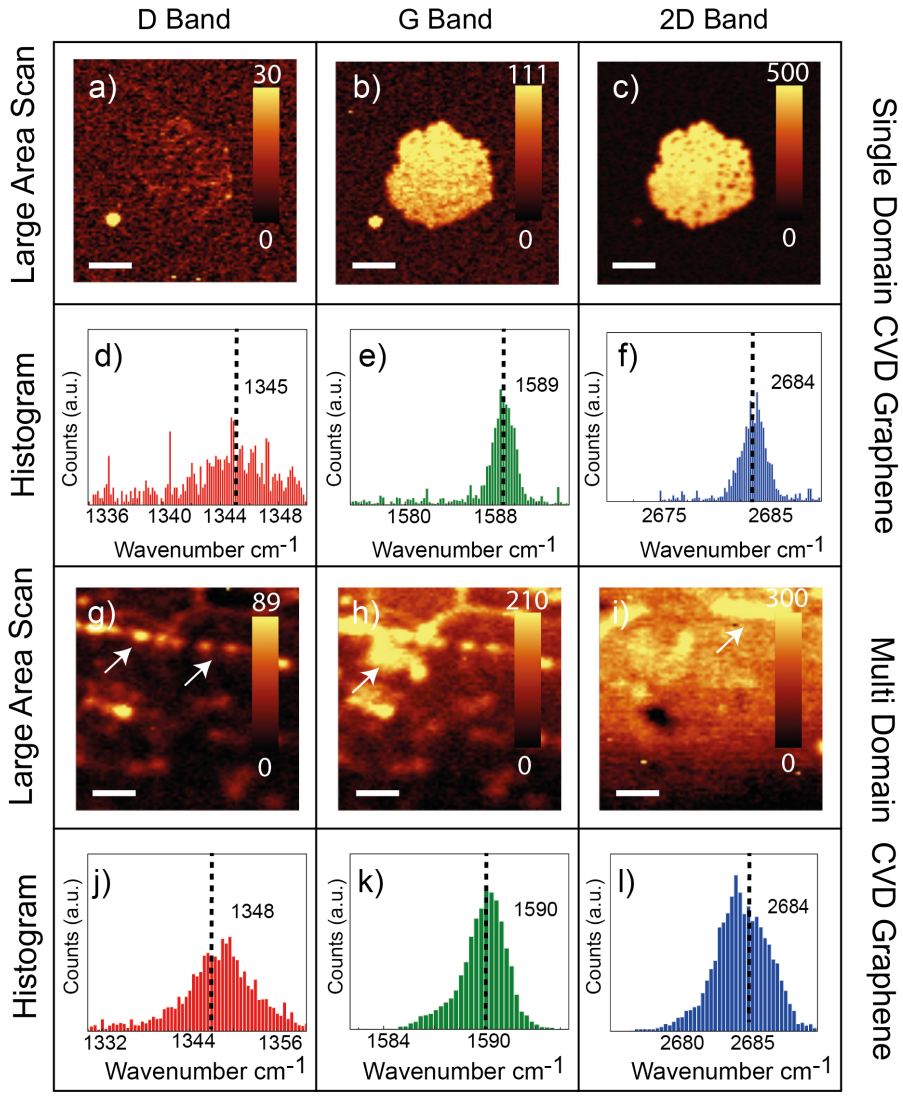


**Figure 6.3:** Large area Raman scans of D, G and 2D bands (a-c, g-i) and peak position-histograms of SD (d-f) and MD (j-l) graphene. The average peak positions are marked with black dotted lines for D, G and 2D bands. Features in the large area scans are marked using white arrows. Scale bars: 4 $\mu$m (SD) and 2 $\mu$m (MD).

## 6.4. Field effect comparison of single and multi domain CVD graphene

In order to compare the electrical transport characteristics, the sheet resistance $R_{\square}$ is shown in figure 3 as a function of the charge carrier density $n_e$ for both SD and MD graphene. The SD sample (see: fig. C.27) was fabricated on a single graphene grain, while no pre-selection of a graphene region was made in case of MD graphene. After fabrication, the samples under-went thermal annealing in a forming gas ($Ar/H_2$) flow at 300°C for 3 hours to reduce the polymer residues from the graphene film [122]. After thermal annealing, the electrical transport measurements were performed under low vacuum condition of $10^{-4}$ mbar in order to avoid p-doping due to exposure to ambient conditions.

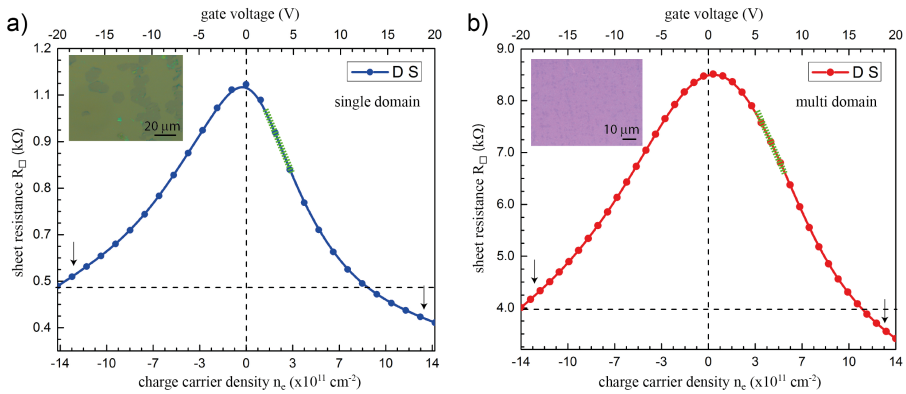


**Figure 6.4:** Source drain (DS) measurement of the sheet resistance $R_{\square}$ as a function of the charge carrier density $n_e$ for both SD (a) and MD (b) graphene samples, using a bias voltage of $V_{SD} \sim 10$mV. Inset: Optical image of the SD and MD graphene on $SiO_2$. The field effect mobility was calculated using the slope of the conductance curve determined by the green stripes. The dotted lines and arrows highlight the asymmetry in the field-effect characteristics.

The transport characteristics of both SD and MD graphene show almost no p-doping, with Dirac peak close to $V_g$ = 0V (fig. 6.4 a, b). We also observe an asymmetric $R_{\square}$ vs. $n_e$ characteristic for both the SD and MD types, which is due to contact doping at the metal-graphene interface at the source and drain con-tacts of the device [123]. The mobility $\mu_{FET}$ for SD and MD graphene differ significantly, from $\mu_{FET}$ = 6000 $cm^2$/Vs for SD to $\mu_{FET}$ = 1200 $cm^2$/Vs for MD, i.e. a five times higher mobility in SD graphene (see: fig. 6.4 a, b) (see: fig. C.25 for mobility

estimation procedure).

## 6.5. Discussion

Large area confocal Raman characterization of SD and MD graphene (figure 1a-c) gives an insight into the G and 2D peak position variations over CVD graphene's surface, from which one can ascertain the doping concentration. In comparison, the G and 2D peak position in the as transferred CVD graphene samples without thermal annealing show an upshift by $\sim$ 4 $cm^{-1}$ and 10 $cm^{-1}$ when compared to exfoliated graphene on Si/$SiO_2$ substrate, where $\Delta$G of 0.5 $cm^{-1}$ $\sim$ 2.4x$10^{11}$ $cm^{-2}$ [122].

Such a high p-doping of CVD graphene, observed prior to annealing, can occur due to presence of water vapor, oxygen molecules and polymeric residues on CVD graphene films and the exposure to these constituents is unavoidable during the wet transfer process of CVD graphene. It has been reported that exposure to ambient conditions can cause p-doping of graphene films and the underlying mechanism has been identified as the redox couple reaction between $H_2O$ and $O_2$ molecules [101]. Consequently, lower G and 2D peak position values observed in the exfoliated graphene can be due to absence of exposure to water during graphene exfoliation. However, we cannot ignore the presence of water vapor on the $SiO_2$ surface during exfoliation, which are trapped under the exfoliated graphene flake, thus leading to slight p-doping of exfoliated graphene. Interestingly, although both SD and MD graphene samples were grown under slightly different conditions, the observed G and 2D peak upshift is similar in both the samples. This suggests that the impact of the polymer assisted wet-transfer process is similar in both types independent of the growth conditions.

In particular, the upshift of the 2D peak position is twice the shift in the G peak. Although the 2D peak position and its FWHM have been found to be sensitive to doping, it has also been reported to be sensitive to nanoscale strain variations [77], hence a careful interpretation of the spectral variations is of utmost importance to disentangle effects due to doping and strain in the graphene film. Such strain variations and doping cause a broadening of the 2D peak due to enhanced electron-electron and electron-defect scattering [77, 82]. Commercially available copper foil surface have corrugations over the entire surface, which occur during the foil production process. However, when a conformally grown CVD graphene film covering the corrugated copper surface is transferred onto a flat $SiO_2$ substrate,

it results in a non-conformal transfer of the graphene layer on the $SiO_2$ surface, leading to wrinkles, folds and inhomogeneous strain fluctuations in the graphene sheet [77, 82].

Since G and 2D peaks are both sensitive to strain and doping, it is necessary to distinguish the dominant factor behind the observation of the Raman upshifts in our case. By comparing our measurements of average G and 2D peak position values of CVD graphene with the work of Lee et.al [82], we can see that the G and 2D frequencies lie in the region of G and 2D frequencies for compressively strained graphene film. It has also been shown in other reports that as-transferred CVD graphene films on $SiO_2$ substrate is compressively strained due to the wet transfer process, while exfoliation of graphene film leads to tensile strain [124]. The presence of large uni-axial strain ($> 0.4$ %) leads to the splitting of G peak into G$+$ and G$-$ and results in the broadening of the Dirac peak. Clearly, the above mentioned Raman and electrical transport features are not observed in any of our samples. Moreover, large shift ratios of $\Delta\omega$2D/$\Delta\omega$G in the range of 2.25 - 2.8 have been predicted and measured in highly strained graphene [82].

In our case, we find a shift ratio of $\Delta\omega 2D^{CVD-susp}/\Delta\omega G^{CVD-susp} \sim 1$ by comparing the average 2D and G peak position of our CVD graphene ($\omega$2D-CVD $\sim$ 2684 cm$^{-1}$, $\omega$G-CVD $\sim$ 1589 cm$^{-1}$) with suspended graphene ($\omega$2D-susp $\sim$ 2677 cm$^{-1}$, $\omega$G-susp $\sim$ 1582 cm$^{-1}$) from the work of Lee et al. [82], it is assumed that the suspended graphene film was strain-free. Since $\Delta\omega 2D^{CVD-susp}/\Delta\omega G^{CVD-susp} \sim 1$, the upshift in G and 2D peak position in our case is predominantly due to the effects of p-doping from exposure to water and ambient conditions, although the CVD graphene films are strained from transfer.

More features can be observed in the large area scan of the D and G band scans of MD graphene (fig. 6.3 g, h). The bright line-like features are caused by wrinkles and folds from the transfer, while patches (brighter spots) in the G band scan are due to the presence of bi-layer graphene regions and polymeric residues. The Raman spectra measured on the polymer residue show a more pronounced D peak intensity with a minimal broadening of the 2D peak when compared to bilayer graphene (BLG) Raman spectra. This is helpful in distinguishing a BLG from a polymer residue in transferred graphene film (see: fig. 4.2 4.6for spectral details).

In order to reduce the polymeric residues from the transfer process and avoid the p-doping effects due to exposure to ambient conditions, electrical transport measurements were performed after a thermal annealing of SD and MD graphene in low vacuum of $10^{-4}$ mbar to study the differences in the sheet resistance of

both the samples. The transport characteristics show a Dirac peak close to 0V (fig. 6.3) and the MD graphene sample mobility $\mu_{FET}$ is five times lower and the sheet resistance $R_{\square}$ is higher than in the SD graphene sample. This reduction in the charge carrier mobility is due to the presence of increased grain boundaries, polymer residues and defects, which affect the transport properties. In addition, the sample quality can also be deteriorated by charge traps on the $SiO_2$ surface, by local strain variations due to film transfer and by crystal defects in both SD and MD graphene sample [77, 125, 126].

Although the crystal growth quality can be controlled by using a suitable set of growth parameters such as the carbon concentration and temperature, the control of charge traps and nanoscale strain variations is more challenging due to other limitations such as corrugated growth substrate and polymer assisted wet-transfer process of the CVD graphene film. However, the influence of charge traps on $SiO_2$ substrate can be reduced by performing a passivation of the surface using HMDS (Hexamethyldisilazane) prior to the CVD graphene transfer [12, 105, 107]. Other surface treatments of the copper foil surface using electro-polishing or annealing are helpful in minimizing the corrugations on the copper surface. An additional systematic investigation is required to study the effects of such treatments on CVD graphene quality using large area Raman characterization coupled to electrical transport measurements.

## 6.6. Conclusion

By performing a systematic Raman characterization of as transferred SD and MD graphene, we find a similar upshift of the G and 2D peak positions for both graphene morphology when compared to polymer free freshly exfoliated graphene on $SiO_2$/Si substrate. Although CVD graphene films can be compressively strained due to the transfer process, the observed shift in our case can be predominantly attributed to p-doping in the presence of water and oxygen molecules under ambient conditions. Electrical transport measurements performed after thermal annealing in low vacuum show a Dirac peak close to 0 V, suggesting the absence of p-doping. The field-effect mobility of SD graphene is found to be about five times higher than in MD graphene. The higher sheet resistance values measured in MD graphene reveals an increased charge scattering due to grain boundaries, wrinkles, folds and crystal defects although the Raman mapping of SD and MD graphene show similar characteristics.

# 7

# Restoring the electrical properties of CVD graphene via physisorption of molecular adsorbates

**Abstract**

Chemical vapor deposition (CVD) is a powerful technique to produce graphene for large scale applications. Polymer-assisted wet transfer is commonly used to move the graphene onto silicon substrates but the resulting devices tend to exhibit p-doping which decreases the device quality and reproducibility. In an effort to better understand the origin of this effect we coated graphene with n-methyl-2-pyrrolidone (NMP) and hexamethyldisilazane (HMDS) molecules that exhibit negligible charge transfer to graphene but bind more strongly to graphene than ambient adsorbents. Using Raman spectroscopy, X-ray photoelectron spectroscopy (XPS), electrical transport measurements, and quantum mechanical computer simulations, we show that the molecules help in the removal of p-doping and our data indicates that the molecules do this by replacing ambient adsorbents (typically, $O_2$ and water) on the graphene surface. This very simple method of improving the electronic properties of CVD graphene by passivating its surface with common solvent molecules will accelerate the development of CVD graphene based devices. This chapter has been published in reference [127].

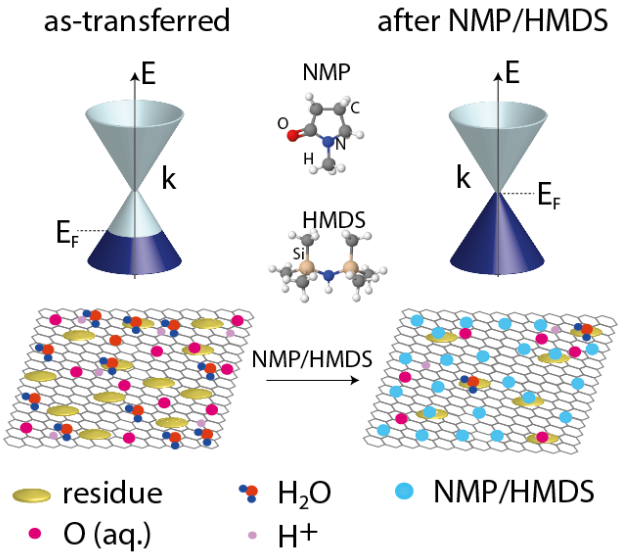


**Figure 7.1:** Illustration of physisorption effects of NMP and HMDS on CVD graphene

## 7.1. Introduction

Graphene, a single atom thick two-dimensional material with sp2 hybridized carbon atoms arranged in a honeycomb lattice has attracted huge interest for its potential use in biological, chemical and electronic applications due to its unique electronic and mechanical properties [4]. Keeping the physical structure of the graphene film intact, some of the non-destructive methods that allow direct detection of adsorbents include: a) charge-transfer based electronic property modulation; b) radio-frequency (RF) based nanomechanical mass sensor; c) plasmonics based optical sensor, and d) photothermoelectric effect based detectors [128–132]. Chemical vapor deposition (CVD) is a powerful technique to produce graphene for large scale applications. CVD of graphene is typically performed on a variety of metals; hence its transfer onto a given substrate is usually necessary for device applications. One of the most widely used transfer techniques is the polymer-assisted wet transfer process, in which the as-grown CVD graphene on metal is supported by a thin polymer film during metal etching [46]. Subsequently the polymer film is usually dissolved in solvents after the graphene transfer or can even be sublimated by thermal annealing.

The observation of p-doping due to the transfer process is very common in

as-transferred and as-fabricated CVD graphene samples and decreases the reproducibility of device properties [122]. Although several factors have been proposed as the underlying reason behind the observation of such p-doping; a comprehensive study confirming the main factor and a simplified solution to circumvent the issue remains elusive. However, it is interesting to note that electrochemical charge transfer with $O_2$ and $H_2O$ adsorbents has been identified as the main mechanism behind the observation of p-type conductivity in hydrogenated diamond surfaces and the suppression of n-type charge carriers in carbon nanotubes (CNTs) [102, 133]. Hence, factors directing such an electronic modulation of graphene properties have been posited to include: a) polymer contamination during transfer; b) redox reactions in the aqueous layer on top of graphene and c) presence of charged oxide traps in the graphene-oxide interface [99, 101, 102]. It is still unknown whether any, some or all of these factors induce p-doping in CVD graphene. The understanding and ultimate removal of this modulation would be a key step towards developing CVD graphene based applications.

To address this issue, we performed a systematic and detailed study using Raman spectroscopy, X-ray photoelectron spectroscopy (XPS) and electrical transport measurements supported by quantum mechanical computer simulations, which taken together give a detailed insight into the doping mechanisms taking place in graphene due to organic contaminants. Our experimental design involves introducing adsorbents with negligible charge transfer to graphene but stronger binding affinity than ambient adsorbents water and oxygen. This allows us to map the changes in the electrical properties of CVD graphene as it undergoes surface treatments of the two organic compounds most commonly used during fabrication, n-methyl-2-pyrrolidone (NMP) and hexamethyldisilazane (HMDS). We perform large area Raman mapping, electrical transport measurements (ambient and 0.3K), XPS measurements and dispersion-corrected density functional theory (DFT) calculations [134] of their complexes with graphene in an effort to identify the prime reason behind the high p-doping observed in as-transferred CVD graphene [99, 101, 122].

## 7.2. Experimental section

NMP is used as a resist stripper during the lift-off process, while HMDS promotes resist adhesion on substrates during lithography. Moreover, NMP is among the top organic solvents of choice for liquid phase exfoliation of graphene flakes due to its low enthalpy of mixing [135]. NMP is hydrophilic and readily miscible with water

but HMDS is a hydrophobic organic solvent. These two solvents not only have contrasting properties and applications but also have a stronger binding affinity to graphene surface in comparison with two of the most commonly found adsorbents on graphene, i.e., water and oxygen molecules (see also DFT calculations below). This provides us with an ideal model system to test the influence of such adsorbents on as-transferred CVD graphene films.

CVD graphene was produced by low pressure chemical vapor deposition (LPCVD) and the transfer of graphene onto $SiO_2$/Si substrates performed using polymer assisted wet transfer (see appendix section for CVD growth and transfer procedure) [59]. Raman spectroscopy is the method of choice to characterize doping, defects, strain, and number of layers in graphene films [13]. Here, we use large area Raman maps to study the regional spectral variations of as-transferred and solvent treated CVD graphene. Studying regional variations rather than a single Raman spectrum can be extremely useful to understand the effects of polymer transfer and solvent treatment at large scales. The characteristics of the G and 2D peaks, i.e., peak position and FWHM, is helpful in characterizing the doping and strain in the graphene film [77, 119, 120]. However, differentiating the effects of strain and the effects of doping is not a trivial task, especially in as-transferred CVD graphene on substrate.

The G and 2D peak positions shift to higher wavenumbers and the FWHM of G peak decreases with increase in electron and hole doping [119]. In the case of uni-axial strain, the G peak splits into G+ and G- for strain larger than $> 0.4\%$ and both G and 2D peaks shift to higher wavenumbers [136]. However, in the bi-axial case, there is no splitting of the G peak and depending on the type of strain, tensile or compressive, the G and 2D peak position downshift or upshift in wavenumbers [124, 137]. Although CVD graphene films are compressively strained from the wet transfer process, our data indicates that shifts in the G and 2D peaks are predominantly due to doping from polymer contamination and/or adsorption of ambient molecules [124].

## 7.3. Large area Raman mapping of as-transferred and NMP treated graphene

In fig. 7.2a we show a large area ($10\mu$m x $10\mu$m) Raman map of as-transferred, NMP treated and thermally-annealed CVD graphene. The bottom axis of the

histogram G (fig. 7.2b) and 2D (fig. 7.2c) band map shows the spread in peak position and the top x-axis shows the spread in the FWHM of the G and 2D peaks, respectively. The average value of the peak position and FWHM is highlighted using dashed lines.

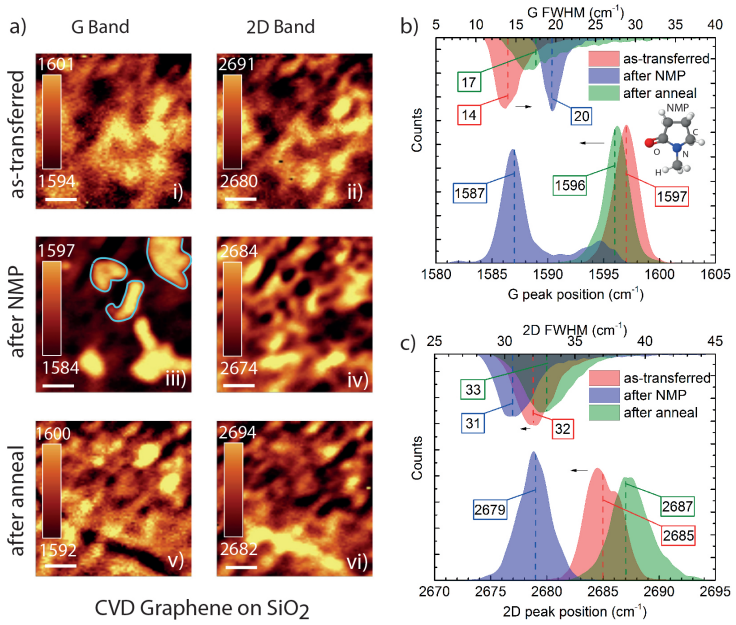


**Figure 7.2:** a) Raman map (10$\mu$m x 10$\mu$m) of G and 2D peak positions of as-transferred (i, ii), NMP treated (iii, iv) and thermal annealed (v, vi) CVD graphene on $SiO_2$ substrate. Scale bar: 2 $\mu$m. The polymer residues are marked using light-blue contours (fig. 7.2a iii); see fig. C for more details. The corresponding peak positions in the G and 2D band maps can be found using the color bar. b, c) Histogram of the peak position (bottom x-axis) and FWHM (top x-axis) of the respective G band (fig. 7.2a i, iii, v) and 2D band (fig. 7.2 a ii, iv, vi) maps of CVD graphene after different treatment procedures. Inset fig. 7.2b: molecular structure of NMP. The average peak positions of the histogram are denoted by red, blue and green dashed lines within the histogram. All the Raman measurements were performed under ambient conditions.

Several features in the large area Raman map can be observed. In fig. 7.2a iii-iv the polymeric residues from the transfer process are clearly visible and appear as bright spots in the G and 2D Raman maps. The polymer residues in fig. 7.2a iii are highlighted using light-blue contour (see: fig. 3.8 for optical images) and the respective peak positions can be found using the color bar of the Raman maps. We can observe that for as-transferred CVD graphene, the average G and 2D peak position is found at: $G_{as-tr.} \sim 1597$ cm$^{-1}$, $2D_{as-tr.} \sim 2685$ cm$^{-1}$ (fig. 7.2b, c - red

histogram). Such values denote the presence of doping and/or strain in the CVD graphene film (see: fig. C.14 for Raman mapping of second NMP-treated CVD graphene). For comparison purposes, we freshly exfoliated graphene on $SiO_2$/Si substrate and find that the G and 2D peaks are at: $G_{exf} \sim 1584$ cm$^{-1}$ and $2D_{exf} \sim 2674$ cm$^{-1}$ (see: fig. C.21). Clearly, the $G_{as-tr.}$ and $2D_{as-tr.}$ values are up-shifted by as much as 13 cm$^{-1}$ and 11 cm$^{-1}$ for G and 2D peak positions, respectively. Even though the CVD graphene films are compressively strained from transfer, our data (and analysis below) indicate that p-doping by adsorbates could play the dominant role behind the upshift of G and 2D peaks.

After the NMP treatment (see: fig. B for detailed procedure and fig. C.28 for rolling of graphene after NMP treatment) the large area Raman maps (fig. 7.2a iii, iv) reveal a substantial downshift of both G and 2D peak positions (fig. 7.2b, c - blue histogram). The average peak position after NMP treatment was found to be $G_{NMP} \sim 1587$ cm$^{-1}$ and $2D_{NMP} \sim 2679$ cm$^{-1}$. In comparison to $G_{as-tr.}$ and $2D_{as-tr.}$, the downshift is $\sim 10$ cm$^{-1}$ and 6 cm$^{-1}$ for G and 2D peaks, respectively. Moreover, in the NMP treated graphene, we can also observe a slight broadening of the $G_{NMP}$ FWHM and sharpening of the $2D_{NMP}$ FWHM by 6 cm$^{-1}$ and 1 cm$^{-1}$, which indicates reduction in charge doping.

In order to check if the downshift of the peaks is caused by the NMP molecules, we performed thermal annealing of the NMP treated graphene. The thermal annealing was performed at 350 °C to intentionally desorb the NMP molecules from the graphene surface ($bp_{NMP} \sim 200$ °C). Interestingly, we find the G and 2D peak positions upshift to $G_{Th.} \sim 1596$ cm$^{-1}$ and $2D_{Th.} \sim 2687$ cm$^{-1}$, similar to the values measured for $G_{as-tr.}$ and $2D_{as-tr.}$ (fig. 7.2b, c - green histogram). Moreover, the ratio of relative change in 2D and G peak position before and after the treatment can be very useful in studying the influence of strain and doping in the graphene film. A ratio of $\Delta\omega$2D / $\Delta\omega$G $\sim$ 2.2-2.8 has been interpreted as diagnostic of large strain in the graphene film while a smaller ratio of $\Delta\omega$2D / $\Delta\omega$G $\sim$ 0.75 denotes hole/electron doping [18, 82].

In our case, by considering the average G and 2D peak positions for as-transferred and NMP treated CVD graphene, we obtain $\Delta\omega 2D_{as-tr-NMP}$/ $\Delta\omega G_{as-tr-NMP}$ $\sim$ 0.6, which indicates the presence of doping. Moreover, considering the peak position values of a reference suspended graphene sample [82] of $G_{susp.} \sim 1581.6$ cm$^{-1}$ and $2D_{susp.} \sim 2676.9$ cm$^{-1}$, we obtain $\Delta\omega 2D_{as-tr-susp}$/ $\Delta\omega G_{as-tr-susp} \sim$ 0.5 for the as-transferred graphene and $\Delta\omega 2D_{NMP-susp}$/ $\Delta\omega G_{NMP-susp} \sim 0.4$ for NMP treated graphene. These ratios are much lower than the values expected for

the case of strained graphene and indicate the presence of doping. However, we do not rule out the presence of anisotropic residual compressive strain ($< 0.1\%$) in our transferred graphene film.

## 7.4. HMDS treatment of CVD graphene

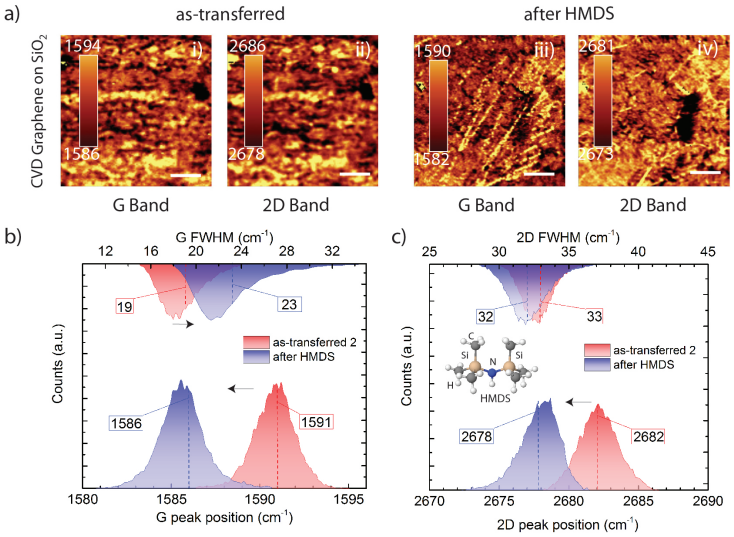


**Figure 7.3:** Raman map (50$\mu$m x 50$\mu$m) of as-transferred and HMDS-treated CVD graphene on $SiO_2$ substrate. a) Confocal Raman imaging of G and 2D peak position of as-transferred CVD graphene (i, ii) and after HMDS treatment (iii, iv) scale bar: 10 $\mu$m. The corresponding peak positions in the G and 2D band maps can be found using the color bar. b, c) Histogram of peak position and FWHM (top axis) of the respective G band (fig. 7.3a i, ii) and 2D band (figure a iii, iv) maps of as-transferred CVD graphene and after HMDS treatment. Inset 2c: molecular structure of HMDS. The average peak position of the histogram is marked using red and blue dotted lines. All the Raman measurements were performed in ambient conditions.

In order to test our model further, we left the as-transferred CVD graphene overnight in HMDS (hexamethyldisilazane). HMDS is a commonly used resist primer and is also known to improve the performance of graphene transistors [105–107]. In figure 7.3, we show the large area Raman map of as-transferred and HMDS treated CVD graphene (figure 2a). The optical images of as-transferred CVD graphene on substrate before HMDS treatment is shown in fig. C.16. We can see that in the as-transferred CVD graphene sample, the average peak positions lie at $G_{as-tr2} \sim 1591$ cm$^{-1}$ and $2D_{as-tr2}$ 2682 cm$^{-1}$ and after the HMDS treatment,

the peaks downshift to $G_{HMDS}$ 1586 $cm^{-1}$ and $2D_{HMDS}$ 2678 $cm^{-1}$ by 5 $cm^{-1}$ and 4 $cm^{-1}$ wavenumbers (fig. 7.3b, c). The average peak position after HMDS treatment is similar to the values observed in the case of the NMP treated CVD graphene sample (see: fig. C.15 for large area Raman mapping of second HMDS-treated CVD graphene). Although NMP and HMDS have different physical properties, their influence on CVD graphene is similar.

Furthermore, we performed stability and reversibility tests on NMP treated CVD graphene using Raman characterization and the results can be found in C.20. We obtained Raman maps of G and 2D bands of as-transferred (fig. C.20a) and NMP treated CVD graphene (fig. C.20b i, ii). As summarized in figure 7.2, we observe a downshift of the G and 2D peaks after NMP treatment as measured on Day 1. This same downshift of peak position remains the same when measured in air over five days, which suggests that re-adsorption of ambient molecules on graphene is hindered by NMP (fig. C.20b iii, iv). Next, we performed thermal annealing of the same NMP treated graphene at 400°C ($bp_{NMP}$ 200°C) served an upshift of the G and 2D peaks (figure C.20c). This upshift of G and 2D peaks may be due to re-adsorption of ambient molecules on top of CVD graphene; the NMP molecules can undergo desorption during thermal annealing and leave the graphene surface exposed to ambient molecules. An annealing temperature of 400°C was intentionally chosen to aid thermal desorption of NMP molecules. However, we do not rule out the possibility of thermal degradation of the NMP molecule into other nitrogenous molecules during annealing.

We performed a second NMP treatment of the thermally annealed graphene to test the reversibility of the NMP treatment (fig. C.20d). Remarkably, the G and 2D peaks downshift to the values observed after the first round of NMP treated graphene. This result shows that the process is reversible and the creation of a physisorbed molecular film on the surface of CVD graphene mitigates the deleterious effects of ambient exposure.

## 7.5. XPS characterization of as-transferred and NMP treated CVD graphene

In order to confirm the presence of NMP, we performed X-ray photoelectron spectroscopy (XPS) characterization of the as-transferred and NMP treated CVD graphene on $SiO_2$/Si substrate (fig. 7.4). The XPS survey of as-transferred (red) and NMP treated CVD graphene (blue) is shown in fig. 7.4. In fig. 7.4 inset, we can notice the absence of the N1s core level, while it is visible in the NMP treated CVD graphene (blue). This presence of N1s peak at 400.0 eV in the NMP treated CVD graphene is expected due to the presence of an N-$CH_3$ group and confirms the presence of NMP in NMP-treated CVD graphene [138].

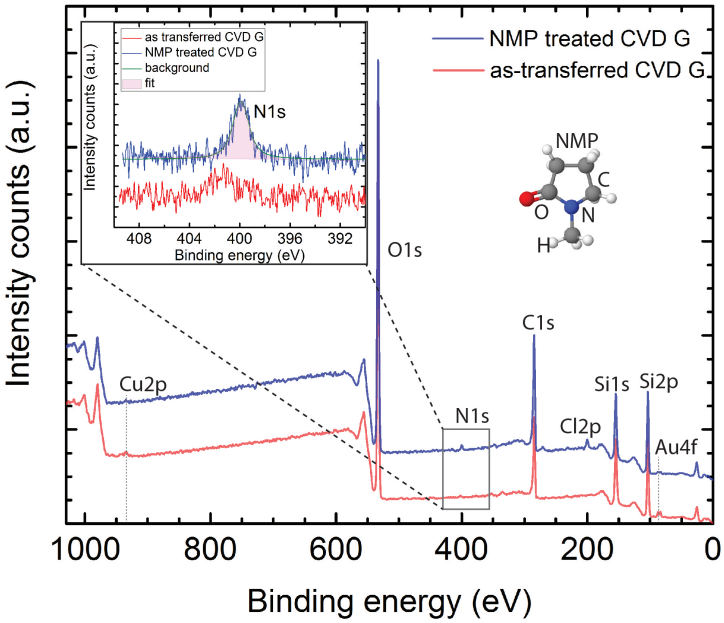


**Figure 7.4:** X-ray photoelectron spectroscopy characterization of the as-transferred and NMP-treated CVD graphene on $SiO_2$/Si substrate. The XPS survey of as-transferred (NMP-treated) CVD graphene is shown in red (blue). The presence of all the species in the samples are as labeled in the figure. Inset: narrow scan measurements of the N1s core level for both the samples and the molecular structure of NMP. We can notice that the N1s transition is absent in as-transferred CVD graphene, while N1s core level is measured in the NMP-treated CVD graphene. This finding supports the presence of NMP molecules on the surface of CVD graphene.

We observe in the XPS spectra the presence of gold and copper originating from gold markers on the $SiO_2$ substrate and presence of residual copper from the wet transfer process. Particularly in the NMP treated XPS spectrum (blue), we can observe also the presence of chlorine (Cl2p). The origin of the Cl2p peak only in NMP treated graphene could be due to the presence of chlorinated impurities/residuals in the NMP solution itself.

## 7.6. Electrical characterization of as-transferred, NMP and HMDS treated CVD graphene

The field effect characteristics of CVD graphene films can be very useful in quantifying doping by observing the direction and the extent of shift of the Dirac peak with reference to gate voltage. In the absence of doping, the Dirac peak is situated at zero gate voltage. In fig. 7.5 we show the electrical transport measurements of as-fabricated, NMP-treated and thermal annealed CVD graphene. We have also performed other treatment procedures which have been previously reported by others on clean graphene surfaces (samples T1 and T2) [139].

The electrical transport characteristics of as-fabricated samples indicate the presence of high p-doping (fig. 7.5, green dashed lines), as observed during the Raman characterization of as-transferred graphene films. Referring to previous studies of exfoliated graphene on $SiO_2$/Si substrate, a G shift of $\sim$ 0.5 $cm^{-1}$ corresponds to a change in charge density $\Delta n_e \sim$ 2.4x$10^{11}$ $cm^{-2}$ and a Dirac peak shift of $\Delta V$ $\sim$ 40V corresponds to $\Delta n \sim$ 3x$10^{12}$ $cm^{-2}$ [73]. Accordingly, a $\Delta$G shift of 12$cm^{-1}$ observed by comparing samples $G_{as-tr}$ and $G_{exf}$ corresponds to $\Delta n \sim$ 6x$10^{12}$ $cm^{-2}$. The latter is clearly observable in the electrical transport characteristic of the as-fabricated sample with its Dirac peak appearing at a gate voltage $<$ 40V, i.e., at a charge density $>$3x$10^{12}$ $cm^{-2}$ (fig. 7.5 dark green dash). Thermal annealing has been suggested as a means to improve transport characteristics, but the Dirac peak in our thermal annealed CVD graphene sample still shows high p-doping (figure 7.5 - red dotted lines). We have also performed other treatment procedures such as acetic acid dip (fig. 7.5 T1, light green) and chloroform dip (fig. 7.5 T2, magenta), but the CVD graphene field effect characteristics still showed p-doping behavior, with Dirac peak $>$40V.

In order to reduce the polymeric contamination from transfer and fabrication we performed a rigorous exposure to NMP solution for an extended duration. After

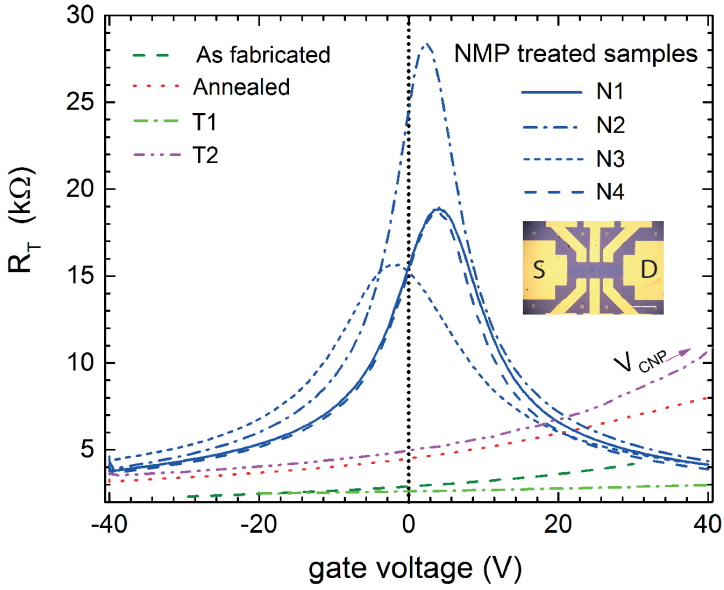


**Figure 7.5:** Total resistance $R_T$ as a function of gate voltage for as-fabricated (dark green dash), thermal annealed (red dot), treatment 1 (T1: acetic acid, green dash-dot), treatment 2 (T2: chloroform, magenta dash-dot-dot), and NMP treated (N1-N4, dark blue) CVD graphene ($V_{SD} \sim 10$mV). Inset: optical image of a typical CVD graphene Hall bar device (scale bar: 200 $\mu$m). The field effect characteristics show that the Dirac peak is situated close to 0V for NMP treated samples unlike as-fabricated samples and those treated using alternative methods. All the electrical transport measurements were performed in low-vacuum conditions of $10^{-4}$ mbar at room temperature.

placing the as-fabricated CVD graphene in warm NMP (70 °) overnight, we could observe the Dirac peak close to 0 V (fig. 7.5 N1-4, dark blue). The latter shift in the Dirac peak correlates with the downshift of $G_{NMP}$ and $2D_{NMP}$ Raman peak position of the NMP treated graphene observed during the Raman characterization (fig. 7.2). The electrical transport study of HMDS treated CVD graphene can be found in fig. C.26 [106]. The field effect mobility of the NMP treated CVD graphene can be found in fig. C.25.

The influence of such physically adsorbed NMP and HMDS molecules on charge carrier transport in CVD graphene is intriguing. The longitudinal resistance (Rxx) of a Hall bar device in the quantum Hall regime at low temperature can be used as a figure of merit to gauge the influence of physisorbed NMP and HMDS molecules on CVD graphene. A large residual Rxx ($>$k$\Omega$) indicates the presence of high charge carrier scattering in the sample. At a temperature of

0.3K, we performed Quantum Hall effect (QHE) measurements of NMP and HMDS treated CVD graphene (fig. C.22a, b). At magnetic field >8T, we can observe that the Rxx is well below 200$\Omega$ in the NMP treated graphene (fig. C.22ai, ii). For the HMDS treated graphene we observe Rxx <100 $\Omega$ for magnetic fields >7T (fig. C.23b). The residual longitudinal resistance of few hundred ohms or less observed in both the samples can easily occur due to excessive charge scattering at grain boundaries, wrinkles, folds in the graphene film, polymer residues, and oxide traps in the substrate [140–142]. Further in fig. C.4a-d and fig. C.5a-c, we show Raman characterization of wrinkles/folds observed in the as-transferred CVD graphene on $SiO_2$ after the wet transfer process. The minimal Rxx observed in our measurements suggests that adsorption of NMP or HMDS is not likely to cause an increased charge scattering in CVD graphene.

From the experiments discussed above, the improvement in the field effect characteristics and the Raman downshifts in solvent treated graphene can be attributed to one of the following: i) n-doping of CVD graphene: due to charge transfer from NMP molecules, counterbalancing the p-doping resulting from the transfer process; ii) binding of NMP on CVD graphene which prevents the re-adsorption of ambient adsorbents, or iii) removal of polymer residues. To check the possibility of n-doping of CVD graphene due to physisorption of NMP, we performed other control experiments and molecular binding calculations.

As a first control experiment, large area Raman characterization of freshly exfoliated graphene flakes was performed before and after NMP treatment. The exfoliated graphene flake is not exposed to etchants or water during exfoliation and is completely free from polymer residues, so serves as a vital reference for comparison with CVD graphene. Nevertheless, some water vapor, oxygen molecules and oxide traps on substrate may be present in both exfoliated graphene and the CVD graphene sample. In fig. C.21 we show a large area Raman map and histograms of exfoliated graphene flake before and after NMP treatment. Interestingly, we find that the G and 2D peak position of the exfoliated graphene remain unchanged before and after the NMP treatment. This observation is in stark contrast to the observation of the large downshift of G and 2D peak position in the NMP treated CVD graphene sample.

Furthermore, since as-grown CVD graphene on copper foil is also free from polymer residues and is not exposed to etchants and water, we considered it also to serve as a 'clean graphene' reference. In fig. C.17, C.19 we show the large area Raman map and histograms of as-grown and NMP treated CVD graphene

on copper foil. Even in the case of as-grown CVD graphene, we did not observe any shift in the G and 2D peak positions before and after NMP treatment. The two control experiments highlights the following: i) physisorption of NMP does not lead to n-doping of graphene and ii) exposure to etchants, ambient contaminants and polymer residues all strongly influence the quality of as-transferred CVD graphene on $SiO_2$/Si substrate.

Even though NMP is known to dissolve a variety of polymers including PMMA, the polymer residues from transfer still reside on top of graphene (see: fig. C.18), which suggests that these polymer residues bind strongly to the graphene surface. The presence of a large amount of polymer residues may be associated with the exposure of polymethyl methacrylate (PMMA) to ammonium persulphate (APS) during the transfer process (see: fig. 3.8 for more details), which has an oxidizing effect of on PMMA.

## 7.7. Molecular binding simulation of NMP, HMDS, PMMA on graphene

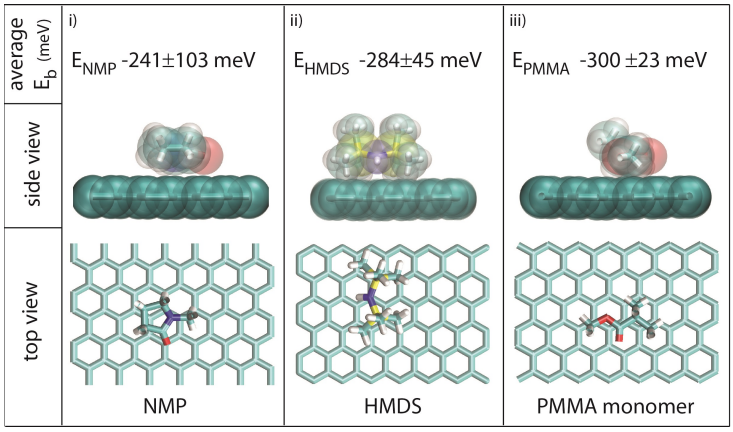


**Figure 7.6:** Molecular binding energy (Eb) calculations of i) NMP ii) HMDS and iii) PMMA-monomer adsorption on graphene. The average binding energy of the molecular adsorption on graphene can be found in the respective columns, with standard deviations computed over the i) four, ii) three, and iii) six stable binding modes found in the calculations. The structures are shown with cylindrical bonds drawn between all covalently-bonded atoms, and semi-transparent vdW space-filling spheres overlaid in the side-on views. For more details about the molecular adsorption calculations and different binding modes of NMP, HMDS and PMMA-monomer molecules on graphene see appendix E.

All the simulation details can be found under the section E. Using molecular binding energy calculations we find that the adsorption of PMMA-monomers on graphene does not lead to any charge transfer and does not cause p-doping of CVD graphene. The calculated molecule-surface complexes show that the binding of NMP or HMDS on graphene is also purely via physisorption, a van der Waals interaction with negligible charge transfer between the adsorbed molecules and graphene (see fig. E.1, E.2, E.3). Importantly, the average binding energy is $Eb_{NMP}$ = -241$\pm$103 meV for NMP and $Eb_{HMDS}$ = -284$\pm$45 meV for HMDS on graphene, which are roughly twice the known binding energies of water ($Eb_{water} <$ -100 meV) and oxygen ($Eb_{oxygen} =$ -130 meV) [117, 143].

The control experiments (C.21, C.19) substantiated by the computed molecule-graphene complexes, indicate that NMP and HMDS do not n-dope graphene. Taken together, our data indicate that the replacement of ambient adsorbents such as water and oxygen by NMP or HMDS on as-transferred CVD graphene surface is the prime reason behind the observation of large Raman downshifts and improvement in the field effect characteristics in NMP and HMDS treated CVD graphene.

The G and 2D Raman shifts measured for various treatment procedures are summarized in Table 7.1 together with the average binding energies calculated for the adsorption of various molecules on graphene. Our data shows that it is possible to remove undesired adsorbents from the surface of CVD graphene without inducing doping simply by using an electronically non-interacting molecule with higher binding affinity to graphene. This technique can help avoid doping due to redox reactions in the aqueous layer consisting mainly of ambient water and oxygen molecules on top of as-transferred and as-fabricated CVD graphene [133].

| sample | G peak | 2D peak | model[a)] | $E_b$ (meV) |
|---|---|---|---|---|
| as-transferred | 1597 | 2685 | NMP on graphene | -241$\pm$103 |
| as-transferred 2 | 1591 | 2682 | HMDS on graphene | -284$\pm$45 |
| NMP treated | 1587 | 2679 | PMMA monomer on graphene | -301$\pm$23 |
| HMDS treated | 1586 | 2678 | PMMA-amine salt on graphene | -233$\pm$55 |
| thermal annealed | 1596 | 2687 | $H_2O$ on graphene | -100 [143] |
| exfoliated graphene on $SiO_2$ | 1584 | 2674 | Oxygen on graphene | -130 [117] |
| suspended exf. graphene | 1582 | 2677 | | |

**Table 7.1:** Overview of the average G and 2D peak positions of CVD graphene for different treatment procedures and various computed molecule-graphene binding energies. Note: a) see E for more details; A final set of control calculations of co-adsorbed water and NMP on graphene can be found in E.5)

## 7.8. Discussion and Conclusion

Stacking of CVD graphene on hexagonal boron nitride (hBN) has been proven to improve the transport characteristics but a large scale production of such devices is yet to be realized [144]. Wet-transfer of CVD graphene onto any substrate of interest is comparatively easier to realize on an industrial scale, yet the presence of adsorbents and polymer residues affect graphene transport properties [51]. The electronic perturbation of graphene can be overcome by considering the surface treatments discussed in this letter. After the NMP treatment, the presence of NMP molecules on graphene is inevitable and its effect was measured using large area Raman characterization, transport and XPS measurements. Such type of a molecular film on graphene can also be further used as an ultra thin ($<$5 nm) organic barrier/dielectric on top/below the graphene, similar to a dielectric structure grown via an atomic layer deposition (ALD) process.

Through systematic large area Raman mapping we observe a large downshift of G and 2D CVD graphene peak positions after treatment with NMP or HMDS. The downshift observed in Raman mapping was accompanied by the shift of the Dirac peak close to gate-voltage of 0V, showing the reduction in p-doping after the chemical treatment. This type of improvement is due to the binding of NMP or HMDS molecules and consequent removal of adsorbents on the CVD graphene surface. By performing systematic control experiments and calculating the binding energies of a range of molecule-graphene complexes we find that the NMP and HMDS molecules have higher binding affinity than ambient molecules to graphene but negligible electronic interaction with graphene and can be useful towards minimizing the undesired p-doping effects resulting from $H_2O/O_2$ redox reactions on graphene. We also find that even though the wet transfer process leads to polymer leftovers on the graphene surface, these residues do not contribute towards p-doping of CVD graphene. Low-temperature QHE characterization shows that the adsorption of NMP or HMDS molecules does not lead to an increase in longitudinal resistance and the observed residual Rxx is due to the scattering of charge carriers at defects such as grain boundaries, wrinkles and folds in the graphene film. Although the possible presence of some remaining $O_2/H_2O$ cannot be completely ruled out and the possibility of oxide traps on the substrate itself cannot be overlooked, our surface treatment technique can be used to help passivate the CVD graphene surface from ambient adsorbents that have a significant influence on residual doping in as-transferred CVD graphene.

# 8

# High quality CVD graphene for quantum Hall resistance standards

**Abstract**

In electrical metrology, macroscopic quantum effects offer the possibility to realize primary standards with an unprecedented accuracy. The quantized Hall resistance (QHR) takes values only defined by the fundamental constants *h* and *e* and can be measured with an uncertainty on the order of 1 part in $10^9$. When compared with GaAs heterostructures, the larger energy level spacing observed between the first two Landau levels in graphene makes it an ideal candidate to realize a QHE standard operational under relaxed experimental conditions i.e. at higher temperatures and/or at lower magnetic field strengths. However, low dissipation in the QHE regime in CVD graphene samples has been elusive.

In this work the first observation of low-residual longitudinal resistance and high accuracy of quantization of quantum Hall plateaus in CVD graphene transferred onto $SiO_2$/Si substrate is demonstrated. A direct dependence is found between the structure of the graphene film and the residual longitudinal resistance. Using a cryogenic current comparator, high precision measurements of the QHR on plateau i=2 reveal a quantization accuracy of within $\pm$ 30 parts in $10^9$. These results show that CVD graphene films can offer the quality required for metrological applications. Part of this chapter will be published in reference [145].

## 8.1. Introduction

The discovery of the Quantum Hall Effect (QHE) in 1980 has led to the development of a new quantum standard of resistance [23]. The vast majority of these resistance standards are based on GaAs heterostructures which require low temperature and high magnetic field to exhibit quantized Hall plateaus suited for high precision measurement. With this respect, graphene based QHR are particularly attractive since their resistance is quantized with high accuracy under relaxed experimental conditions i.e. at a relatively low magnetic fields and high temperatures [146]. This characteristic stems from the much larger energy difference observed between the first two landau levels in graphene [34, 44, 146].

This unique advantage of graphene is pivotal towards developing compact and affordable standards and promoting the dissemination of such high-grade resistance standards to industrial laboratories [146]. Major requirements from a QHR are mainly: 1) relaxed experimental conditions, 2) possibility to apply large bias currents ($I_{SD}$) without the risk of QHE breakdown in-order to obtain better signal-to-noise ratio (SNR) and 3) high precision quantization of Hall plateau. Such QHR play a pivotal role in the proposed 'Quantum SI', wherein the SI (Système International) units will be described using fundamental constants in 2018 [40].

The prime techniques used to produce graphene for QHR are namely: 1) graphene exfoliation 2) epitaxial graphene and 3) chemical vapor deposition (CVD) of graphene. Exfoliated graphene and stacking of exfoliated graphene between hexagonal Boron nitride (hBN) flakes is used to fabricate high-quality graphene devices. However, due to the limitation in the size of the exfoliated graphene flakes, large critical current in QHE regime and mass production of samples for high precision measurements is challenging [36, 43].

High accuracy (few parts per billion) of quantum Hall plateau i=2 quantization has been measured in epitaxial graphene grown on silicon carbide (SiC) substrates [34, 37, 44]. However, the control of charge doping density and its stability in as-grown epitaxial graphene film has been found to be a challenging task. Due to the lack of bulk back gate, one of the popular techniques used to tune the charge carrier density in epitaxial graphene is the UV exposure of bi-layer ZEP/PMMA (poly-methyl methacrylate) polymer film [147]. This technique has been shown to tune the charge carrier density but the photo-gating is lost during thermal recycling. Moreover, bi-layer graphene film stripes developed during epitaxial growth process have been shown to shorten the opposite sides of the edge states which contribute

towards non-residual longitudinal resistance ($R_{xx}$) [148, 149].

Although quantum Hall effect in CVD graphene has been widely studied, the observation of low residual $R_{xx}$ and high accuracy quantization of Hall plateaus in CVD graphene has been elusive until now [42, 140]. In many QHE characterization of CVD graphene samples, the longitudinal resistance ranged from few hundreds of ohms to kilo ohms [42, 150, 151]. The residual $R_{xx}$ in such CVD graphene samples can be related to presence of contamination or defects on/in the graphene film. Moreover, the understanding of dissipation mechanisms and limitations in samples prepared using the CVD technique is of utmost importance to better understand graphene based QHR and its realization.

Here we demonstrate the first observation of low-residual longitudinal resistance and high accuracy of quantum Hall plateau quantization in CVD graphene films on $SiO_2$/Si substrate. Importantly, the CVD approach does not involve any special requirements for sample treatment or stacking procedures. Large area Raman mapping, QHE and high precision measurements were performed on two different types of CVD graphene films namely: 1) small-grain (SG) and 2) large-grain (LG). Using a cryogenic current comparator (CCC), the high precision measurements of the QHR on the i=2 plateau were performed on large-grain (LG) devices [33]. A direct influence of the grain boundaries was found on the dissipation in CVD graphene in the QHE regime. A high accuracy quantization of the Hall plateau i=2 was measured with an accuracy of within $\pm$30 parts in $10^9$ in LG samples. The observation of low-residual $R_{xx}$ transport and a high accuracy of quantum Hall plateau quantization in CVD graphene attests the high quality of the CVD graphene films used in this study and marks an important step on the road towards using CVD graphene samples as resistance standards. Please note that the samples and the measurements discussed in this chapter are not the samples discussed in the previous chapters.

## 8.2. Optical images of SG and LG graphene grain and film

Chemical vapor deposition of graphene was performed on commercially available polycrystalline copper foils to produce large area graphene films (see: chapter 3). By primarily changing the methane concentration the size of individual graphene grains was controlled to grow two types of graphene films, namely: small grain

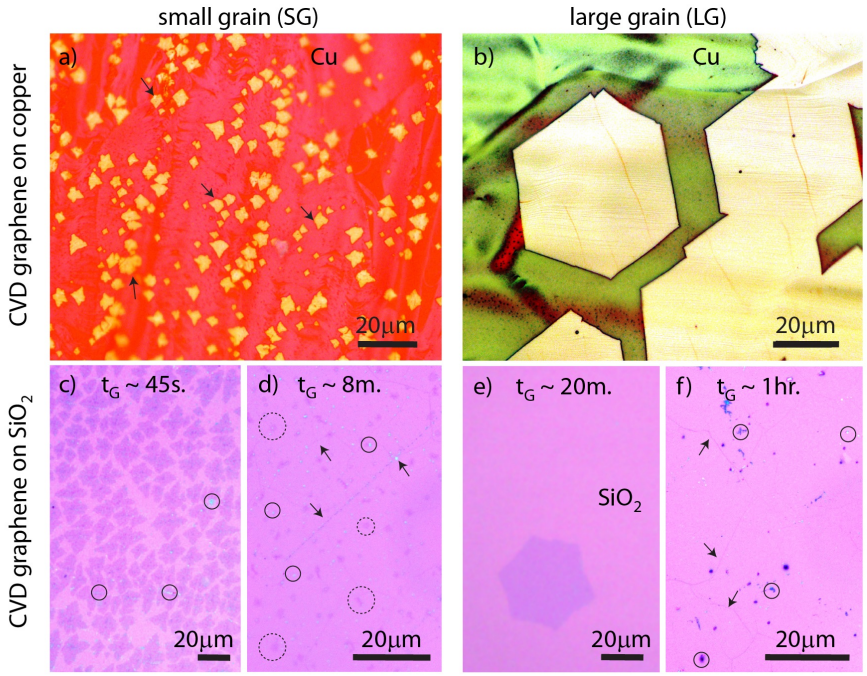


**Figure 8.1:** Optical images of small-grain (SG) and large grain (LG) CVD graphene samples as-grown on copper foil (a, b) and as-transferred on $SiO_2$ substrate (c-f). As-transferred SG CVD graphene film on $SiO_2$ substrate at growth times ($t_G$) of 45 seconds (c), 8 minutes (d); LG CVD graphene sample at 20 minutes (e), 1 hour (f). In figure a, b the copper foil was heated to 200 °C for 5 minutes to oxidize regions of copper exposed to ambient air.

(SG) and large grain (LG) graphene film. As-grown graphene on copper foils were transferred onto $SiO_2$/Si substrates following the PMMA-assisted transfer process.

The optical images of the SG and LG graphene are shown in fig. 8.1. In fig. 8.1a and b we can see individual SG and LG graphene grains. The optical images were taken after heating the as-grown copper foils at 200°C for 5 minutes during which the regions of copper foil exposed to air is oxidized. In figure 8.1c-d we show the as-transferred SG graphene grains after growth time ($g_\tau$) ∼45 seconds (fig. 8.1c), ∼8 minutes (fig. 8.1d) and SG graphene film after $g_\tau$ ∼20 minutes (fig. 8.1e), ∼1 hour (fig. 8.1f). Polymer residues and wrinkles from transfer process on SLG are as marked using dotted circles and arrows. The typical size of the SG and LG graphene grains is ∼10-30 $\mu$m and ∼100 $\mu$m. For additional details about the growth recipe and selected growth recipe chart see 3.

Although the polymer assisted transfer is useful in transferring large area

graphene films with minimal damage, irremovable polymer residues remain on CVD graphene surface which are impossible to dissolve in solvents or thermal annealing completely [59]. Polymeric residues from transfer are highlighted in fig. 3.8. For further AFM characterization of folds/wrinkles in as-transferred CVD graphene please refer to appendix C.7.

## 8.3. SG and LG CVD graphene characterization using large area Raman mapping

CVD graphene films was characterized using Raman spectroscopy by performing large area Raman mapping (100 $\mu$m x 100 $\mu$m) and analyze the distribution of the prominent Raman peaks of graphene. Relying on large area mapping is an extremely useful technique to understand the homogeneity and regional variations in doping density and strain in as-transferred CVD graphene film [13, 77]. As discussed in chapter 4, the first order Raman peak of graphene on $SiO_2$/Si around $\sim$1585 cm$^{-1}$, the 'G' peak can be used to estimate the charge density of the graphene film. The second order Raman peak of graphene at $\sim$2675 cm$^{-1}$ namely the '2D' peak full-width-half-maximum (FWHM) can be used to extract strain variations in the as-transferred CVD graphene film [77, 82].

In fig. 8.2 we show the large area Raman characterization of as-transferred SG and LG graphene films. In fig. 8.2a i-ii (iii-iv) we can see the large area map of small grain (large grain) graphene film G and 2D band, the respective peak positions can be found using the scale bar. In fig. 8.2b we can see the histogram of G and 2D peak positions on the bottom axis and respective FWHM on top x-axis of SG (red) and LD (blue) graphene film shown in fig. 8.2a. Interestingly, the average G and 2D peak position and FWHM (dotted lines: fig. 8.2b) for both SG and LG graphene is found to be similar.

This suggests that the polymer-assisted wet transfer process has a similar impact on the two types of graphene films, although they were produced under different growth conditions and consist of different sized graphene grains (fig. 8.1). Bi and multi layer graphene and polymer residues are highlighted using arrows and contours in fig. 8.2a ii, iv. The average G and 2D peak wavenumbers is 1587 (1588) and 2678 (2681) cm$^{-1}$ for SG (LG) graphene films, these values are close to what is observed in freshly exfoliated graphene flakes (1585 cm$^{-1}$, 2674 cm$^{-1}$) on $SiO_2$/Si substrate [59]. The distribution/width in the G and 2D wavenumbers

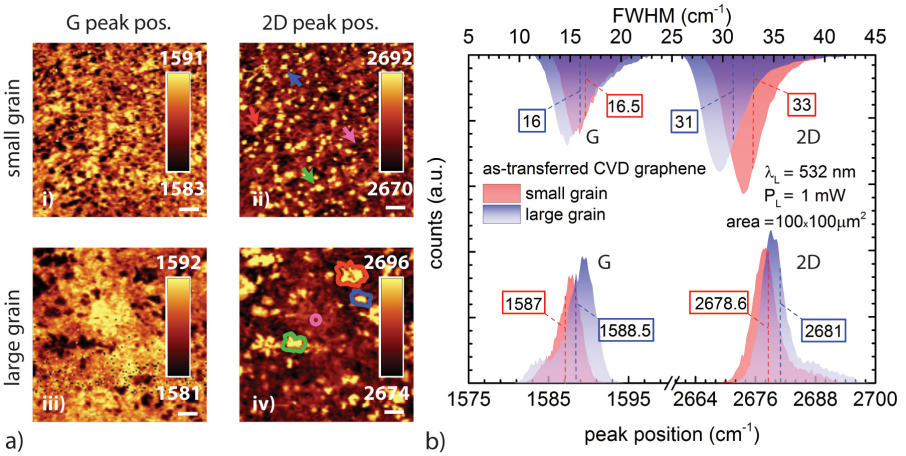


**Figure 8.2:** a, b) Large area (100$\mu$m x 100$\mu$m) Raman mapping of G and 2D peak positions of as-transferred SG (i, ii) and LG (iii, iv) CVD graphene on $SiO_2$. Scale bar: 10 $\mu$m. The polymer residues and bi-layer graphene are marked using colored arrows. The corresponding peak positions in the G and 2D band maps can be found using the color bar. b) Histogram of the peak position (bottom x-axis) and FWHM (top x-axis) of the respective G band (figure 1a i, iii) and 2D band (figure 1a ii, iv) map of the two CVD graphene films. The average peak positions of the histogram are denoted by red and blue dashed lines within the histogram. The Raman characterization was performed under ambient conditions.

in the histogram is observed to be around $\sim$ 8 - 10 $cm^{-1}$ which shows that the as-transferred CVD graphene films are prone to inhomogeneous local doping due to contaminants. Assuming $\Delta G \sim 0.5$ $cm^{-1}$ is equivalent to charge density of $\Delta n_e$ $\sim$ 2.4x$10^{11}$ $cm^{-2}$, a spread of $\sim$ 8 – 10 $cm^{-1}$ relates to a charge density of $\Delta n$ $\sim$ 5x$10^{12}$ $cm^{-2}$ [73]. This type of inhomogeneous local doping can be introduced during transfer, fabrication, charge traps on $SiO_2$ or due to exposure to ambient contaminants.

It is known that the redox reaction between water and oxygen molecules in the aqueous layer on top of CVD graphene is the cause behind p-doping [101, 102]. The spread in the charge density $\Delta n$ measured in our case is in very good agreement with previous scanning tunneling microscopy studies on graphene surface [152]. The effects due to doping from such contaminants can be partially overcome by various techniques such as: thermal annealing, solvent/substrate treatments and by performing transport measurements under low-vacuum conditions, all of which are helpful in desorption of contaminants from graphene's surface [127].

## 8.4. Field effect transport characterization of SG and LG graphene devices

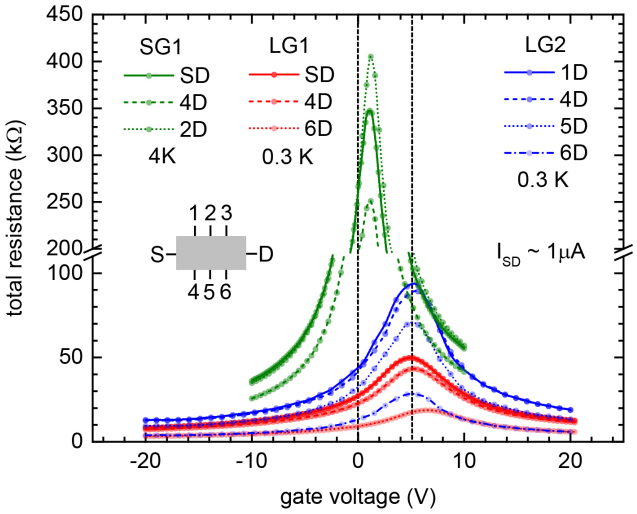


**Figure 8.3:** Sheet resistance as a function of gate voltage of SG/LG graphene devices (LG1 (red), LG2 (blue), SG1 (green). Inset: Hall bar device schematic (device dimension: 1000$\mu$m x 200$\mu$m). The samples underwent thermal annealing process prior to transport measurements. The electrical transport measurements ($I_{SD}$ = 1$\mu$A) were performed at 0.3 K in $^3$He.

Electrical transport measurements of SG/LG Hall bar CVD graphene devices across different contact pairs are shown in fig. 8.3. All the devices were thermal annealed in forming gas (Ar, $H_2$ 5%) at 300°C for 3 hours prior to transport measurements to reduce contaminants from fabrication and CVD graphene transfer. The two-terminal total resistance $R_T$ is symmetric around the charge neutrality point (CNP), which is located around $V_g$ = 5V for the LG sample and $V_g$ = 1V for the SG sample. The presence of the CNP close to zero gate voltage suggests low residual doping from fabrication and transfer process. The charge carrier density can be tuned across the CNP using the highly p-doped silicon back gate. The charge tunability was achieved without the use of additional solvent based treatment procedures.

The field-effect mobility of the LG devices is in the range of 1500 cm$^2$/Vs up-to 5852 cm$^2$/Vs and 1000 – 1500 cm$^2$/Vs for SG devices. The field effect mobility

in SG devices is in general two to six times lower than in the LG devices (see appendix C D.15) field effect mobility characterization details) due to the charge scattering at the grain boundaries [59, 141]. For the SG device with a dimension of: 1000 $\mu$m (L) x 200 $\mu$m (W) from figure 8.1a, c, d we can see that the density of grain boundaries in SG film is much higher than in LG film (fig. 8.1 b, e, f).

## 8.5. Magneto transport characterization of SG and LG graphene devices

In fig.8.4 the quantum Hall effect characterization of SG (fig. 8.4a, b) and LG (fig. 8.4c-f) devices is shown. In fig. 8.4 in the right panel (b, d, f) the longitudinal resistance $R_{xx}$ is plotted in log scale to emphasize the magnitude of residual $R_{xx}$. Around $B_\perp$ = 11T a sharp drop is observed in $R_{xx}$ which goes below 100 m$\Omega$ as highlighted by the black arrow. This drop in $R_{xx}$ can be an artefact as the drop is only observable at $B_\perp$ = 11T and $R_{xx}$ starts to increase for higher magnetic field. The $R_{xx}$ does not decrease for negative magnetic fields, which could be due to the poor signal-to-noise ratio at the low signal level. However, $R_{xx}$ below 100 m$\Omega$ over a (finite) range of gate voltages has not been observed in SG1.

Interestingly, in samples LG1 and LG2 we can observe low $R_{xx}$ (i.e. smaller than 100 m$\Omega$), over a range of gate voltage at a fixed magnetic field of B$\perp$ = 12 T (see shaded areas in fig. 8.4). Low residual $R_{xx}$ measured in large-grain CVD graphene devices over a range of gate voltages is due to the reduced charge scattering at the grain boundaries in comparison to the small-grain CVD graphene [140, 153]. In chapter 6 it was shown that the field effect mobility in multi domain graphene films are lower than the single domain graphene. In fig. 8.4 e, we can observe an increase in the $R_{xx}$ at lower charge densities i.e. near the charge neutrality point (CNP) which is enhanced due to the presence of electron-hole puddles in the underlying substrate [154, 155]. Increasing the gate voltage across the CNP (i.e. increasing the electron density) leads to a decrease in $R_{xx}$ leading to quantum Hall plateau i=2 (fig. 8.4 d). The range of gate voltages for which the $R_{xx}$ drops below 100 m$\Omega$ is marked using shaded areas in fig. 8.4 d, f. The noise in $R_{xx}$ observed in the shaded area in fig. 8.4 d, f is due to the noise of our digital voltmeter (DVM) at the low level current used for these measurements.

When the source current $I_{SD}$ is increased, the dissipation ($R_{xx}$) suddenly increases at the critical current $I_c$, leading to the breakdown of the QHE. For sample

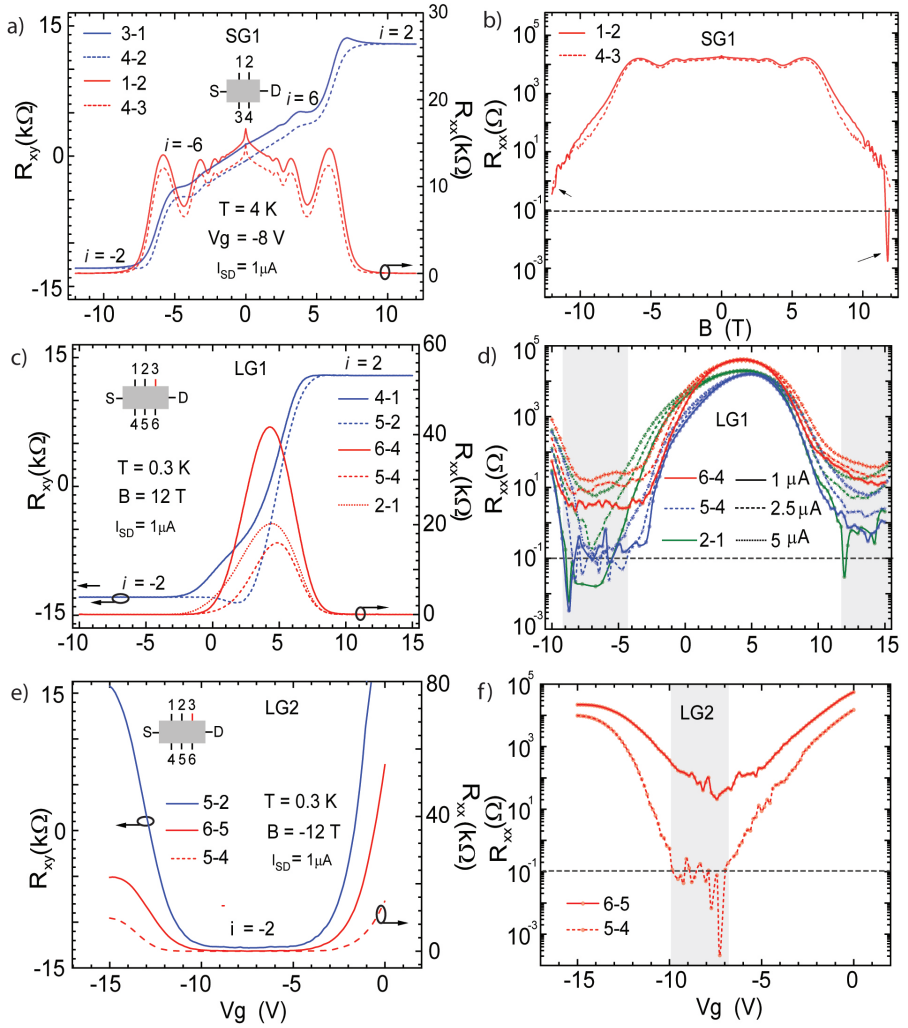


**Figure 8.4:** Low temperature measurements of the Hall resistance $R_{xy}$ and the longitudinal resistance $R_{xx}$ as a function of the magnetic field B and the gate voltage $V_g$ for sample SG1, LG1 and LG2. Left panel: $R_{xy}$ and $R_{xx}$ as a function of $V_g$ (V) or B (T) at a fixed source current of $I_{SD}$ = 1 $\mu$A. Right panel: log scale plot of $R_{xx}$ vs. B or $V_g$ of SG1 (d), LG1 (d) and LG2 (f). The magnetic field sweep was performed at a constant gate voltage of $V_g$ = -8V for the SG sample and gate voltage sweep at a constant magnetic field of B = 12T was performed for LG samples. Low longitudinal resistance ($R_{xx} < 0.1\ \Omega$) can be observed for a range of gate voltages which is highlighted using shaded areas in d, f.

LG1, the critical current was found to be 10 $\mu$A and the critical current density $j_c$ = $I_c$/w= 0.05 A/m with w = 200 $\mu$m. The breakdown of the QHE can be interpreted with a quasi-elastic inter-Landau level scattering (QUILLS) mechanism which was

identified in a similar experiment in exfoliated graphene sample on $SiO_2$/Si substrate [36]. Moreover, an asymmetry in $R_{xx}$ can be observed in fig. 8.4 d. Interestingly, the low $R_{xx}$ values are observed away from the charge neutrality point of graphene and in particular in the hole regime. This type of an asymmetry can arise due to strain, charge-defect related scattering mechanisms and contact doping [156].

Using the three-terminal contact resistance measurement technique described in Jeckelmann et al.[[33]], we measure low contact resistance $R_c$ below $< 1\Omega$ for certain contact pairs, a value compatible with metrological standards (see: 5.18). Further contact measurements were made in LG1 and LG2 sample at different bias currents (1 - 5 $\mu$A) shown in D.8 and D.9. Other low longitudinal resistance observation in LG graphene samples (**LG3**) is further detailed in the appendix D.10 - D.14. Although $R_c$ is not uniform across all the contacts throughout the device, it is possible to achieve high accuracy resistance quantization on certain contact pairs, as discussed in the following section 8.5.

## 8.6. High precision measurements of LG graphene devices

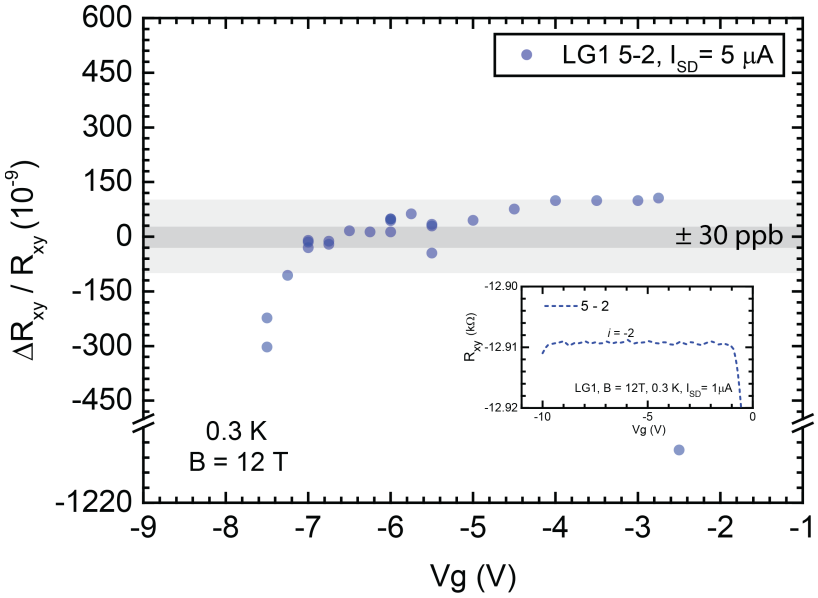


**Figure 8.5:** High precision measurements of the Hall resistance $R_{xy}$ of LG1 (blue, circle) at a fixed magnetic field and a source current of $I_{SD}$ = 5 $\mu$A respectively. The shaded areas highlight two regions wherein $R_{xy}$ is quantized within $\pm$100 parts in $10^9$ (light grey) and $\pm$30 parts in $10^9$ (dark grey) for a range of gate voltages. All the measurements were performed at 0.3 K using a cryogenic current comparator. In the inset, a close-up of LG1 Hall plateau (fig. 8.4b) is shown.

To measure the quantization accuracy on the quantum Hall plateau i=2, $R_{xy}$ is compared to $R_K/2$ in LG 1 (blue, circle) CVD graphene device using a high precision cryogenic current comparator (CCC) (see fig. 8.5). The measurements were performed at a temperature of 0.3 K. The graphene device was compared to a well characterized 100 $\Omega$ resistor whose value is known with an uncertainty on the order of 1 part in $10^9$ using a traditional GaAs heterostructure in the quantum Hall regime. A schematic of the CCC bridge and details about the measurement are detailed in the appendix D.5 [33].

The samples with low $R_{xx} < 0.1\ \Omega$ were chosen for high precision measurements with CCC bridge. For the LG1 device the quantum Hall plateau i=2 is quantized with high accuracy well below $\pm$30 parts in $10^9$ for a gate voltage range

of -7V to -6V. The quantization accuracy is well within $\pm$100 ppb for a broader range of gate voltage of -7V to -2.5V. All the high precision measurements for LG1 device were performed for a source current $I_{SD}$ = 5 $\mu$A.

In appendix D.6 we show high precision measurement of another LG graphene sample (**LG2**) in which we can observe a deviation of $R_{xy}$ from $R_K/2$ of +100 parts in $10^9$ over a comparatively shorter range of gate voltage of -7.8V to -8.2V ($I_{SD}$ = 2 $\mu$A). The measuring currents were imposed by taking into account of the minimum current at which the $R_{xx}$ increases beyond 0.1 $\Omega$ in these devices. With current of this magnitude, the signal to noise ratio of the CCC bridge is not ideal and the accuracy of the measurement is reduced accordingly.

Further $R_{xx}$ measurements of LG2 sample at different magnetic fields (10-12T) and gate voltage are shown in D.7, where $R_{xx}$ values less than **500** $\mu\Omega$ can be observed between -10.5 T to -12 T for a range of gate voltage. Observation of low $R_{xx}$ values in another large grain CVD graphene sample '**LG3**' is shown in detail in appendix D.10, D.12, D.11, D.13 and D.14. These measurements demonstrate that the quality of CVD graphene devices has nearly reached the level sufficient for metrological applications.

## 8.7. Further experiments

### 8.7.1. Weak localization measurements

Weak localization (WL) in our CVD graphene samples was studied to understand the different scattering processes. Weak localization occurs when electrons are scattered by impurities which are distributed randomly in the conductor (diffusive transport). The electrons are weakly localized and this results in a constructive interference of the wave functions, as described in fig. 8.6 a. For instance, in fig. 8.6 a) assuming that the electron trajectory follows the blue arrows after the injection (black arrow) and the red path denotes the time reversed path of the blue path, given that both these paths are the same length, this gives rise to constructive interference at the end point. This results in the enhancement of the backscattering probability; termed as the weak localization mechanism.

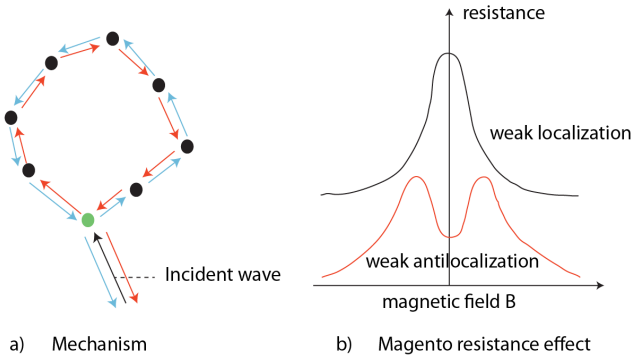


**Figure 8.6:** a) Description of weak localization mechanism b) WL and anti-WL magneto-resistance effect.

The WL is partially destroyed in the presence of a perpendicular magnetic field, which results in a negative magneto-resistance as shown in fig. 8.6 b. If the WL is suppressed by the rotation of spins at zero magnetic field, this leads to weak antilocalization fig. 8.6 b. The presence of WL in our CVD graphene sample can be clearly observed in fig. 8.7. The WL theory from Mc Cann et al. ([157]) was applied for the WL curve shown in fig. 8.7 to study the different scattering processes such as: $\tau_\phi$ (inelastic dephasing time), $\tau_{iv}$ (elastic intervalley scattering time) and $\tau_*$ (elastic intravalley scattering time) [158, 159].

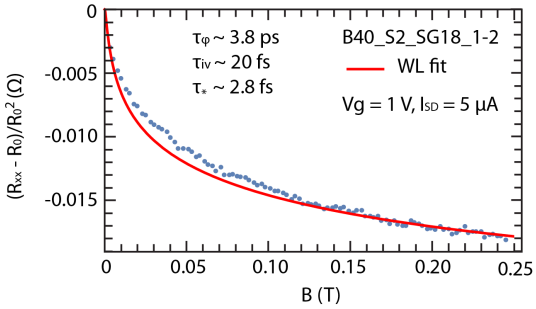


**Figure 8.7:** WL characterization of an LG graphene sample at $V_g$ = 1V. The fit to the WL data is shown in red line, respective scattering rates can be found in the plot. The WL measurements were performed at 0.3K.

The WL function from Mc Cann et al is given by [157]:

$$\frac{\Delta\rho_{xx}}{\rho_0^2} = -\frac{e^2}{\pi h}\left[F\left(\frac{\tau_B^{-1}}{\tau_\phi^{-1}}\right) - F\left(\frac{\tau_B^{-1}}{\tau_\phi^{-1}+2\tau_{iv}^{-1}}\right) - 2F\left(\frac{\tau_B^{-1}}{\tau_\phi^{-1}+\tau_*^{-1}}\right)\right] \tag{8.1}$$

where $\Delta\rho_{xx} = \rho_{xx} - \rho_0$; $\rho_0$ is the resistance at B= 0T, $\tau_\phi$, $\tau_{iv}$ and $\tau_*$ are the inelastic dephasing (decoherence) time, elastic intervalley scattering time and elastic intravalley scattering time. The term F(z) = ln(z) + $\psi(0.5 + z^{-1})$, where $\psi(z)$ is a digamma function. Further, $\tau_B^{-1}$ = 4DeB/$\hbar$, where D is the diffusion coefficient. The term $D$ can be calculated using D = $\nu_f$l/2, l = h/2e$^2$k$_f\rho$, where $\nu_f$ = 1.1×10$^6$ m/s, k$_f$ = $(\pi n)^{1/2}$ is the Fermi wave number. Using the scattering rates the respective scattering lengths can be found using: L$_{\phi,iv,*}$ = $\sqrt{D\tau_{\phi,iv,*}}$ [158, 159].

By using the equation 8.1, the WL data of another LG graphene sample at $V_g$ =1V was fit respectively and is shown in fig. 8.7. It can be observed that the $\tau_\phi$ $\tau_{iv}$ $\tau_*$, which is a similar trend observed in other graphene samples on $SiO_2$ substrate [158–160]. Using $\tau_\phi$= 3.8 ps, we find a dephasing scattering length L$_\phi$ $\approx$ 0.3 $\mu$m. At low temperatures, inelastic scattering is considered as one of the most dominant mechanism of electron-electron interaction in graphene. Further temperature dependent WL measurements can be found in appendix D.2, D.3 and D.4.

Further, as discussed previously, the critical current in our CVD graphene devices is limited. In graphene, due to its large optical phonon energies, the dominant cooling mechanism for charge carriers at low temperatures takes place

via acoustic phonons. The cooling of acoustic phonons is a weak mechanism which causes the charge carriers to attain temperatures in excess of the lattice temperature ($T_l$, measurement temperature). This effect can be explained by using the theory developed by Kubakaddi [161], where the carrier temperature ($T_e$) is given by:

$$F(T) = \alpha\left(T_e^4 - T_l^4\right) \tag{8.2}$$

where $T_e$ is the carrier temperature and $T_l$ is the lattice temperature. For a given value of $R_{xx}$ and current, the equation 8.2 can be equated to the power input per charge carrier given by:

$$\alpha\left(T_e^4 - T_l^4\right) = \frac{I^2 R_{xx}}{nA} \tag{8.3}$$

where n is the charge density, A is the sample area (3 mm by 500 $\mu$m) and $\alpha$ = 5.36x10$^{-18}$ WK$^{-4}/\sqrt{n}$ is a scaling constant which is weakly carrier density dependent. We performed QHE measurements on sample B40-S2 and the $R_{xx}$ values in the quantum Hall plateau (i = -2, $V_g$=10V) were extracted and were substituted in the equation 8.3 and the subsequent carrier temperature $T_e$ is plotted in 8.8. The lattice temperature $T_l$ was fixed at 0.3K. The extrapolation of the data is shown in red. These observations are similar to previous measurements performed on other CVD graphene samples and show that an increase in bias currents can give rise a subsequent rise in the carrier temperature [162]. In previous studies it was observed that currents as low as 0.01 nA were enough to rise $T_e$ and lead to hot-electron artifacts in the measurements [162].

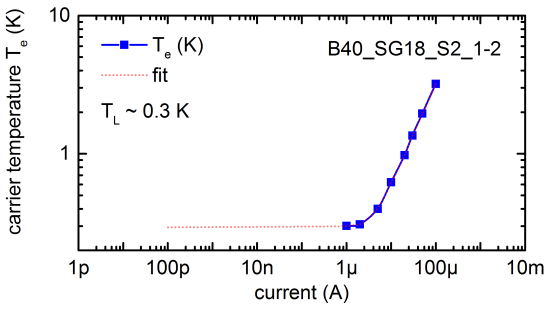


**Figure 8.8:** Minimum carrier temperature $T_e$ for a given current for the CVD graphene sample from batch B40 at $T_l$ of 0.3K and $V_g$ = 10V. The red line shows the extrapolation of the measurements.

## 8.8. Discussion and Conclusion

In our previous studies, we find the presence of high density of grain boundaries limits the field effect mobility and the presence of polymer residues from CVD graphene transfer was inevitable [59, 127]. Transmission electron microscopy techniques have been used to study defects in CVD graphene sample. It was observed that the grain boundaries were finely stitched together predominantly via 5-7 carbon rings [163]. In a theoretical study it has been reported that the line defects or grain boundaries consisting of 5-7 carbon rings can host defect states. These line defects can possibly host residues from transfer such as PMMA molecules or even remnant copper residues [127]. Such line defects spanning across the Hall bar can connect the edge states on opposite sides leading to a residual $R_{xx}$ [164]. A high density of grain boundaries in a SG sample can lead to a large longitudinal resistance.

The observation of low dissipation, of low contact resistance and of high accuracy quantization demonstrates the high quality of our CVD graphene devices. However, these observations could only be achieved at low current level since the critical current of these devices is small (10 $\mu$A). In table 8.1 the critical current densities jc measured in graphene samples produced using different growth techniques are summarized. The critical current measured in our CVD sample is one order of magnitude smaller than in exfoliated graphene and nearly two orders of magnitude smaller than in SiC graphene. This significant reduction of critical current density can be due to various factors. First, the as-transferred graphene films contain transfer induced wrinkles, folds and contaminants in comparison to other graphene production techniques (see C.7 C.6 for images of AFM characterization). In a scanning joule expansion microscopy (SJEM) study of CVD graphene devices, it was observed that the presence of grain boundaries and wrinkles/folds lead to highly localized resistive heating and rise in temperature [165]. Furthermore, joule heating at the contacts due to increase in bias currents can also lead to an increase in $R_c$ and hinder the high precision resistance quantization (see: D.8, D.9). The polymer residues at the graphene-metal contact interface can lead to an increase in $R_c$ and influence non-uniformity of $R_c$ across different contact pairs. In D.8 and D.9 we can see that with the increase in bias current the $R_c$ of contacts does not increase uniformly at all the metal contacts.

A possible solution to increase the critical current density is to perform QHE measurements on samples of smaller dimensions. This allows the patterning

of the Hall bar within a large single crystal-grain of graphene thus significantly reducing the density of grain boundaries or wrinkles/folds in the graphene film. Direct patterning of metal contacts on as-grown graphene on copper foil can be useful in fabrication of polymer residue-free graphene-metal interfaces and therby improving the stability of $R_c$ uniformly across the entire device. However the limited critical currents observed in this study warrants further investigation to improve the breakdown features associated with CVD graphene on $SiO_2$/Si.

| Growth | B (T) | $I_c$ ($\mu$A) | w ($\mu$m) | $j_c$ (A/m) |
|---|---|---|---|---|
| **CVD graphene**$^*$ | 12 | 10 | 200 | 0.05 |
| Silicon Carbide$^\diamond$ | 7 | 150 | 35 | 4.3 [166] |
| Silicon Carbide$^\diamond$ | 5 | 60 | 30 | 2 [38] |
| Silicon Carbide | 8 | 500 | 100 | 2 [44] |
| Exfoliated | 18.5 | 1 | 2 | 0.5 [36] |

**Table 8.1:** Overview of the critical current density measured in graphene samples produced using different techniques. 'w' is the sample width, $I_c$ is the critical current and jc is the critical current density, given by $j_c = I_c/w$.), $^\diamond$with photo-gating, $^*$This work.

The observation of low dissipation QHE transport in CVD graphene necessitates the importance of graphene film quality and transfer procedure. This type of a QHE characterization can be useful in characterizing CVD graphene film quality. Such measurable quantities can be used for the development of new standards to characterize CVD graphene quality in combination with other characterization techniques.

In summary, the first demonstration of high accuracy quantization of i=2 plateau within $\pm$ 30 parts in $10^9$ over a range of gate voltage in CVD graphene on $SiO_2$/Si is demonstrated. Low temperature measurements of the longitudinal resistance of a Hall bar in the QHE regime have demonstrated that the size of individual CVD graphene grain in a continuous film has a direct influence on the magnitude of the dissipation in the QHE. By increasing the individual grain size it was found that CVD graphene films with grains larger than 100 $\mu$m are good candidates for the development of QHR based on CVD graphene. These results show that CVD graphene has reached a quality which can match the stringent requirements of metrological measurements. This represents an important step towards the development of CVD graphene based quantum Hall resistance metrology standards.

# 9

# Conclusions and Outlook

The prospects of developing novel electrical quantum resistance standards using CVD graphene has been the subject of this thesis. Various aspects detailing the graphene production, transfer, sample fabrication and transport measurements have been presented. In **chapter 3** we demonstrated the possibility to tune the size of individual graphene grains in the graphene film by lowering the methane concentration. We demonstrated the growth of graphene films with varying crystal sizes ranging from micrometer to millimeter-scale. We investigated the influence of etching solution on PMMA to understand the cause of polymer residues on graphene. It was found that the exposure of PMMA films to etching solution (APS) is mildly oxidative. This lead to PMMA residues that cannot be dissolved in solvents. Different transfer techniques and their limitations were tested, it was found that the PMMA-assisted transfer offers large-area graphene films with minimal damage.

Raman spectroscopy has been an extremely valuable tool during the characterization of our CVD graphene films. Main parameters characterized using large-area Raman mapping of graphene are: 1) doping, 2) residual strain, 3) PMMA residues on graphene and 4) folds/wrinkles in the graphene film. A study consisting of Raman mapping of graphene's Raman peaks helped in the understanding of charge density of the as-transferred graphene films. This is also useful in characterizing residual strain in graphene films. Consistent shifts in CVD graphene's Raman peaks were observed when compared with exfoliated graphene flakes on $SiO_2$/Si sub-

strate. It was found that it is more likely that a mixture of residual strain and doping can lead to such Raman shifts in CVD graphene, with doping being the dominant cause. Further, Raman peaks of PMMA residues and graphene were separately characterized to help distinguish one from another. To obtain structural information of the graphene films, low-energy-electron microscopy was performed. Uniform single layer graphene with low density of bi-layer islands and grain boundaries were observed. At certain regions in the graphene film, line defects/grain boundaries and particulates along such features were also observed during LEEM imaging. Further, XPS spectroscopy was performed to obtain elemental information about the as-transferred graphene films and PMMA residues. Residue of copper were observed in the XPS survey spectra, indicating that the particulates found in the line-defects/grains boundaries can be residual copper from the transfer process.

Through these characterization techniques we were able to investigate that the doping of graphene films does come from the adsorption of ambient molecules rather than from the growth itself. Two techniques were studied to circumvent the p-doping in graphene films, namely: 1) thermal annealing and 2) solvent treatment. It was observed that thermal annealing of graphene samples under low-pressure conditions reduced the residual doping. The mechanism behind this technique is the thermally-assisted desorption of adsorbates during the annealing process. Another alternate technique developed is the solvent treatment. By performing several systematic experiments and molecular binding simulations, it was found that molecules with a strong binding affinity to graphene can be useful in replacing unwanted ambient adsorbates. Importantly, strong binding molecules are to be chosen such that there is no charge transfer between the solvent molecule and graphene. This intricate interplay of molecules turned out to be the key mechanism leading to the improvement of field effect properties of CVD graphene transistors.

By combining these things we developed CVD graphene Hall bar samples to test its feasibility for quantum resistance standards. Two types of samples were studied comprising of graphene films with smaller grains and larger grains. In samples with graphene films with large individual graphene grains we were able to demonstrate low dissipation quantum Hall effect transport for the first time in CVD grown graphene films on copper. An uncertainty of within $\pm$30 parts in $10^9$ was observed for a range of gate voltages. Consistent low longitudinal resistance $R_{xx}$ was measured in other large-grain graphene samples (see: D.7 - D.14). However, in the small grain graphene samples high residual $R_{xx}$ was observed consistently. This is indicative of our understanding that higher density of

grain boundaries lead to a higher dissipation in QHE regime. It is worth highlighting that the sample preparation procedures are vastly different in exfoliation, epitaxial and CVD techniques. In particular the density of residues and conformity of the graphene flakes are among the two main things that vastly vary in samples produced using these three techniques.

Although many reports have presented the growth of high-quality graphene, there were no demonstration of high precision quantization in CVD graphene grown on metal films until now. This can either be due to the poor-quality of graphene films or due to the lack of stringent sample production protocols. The latter can lead to difference in overall quality of the as-fabricated graphene sample between different research groups. This warrants for the establishment of standard fabrication protocols and highlights the influence of sample fabrication on 2D materials. Further, CVD graphene samples tend to have more features such as wrinkles, folds, ruptures due to the transfer process, which is absent in epitaxial or exfoliated graphene fabrication routines. During this work, alternative approaches were studied to obtain residue-free graphene surface such as the consideration of hBN/graphene/hBN heterostructure and metal etch mask approach. However, due to the limitation in the quality of the CVD hBN films, the transport characteristics could not be further improved. Further, fabrication issues in the metal etch mask approach hindered the usage of metal thin films as masks to prevent graphene coming in contact with polymers during fabrication and transfer.

Secondly, as discussed in **chapter 5**, the contact resistance ($R_c$) plays a vital role during the high precision quantization measurements. The polymer residues present at the graphene-metal interface, as observed during the Raman characterization can limit the high precision QHE measurements at higher bias currents. In the $R_c$ versus bias current measurements, we can observe an increase in $R_c$ with $I_c$. Although the contact area of graphene-metal contact were uniform in size, the difference in $R_c$ values is due to the sporadic presence of residues at contact region. These observations are the prime reason for low critical currents (5-10 $\mu A$) and subsequent critical current densities ($j_c$) in our CVD graphene samples.

As an outlook, we have developed an understanding in growing high-quality graphene films and the fabrication of high field effect mobility Hall bar devices on $SiO_2$/Si substrates. We were able to demonstrate the first observation of high accuracy resistance quantization in CVD graphene samples and showed that CVD graphene can offer the required quality for developing resistance standards for metrological applications. We find that graphene films with CVD graphene grains of

$\approx$ 100 $\mu$m are ideal candidates to develop CVD graphene based QHRs. However, there is still a scope for improvement in increasing the critical current of CVD graphene QHRs. First, it would be interesting to perform transport measurements in Hall bars fabricated on a single grain of CVD graphene with comparatively smaller device dimension. Such single-domain graphene samples were produced during this work but due to sample doping issues the high precision measurements could not be performed. Such a single-domain sample can help reduce the wrinkles and grain boundaries further, which can improve the $I_c$ further.

Second, cleaner/alternative substrates such as multilayer hBN and improved transfer techniques can be useful in minimizing wrinkle/folds to yield flat graphene surfaces. This can be achieved by automating the transfer process and performing growth on copper foil with lower defects (trenches and pinholes). Thermally evaporated copper thin film substrates were produced to test an alternative growth substrate for graphene. However, presence of pinholes and trenches hindered the use of it. Third, the graphene-metal contact interface has to be studied for its stability at higher bias currents on alternative substrates. The latter is helpful in studying the influence of substrate on $R_c$ as the presence of residues can influence the $R_c$ value. Another approach can also be the metal contact evaporation process directly on as-grown graphene on copper. This step can yield a cleaner graphene-metal interface and thereby limiting the influence of residues and produce reproducible contact resistances across the entire device.

Furthermore, with new developments in the field of topological insulators (TIs), several new phenomenon have been proposed and studied. One of them is the observation of anomalous quantum Hall effect in three-dimensional topological insulator thin film with ferromagnetic doping. At near-zero magnetic fields exact quantization with accuracy within one part in 10,000 has been observed. These observations were made in few nanometre thick film of $(Cr_{0.12}Bi_{0.26}Sb_{0.62})_2Te_3$ thin films grown via molecular beam epitaxy on GaAs substrates and protected with alumina capping layer [167, 168]. Although the experimental conditions are not suited for a turn-key tabletop resistance standard at the moment, with progress in material growth and processing of TIs, it can offer exciting prospects for the development of resistance standards under relaxed measurement conditions and without the need for a magnetic field [167, 168].

# Bibliography


1. Irvine, M. M. Early Digital Computers at Bell Telephone Laboratories. *IEEE Annals of the History of Computing* **23,** 22–42. ISSN: 1058-6180 (2001).
2. IBM. *POWER9* https://en.wikipedia.org/wiki/POWER9.
3. Novoselov, K. S. *et al.* Two-dimensional gas of massless Dirac fermions in graphene. **438,** 197–200 (2005).
4. Geim, A. K. & Novoselov, K. S. The rise of graphene. *Nat Mater* **6,** 183–191 (2007).
5. Jiang, Z. *et al.* Quantum Hall effect in graphene. *Solid State Communications* **143,** 14–19. ISSN: 00381098 (2007).
6. Fuhrer, M. S., Lau, C. N. & MacDonald, A. H. Graphene: Materially Better Carbon. *MRS Bulletin* **35,** 289–295 (2010).
7. Castro Neto, A. H. *et al.* The electronic properties of graphene. *Rev. Mod. Phys.* **81,** 109–162 (1 2009).
8. Das Sarma, S. *et al.* Electronic transport in two-dimensional graphene. *Reviews of Modern Physics* **83,** 407–470. ISSN: 0034-6861 (2011).
9. Wallace, P. R. The Band Theory of Graphite. *Phys. Rev.* **71,** 622–634 (9 1947).
10. A., D. *et al.* Monitoring dopants by Raman scattering in an electrochemically top-gated graphene transistor. *Nat Nano* **3,** 210–215. ISSN: 1748-3387 (Apr. 2008).
11. Malard, L. M. *et al.* Raman spectroscopy in graphene. *Physics Reports* **473,** 51–87. ISSN: 03701573 (2009).
12. Ferrari, A. C. Raman spectrum of graphene and graphene layers. *Phys. Rev. Lett.* **97,** 187401– (2006).

13. Ferrari, A. C. & Basko, D. M. Raman spectroscopy as a versatile tool for studying the properties of graphene. *Nature nanotechnology* **8,** 235–246. ISSN: 1748-3387 (2013).

14. Heller, E. J. *et al.* Theory of Graphene Raman Scattering. *ACS Nano* **10,** 2803–2818. ISSN: 1936086X (2016).

15. Venezuela, P., Lazzeri, M. & Mauri, F. Theory of double-resonant Raman spectra in graphene: Intensity and line shape of defect-induced and two-phonon bands. *Physical Review B - Condensed Matter and Materials Physics* **84,** 1–25. ISSN: 10980121 (2011).

16. Beams, R., Cançado, L. G. & Novotny, L. Raman characterization of defects and dopants in graphene. *Journal of Physics: Condensed Matter* **27,** 083002. ISSN: 1361-648X (2015).

17. Piscanec, S. *et al.* Kohn Anomalies and Electron-Phonon Interactions in Graphite. *Phys. Rev. Lett.* **93,** 185503 (18 2004).

18. Froehlicher, G. & Berciaud, S. Raman spectroscopy of electrochemically gated graphene transistors: Geometrical capacitance, electron-phonon, electron-electron, and electron-defect scattering. *Phys. Rev. B* **91,** 205413 (2015).

19. Hall, E. H. On the new action of magnetism on a permanent electric current. *American Journal of Science* **s3-20,** 161–186. ISSN: 0002-9599 (1880).

20. Popovic, R. S. *Hall effect devices* (CRC Press, 2003).

21. Xu, H. *et al.* Batch-fabricated high-performance graphene Hall elements. **3,** 1207 (Feb. 2013).

22. Wang, Z. *et al.* Encapsulated graphene-based Hall sensors on foil with increased sensitivity. *physica status solidi (b)* **253,** 2316–2320. ISSN: 1521-3951 (2016).

23. Klitzing, K. v., Dorda, G. & Pepper, M. New Method for High-Accuracy Determination of the Fine-Structure Constant Based on Quantized Hall Resistance. *Physical review letters* **45,** 494–497. ISSN: 0031-9007 (1980).

24. Prange, R. E. & Girvin, S. M. *The Quantum Hall Effect* Second edition. ISBN: 146123350X (Springer New York, New York, NY, 1990).

25. Landauer, R. Spatial Variation of Currents and Fields Due to Localized Scatterers in Metallic Conduction. *IBM Journal of Research and Development* **1,** 223–231. ISSN: 0018-8646 (1957).

26. Laughlin, R. B. Quantized Hall conductivity in two dimensions. *Phys. Rev. B* **23,** 5632–5633 (10 1981).

27. Prange, R. E. Quantized Hall resistance and the measurement of the fine-structure constant. *Phys. Rev. B* **23,** 4802–4805 (9 1981).

28. Novoselov, K. S. *et al.* Room-Temperature Quantum Hall. **315,** 2007 (2007).

29. Abanin, D, Lee, P & Levitov, L. Charge and spin transport at the quantum Hall edge of graphene. *Solid State Communications* **143,** 77–85. ISSN: 00381098 (2007).

30. Das Sarma, S. & Yang, K. The enigma of the quantum Hall effect in graphene. *Solid State Communications* **149,** 1502–1506. ISSN: 00381098 (2009).

31. V Klitzing, K & Ebert, G. Application of the Quantum Hall Effect in Metrology. *Metrologia* **21,** 11 (1985).

32. Poirier, W. & Schopfer, F. Resistance metrology based on the quantum Hall effect. *The European Physical Journal Special Topics* **172,** 207–245. ISSN: 1951-6401 (2009).

33. Jeckelmann, B. & Jeanneret, B. The quantum Hall effect as an electrical resistance standard. *Reports on Progress in Physics* **64,** 1603. ISSN: 0034-4885 (2001).

34. Tzalenchuk, A. *et al.* Towards a quantum resistance standard based on epitaxial graphene. *Nature nanotechnology* **5,** 186–189. ISSN: 1748-3387 (2010).

35. Janssen, T. J.B. M. *et al.* Graphene, universality of the quantum Hall effect and redefinition of the SI system. *New Journal of Physics* **13,** 093026. ISSN: 1367-2630 (2011).

36. Guignard, J. *et al.* Quantum Hall effect in exfoliated graphene affected by charged impurities: Metrological measurements. *Physical Review B* **85.** ISSN: 1098-0121. doi:\url{10.1103/PhysRevB.85.165420} (2012).

37. Lafont, F. *et al.* Quantum Hall resistance standards from graphene grown by chemical vapour deposition on silicon carbide. *Nature communications* **6,** 6806. ISSN: 2041-1723 (2015).

38. Janssen, T. J.B. M. *et al.* Operation of graphene quantum Hall resistance standard in a cryogen-free table-top system. *2D Materials* **2,** 035015 (2015).

39. Novoselov, K. S. *et al.* A roadmap for graphene. *Nature* **490,** 192–200. ISSN: 1476-4687 (2012).

40. Schopfer, F. & Poirier, W. Graphene-based quantum Hall effect metrology. *MRS Bulletin* **37,** 1255–1264 (2012).

41. Woszczyna, M. *et al.* Precision quantization of Hall resistance in transferred graphene. *Applied Physics Letters* **100,** 164106. ISSN: 0003-6951 (2012).

42. Shen, T. *et al.* Quantum Hall effect on centimeter scale chemical vapor deposited graphene films. *Applied Physics Letters* **99,** 232110. ISSN: 0003-6951 (2011).

43. Giesbers, A. J. M. *et al.* Quantum resistance metrology in graphene. *Applied Physics Letters* **93,** 222109. ISSN: 0003-6951 (2008).

44. Ribeiro-Palau, R. *et al.* Quantum Hall resistance standard in graphene devices under relaxed experimental conditions. *Nature nanotechnology* **10,** 965–971. ISSN: 1748-3387 (2015).

45. Wolf, E. L. *Applications of Graphene: An Overview* ISBN: 9783319039459. doi:\url{10.1007/978-3-319-03946-6} (Springer International Publishing, Cham and s.l., 2014).

46. Reina, A. *et al.* Transferring and Identification of Single- and Few-Layer Graphene on Arbitrary Substrates. *The Journal of Physical Chemistry C* **112,** 17741–17744. ISSN: 1932-7447 (2008).

47. Sun, Z. *et al.* Growth of graphene from solid carbon sources. *Nature* **468,** 549–552. ISSN: 1476-4687 (2010).

48. Li, X. *et al.* Graphene films with large domain size by a two-step chemical vapor deposition process. *Nano letters* **10,** 4328–4334. ISSN: 1530-6992 (2010).

49. Banszerus, L. *et al.* Ultrahigh-mobility graphene devices from chemical vapor deposition on reusable copper. *Science Advances* **1,** – (July 2015).

50. Calado, V. E. *et al.* Ballistic transport in graphene grown by chemical vapor deposition. *Applied Physics Letters* **104,** 023103. ISSN: 0003-6951 (2014).

51. Bae, S. *et al.* Roll-to-roll production of 30-inch graphene films for transparent electrodes. *NATURE NANOTECHNOLOGY* **5,** 574–578. ISSN: 1748-3387 (2010).

52. Kobayashi, T. *et al.* Production of a 100-m-long high-quality graphene transparent conductive film by roll-to-roll chemical vapor deposition and transfer process. *Applied Physics Letters* **102,** 023112. ISSN: 00036951 (2013).

53. Shin, Y. C. & Kong, J. Hydrogen-excluded graphene synthesis via atmospheric pressure chemical vapor deposition. *Carbon* **59,** 439 –447. ISSN: 0008-6223 (2013).

54. Cooper, D. R. *et al. Experimental Review of Graphene* 2012. doi:10.5402/2012/501686.

55. Antonova, I. V. Chemical vapor deposition growth of graphene on copper substrates: current trends. *Physics-Uspekhi* **56,** 1013 (2013).

56. Bhaviripudi, S. *et al.* Role of kinetic factors in chemical vapor deposition synthesis of uniform large area graphene using copper catalyst. *Nano letters* **10,** 4128–4133. ISSN: 1530-6984 (2010).

57. Vlassiouk, I. *et al.* Role of Hydrogen in Chemical Vapor Deposition Growth of Large Single-Crystal Graphene. *ACS Nano* **5.** PMID: 21707037, 6069–6076 (2011).

58. Losurdo, M. *et al.* Graphene CVD growth on copper and nickel: role of hydrogen in kinetics and structure. *Phys. Chem. Chem. Phys.* **13,** 20836–20843 (46 2011).

59. Thodkar, K. *et al.* Comparative study of single and multi domain CVD graphene using large-area Raman mapping and electrical transport characterization. *physica status solidi (RRL) - Rapid Research Letters* **10,** 807–811. ISSN: 18626254 (2016).

60. Gao, L. *et al.* Repeated growth and bubbling transfer of graphene with millimetre-size single-crystal grains using platinum. *Nat Commun* **3,** 699– (Feb. 2012).

61. Gan, L. & Luo, Z. Turning off Hydrogen To Realize Seeded Growth of Subcentimeter Single-Crystal Graphene Grains on Copper. *ACS Nano* **7.** PMID: 24053313, 9480–9488 (2013).

62. Yan, Z, Peng, Z. W. & Tour, J. M. Chemical Vapor Deposition of Graphene Single Crystals. *Accounts of Chemical Research* **47,** 1327–1337 (2014).

63. Yan, Z. *et al.* Toward the Synthesis of Wafer-Scale Single-Crystal Graphene on Copper Foils. *ACS Nano* **6,** 9110–9117. ISSN: 1936-0851 (Oct. 2012).

64. Miseikis, V *et al.* Rapid CVD growth of millimetre-sized single crystal graphene using a cold-wall reactor. *2D Materials* **2,** 014006 (2015).

65. Vlassiouk, I. *et al.* Graphene Nucleation Density on Copper: Fundamental Role of Background Pressure. *The Journal of Physical Chemistry C* **117,** 18919–18926 (2013).

66. Fu, W. *et al.* Graphene transistors are insensitive to pH changes in solution. *Nano letters* **11,** 3597–3600. ISSN: 1530-6984 (2011).

67. De la Rosa, C. J. L. *et al.* Frame assisted H2O electrolysis induced H2 bubbling transfer of large area graphene grown by chemical vapor deposition on Cu. *Applied Physics Letters* **102,** 022101. ISSN: 00036951 (2013).

68. Lee, J. *et al.* Clean transfer of graphene and its effect on contact resistance. *Applied Physics Letters* **103,** 103104. ISSN: 00036951 (2013).

69. Song, L. *et al.* Transfer Printing of Graphene Using Gold Film. *ACS Nano* **3.** PMID: 19438194, 1353–1356 (2009).

70. Thomsen, C. & Reich, S. Double Resonant Raman Scattering in Graphite. *Physical Review Letters* **85,** 5214–5217. ISSN: 0031-9007 (2000).

71. Kalbac, M. *et al.* The Influence of Strong Electron and Hole Doping on the Raman Intensity of Chemical Vapor-Deposition Graphene. *ACS Nano* **4.** PMID: 20931995, 6055–6063 (2010).

72. Chen, C.-F. *et al.* Controlling inelastic light scattering quantum pathways in graphene. *Nature* **471,** 617–620. ISSN: 0028-0836 (Mar. 2011).

73. Stampfer, C. *et al.* Raman imaging of doping domains in graphene on SiO2. *Applied Physics Letters* **91,** 241907. ISSN: 0003-6951 (2007).

74. Casiraghi, C. *et al.* Raman fingerprint of charged impurities in graphene. *Applied Physics Letters* **91.** ISSN: 00036951. doi:10.1063/1.2818692 (2007).

75. Ni, Z. H. *et al.* Uniaxial strain on graphene: Raman spectroscopy study and band-gap opening. *ACS Nano* **2,** 2301–2305. ISSN: 19360851 (2008).

76. Larsen, M. B. B. *et al.* Transfer induced compressive strain in graphene: Evidence from Raman spectroscopic mapping. *Microelectronic Engineering* **121.** Nano Fabrication 2013, 113 –117. ISSN: 0167-9317 (2014).

77. Neumann, C. *et al.* Raman spectroscopy as probe of nanometre-scale strain variations in graphene. *Nature communications* **6,** 8429. ISSN: 2041-1723 (2015).

78. Bousige, C. *et al.* Biaxial Strain Transfer in Supported Graphene. *Nano Letters* **17.** PMID: 28073255, 21–27 (2017).

79. Shin, Y. *et al.* Raman spectroscopy of highly pressurized graphene membranes. *Applied Physics Letters* **108,** 221907 (2016).

80. Androulidakis, C. *et al.* Graphene flakes under controlled biaxial deformation. **5,** 18219 (Dec. 2015).

81. Ding, F. *et al.* Stretchable Graphene: A Close Look at Fundamental Parameters through Biaxial Straining. *Nano Letters* **10.** PMID: 20695450, 3453–3458 (2010).

82. Lee, J. E. *et al.* Optical separation of mechanical strain from charge doping in graphene. *Nature communications* **3,** 1024. ISSN: 2041-1723 (2012).

83. Lin-Vien, D. *et al. The Handbook of infrared and raman characteristic frequencies of organic molecules* ISBN: 9780124511606 (Academic Press, Boston, 1991).

84. Fink, H.-W., Stocker, W. & Schmid, H. Holography with low-energy electrons. *Phys. Rev. Lett.* **65,** 1204–1206 (10 1990).

85. Longchamp, J.-N. *et al.* Non-destructive imaging of an individual protein. *Applied Physics Letters* **101,** 093701 (2012).

86. Longchamp, J.-N. *et al.* Low-energy electron holographic imaging of individual tobacco mosaic virions. *Applied Physics Letters* **107,** 133101 (2015).

87. Longchamp, J.-N. *et al.* Imaging proteins at the single-molecule level. *Proceedings of the National Academy of Sciences* **114,** 1474–1479 (2017).

88. Longchamp, J.-N. *et al.* Low-energy electron transmission imaging of clusters on free-standing graphene. *Applied Physics Letters* **101,** 113117 (2012).

89. Longchamp, J.-N., Escher, C. & Fink, H.-W. Ultraclean freestanding graphene by platinum-metal catalysis. *Journal of Vacuum Science & Technology B, Nanotechnology and Microelectronics: Materials, Processing, Measurement, and Phenomena* **31,** 020605 (2013).

90. Hüfner, S. *Photoelectron Spectroscopy: Principles and Applications* Third rev. and enlarged edition. ISBN: 3662092808 (Springer Berlin Heidelberg, Berlin, Heidelberg, 2003).

91. Walls, J. M. & Smith, R. Surface science techniques. *Vacuum* **45,** 649–652. ISSN: 0042207X (1994).

92. Hesse, R., Chassé, T. & Szargan, R. Peak shape analysis of core level photoelectron spectra using UNIFIT for WINDOWS. *Fresenius' Journal of Analytical Chemistry* **365,** 48–54. ISSN: 1432-1130 (1999).

93. Eren, B. *et al.* The effect of low temperature deuterium plasma on molybdenum reflectivity. *Nuclear Fusion* **51,** 103025 (2011).

94. Rosencrance, S. W. *et al.* Polymethylmethacrylate by XPS. *Surface Science Spectra* **2,** 71–75 (1993).

95. Sezen, H. *et al.* Charging/Discharging of Thin PS/PMMA Films As Probed by Dynamic X-ray Photoelectron Spectroscopy. *Macromolecules* **40,** 4109–4112. ISSN: 0024-9297 (2007).

96. Cunge, G. *et al.* Dry efficient cleaning of poly-methyl-methacrylate residues from graphene with high-density H 2 and H 2 -N 2 plasmas. *Journal of Applied Physics* **118,** 123302. ISSN: 0021-8979 (2015).

97. Novoselov, K. S. *et al.* Electric field effect in atomically thin carbon films. *Science (New York, N.Y.)* **306,** 666–9. ISSN: 1095-9203 (2004).

98. Schwierz, F. Graphene transistors. *Nat Nano* **5,** 487–496. ISSN: 1748-3387 (July 2010).

99. Ryu, S. *et al.* Atmospheric Oxygen Binding and Hole Doping in Deformed Graphene on a SiO2 Substrate. *Nano Letters* **10,** 4944–4951 (2010).

100. Guo, B. *et al.* Controllable N-Doping of Graphene. *Nano Letters* **10.** PMID: 20968305, 4975–4980 (2010).

101. Levesque, P. L. *et al.* Probing charge transfer at surfaces using graphene transistors. *Nano letters* **11,** 132–137. ISSN: 1530-6984 (2011).

102. Aguirre, C. M. *et al.* The Role of the Oxygen/Water Redox Couple in Suppressing Electron Conduction in Field-Effect Transistors. *Advanced Materials* **21,** 3087–3091. ISSN: 09359648 (2009).

103. Cheng, Z. *et al.* Toward intrinsic graphene surfaces: a systematic study on thermal annealing and wet-chemical treatment of SiO2-supported graphene devices. *Nano letters* **11,** 767–771. ISSN: 1530-6984 (2011).

104. Lin, Y.-C. *et al.* Graphene annealing: how clean can it be? *Nano Letters* **12,** 414–419 (2012).

105. Chowdhury, S. F. *et al.* Improvement of graphene field-effect transistors by hexamethyldisilazane surface treatment. *Applied Physics Letters* **105.** doi:\url{10.1063/1.4891364} (2014).

106. Thodkar, K. *et al. Characterization of HMDS treated CVD graphene 2016 Conference on Precision Electromagnetic Measurements (CPEM 2016)* (IEEE, 2016), 1–2. ISBN: 978-1-4673-9134-4. doi:\url{10.1109/CPEM.2016.7540498}.

107. Lafkioti, M. *et al.* Graphene on a Hydrophobic Substrate: Doping Reduction and Hysteresis Suppression under Ambient Conditions. *Nano Letters* **10,** 1149–1153 (2010).

108. Xia, F. *et al.* The origins and limits of metal-graphene junction resistance. *Nature nanotechnology* **6,** 179–184. ISSN: 1748-3395 (2011).

109. Allain, A. *et al.* Electrical contacts to two-dimensional semiconductors. *Nat Mater* **14,** 1195–1205. ISSN: 1476-1122 (Dec. 2015).

110. Russo, S. *et al.* Contact resistance in graphene-based devices. *Physica E: Low-dimensional Systems and Nanostructures* **42,** 677–679. ISSN: 13869477 (2010).

111. Venugopal, a, Colombo, L & Vogel, E. Contact resistance in few and multilayer graphene devices. *Applied Physics Letters* **96,** 013512. ISSN: 00036951 (2010).

112. Yager, T. *et al.* Low contact resistance in epitaxial graphene devices for quantum metrology. *AIP Advances* **5,** 087134 (2015).

113. Jia, Y. *et al.* Toward High Carrier Mobility and Low Contact Resistance: Laser Cleaning of PMMA Residues on Graphene Surfaces. *Nano-Micro Letters* **8,** 336–346. ISSN: 2150-5551 (2016).

114. Franklin, A. D., Farmer, D. B. & Haensch, W. Defining and Overcoming the Contact Resistance Challenge in Scaled Carbon Nanotube Transistors. *ACS Nano* **8.** PMID: 24999536, 7333–7339 (2014).

115. Chen, C. *et al.* Graphene mechanical oscillators with tunable frequency. *Nature Nanotechnology* **8,** 923–927. ISSN: 1748-3395 (2013).

116. Li, X. *et al.* Large-Area Graphene Single Crystals Grown by Low-Pressure Chemical Vapor Deposition of Methane on Copper. *J. Am. Chem. Soc.* **133,** 2816–2819. ISSN: 0002-7863 (Mar. 2011).

117. Yan, H. J. *et al.* First-principles study of the oxygen adsorption and dissociation on graphene and nitrogen doped graphene for Li-air batteries. *Journal of Applied Physics* **112.** doi:\url{10.1063/1.4766919} (2012).

118. Gupta, A. *et al.* Raman scattering from high-frequency phonons in supported n-graphene layer films. *Nano Lett.* **6,** 2667–2673 (2006).

119. Das A. *et al.* Monitoring dopants by Raman scattering in an electrochemically top-gated graphene transistor. *Nat Nano* **3,** 210–215 (2008).

120. Pisana, S. *et al.* Breakdown of the adiabatic Born-Oppenheimer approximation in graphene. *Nat Mater* **6,** 198–201 (2007).

121. Cancado, L. G. *et al.* Quantifying Defects in Graphene via Raman Spectroscopy at Different Excitation Energies. *Nano Lett.* **11,** 3190–3196. ISSN: 1530-6984 (Aug. 2011).

122. Pirkle, A. *et al.* The effect of chemical residues on the physical and electrical properties of chemical vapor deposited graphene transferred to SiO2. *Applied Physics Letters* **99,** 122108. ISSN: 00036951 (2011).

123. Huard, B. *et al.* Evidence of the role of contacts on the observed electron-hole asymmetry in graphene. *Physical Review B* **78.** ISSN: 1098-0121. doi:\url{10.1103/PhysRevB.78.121402} (2008).

124. Larsen, M. B. B. *et al.* Transfer induced compressive strain in graphene: Evidence from Raman spectroscopic mapping. *Microelectronic Engineering* **121,** 113–117. ISSN: 01679317 (2014).

125. Yagi, K. *et al.* Dependence of Field-Effect Mobility of Graphene Grown by Thermal Chemical Vapor Deposition on Its Grain Size. *Japanese Journal of Applied Physics* **52,** 110106 (2013).

126. Song, H. S. *et al.* Origin of the relatively low transport mobility of graphene grown through chemical vapor deposition. **2,** 337 (Mar. 2012).

127. Thodkar, K. *et al.* Restoring the Electrical Properties of CVD Graphene via Physisorption of Molecular Adsorbates. *ACS Applied Materials & Interfaces* **9.** PMID: 28675296, 25014–25022 (2017).

128. Cai, X. *et al.* Sensitive room-temperature terahertz detection via the photothermoelectric effect in graphene. *Nat Nano* **9,** 814–819 (2014).

129. Marini, A., Silveiro, I. & Javier Garcia de Abajo, F. Molecular Sensing with Tunable Graphene Plasmons. *ACS PHOTONICS* **2,** 876–882. ISSN: 2330-4022 (2015).

130. Koppens, F. H. L., Chang, D. E. & Javier Garcia de Abajo, F. Graphene Plasmonics: A Platform for Strong Light-Matter Interactions. *Nano Letters* **11,** 3370–3377 (2011).

131. Chen, C. *et al.* Performance of monolayer graphene nanomechanical resonators with electrical readout. *Nat Nano* **4,** 861–867 (2009).

132. Schedin, F. *et al.* Detection of individual gas molecules adsorbed on graphene. *Nat Mater* **6,** 652–655 (2007).

133. Chakrapani, V. *et al.* Charge transfer equilibria between diamond and an aqueous oxygen electrochemical redox couple. *Science (New York, N.Y.)* **318,** 1424–1430. ISSN: 0036-8075 (2007).

134. Grimme, S. *et al.* A consistent and accurate ab initio parametrization of density functional dispersion correction (DFT-D) for the 94 elements H-Pu. *The Journal of chemical physics* **132,** 154104. ISSN: 0021-9606 (2010).

135. Hernandez, Y. *et al.* High-yield production of graphene by liquid-phase exfoliation of graphite. *Nat Nano* **3,** 563–568 (2008).

136. Mohiuddin, T. M. G. *et al.* Uniaxial strain in graphene by Raman spectroscopy: G peak splitting, Gruneisen parameters, and sample orientation. *Phys. Rev. B* **79.** doi:\url{10.1103/PhysRevB.79.205433} (2009).

137. Zabel, J. *et al.* Raman spectroscopy of graphene and bilayer under biaxial strain: bubbles and balloons. *Nano letters* **12,** 617–621. ISSN: 1530-6984 (2012).

138. Sun, H. *et al.* Binder-free graphene as an advanced anode for lithium batteries. *J. Mater. Chem. A* **4,** 6886–6895. ISSN: 2050-7488 (2016).

139. Her, M., Beams, R. & Novotny, L. Graphene transfer with reduced residue. *PHYSICS LETTERS A* **377,** 1455–1458. ISSN: 0375-9601 (2013).

140. Lafont, F. *et al.* Anomalous dissipation mechanism and Hall quantization limit in polycrystalline graphene grown by chemical vapor deposition. *Physical Review B* **90.** ISSN: 1098-0121. doi:\url{10.1103/PhysRevB.90.115422} (2014).

141. Yu, Q. *et al.* Control and characterization of individual grains and grain boundaries in graphene grown by chemical vapour deposition. *Nature materials* **10,** 443–449. ISSN: 1476-1122 (2011).

142. Koepke, J. C. *et al.* Atomic-scale evidence for potential barriers and strong carrier scattering at graphene grain boundaries: a scanning tunneling microscopy study. *ACS Nano* **7,** 75–86 (2013).

143. Ma, J. *et al.* Adsorption and diffusion of water on graphene from first principles. *Phys. Rev. B* **84,** 33402 (2011).

144. Wang, L. *et al.* One-dimensional electrical contact to a two-dimensional material. *Science (New York, N.Y.)* **342,** 614–617. ISSN: 0036-8075 (2013).

145. Thodkar, K. *et al.* High quality CVD graphene for quantum Hall resistance standards. to be submitted (2017).

146. Janssen, T. J.B. M. *et al.* Anomalously strong pinning of the filling factor n=2 in epitaxial graphene. *Physical Review B* **83.** ISSN: 1098-0121. doi:\url{10.1103/PhysRevB.83.233402} (2011).

147. Lara-Avila, S. *et al.* Non-volatile photochemical gating of an epitaxial graphene/polymer heterostructure. *Advanced materials (Deerfield Beach, Fla.)* **23,** 878–882. ISSN: 0935-9648 (2011).

148. Chua, C. *et al.* Quantum Hall effect and quantum point contact in bilayer-patched epitaxial graphene. *Nano letters* **14,** 3369–3373. ISSN: 1530-6984 (2014).

149. Schumann, T. *et al.* Anisotropic quantum Hall effect in epitaxial graphene on stepped SiC surfaces. *Phys. Rev. B* **85,** 235402 (23 2012).

150. Cao, H. *et al.* Electronic transport in chemical vapor deposited graphene synthesized on Cu: Quantum Hall effect and weak localization. *Appl. Phys. Lett.* **96,** 122106. ISSN: 0003-6951 (Mar. 2010).

151. Xu, X. *et al.* Ultrafast growth of single-crystal graphene assisted by a continuous oxygen supply. *Nat Nano* **11,** 930–935. ISSN: 1748-3387 (Nov. 2016).

152. Martin, S. C. *et al.* Disorder and screening in decoupled graphene on a metallic substrate. *Physical Review B* **91.** ISSN: 1098-0121. doi:\url{10.1103/PhysRevB.91.041406} (2015).

153. Cummings, A. W., Cresti, A. & Roche, S. Quantum Hall effect in polycrystalline graphene: The role of grain boundaries. *Physical Review B* **90.** ISSN: 1098-0121. doi:\url{10.1103/PhysRevB.90.161401} (2014).

154. Martin, J. *et al.* Observation of electron-hole puddles in graphene using a scanning single-electron transistor. *Nat Phys* **4,** 144–148. ISSN: 1745-2473 (Feb. 2008).

155. Cho, S. & Fuhrer, M. S. Charge transport and inhomogeneity near the minimum conductivity point in graphene. *Phys. Rev. B* **77,** 081402 (8 2008).

156. Bai, K.-K. *et al.* Detecting giant electron-hole asymmetry in a graphene monolayer generated by strain and charged-defect scattering via Landau level spectroscopy. *Physical Review B* **92.** ISSN: 1098-0121. doi:\url{10.1103/PhysRevB.92.121405} (2015).

157. McCann, E. *et al.* Weak-Localization Magnetoresistance and Valley Symmetry in Graphene. *Phys. Rev. Lett.* **97,** 146805 (14 2006).

158. Gorbachev, R. V. *et al.* Weak Localization in Bilayer Graphene. *Phys. Rev. Lett.* **98,** 176805 (17 2007).

159. Tikhonenko, F. V. *et al.* Weak Localization in Graphene Flakes. *Phys. Rev. Lett.* **100,** 056802 (5 2008).

160. Xiang, S. *et al.* Low-temperature quantum transport in CVD-grown single crystal graphene. *Nano Research* **9,** 1823–1830. ISSN: 1998-0000 (June 2016).

161. Kubakaddi, S. S. Interaction of massless Dirac electrons with acoustic phonons in graphene at low temperatures. *Physical Review B* **79.** ISSN: 1098-0121. doi:\url{10.1103/PhysRevB.79.075417} (2009).

162. Baker, A. M. R. *et al.* Weak localization scattering lengths in epitaxial, and CVD graphene. *Phys. Rev. B* **86,** 235441 (23 2012).

163. Huang, P. Y. *et al.* Grains and grain boundaries in single-layer graphene atomic patchwork quilts. *Nature* **469,** 389–392. ISSN: 0028-0836 (Jan. 2011).

164. Bergvall, A., Carlsson, J. M. & Löfwander, T. Influence of [0001] tilt grain boundaries on the destruction of the quantum Hall effect in graphene. *Physical Review B* **91.** ISSN: 1098-0121. doi:\url{10.1103/PhysRevB.91.245425} (2015).

165. Grosse, K. L. *et al.* Direct observation of resistive heating at graphene wrinkles and grain boundaries. *Appl. Phys. Lett.* **105,** 143109. ISSN: 0003-6951 (Oct. 2014).

166. Alexander-Webber, J. A. *et al.* Phase Space for the Breakdown of the Quantum Hall Effect in Epitaxial Graphene. *Phys. Rev. Lett.* **111,** 096601 (9 2013).

167. Bestwick, A. J. *et al.* Precise Quantization of the Anomalous Hall Effect near Zero Magnetic Field. *Physical review letters* **114,** 187201. ISSN: 0031-9007 (2015).

168. Chang, C.-Z. *et al.* High-precision realization of robust quantum anomalous Hall state in a hard ferromagnetic topological insulator. *Nat Mater* **14,** 473–477. ISSN: 1476-1122 (May 2015).

169. Kresse, G. & Hafner, J. Ab initio molecular dynamics for liquid metals. *Physical Review B* **47,** 558–561. ISSN: 1098-0121 (1993).

170. Perdew, Burke & Ernzerhof. Generalized Gradient Approximation Made Simple. *Physical review letters* **77,** 3865–3868. ISSN: 0031-9007 (1996).

171. Blöchl, P. E. Projector augmented-wave method. *Physical Review B* **50,** 17953–17979. ISSN: 1098-0121 (1994).

172. Grimme, S. Semiempirical GGA-type density functional constructed with a long-range dispersion correction. *Journal of computational chemistry* **27,** 1787–1799. ISSN: 0192-8651 (2006).

173. Meng, Y. *et al.* Signatures in vibrational and UV-visible absorption spectra for identifying cyclic hydrocarbons by graphene fragments. *Nanoscale* **5,** 12178–12184 (24 2013).

# A

# Fabrication

## $SiO_2$/Si substrate characteristics

| | |
|---|---|
| Substrate material (bulk) | highly doped Silicon |
| Dopant | p, Boron |
| Resistivity | 0.001-0.005 $\Omega$cm |
| Oxide layer | $SiO_2$, 300 nm |

## Substrate preparation for CVD graphene transfer

- Sonicate the substrate in acetone: 10 mins
- Rinse in 2-propanol and blow dry in $N_2$

## UV lithography protocol for patterning and contacts

- Blow dry the substrate thoroughly while affixed on the spinner chuck prior to resist spin coating
- Blow dry and clean the pipette thoroughly before pipetting the resist
- Spin coat the UV resist (ma-N 415, micro resist technology GmBH, Germany) at 3000 rpm, 45s ($\sim$1.5 $\mu m$ thickness)
- Bake for 90s at 95$^\circ C$
- UV exposure (MJB4, S*ü*ss MicroTec, Germany) for 8s (365 nm, 32 mW/cm$^2$)
- Develop for 80s in ma-D 332, rinse in DI water and blow dry in $N_2$

### e-beam lithography protocol for patterning and contacts

- Blow dry the substrate thoroughly while affixed on the spinner chuck prior to resist spin coating
- Blow dry and clean the pipette thoroughly before pipetting the resist
- Spin coat the e-beam resist (ZEP 520A, Zeon Co., Japan) at 4000 rpm, 45s ($\sim$350 nm thickness)
- Bake for 180s at 180$^{\circ}C$
- Substrate alignment and e-beam exposure (Zeiss supra 40, Zeiss, Germany) using 10 kV accelerating voltage, working distance of 17 mm. Apertures used: 10 $\mu$m for smaller structures and 120 $\mu$m for larger structures. Dose: 32 $\mu$C/cm$^2$
- develop in amyl acetate (60s), stop development in Iso-butyl Ketone (10s), rinse in IPA and blow dry in $N_2$

★ **Note:** All the mask design was performed in CleWin3 and exported as GDS files into ELPHY

### Contact fabrication

- Sharon Vacuum (MA, USA) system was used to fabricate contacts for GFETs via thermal evaporation process.
- Palladium (6 to 10 nm) - Gold (50 to 80 nm) contact was our first choice for contacting GFETs
- Evaporation rate: Pd ($<$0.5 Å/s), Au ($<$1 Å/s)
- Evaporation pressure: $<$0.1 $\mu$Torr

★ **Tip:** At times the substrate edges were covered using scotch tape stripes. This was done to prevent metalization from short-circuiting the oxide and bulk Si

### Lift Off procedure

- Samples with ma-N 415 resist, the lift-off procedure was performed in acetone (60$^{\circ}$C) for 20 mins, rinsed in IPA and blow dried in $N_2$
- Samples with ZEP 520A resist, the lift-off was performed in N-methyl-2-pyrrolidone (NMP) at 60 $^{\circ}$C for 20 mins, pre-rinse in acetone, second rinse in IPA and blow dried in $N_2$

★ **Tip:** In the instances of graphene rolling-up during the lift-off procedure, Xylene was preferred over NMP. Lift-Off was performed in Xylene (60 $^{\circ}$C) for 20 mins., rinsed in Hexane and blow dried in $N_2$

### Graphene patterning and contact using Kapton foil mask

- The substrates are diced into dimension similar to that of the Kapton foil mask. CVD graphene is then transferred onto such diced substrates.
- A PMMA layer (50K PMMA, 4000 rpm, 45s, $\sim$300 nm thickness) was spun on CVD G on substrate. The graphene patterning mask is then aligned ontop of the substrate and clamped using the respective sample holders.
- The sample holder together with the aligned mask and substrate is exposed to Ar/$O_2$ plasma (250 mbar, Ar (8%)/$O_2$(16%), 150s, 60W). This step is performed to etch PMMA & graphene which is exposed to plasma and thus pattern graphene into Hall bar structures.
- The PMMA is dissolved in acetone, substrate is rinsed in IPA and blow dried in $N_2$.
- The Kapton foil mask for contact patterning is aligned on substrate and is clamped using the metal holder. This is loaded into the thermal evaporator and undergoes a similar metal deposition process detailed earlier.

★ **Tip:** It was observed using Raman spectroscopy that graphene was damaged during the plasma process if it was not protected using a PMMA layer. This can occur if the mask is not in close proximity with graphene during the clamping of the mask on graphene. Hence, a PMMA layer was used to protect graphene during the plasma.

**Graphene suspension** Several suspended graphene samples were produced during collaborative projects for different applications. The process of graphene suspension are described below.

- Transfer PMMA/CVD G stack onto pre-patterned substrates with trenches.
- Perform a soft bake at 90 °C after drying for 15 minutes.
- Dissolve the PMMA in Xylene (10 mins.) and rinse in Hexane. Do not blow dry.

★ **Tip:** It is also possible to thermally sublimate PMMA layer (350°C) and obtain suspended graphene films. This has to performed under non-oxidative environments to prevent damage to graphene film.

# B

# CVD graphene growth, transfer and solvent treatment

## Copper foil preparation

- The CVD growth of graphene was performed on commercially available 25¯m thick copper foils (Sigma Aldrich Nr.13382) in a low pressure hot wall CVD reactor
- The copper foils were first rinsed in acetic acid for 15 minutes and rinsed in DI water and ethanol

## Copper foil electropolishing solution

- Mix 5 : 1 - DI Water (150mL) : $H_3PO_4$ (50mL) (Ortho Phosphoric acid)
- Add Ethanol (50ml) and 10ml of IPA to the above solution
- Add 1g/0.5g of Urea at the end and shake gently

## Copper foil electropolishing solution

- Mix 5 : 1 - DI Water (150mL) : $H_3PO_4$ (50mL) (Ortho Phosphoric acid)
- Add Ethanol (50ml) and 10ml of IPA to the above solution
- Add 1g/0.5g of Urea at the end and shake gently

★ **Tip**: The solution can be made more concentrated by reducing the DI water concentration. A gentle stirring of the solution during electropolishing is recommended.

## Copper foil electropolishing procedure

- Add the EP solution into a glass beaker
- Negative electrode - (Electro deposited side, can be another copper foil)
- Positive electrode- the Copper foil you would like to use
- Use tweezers to hold the copper pieces
- Start at ∼1.2 V - Shake the solution mildly - Repeat for min. 40 seconds
- Ramp the voltage in steps of ∼0.5 V - Repeat Step V
- Ramp the Voltage until ∼6V
- Dip EP foil in DI water and blow dry in $N_2$ - 'foil ready for growth'
- Rinse the beakers thoroughly and let dry in the hood

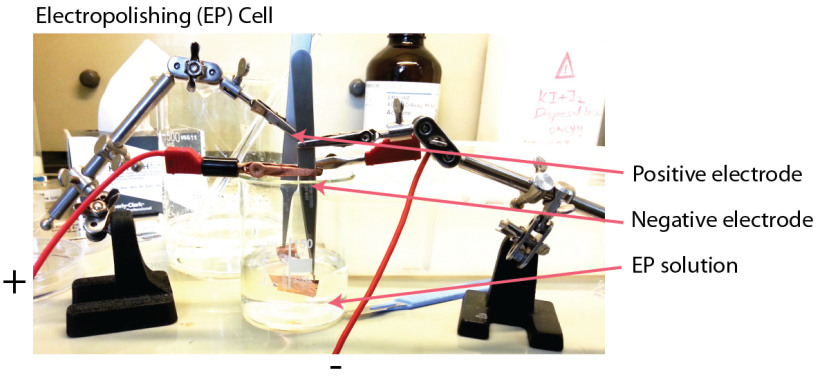


**Figure B.1:** The optical picture of home-made electro-polishing cell for copper foil electropolishing prior to CVD growth. Note: The millimeter scale single crystal CVD graphene grains were grown on such electropolished copper foils.

## Graphene growth process

- The foils are then loaded into the CVD chamber and undergo thermal annealing at 1000 °C for 3 hours in 200 sccm argon gas flow.
- After the annealing, Hydrogen and methane were let into the CVD chamber to initiate graphene growth (mixture according to recipe).
- The methane gas flow was stopped and the chamber was cooled down to ambient temperature in argon and hydrogen gas flow.

★ **Tip**: The pressure during the growth was manipulated using a valve, positioned at the exit of the quartz tube and in series with the scroll pump.

## CVD graphene transfer

- The top side of copper foil with CVD graphene was spin coated with ∼400 nm thick (3000 rpm, 45 seconds) 50K PMMA layer (allresist Nr.63212) and baked at 150 °C for 3 minutes.
- The graphene layer on the bottom side of the copper foil was etched using oxygen plasma (30W, 250 mbar, 45 seconds) and then the copper/CVD graphene/PMMA was placed in ammonium persulphate (0.1M) solution to etch the copper.
- After the completion of copper etching the CVD graphene/PMMA stack was rinsed in DI water and then transferred onto 300 nm $SiO_2$/Si substrate and left dry for 30 minutes.
- Before the PMMA removal, a brief hot plate anneal (100°C) for 20 mins. was performed to improve the adhesion of graphene film on substrate.
- The PMMA film was then dissolved in warm acetone (50 °C) and rinsed in iso-propyl alcohol (IPA) and blow dried in $N_2$ gas flow.

★ **Tip**: Check for substrate hydrophilicity before transfer. Higher the hydrophilicity better the graphene transfer uniformity i.e. lesser cracks, holes and ruptures.

## CVD graphene solvent treatment

- **NMP treatment**: The CVD graphene sample was placed in NMP solution (Sigma Aldrich Nr.M79204) overnight (∼8 hours) in a water bath maintained at 70°C.
- **HMDS treatment**: The CVD graphene sample was placed in HMDS solution (Sigma Aldrich Nr.440191) overnight (∼8 hours) at ambient temperature.

## CVD graphene FET thermal annealing

- The thermal annealing of the respective CVD graphene samples were performed using a Rapid Thermal Annealing (RTA) oven AO600 from MBE Komponenten.
- The samples were annealed at 350°C for 3 hours in forming gas flow ($N_2$/$H_2$, 8% $H_2$) and the chamber pressure was maintained at 80 mbar.

★ **Tip**: Lower annealing pressures were found to improve the FET characteristics.

## Gold etching recipe

- Add Potassium Iodide (KI) - 4g, Iodine (I) - 1g, DI Water - 150 mL, etch rate- 25 nm/min

### Hexagonal boron nitride etching recipe

- $CHF_3$ (80 sccm) / $O_2$ (4 sccm)/ 12 mins/ 60 W/ 50 mTorr (rate $\sim$ 10-20 nm/min).

### Other tested transfer techniques

1) Alakane thiol intercalation technique

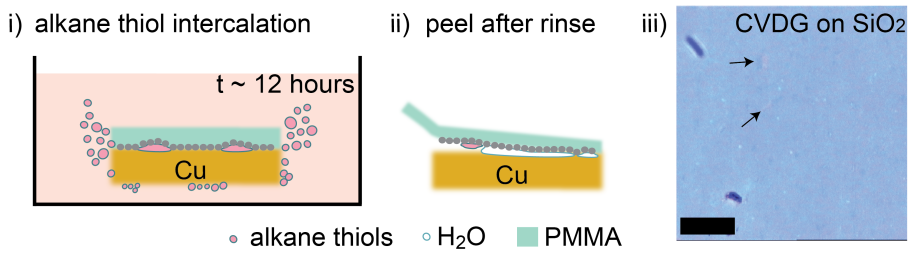


**Figure B.2:** Alkane thiol (octane thiol) assisted peeling of CVD graphene. i) Representation of alkane thiol intercalation between graphene-copper interface ii) peel CVDG from copper with help of PMMA layer iii) optical image of CVD graphene transferred onto $SiO_2$/Si substrate using the peeling technique, scale bar: 20 $\mu$m.

Another CVD graphene transfer process tried during the thesis is detailed in B.2. In this technique, the as-grown CVD graphene on copper foil was immersed in octane-thiol solution overnight ($\sim$12 hours). Due to the higher affinity of thiol linking groups to metal surface (copper surface in our case), the thiol molecules intercalate between graphene-copper interface. Thin layer of PMMA is spun on CVD G/Cu and peeled from copper surface. This way graphene can be transferred from copper surface onto PMMA and subsequently transferred onto different substrates. However, several cracks and thiol residues were found in the transferred graphene on substrate (B.2 iii).

# C

# Setup details and further graphene characterization

## Details of our Raman spectroscopy setup used for graphene film characterization

The Raman measurements were performed using a commercial alpha 300 confocal system from Witec with a laser excitation wavelength of 533 nm (2.33 eV). The Raman scans were performed using linear polarization. A 50x (LMPlanIR 50x) objective with a fixed 0.2 second integration time per spectra was used during the scans. Lorentzian peak was used to fit G and 2D peaks of every Raman spectra in the map to extract the respective peak position and its FWHM for the analysis in the study. This system is equipped with an UHTS 300 spectrometer with grating options: 600 and 1800 groves per mm. The resolution of the CCD is 1024x127 pixels.

## Details of electrical characterization of graphene FETs

Some of the preliminary ambient temperature transport measurements were performed in a probe station from MMR technologies at $10^{-4}$ mbar. A voltage bias $V_{SD}$ of 1 mV was applied during the ambient temperature measurements.

## Details of Imina probe station for electrical characterization of graphene FETs

The Hall bars fabricated using the Kapton foil masks were characterized in the home-built/integrated chamber consisting of joy-stick controlled Imina probers. The Imina prober setup is as shown in the C.1 consisting of four mini bots on top of SEM compatible stage. The chamber is equipped with a heater stage for annealing of CVD graphene sample prior to transport characterization. One of the special possibilities of this setup apart from the standard probing is that it brings forth in-situ annealing and electrical probing at the same time under low-vacuum conditions. The latter can be useful while probing graphene FETs during thermal annealing.

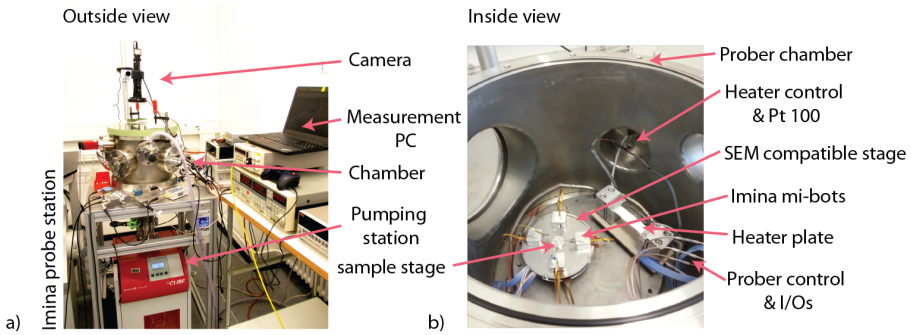


**Figure C.1:** The Imina probe station. a) The outside view of the prober setup. A long working distance camera from THOR labs is used to visualize the samples. All the measurements control and the prober control is performed using the PC and joystick. b) The inside view of the prober. Note: The thermal plate inside was installed after dismantling an old thermal anneal oven. The probe station can be pumped down to base pressure of $10^{-6}$ mbar.

## Calibration details of Raman spectroscopy setup used for graphene film characterization

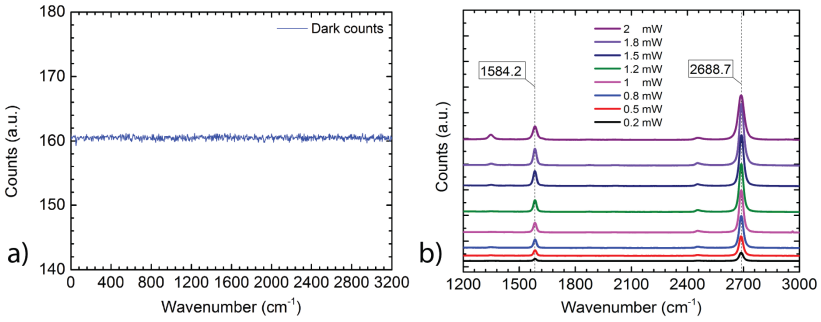


**Figure C.2:** Calibration details of our Raman setup. a) Dark count level of the charge coupled detector (CCD) of our Raman setup collected at 0.2 second integration time. b) Raman spectras of CVD graphene taken at different laser power (mW), the average peak position is highlighted in dashed lines.

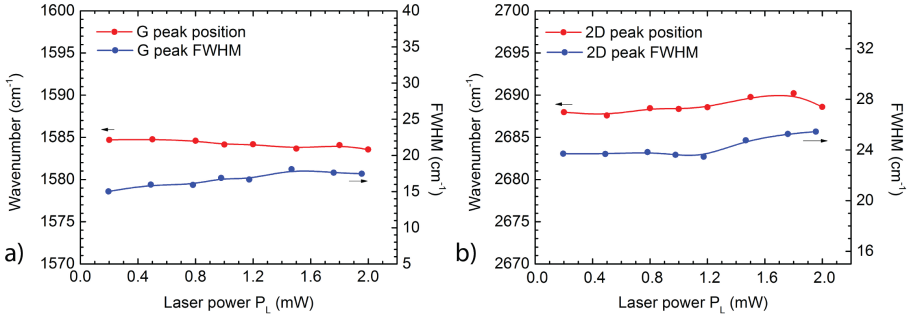


**Figure C.3:** a) & b) The peak position (left Y-axis) and FWHM (right Y-axis) values of the G (fig. a) and 2D (fig. b) peaks of CVD graphene versus the laser power $P_L$ (mW). It can be noticed from figure a-b that the peak position and the FWHM of the G and 2D peaks remain stable for PL$\leq$ 2 mW.

## Raman characterization or wrinkles in graphene film

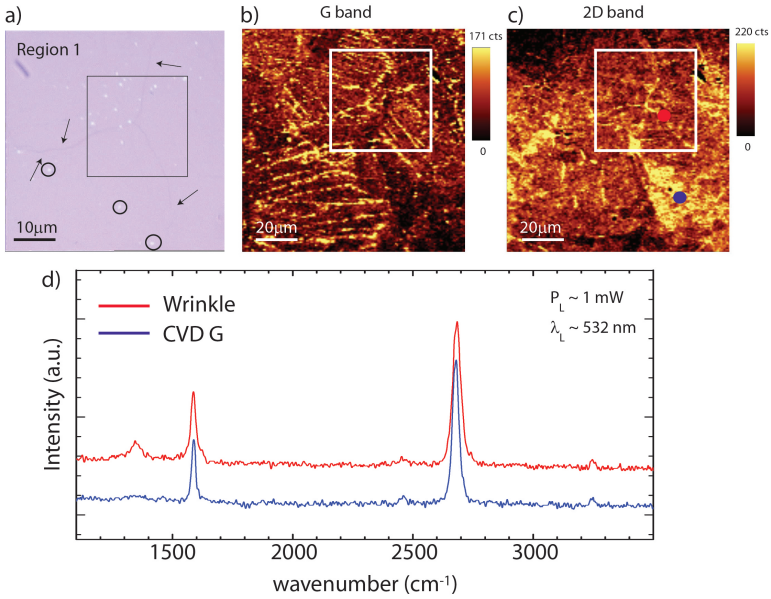


**Figure C.4:** a) Optical image of as-transferred CVD graphene on $SiO_2$ substrate. Inset: Region consisting of a wrinkle in the graphene film is highlighted within the marked square (black). Lines of wrinkles are also highlighted using arrows and the polymer residues from transfer are marked using circles. The respective G and 2D Raman maps of the graphene region in panel fig.a can be seen in panel fig.b & c. The wrinkle in fig.a can be observed in the Raman maps as within the square (white). The Raman spectrum of CVD graphene (blue) and CVD G-wrinkle (red) are plotted in panel d. The D peak is more pronounced on wrinkles.

## Optical images of wrinkles in graphene film

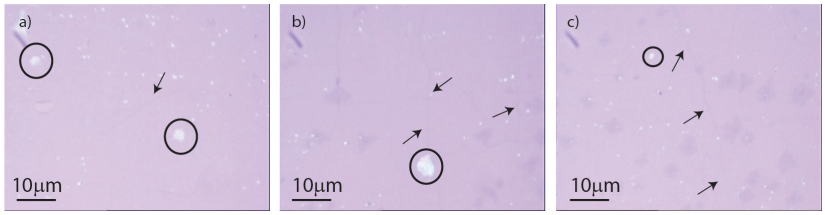


**Figure C.5:** Optical images of wrinkles in as-transferred CVD graphene on $SiO_2$ substrate. Lines of wrinkles are highlighted using arrows and the polymer residue leftover from transfer are marked using circles.

## Atomic force microscopy image of copper foil prior to CVD graphene growth

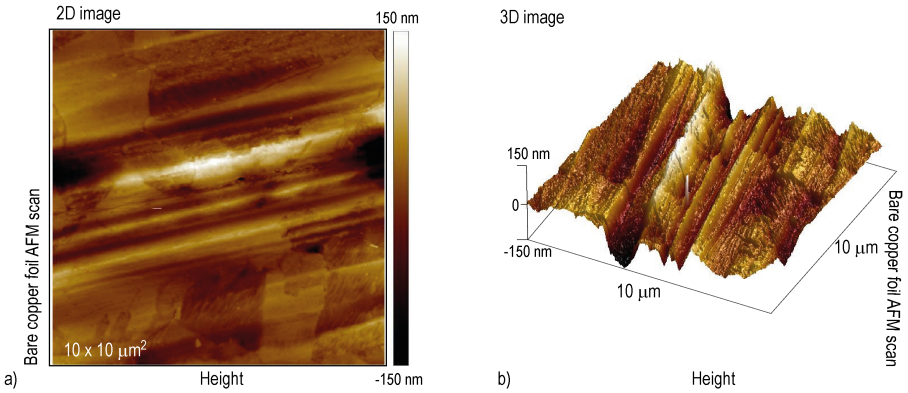


**Figure C.6:** AFM scan of commercial copper foil used for CVD graphene growth. a) 2D image of AFM scan and b) 3D image depicting the corrugations in copper foil.

## Atomic force microscopy image of as-transferred CVD graphene growth

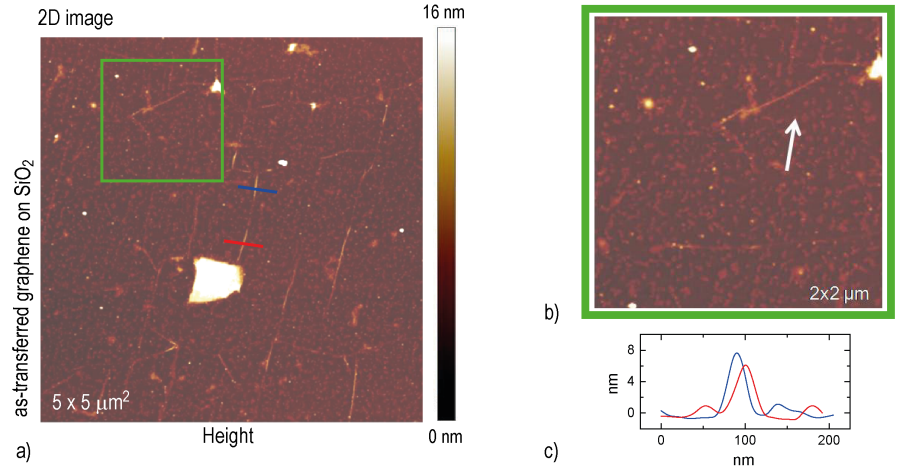


**Figure C.7:** a)AFM scan of as-transferred CVD graphene on $SiO_2$ substrate. b) A close-up AFM image depicting the wrinkles and c) AFM height profile of lines depicted in b. The faint white spots in C.7 b is indicative of PMMA residues on graphene (1-3 nm in height).

### Attempt to grow graphene on thermal evaporated copper thin films on $SiO_2$/Si wafer

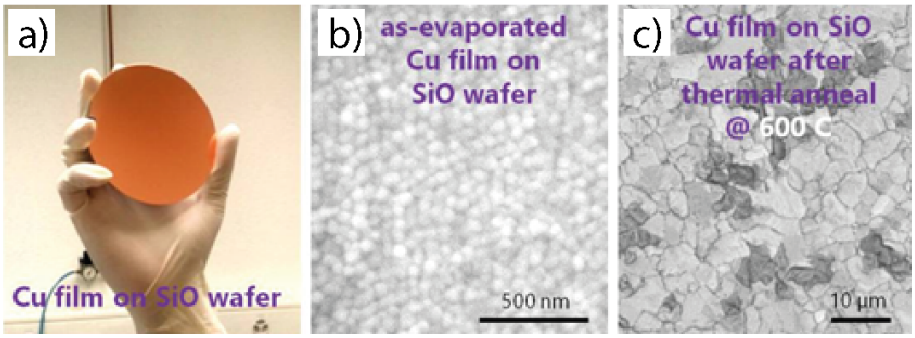


**Figure C.8:** a) Thermal evaporated copper film (2 $\mu$m) on three inch SiO wafer for high quality CVD graphene synthesis. b, c) Copper thin film before and after thermal annealing under ambient pressure at 600$^{\circ}C$. We can notice that the nanocrystalline islands of Copper grow into larger grains after thermal annealing process. Due to the dense roughness still present after thermal annealing, this substrate was not used for graphene growth.

### Optical image of a transfer length sample

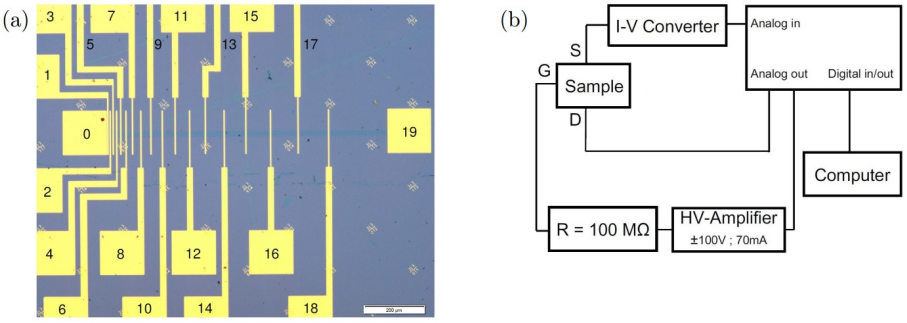


**Figure C.9:** a) Optical image of CVD graphene sample for TLM measurements. The contacts are as numbered. Scale: 200 $\mu$m; b) Circuit diagram for the TLM measurement (S,D and G denote the source, drain and gate of the device).

## Optical images of hBN-CVD graphene-hBN stack sample

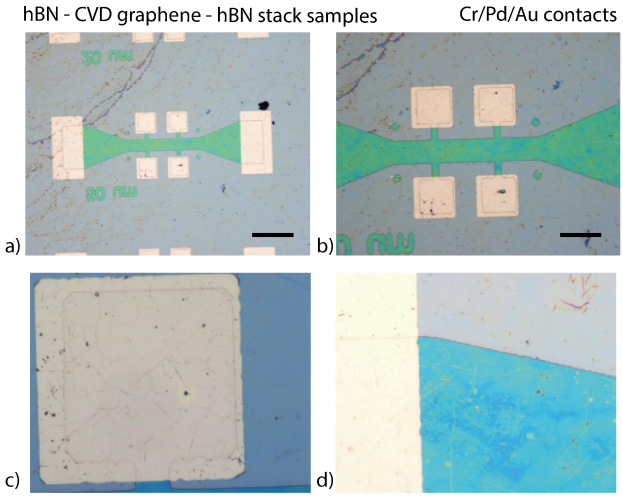


**Figure C.10:** a-d) Optical images hBN/graphene/hBN encapsulated sample. Thickness of stack $\sim$ 30 nm. Scale: 100 $\mu$m. Note: The multi layer hBN was a commercial sample from graphenea.

## Electrical transport characteristic of an hBN-CVD graphene-hBN stack sample

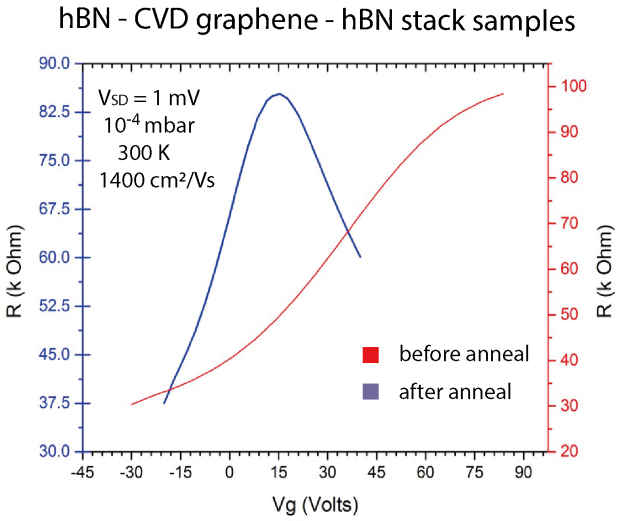


**Figure C.11:** Electrical transport characteristic curve ($R_T$ vs. Vg) of hBN-CVD graphene-hBN sample.

## Optical images of device fabrication with aluminium etch mask

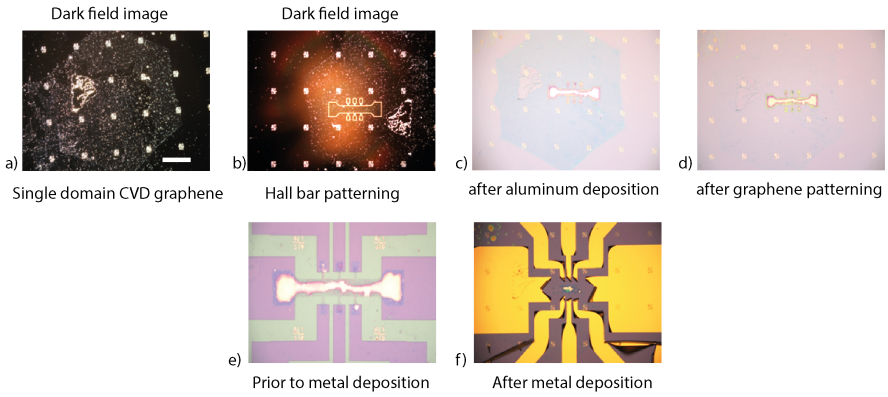


**Figure C.12:** a-f) Optical images of trials with device fabrication (single domain) with aluminium etch mask. Scale: 200 $\mu$m. Note: Aluminium was etched using ortho-phosphoric acid and DI water (1:3).

## Optical images of single domain CVD graphene Hall bar sample fabrication

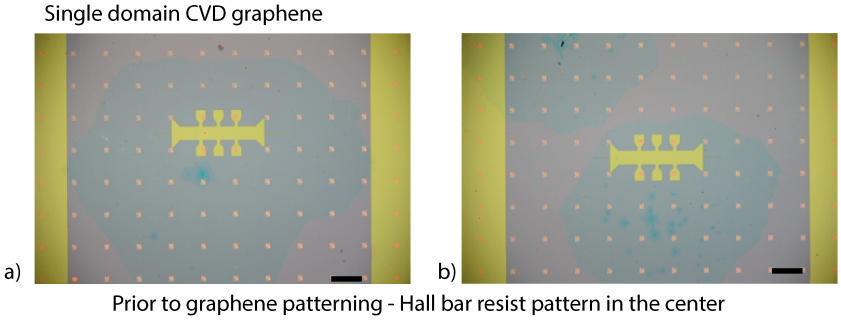


**Figure C.13:** a-f) Optical images of single domain CVD graphene Hall bar sample fabrication. Images taken prior to graphene patterning. The ZEP resist pattern can be noticed in the centre of the sample. Scale: 200 $\mu$m.

## Large area Raman characterization of NMP treated CVD graphene

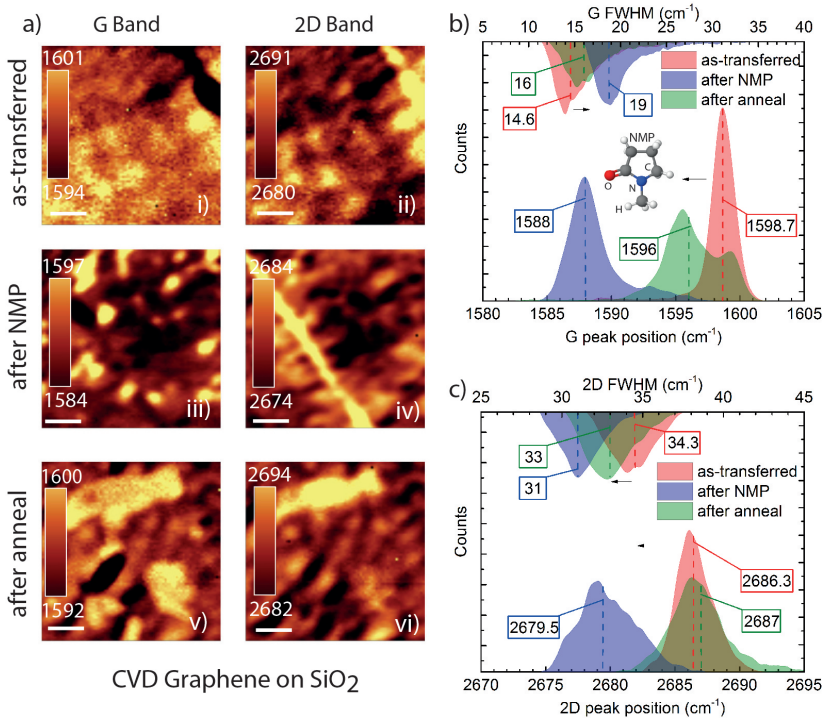


**Figure C.14:** Large area Raman imaging of region 2 (10 $\mu$m x10 $\mu$m) of as-transferred/NMP treated and thermally annealed CVD graphene on $SiO_2$ substrate. a) Confocal Raman imaging of G and 2D peak position of as-transferred CVD graphene (i, ii), after NMP treatment (iii, iv) and thermal annealing (v, vi). Scale bar: 2 $\mu$m. The corresponding peak positions in the G and 2D band maps can be found using the color bar. b, c) Histogram of the peak position and FWHM (top axis) of the respective G band (figure 1a i, iii, v) and 2D band (figure 1a ii, iv, vi) maps of as-transferred CVD graphene, after NMP treatment and thermal annealing. The average peak position of the histogram is as highlighted using red and blue dotted lines. All the Raman measurements were performed in ambient conditions.

## Large area Raman characterization of HMDS treated CVD graphene

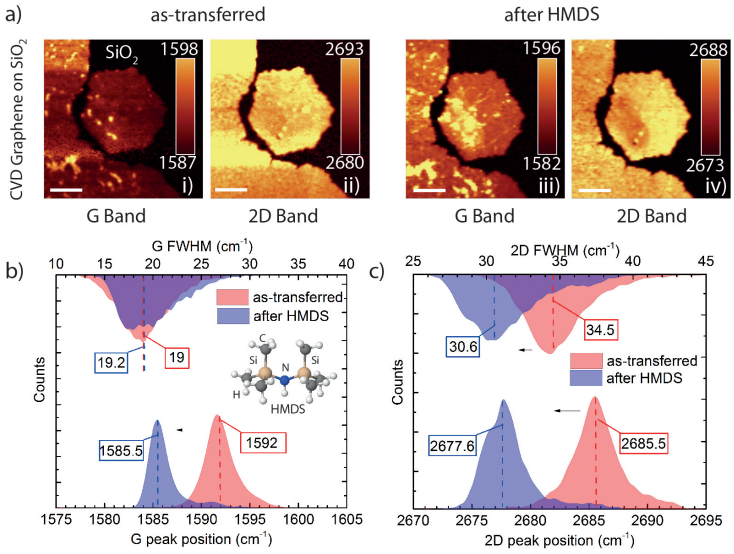


**Figure C.15:** Raman map of region 2 (50 $\mu$m x 50 $\mu$m) of as-transferred and HMDS-treated CVD graphene on $SiO_2$ substrate. a) Confocal Raman imaging of G and 2D peak position of as-transferred CVD graphene (i, ii) and after HMDS treatment (iii, iv) scale bar: 10 $\mu$m. The corresponding peak positions in the G and 2D band maps can be found using the color bar. b, c) Histogram of peak position and FWHM (top axis) of the respective G band (figure a i, ii) and 2D band (figure a iii, iv) maps of as-transferred CVD graphene and after HMDS treatment. Inset b: molecular structure of HMDS. The average peak position of the histogram is marked using red and blue dotted lines. All the Raman measurements were performed in ambient conditions.

## Optical image of HMDS treated CVD graphene

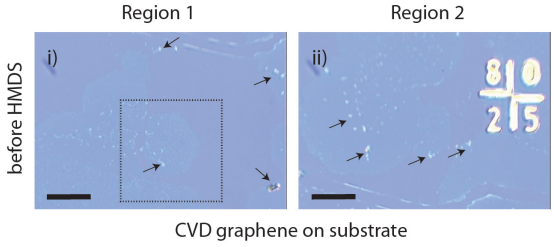


**Figure C.16:** Optical images of as-transferred CVD graphene on substrate before HMDS treatment. Scale bar: 20 $\mu$m. The region of the Raman scan is marked by the dotted square and some of the polymer residues are marked using the black arrows.

## Raman spectras of as-grown CVD graphene on copper foil

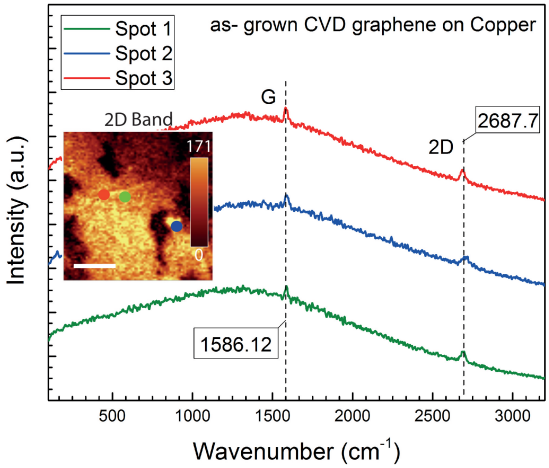


**Figure C.17:** Selected Raman spectra from the Raman map of as-grown CVD graphene on copper foil. Inset: The corresponding 2D band image of as-grown CVD graphene on copper and its intensity count can be found on the scale bar. The Raman spectra were recorded at the corresponding spots marked by colored circles. Scale bar: 5 $\mu$m. The average peak position of G and 2D peak is as highlighted using black dotted lines. All the Raman measurements were performed in ambient conditions. The background due to the copper substrate is clearly visible in the Raman spectra.

## Optical image of single domain graphene grain

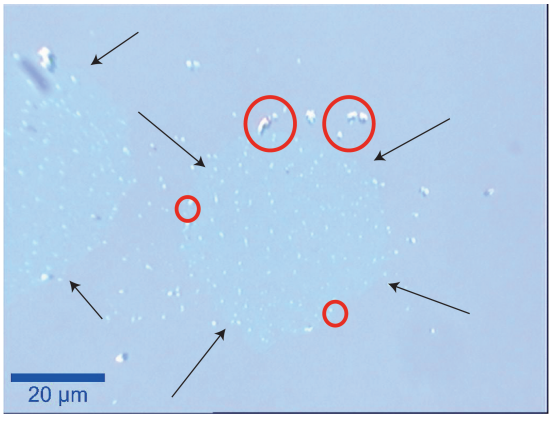


**Figure C.18:** Optical image of SD graphene grain on $SiO_2$/Si substrate. Graphene grains are marked using black arrows, polymer residues on graphene are highlighted in red circles.

## Raman spectras of as-grown CVD graphene on copper foil before and after NMP treatment

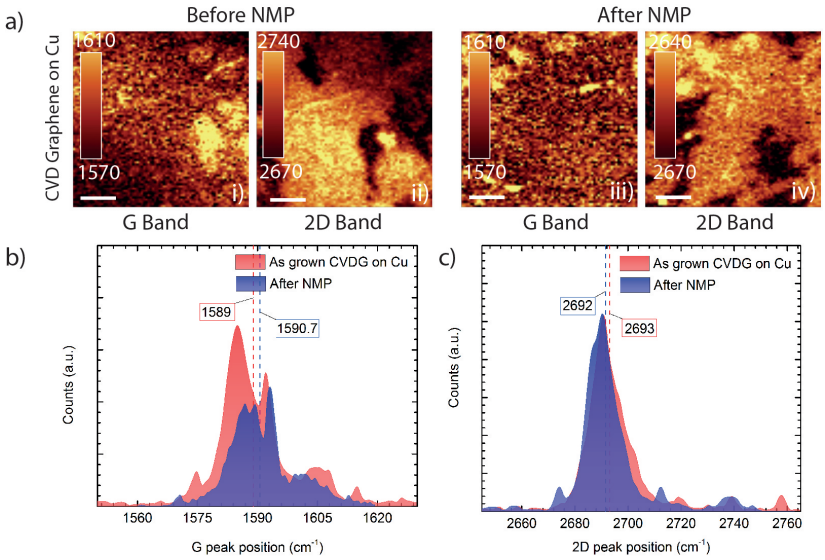


**Figure C.19:** Large area Raman imaging of as-grown/NMP treated CVD graphene on copper foil. a) Confocal Raman imaging of G and 2D peak position of as-grown CVD graphene on copper (i, ii) and after NMP treatment (iii, iv). Scale bar: 5 $\mu$m. The corresponding peak positions in the G and 2D band maps can be found using the color bar. b) Histogram of peak position of the respective G band (panel a i, iii) and 2D band (panel a ii, iv) maps of as-grown and NMP treated CVD graphene on copper foil. The average peak position of the histogram is as highlighted using red and blue dotted lines. All the Raman measurements were performed in ambient conditions.

## Stability and reversibility test of NMP treatment on CVD graphene

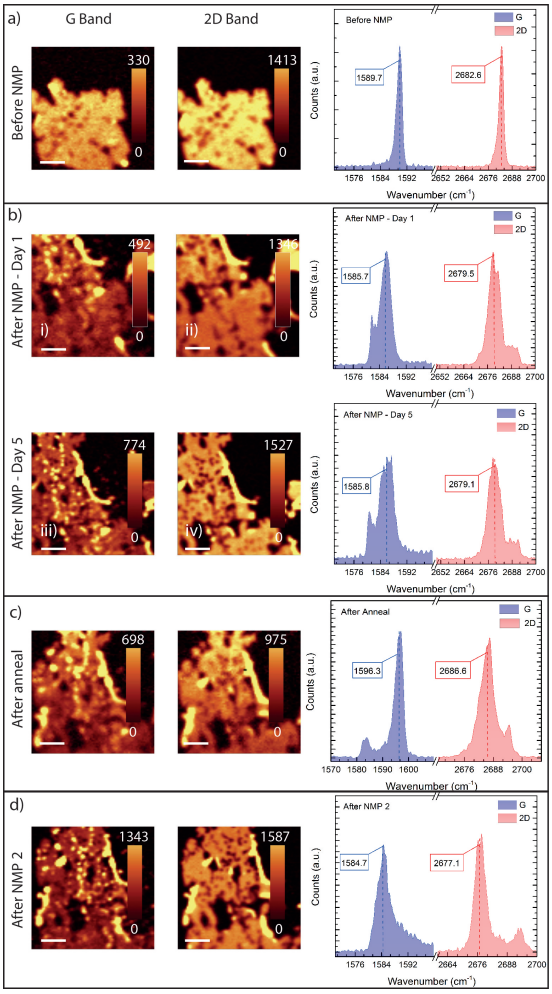


**Figure C.20:** Large area Raman mapping of G and 2D bands and their respective histograms of as-transferred/NMP treated CVD graphene and thermal annealed CVD graphene for stability and reversibility test. a) Raman maps of as-transferred CVD graphene on $SiO_2$/Si substrate. b) After NMP treatment-Day1 (i, ii) and Day-5 (iii, iv). We can observe a downshift of G and 2D peak position after the NMP treatment and this downshift remains stable over a span of five days. c) the peak positions after thermal annealing at 400 °C in $N_2/H_2$ gas flow (8% $H_2$) for 2 hours at 80 mbar. We can observe a large shift in peak positions to higher wavenumbers. d) Reversibility test: second NMP treatment on thermal annealed samples. Interestingly, after the second NMP treatment we can observe a downshift of average peak position to values similar to the first case of NMP treatment. The corresponding intensity count of the maps can be found using the color bar. Scale bar: 5 $\mu$m.

## Large area Raman mapping of as-transferred and NMP treated exfoliated graphene on $SiO_2$/Si substrate

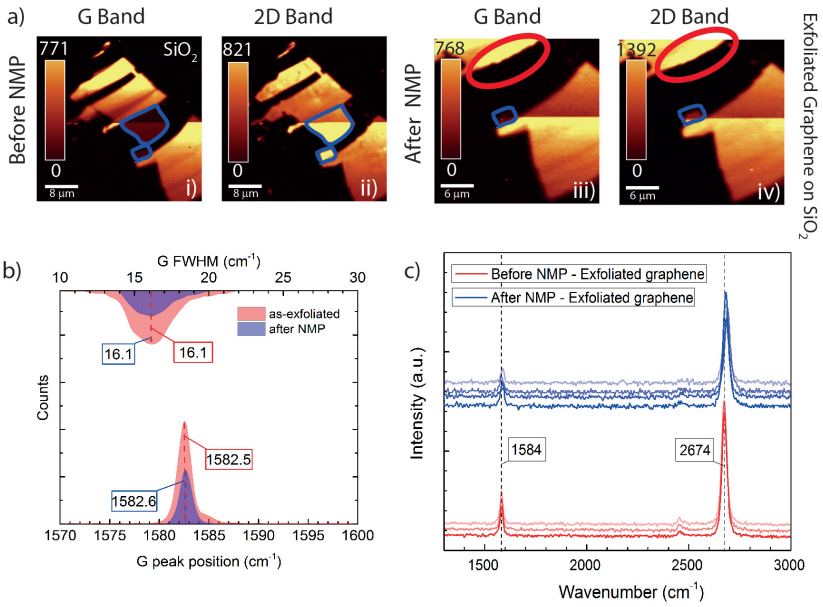


**Figure C.21:** Large area Raman imaging of as-transferred/NMP treated exfoliated graphene on $SiO_2$/Si substrate. a) Confocal Raman imaging of G and 2D peak position of as-transferred CVD graphene (i, ii) and after NMP treatment (iii, iv). Scale bar: 8 and 6 $\mu$m, before/after NMP treatment. The corresponding peak intensities of the G and 2D band maps can be found using the color bar. b) Histogram of peak position and FWHM (top axis) of the respective G band (figure 1a i, iii) maps of as-transferred and NMP treated exfoliated graphene flake. Inset in panel i: single layer graphene (SLG) flake is marked in dark blue. After the NMP treatment, the larger SLG flake on the top is rolled up as marked in red. The average peak position of the histogram is as highlighted using red and blue dotted lines. c) Selected Raman spectra of as-exfoliated (red) and after NMP treatment (blue) of exfoliated graphene on substrate. All the Raman measurements were performed in ambient conditions.

## Quantum Hall effect characterization of NMP treated CVD graphene

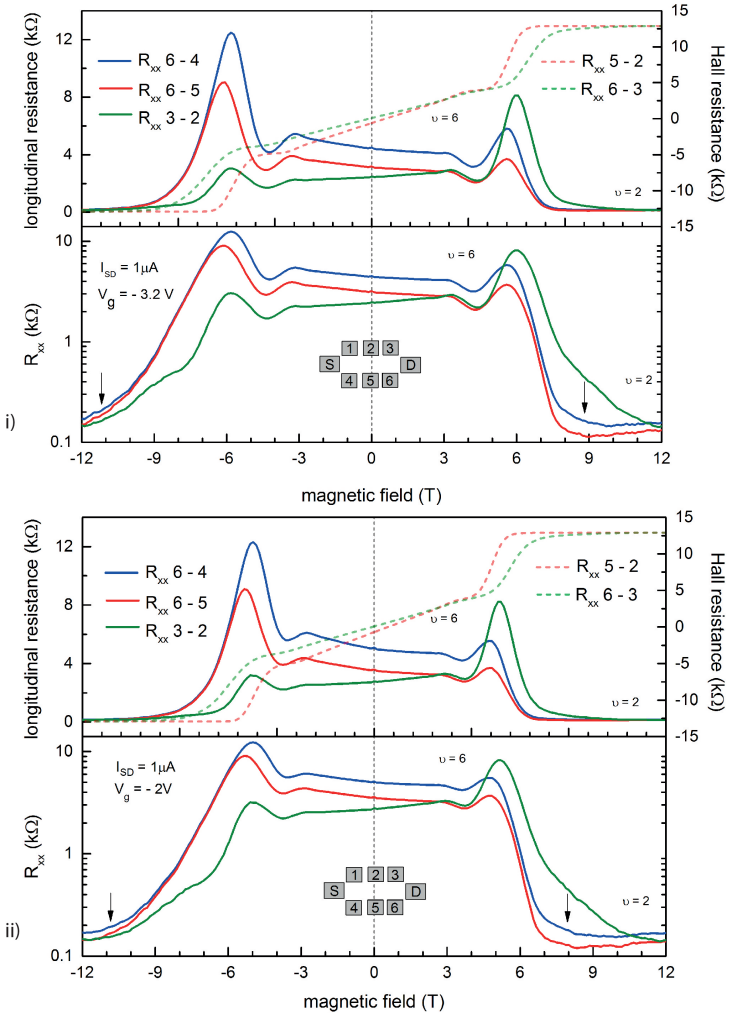


**Figure C.22:** Quantum Hall effect characterization of NMP-treated CVD graphene Hall bar device. i, ii) top panel: longitudinal resistance (Rxx), Hall resistance (Rxy) vs. magnetic field. Lower panel: Log scale of longitudinal resistance (Rxx) vs. magnetic field sweep at $I_{SD}$= 1$\mu$A, Vg -2V (i) and $I_{SD}$ = 1$\mu$A, Vg= -3.2V (ii). The black arrow highlights the observation of low Rxx values in QHE regime at higher magnetic fields $>$ 8T. Inset: Hall bar sample schematic. All the low temperature electrical transport measurements were performed at 0.3K.

## Quantum Hall effect characterization of HMDS treated CVD graphene

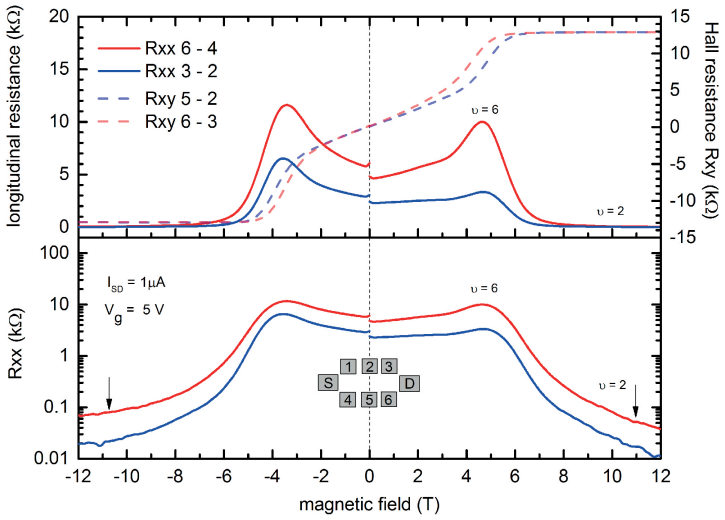


**Figure C.23:** Quantum Hall effect characterization of HMDS-treated CVD graphene Hall bar device. b) Top panel: longitudinal resistance (Rxx), Hall resistance (Rxy) vs. magnetic field. Lower panel: Log scale of longitudinal resistance (Rxx) vs. magnetic field sweep at $I_{SD}$ = 1$\mu$A, Vg = 5V. The black arrow highlights the observation of low Rxx values in QHE regime at higher magnetic fields $>$ 6T. Inset: Hall bar sample schematic. All the low temperature electrical transport measurements were performed at 0.3K.

## Field effect mobility and charge carrier density estimation

The field effect mobility $\mu_{FET}$ and charge carrier density $n_e$ were calculated using:

$$\mu_{FET} = \frac{L}{W}\frac{1}{C_g}\frac{\delta_G}{\delta_{Vg}} \tag{C.1}$$

$$C_g = \frac{\epsilon_0 \epsilon_r}{t_{ox}} \tag{C.2}$$

$$n_e = \frac{C_g V_g}{q} \tag{C.3}$$

where, L/W is the aspect ratio (length/width) of the device, G is the film conductance, q is the electron charge (1.6x10$^{-19}$ C) and Vg is the gate voltage, Cg is the gate capacitance per unit area Cg $\sim$ 11 nF/cm$^2$ ($t_{ox} \sim$ 300 nm, $\epsilon_r \sim$ 3.9), tox is the oxide thickness, $\epsilon_r$ is the relative permittivity of silicon dioxide. The aspect ratios of the devices are $\sim$ 1.5 and 5 for the SD and MD samples, respectively.

**Schematic of electron-transfer mechanism between graphene and water/oxygen aqueous layer**

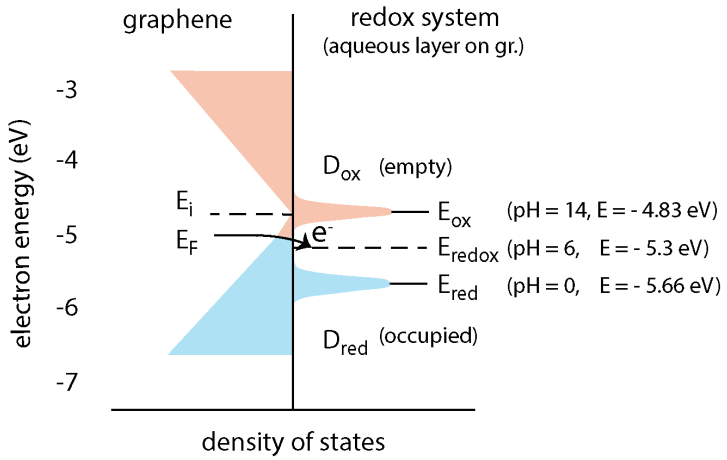


**Figure C.24:** Schematic of electron-transfer mechanism between graphene and water/oxygen redox couple density of states (DOS) for an equivalent concentration of both oxidizing and reducing species. The arrow indicates the direction of rge charge transfer reaction. The picture is adapted with permission from P. Levesque et al. [101].

The main electrochemical reactions involving dissolved oxygen in equilibrium with air are as [133]:

$$\mathrm{O_2(aq) + 4\,H^+ + 4\,e^-\,(graphene) \rightleftharpoons 2\,H_2O} \tag{C.4}$$

$$\mathrm{O_2(aq) + 2\,H_2O + 4\,e^-\,(graphene) \rightleftharpoons 4\,OH^-} \tag{C.5}$$

The reaction in C.4 dominate under acidic conditions and C.5 dominate under basic condition. Both the equations are related by the water equilibrium shown in C.6.

$$\mathrm{H_2O \rightleftharpoons H^+ + OH^-} \tag{C.6}$$

The electrochemical potential $\mu_e$ defined using the Nernst equation can be written as (w.r.t vacuum):

$$\mu_e(eV) = -4.44 + (-1)(+1.229) + \frac{0.0592}{4}[4pH\ -\ log_{10}(p_{O_2})] \qquad \text{(C.7)}$$

where the partial pressure of oxygen is in bar (0.21 bar), the standard hydrogen electrode (SHE, w.r.t vacuum) is $\mu_e$(SHE) = -4.44 eV, the standard electrode potential of reaction C.4, C.5 versus SHE are +1.229 V and +0.401 V. From electrical transport measurements, high p-doping is noticed in GFETs. From the electro-chemical transfer model, the Fermi level of graphene is higher than the electrochemical potential $\mu_e$ of the adsorbed water layer on graphene (see:C.24). The electrons in this case flow from graphene to the aqueous layer and compensate the anions in the water layer. This results in the hole-doping graphene film, as observed in the transport and Raman measurements. The $E_{redox}$ potential in C.24 was calculated for pH=6 (dissolving of $CO_2$ in aqueous layer) using C.7, similar to $E_{red}$, $E_{ox}$ values for pH = 0, 14.

## Field effect mobility characterization of NMP treated CVD graphene samples

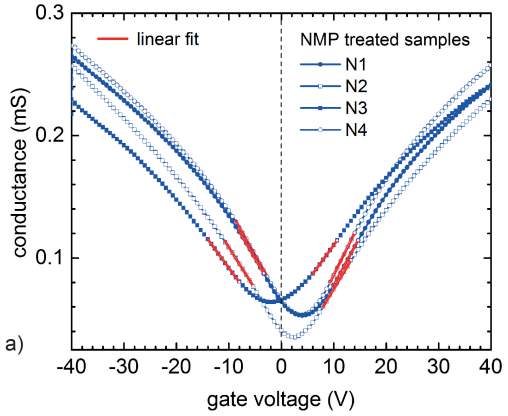


b)

| mobility ($cm^2$/Vs) | $\mu_{electron}$ | $\mu_{hole}$ |
|---|---|---|
| N1 | 3452.6 | 3197.8 |
| N2 | 3106.0 | 2970.8 |
| N3 | 2547.8 | 2521.7 |
| N4 | 3754.6 | 3289.5 |

**Figure C.25:** Field effect calibration of NMP treated CVD graphene samples. a) total conductance versus gate voltage for samples N1-4. b) Table of electron/hole field effect mobility of all the samples N1-4. The slope of the conductance curve was measured in the region highlighted in red. All the electrical characterization was performed under low vacuum conditions of $10^{-4}$ mbar.

## Electrical characterization of as-fabricated and HMDS treated CVD graphene

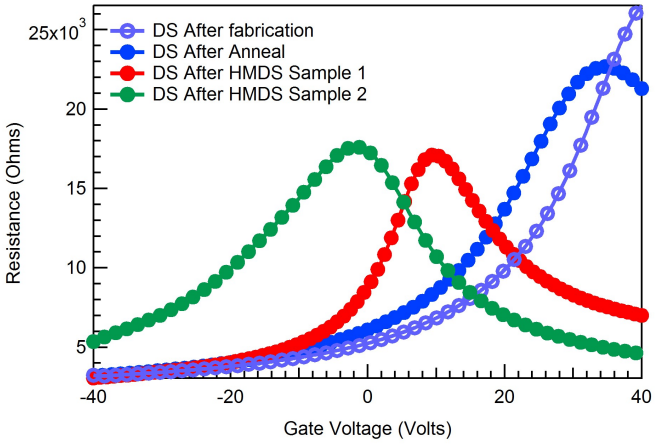


**Figure C.26:** Electrical characterization of CVD graphene of as-fabricated, after thermal-anneal and after HMDS treatment. These measurements were performed under low-vacuum conditions of $10^{-4}$ mbar. The sample bias was $V_{SD}$=1mV.

## Optical image of SD and MD graphene devices

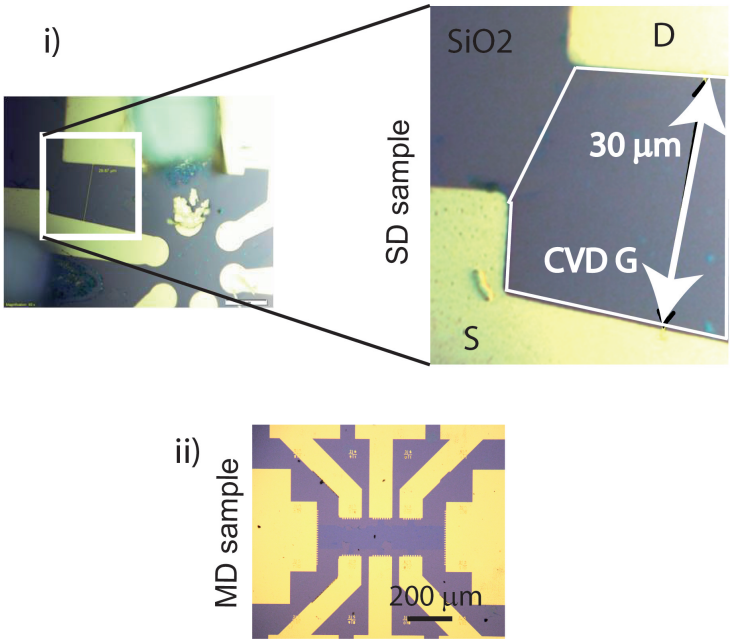


**Figure C.27:** Optical image of SD (i) and MD (ii) graphene devices. CVD graphene region is highlighted in white lines. The aspect ratio of the SD graphene sample is 1.5 (L = 30 $\mu$m, W = 20 $\mu$m) and is 5 (L=1000 $\mu$m, W = 200 $\mu$m) for the the MD graphene sample.

## Rolling of CVD graphene after NMP treatment

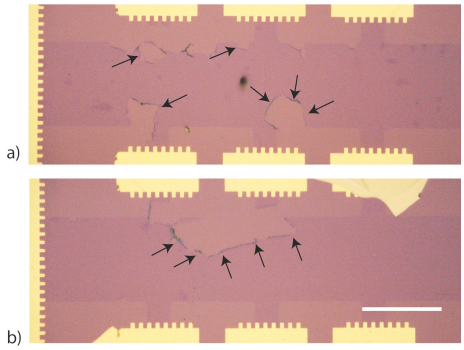


**Figure C.28:** Optical images showing the rolling up of CVD graphene after extended hours of NMP treatment. Some of the rolled-up regions of the graphene film are marked by the black arrows. Scale bar: 100 $\mu$m.

# D

# Further measurements of LG graphene samples

## Optical images of LG CVD graphene samples

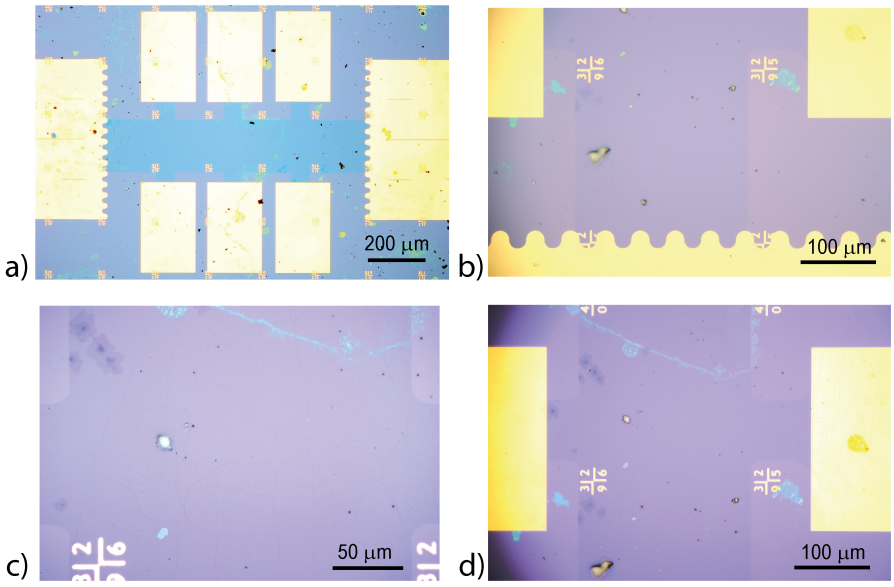


**Figure D.1:** a-d) Optical images of LG (Batch 4) CVD graphene samples after fabrication.

## Weak localization measurements of CVD graphene samples

Weak localization characterization of LG graphene sample (batch 40 - LG3). The fit to the low magnetic field vs $R_{xx}$ data is shown in red. The WL equation in 8.1 was used for the fits to curves measured at two different gate voltages.

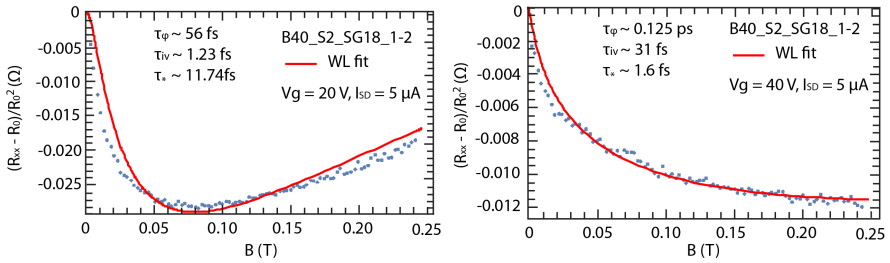


**Figure D.2:** WL characterization of an LG graphene sample at a) Vg = 20V, b) Vg = 40V. The fit to the WL data is shown in red line, respective scattering rates can be found in the plot. The WL measurements were performed at 0.3K.

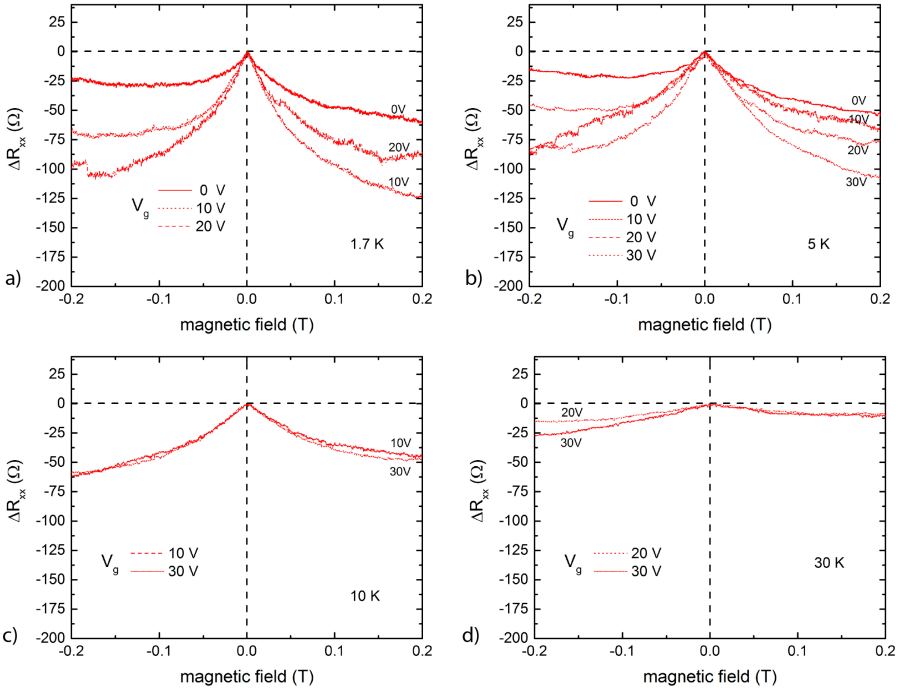


**Figure D.3:** WL characterization of another CVD graphene sample at different gate voltages and temperatures a-d. Note that the y-axis denotes $R_{xx}$ - $R_0$, where $R_0$ is the resistance at B = 0T.

## Weak localization measurements in presence of a fixed parallel magnetic field

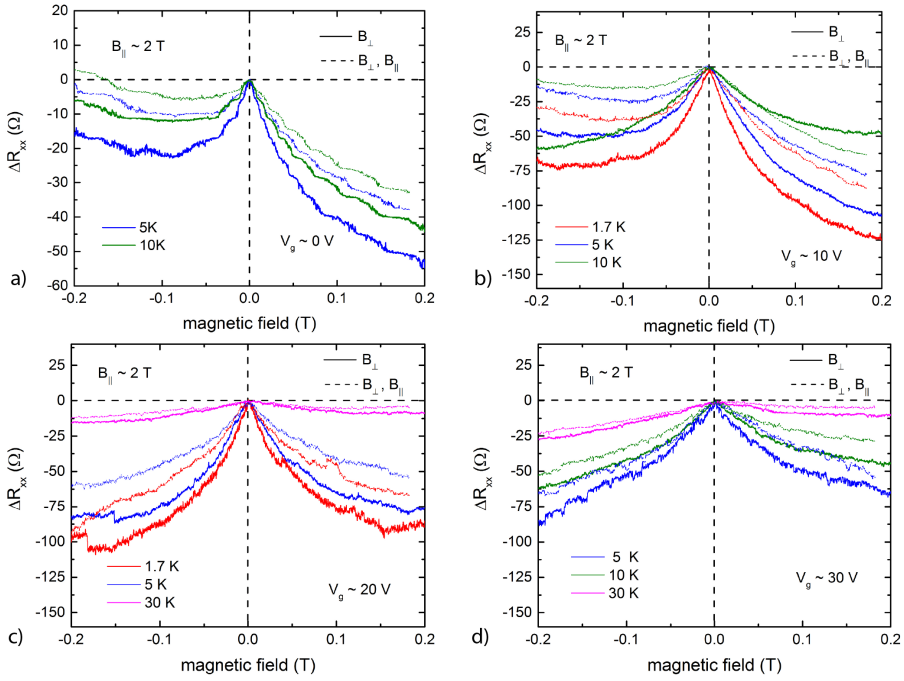


**Figure D.4:** WL characterization of an LG graphene sample at different gate voltages and temperatures a-d in the presence of a fixed parallel magnetic field. Note that the y-axis denotes $R_{xx}$ - $R_0$, where $R_0$ is the resistance at B = 0T.

## Measurements with cryogenic current comparator (CCC):

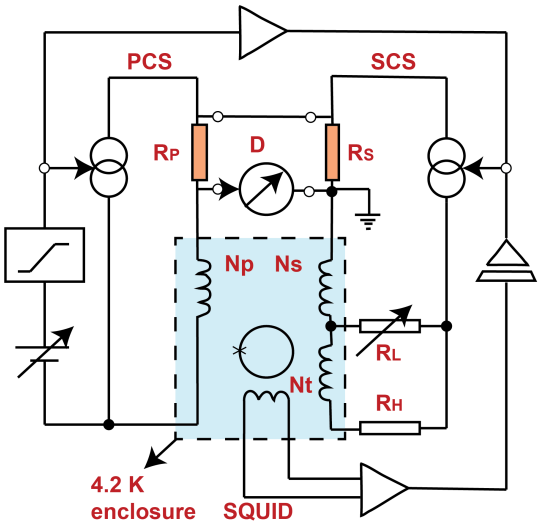


**Figure D.5:** Schematic of a cryogenic current comparator bridge used during the high precision measurements of resistance quantization of LG graphene devices. Redrawn with permission from Jeckelmann et al [33].

A CCC device is useful in precise measurements of the ratio of two direct currents, which is useful during the measurements of resistances. The CCC operation is based on the principle of Meisner effect. The schematic diagram of a CCC device is shown fig. D.5, which consists of windings $N_P$ and $N_S$ with currents $I_P$ and $I_S$, placed inside a torus shaped structure (P(S)CS: primary (secondary) current source). The net magnetic flux created by the shielding current on the torus is proportional to $N_p I_p + N_s I_s$. The ratio of the windings $N_p/N_s$ is adjusted as close as possible to the ratio of $R_p/R_s$. The output voltage of SQUID regulates the secondary current in the feedback loop, which assures that $N_p I_p = N_s I_s$. The detector consisting of a nanovoltmeter indicates the difference between the resistance ratio and the winding ratio. The detector can be further balanced using the divider circuit consisting of trim coil $N_t$ and resistors $R_{l,h}$. The ratio to be measured is given by:

$$\frac{R_p}{R_s} = \frac{N_p}{N_s}\frac{1}{(1+d)}\frac{1}{(1+V_m/V)} \tag{D.1}$$

$$d = \frac{N_t}{N_s}\frac{R_l}{(R_l+R_h)} \tag{D.2}$$

where $V_m$ is the detector reading, V is the voltage drop across the resistors,

$R_{l,h}$ is the adjustable resistor used to balance the detector D and $N_t$ is the number of turns of the trim coil. High precision current ratios with a relative accuracy of $10^{-12}$ can be detected using the CCC. The resolution of the CCC bridge is mainly limited by the 1) noise of the SQUID, 2) thermal noise of the resistors itself and 3) detector noise (D).

### High precision measurement of Hall resistance using cryogenic current comparator of LG2 graphene device

In this section the high precision measurements of a second large-grain CVD graphene (LG2) is shown. These measurements were performed with the CCC bridge. The resistance quantization in LG2 sample is outside the ± 30 ppb range which was observed in LG1 sample. However, for a certain gate voltage values (-7.5V to -8V), the quantization accuracy was observed to be around ± 100 ppb.

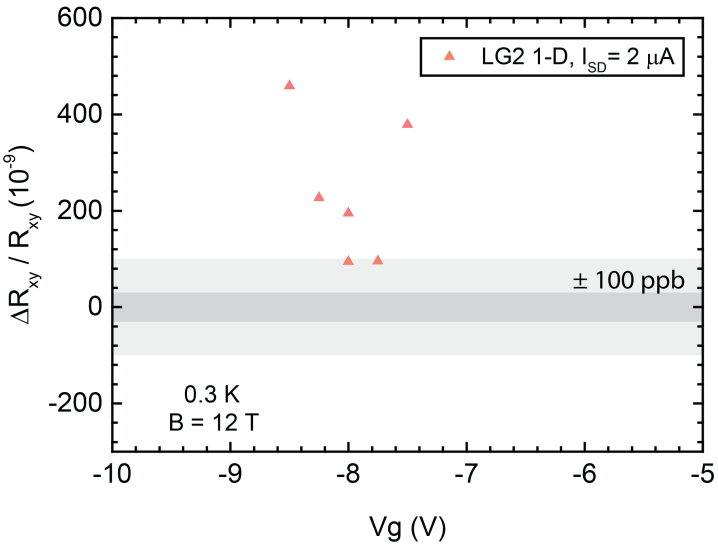


**Figure D.6:** High precision measurements of the Hall resistance $R_{xy}$ of LG2 (red, triangle) at a fixed magnetic field and a source current of $I_{SD}$ = 2 $\mu$A respectively. The shaded areas highlight the regions wherein $R_{xy}$ is quantized within ±100 parts in $10^9$ (light grey) for a range of gate voltages. All the measurements were performed at 0.3 K using a cryogenic current comparator.

### Longitudinal resistance characterization at different magnetic fields of LG2 sample

Further measurements of LG2 sample are shown in this section. In D.7 b) we can see a broader range of $R_{xx}$ values for a range of gate voltages and magnetic fields and in a) we can see a zoom-in of $R_{xx}$ within $\pm 1$ m$\Omega$.

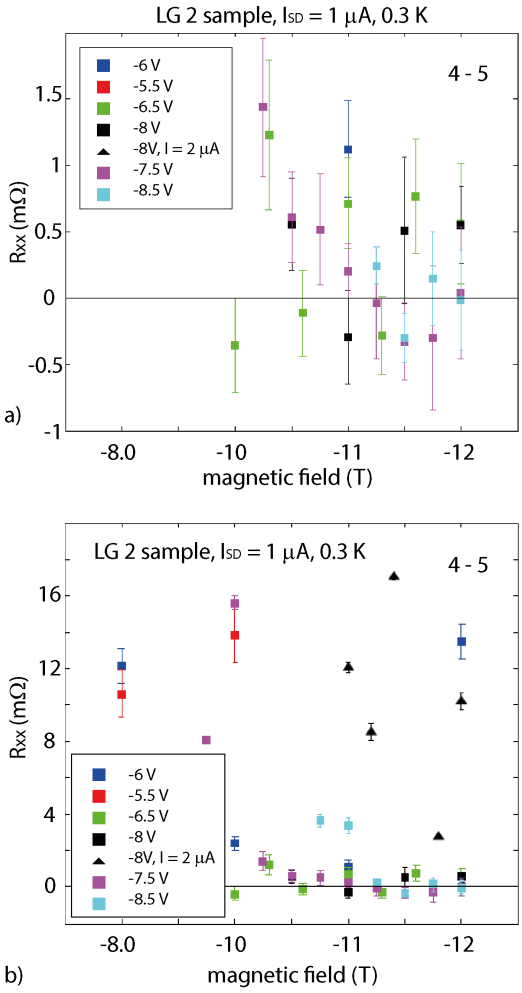


**Figure D.7:** a, b) Longitudinal resistance ($R_{xx}$) measurement at different magnetic fields at $I_{SD}$ = 1 $\mu$A, T = 0.3 K of LG2 (B21-C2-SG80AA) sample.

## Contact resistance characterization of LG2 sample at different bias currents

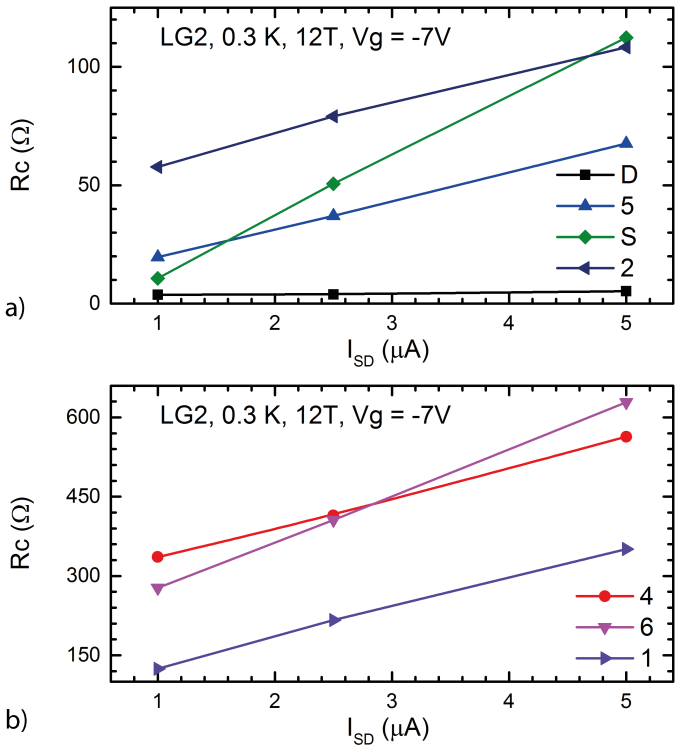


**Figure D.8:** a, b)Contact resistance characterization of LG2 CVD graphene sample at different bias currents. The increase in the $R_c$ values with the currents depicts possible thermal heating effect at the graphene-metal contact interface with the increase in bias currents. These measurements were performed using the direct $R_c$ measurement technique discussed in 5.18.

## Contact resistance characterization of LG1 sample at different bias currents

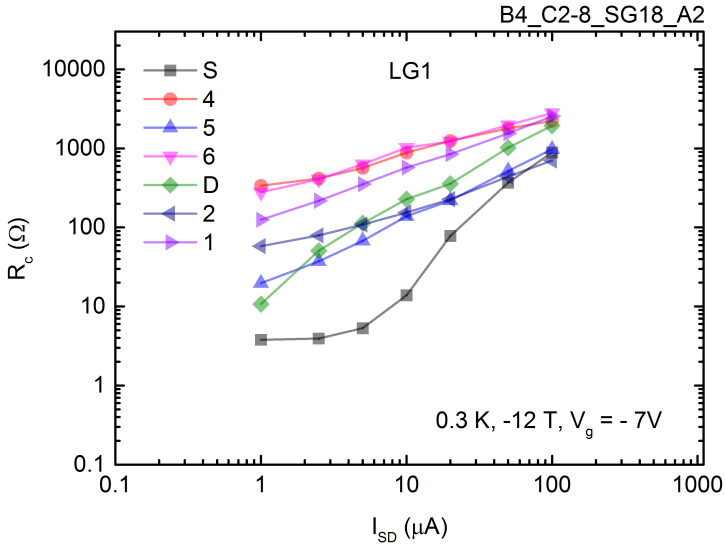


**Figure D.9:** Contact resistance characterization of LG1 CVD graphene sample at different bias currents. The increase in the $R_c$ values with the currents depicts possible thermal heating effect at the graphene-metal contact interface with the increase in bias currents. These measurements were performed using the direct $R_c$ measurement technique discussed in 5.18. A linear fit to the curves 4, 6, 1 gives a slope of $\approx 0.5$.

## Field effect characterization of LG3 sample

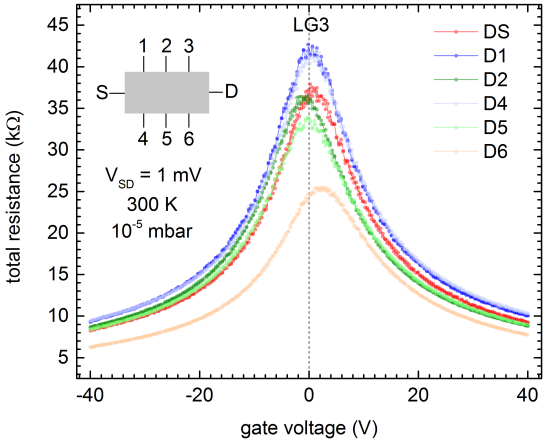


**Figure D.10:** Total resistance vs. gate voltage characteristic of LG3 CVD graphene sample.

## Longitudinal resistance measurement of LG3 sample at different magnetic fields

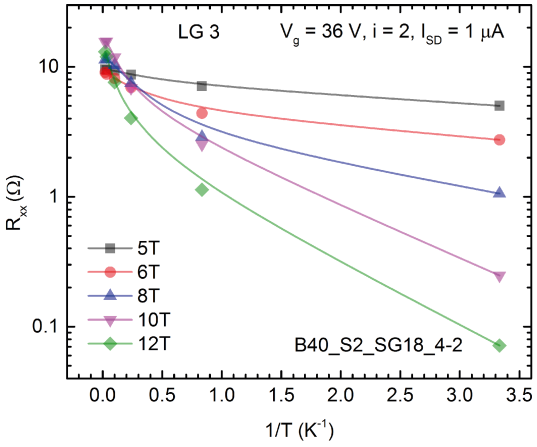


**Figure D.11:** Longitudinal resistance measurement at different magnetic fields of LG3 CVD graphene sample. The $R_{xx}$ values were extracted at $V_g$=36V i.e. on the quantum Hall plateau i=2.

### Longitudinal resistance measurement of LG3 sample at different bias currents

Another observation of low $R_{xx}$ in LG graphene sample (LG3) is shown below.

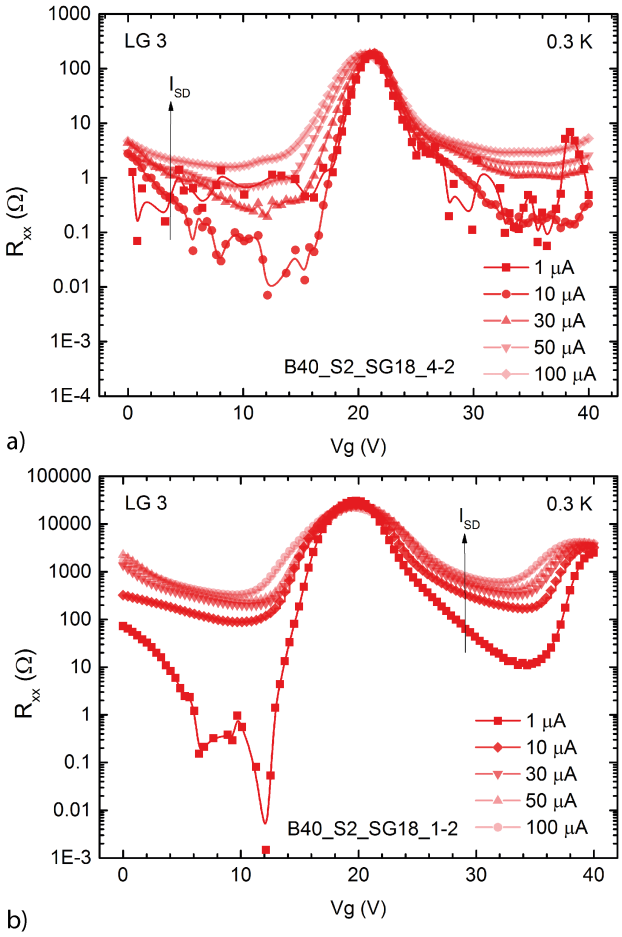


**Figure D.12:** Longitudinal resistance measurement at different bias current and fixed magnetic field of LG3 CVD graphene sample.

## Longitudinal resistance measurement of LG3 sample at different magnetic fields

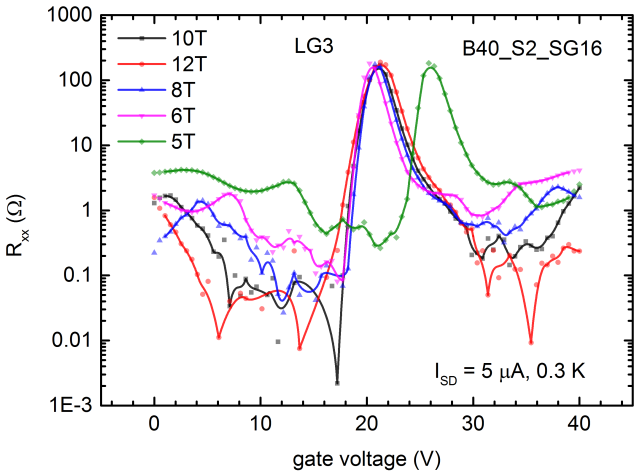


**Figure D.13:** Longitudinal resistance measurement at different magnetic fields and fixed temperature (0.3 K) of LG3 CVD graphene sample.

## Longitudinal resistance measurement of LG3 sample at different magnetic fields and temperature

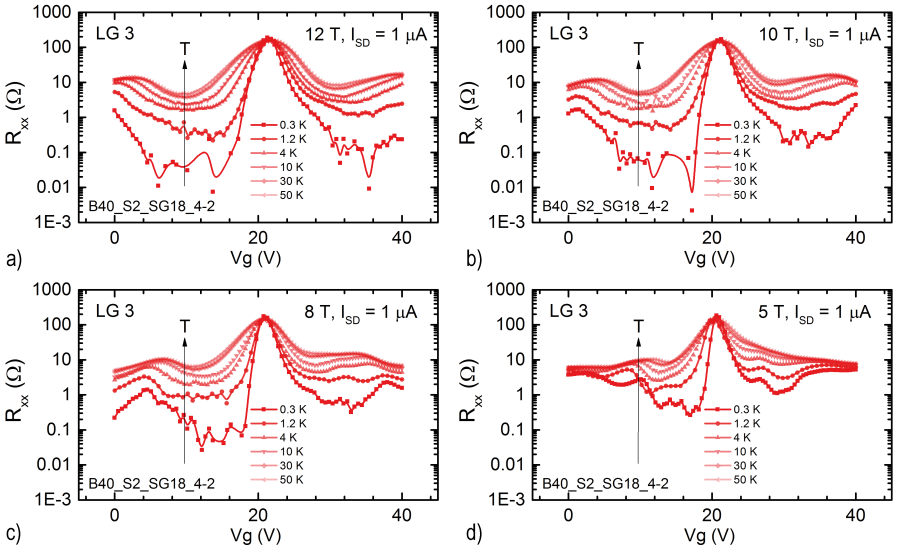


**Figure D.14:** Longitudinal resistance measurement at different magnetic fields and temperature (0.3 K to 50 K) of LG3 CVD graphene sample.

## Field effect mobility characterization of SG and LG-CVDG devices

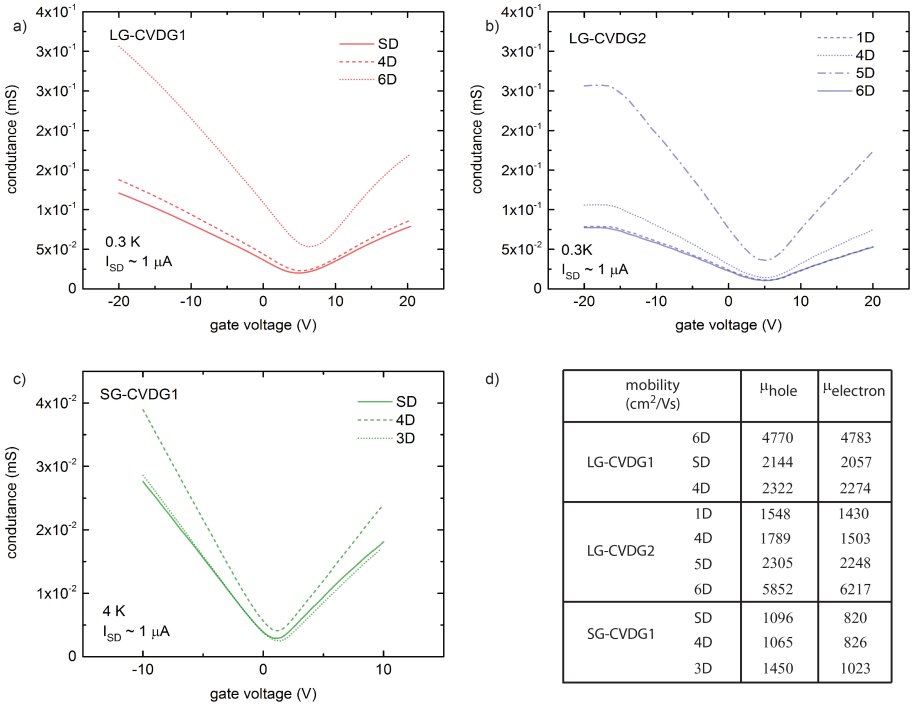


d)

| mobility ($cm^2$/Vs) | | $\mu_{hole}$ | $\mu_{electron}$ |
|---|---|---|---|
| LG-CVDG1 | 6D | 4770 | 4783 |
| | SD | 2144 | 2057 |
| | 4D | 2322 | 2274 |
| LG-CVDG2 | 1D | 1548 | 1430 |
| | 4D | 1789 | 1503 |
| | 5D | 2305 | 2248 |
| | 6D | 5852 | 6217 |
| SG-CVDG1 | SD | 1096 | 820 |
| | 4D | 1065 | 826 |
| | 3D | 1450 | 1023 |

**Figure D.15:** Field effect mobility characterization of SG (a) and LG graphene (b, c) devices. a) Total conductance versus gate voltage gate voltage for samples LG1, 2 (a, b) and SG1 (c). d) Table of hole/electron field effect mobility of all the devices. All the electrical characterization was performed under low vacuum conditions of $10^{-4}$ bar and at 0.3K or 4K at $I_{SD}$ = 1 $\mu$A. The field effect mobility was calculated from the conductance curve, with the charge density estimated from gate voltage and gate capacitance.

# E

# Molecular modeling of adsorbates on graphene

## Details about the molecular modeling of molecular adsorbates on graphene

Molecule-graphene complexes were calculated using the VASP program with the dispersion-corrected GGA-PBE functional, projector augmented wave (PAW) pseudopotentials with a plane wave cut-off of 400 eV and a vacuum spacing of approximately 3 nm in the direction normal to the graphene monolayer [169–171]. All atoms were allowed to fully relax unconstrained until the forces on each atom were $<$3 meV/Å. The vdW interactions were calculated using the Grimme D3 dispersion functional [172]. The molecule-surface complexes were calculated using periodic boundary conditions, and the reported individual molecule-surface binding energies were converged to below 20 meV using a 441 k-point grid. Future work to quantify the binding energies of other organic molecules at elevated temperatures could use also ab initio molecular dynamics simulations [169], and assess the predictive power of alternative methods such as tight-binding schemes and/or empirical London dispersion energy corrections [173]. All the simulations were performed by Dr. Damien Thompson (Department of Physics and Energy, University of Limerick, Ireland) after discussion with K. Thodkar and M. Calame.

## Molecular modeling of NMP on graphene

N-Methyl-2-pyrrolidone (NMP)

| NMP structure | top view | side view | Binding free energy (meV) | |
|---|---|---|---|---|
| | | | substrate-graphene | dispersion-corrected |
| 1 | 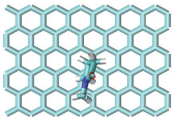 | 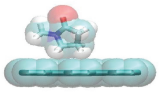 | 35 meV | -180 meV |
| 2 | 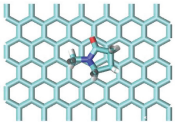 | 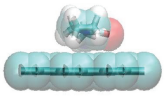 | -38 meV | -345 meV |
| 3 | 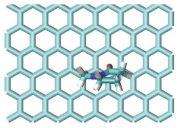 | 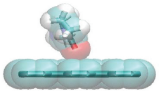 | -23 meV | -130 meV |
| 4 | 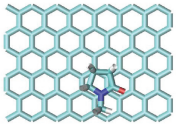 | 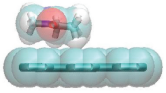 | -1meV | -310 meV |

**Figure E.1:** Molecular binding calculation of NMP adsorption on graphene under different structural configurations. The respective binding energy of each particular binding configuration can be found in the same row, expressed as the substrate-graphene electronic binding energy without and then with dispersion corrections.

## Molecular modeling of HMDS on graphene

Hexamethyldisilazane (HMDS)

| NMP structure | top view | side view | Binding free energy (meV) | |
|---|---|---|---|---|
| | | | substrate-graphene | dispersion-corrected |
| 1 | 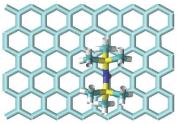 | 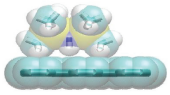 | 110 meV | -240 meV |
| 2 | 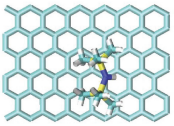 | 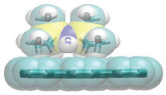 | 213 meV | -280 meV |
| 3 | 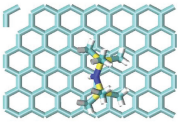 | 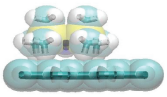 | 77 meV | -331 meV |

**Figure E.2:** Molecular binding calculation of HMDS adsorption on graphene under different structural configurations. The respective binding energy of each particular binding configuration can be found in the same row. Note that for HMDS the substrate-graphene electronic binding energy, prior to addition of vdW forces, is weakly repulsive.

## Molecular modeling of PMMA-monomer on graphene

PMMA-monomer

| PMMA structure | top view | side view | Binding free energy (meV) | |
|---|---|---|---|---|
| | | | substrate-graphene | dispersion-corrected |
| 1 | 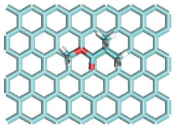 | 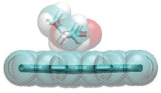 | 42 meV | -274 meV |
| 2 | 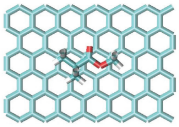 | 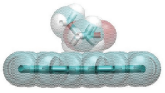 | 43 meV | -303 meV |
| 3 | 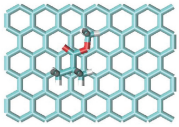 | 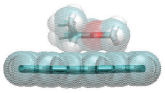 | -2 meV | -276 meV |
| 4 | 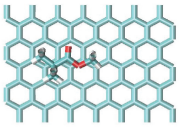 | 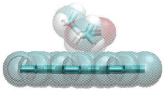 | -11 meV | -303 meV |
| 5 | 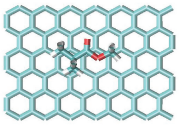 | 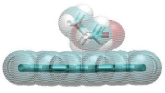 | 24 meV | -331 meV |
| 6 | 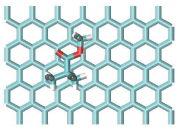 | 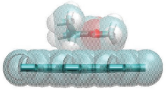 | -8 meV | -318 meV |

**Figure E.3:** Molecular binding calculation of PMMA-monomer adsorption on graphene under different structural configurations. The respective binding energy of each particular binding configuration can be found in the same row.

## Molecular modeling of PMMA-monomer and amine salt on graphene

PMMA-amine salt

| PMMA-salt structure | top view | side view | Binding free energy (meV) | |
|---|---|---|---|---|
| | | | substrate-graphene | dispersion-corrected |
| 1 | 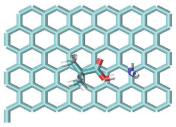 | 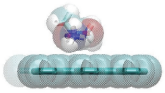 | -43 meV | -281 meV |
| 2 | 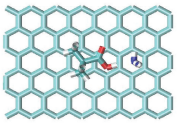 | 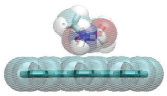 | -41 meV | -294 meV |
| 3 | 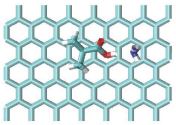 | 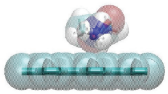 | 4 meV | -267 meV |
| 4 | 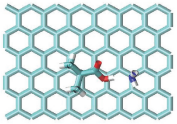 | 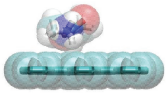 | -38 meV | -213 meV |
| 5 | 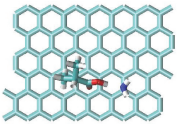 | 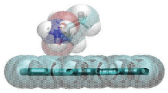 | -1 meV | -174 meV |
| 6 | 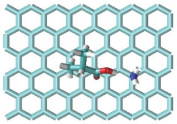 | 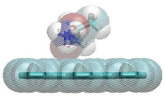 | 13 meV | -169 meV |

**Figure E.4:** Molecular binding calculation of PMMA-amine salt monomer adsorption on graphene under different structural configurations. The respective binding energy of each particular binding configuration can be found in the same row. Note initially-charged salt pairs of $NH^{4+}$/ $COO^{-}$ always reverted to $NH_3$/COOH co-adsorbates in control simulations.

## Molecular modeling of co-adsorption of NMP and water molecule on graphene

co-adsorption of water and NMP on graphene

| structure | top view | side view | Binding free energy (meV) | |
|---|---|---|---|---|
| | | | substrate-graphene | dispersion-corrected |
| 1 | 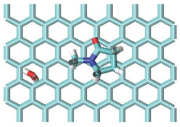 | 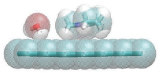 | -57 meV | -122 meV |
| 2 | 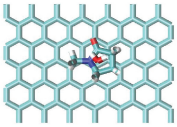 | 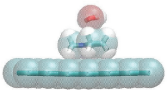 | -36 meV | -162 meV |
| 3 | 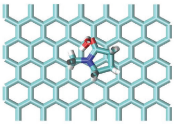 | 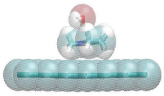 | -79 meV | -194 meV |
| 4 | 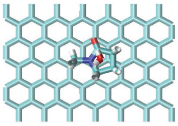 | 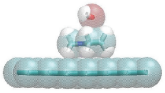 | -46 meV | -155 meV |

**Figure E.5:** Molecular binding calculation of co-adsorption of water and NMP molecules on graphene under different structural configuration. The respective binding energy of water in each particular binding configuration can be found in the same row and the values are consistent with those reported by Wang et al. for calculated water adsorption (alone) on graphene. The side-by-side and on-top water/NMP binding configurations are essentially iso-energetic, with only a very mild preference of 30-70 meV (within the inherent error of DFT) for side-by-side vs. stacked NMP-$H_2O$ adsorption modes on graphene.

# F

# Collaborations

Some of the collaborations during my PhD thesis have been listed below in two parts i.e. within our research group and outside. During my thesis I have had the opportunity to share the CVD grown graphene films as part of academic collaborative projects for various different applications. My main role in these collaborations was to provide high-quality CVD graphene films, assist the collaborators in material transfer onto their substrate of choice and brief experimental assistance in some of the projects. The transfer of graphene at times required alternative approaches especially for the production of suspended graphene structures (protein imaging). All these transfer techniques have been discussed in earlier chapters.

**Internal collaborations**

1. *'Fabrication of graphene nanogaps for contacting molecules.'*
   Maria El Abbassi, PD. Dr. Michel Calame, University of Basel.
2. *'Comprehensive study of effects due to strain in graphene films.'*
   Jan Overbeck, Lujun Wang, Oliver Braun, Peter Makk, Prof. Dr. Christian Schönenberger, PD. Dr. Michel Calame, University of Basel.
3. *'Spin transport in graphene.'*
   David Indolese, Simon Zihlmann, Peter Makk, Prof. Dr. Christian Schönenberger, PD. Dr. Michel Calame, University of Basel.
4. *'Ballistic transport in CVD graphene.'*
   Peter Rickhaus, Lujun Wang, Peter Makk, Prof. Dr. Christian Schönenberger,

PD. Dr. Michel Calame, University of Basel.

5. *'Hyrbid graphene-nano particle array devices.'*
   Anton Vladyka, PD. Dr. Michel Calame, University of Basel.

**External collaborations**

1. *'Suspended graphene as substrate for protein imaging using for low energy electron microscopy.'*
   Dr. Jean Nicolas Longchamp, Prof. Dr. Hans-Werner Fink, Department of Physics, University of Zürich.
2. *'Scanning tunneling microscopy experiments of molecular adsorption on graphene.'*
   Dr. Peter Nirmalraj, Adolphe Merkle Institute, Fribourg, Switzerland. (Previously at: IBM Research labs, Zürich).
3. *'Long range in plane fluctuations in freestanding Graphene membranes using dynamic light scattering.'*
   Mathias Altenburg, Prof. Dr. Georg Maret, Universität Konstanz, Germany.
4. *'Graphene-based photodetector arrays.'*
   Matthias Grotevent, Dr. Ivan Shorubalko, Transport at Nanoscale interfaces, EMPA, Zürich.
5. *'In situ protein crystallization on ultrathin membranes.'*
   Nadia Opara, Prof. Dr. Henning Stahlberg, Prof. Dr. Celestino Padeste, University of Basel & Paul Scherrer Institute, Villigen, Switzerland.

# Curriculum Vitae

Kishan Thodkar Raveendranath Rao
Born November 16 1989 in Bangalore (Karnataka, India)

## Education

2013-2017 PhD in experimental physics at University of Basel. Dissertation at the group of PD. Dr. Michel Calame and Prof. Dr. Christian Schönenberger: ”Chemical vapor depostied graphene for quantum resistance standards”

2011-2013 MSc. in Nanoscience and Nanotechnology (specialization: Nanoelectronics) at Catholic University of Leuven, Belgium and Chalmers University of Technology, Gothenburg, Sweden. Master thesis at the group of Prof. Avgust Yurgens: ”Graphene based NEMS resonators”

2007-2011 Bachelor of Engineering in Electronics and Instrumentation. Bachelor thesis: ”Machine vision system for automated fruit sorting”

## Positions and professional experience

| | |
|---|---|
| 2013-2017 | Teaching assistant for Advanced practical course (Fortgeschrittenenpraktikum), Physics department, University of Basel. |
| 07-09 2013 | Internship at the group of Prof. Dr. Christopher Hierold, Dept. of Mechanical and process engineering, ETH Zürich, Switzerland. Topic: Electrical characterization of CNT resonators. |
| 07-08 2012 | Internship at imec, Belgium. Topic: Design of opto-electro mechanical resonators. |

## Awards

| | |
|---|---|
| ReachOut Award | First place for science communication, EMRS conference May 2016 |
| Science slam Basel Winner, 2015 | First place for science slam presentation on ”Can really really reallly small things deliver? Graphene can” |
| Best Poster prize, Oct. 2015 | 12th Confocal Raman Imaging Conference, Ulm, Germany |
| Science slam Zürich Winner, 2014 | First place for science slam presentation on ”Chemical vapor deposited graphene quantum resistance standards” |
| Erasmus Mundus consortium scholarship, 2011-2013 | Scholarship for Master studies in Nanoscience and nanotechnology. |

# Publications

**Journal publications**


1. Thodkar, K., El Abbassi, M., Lüönd, F., Overney, F., Schönenberger, C., Jeanneret, B. & Calame, M. Comparative study of single and multi domain CVD graphene using large-area Raman mapping and electrical transport characterization. *physica status solidi (RRL) - Rapid Research Letters* **10,** 807–811. ISSN: 18626254 (2016).
2. Stoop, R. L., Thodkar, K., Sessolo, M., Bolink, H. J., Schönenberger, C. & Calame, M. Charge Noise in Organic Electrochemical Transistors. *Phys. Rev. Applied* **7,** 014009 (1 2017).
3. Thodkar, K., Thompson, D., Lüönd, F., Moser, L., Overney, F., Marot, L., Schönenberger, C., Jeanneret, B. & Calame, M. Restoring the Electrical Properties of CVD Graphene via Physisorption of Molecular Adsorbates. *ACS Applied Materials & Interfaces* **9.** PMID: 28675296, 25014–25022 (2017).
4. Thodkar, K., Lüönd, F., Overney, F., Schönenberger, C., Jeanneret, B. & Calame, M. High quality CVD graphene for quantum Hall resistance standards. to be submitted (2017).
5. El Abbassi, M., László, P., Makk, P., Nef, C., Thodkar, K., Halbritter, A. & Calame, M. From Electroburning to Sublimation: Substrate and Environmental Effects in the Electrical Breakdown Process of Monolayer Graphene. Submitted (2017).
6. Nirmalraj, P., Thompson, D., Thodkar, K., Calame, M. & Mayer, M. Surface

Dynamics of Proteins at the Graphene-Water Interface. in preparation.

7. Nirmalraj, P., Thompson, D., Thodkar, K., Calame, M. & Mayer, M. On the Surface Tension of Proteins. in preparation.
8. Zihlmann, S., Makk, P., Castilla, S., Gramich, J., Thodkar, K. & Schönenberger, C. Superconducting tunneling spectroscopy of graphene. in preparation.
9. Indolese, D., Zihlmann, S., Makk, P., Jünger, C., Thodkar, K. & Schönenberger, C. Spin-pumping and inverse spin Hall effect in graphene. in preparation.

**Conference proceedings**

1. Thodkar, K., Schönenberger, C., Calame, M., Lüönd, F., Overney, F., Jeckelmann, B. & Jeanneret, B. *Characterization of HMDS treated CVD graphene Conference on Precision Electromagnetic Measurements* (2016). doi:10.1109/CPEM.2016.7540498.
2. Thodkar, K., Nef, C., Fu, W., Schönenberger, C., Calame, M., Lüönd, F., Overney, F., Jeckelmann, B. & Jeanneret, B. *CVD Graphene for electrical Quantum Metrology Conference on Precision Electromagnetic Measurements* (2014). doi:10.1109/CPEM.2014.6898498.

**Talks**

1. Thodkar, K., Nef, C., Fu, W., Schönenberger, C., Calame, M., Lüönd, F., Overney, F., Jeckelmann, B. & Jeanneret, B. *CVD Graphene for Electrical Quantum Metrology* Talk at Graphene workshop in Basel 2015. Invited talk. Basel, 2015.
2. Thodkar, K., Nef, C., Fu, W., Schönenberger, C., Calame, M., Lüönd, F., Overney, F., Jeckelmann, B. & Jeanneret, B. *CVD Graphene for Electrical Quantum Metrology* Talk at DC & Quantum Metrology meeting 2015 in Bern. Talk. Bern, 2015.
3. Thodkar, K., Nef, C., Fu, W., Schönenberger, C., Calame, M., Lüönd, F., Overney, F., Jeckelmann, B. & Jeanneret, B. *CVD Graphene for Electrical Quantum Metrology* Talk at QSIT Junior meeting 2015. Talk. Passugg Switzerland, 2015.
4. Thodkar, K. e. a. *Optimization of CVD graphene for industrial applications* Talk at EMPIR meeting at METAS, Bern. Talk. Bern, 2017.
5. Thodkar, K. *Physisorption effects on NMP and HMDS molecules on CVD graphene* Talk at MMMT Dec. 2016. Talk. Basel, 2016.

**Poster contributions**

1. Thodkar, K., Nef, C., Fu, W., Schönenberger, C., Calame, M., Lüönd, F., Overney, F., Jeckelmann, B. & Jeanneret, B. *CVD Graphene for Electrical Quantum Metrology* Poster. Switzerland, 2014.
2. Thodkar, K., Nef, C., Fu, W., Schönenberger, C., Calame, M., Lüönd, F., Overney, F., Jeckelmann, B. & Jeanneret, B. *CVD Graphene for Electrical Quantum Metrology* Poster. Kirchberg, Austria, 2014.
3. Thodkar, K., Nef, C., Fu, W., Schönenberger, C., Calame, M., Lüönd, F., Overney, F., Jeckelmann, B. & Jeanneret, B. *CVD Graphene for Electrical Quantum Metrology* Poster. Switzerland, 2014.
4. Thodkar, K., Nef, C., Fu, W., Schönenberger, C., Calame, M., Lüönd, F., Overney, F., Jeckelmann, B. & Jeanneret, B. *CVD Graphene for Electrical Quantum Metrology* Poster. Gothenburg, Sweden, 2014.
5. Thodkar, K., Nef, C., Fu, W., Schönenberger, C., Calame, M., Lüönd, F., Overney, F., Jeckelmann, B. & Jeanneret, B. *CVD Graphene for Electrical Quantum Metrology* Poster. Brazil, 2014.
6. Thodkar, K., Nef, C., Fu, W., Calame, M., Lüönd, F., Overney, F., *et al. Graphene - from mechanical resonators to single crystal CVD growth* Poster. Switzerland, 2015.
7. Thodkar, K., Nef, C., Fu, W., Schönenberger, C., Calame, M., Lüönd, F., Overney, F., Jeckelmann, B. & Jeanneret, B. *CVD Graphene for Electrical Quantum Metrology* Poster. Bilbao, Spain, 2015.
8. Abbassi, E. M., Overbeck, J., Thodkar, K., Schönenberger, C. & Calame, M. *Controlling the Fabrication of Graphene Nanoelectrodes* Poster. Regensburg, Germany, 2015.
9. Thodkar, K., Abbassi, E. M., Nef, C., Fu, W., Schönenberger, C., Calame, M., *et al. Raman characterization of CVD graphene for Molecular electronics and Electrical Metrology* Poster. Ulm, Germany, 2015.
10. Thodkar, K., Abbassi, E. M., Nef, C., Schönenberger, C., Calame, M., Lüönd, F., Overney, F., Jeckelmann, B. & Jeanneret, B. *Raman characterization of CVD graphene for Molecular electronics and Electrical Metrology* Poster. EMPA, Switzerland, 2016.
11. Thodkar, K., Abbassi, E. M., Nef, C., Schönenberger, C., Calame, M., Lüönd, F., Overney, F., Jeckelmann, B. & Jeanneret, B. *Characterization of HMDS treated CVD graphene* Poster. Lille, France, 2016.

12. Abbassi, E. M., Laszlo, P., Makk, P., Thodkar, K., Schönenberger, C., Halbritter, A. & Calame, M. *Graphene molecular junctions* Poster. Paris, France, 2016.

**Other**

1. Honorary Science Slam talk at Basel Science slam 2016, Basel, Switzerland
2. Invited Science Slam talk at the 10th anniversary of the Swiss Nanoscience institute, Basel, Switzerland
3. Finalist in Swiss Famelab 2015
4. Carbon poem recitation, UniNacht 2015, Basel, Switzerland

# Acknowledgments

*"To be or not to be"*
William Shakespeare "Nunnery scene", Hamlet. Act III, Scene I.

During an important moment of my life I found myself trying to find answer to the phrase which sounded like the one from Shakespeare: 'To be or not to be'. In my situation it was: to be or not be a doctor? I chose to be one.

As I write these words, my time during the doctoral studies flashes by. In a ponderous thought I see myself go through a transition during my doctoral work. It makes me realize that not only the PhD project but all the people who have been involved in different ways play an important role too. Aristotle is still right, man is by nature a social animal. I would like to thank Michel Calame for making all of this possible. It has been a life changing experience. Thank you for the overall setting in the group and all the personal interactions, I have been able to develop independency, be constructive and critically scrutinize data and measurements. I have thoroughly enjoyed the summer barbecues, winter fondue sessions, jovial atmosphere within the group and appreciate your efforts towards maintaining it. I would also like to thank Christian Schönenberger for all the interactions during this work. Your energy, desire for good science and persistence has had an influence on me and I will carry it further.

I would like to thank Blaise Jeanneret for his continuous support and sharing his expertise in quantum Hall effect and also during the high precision measurements. I thoroughly enjoyed the regular visits to METAS, performing the sample measurements and our regular meetings. I'd like to thank Felix Lüönd for all the

help with low temperature measurements at METAS. I enjoyed the measurement sessions and the positive outlook. I am also thankful to Fréderic Overney and the staff at METAS for all the help and support. Special thanks also goes to Franz Ahlers and Daniel Neumaier for taking time to read this thesis, I am glad that you decided to join the defence committee. Thanks to Ilaria Zardo for accepting to chair my defence.

I would like to sincerely thank Damien Thompson for your insights in modelling of molecular adsorption on graphene and for all the interactions during our collaboration. The XPS study would not be complete without the support of Lucas Moser and Laurent Marot. Thanks a lot for introducing me to XPS and thorough analysis methods of materials. LEEM characterization was a success thanks to Hans-Werner Fink and Nicholas Longchamp, thanks a lot helping us image and produce some of the cleanest CVD graphene surfaces ever.

This work has been fuelled by the myriad Indian-Friday lunches, Moroccan tajines, several good/expensive Thai-takeaways, Frisbee sessions, samosa, ice creams and of course even the bold trips to the Mensa with my co-workers.

Anton, thanks to you now I know so many tips and tricks in LaTex and Matlab. You're passion for these IT things scared me a few times, but I found a way to appreciate it. Thanks for being an eternal office mate, I had to turn right and you were there, ready to talk science and of-course programming. I would like to thank Maria for the happy ambience in the office and treating us to delicious sweets from Morocco, mint tea and great tajine recipes. Jan, for sharing your passion for dynamic interactions via lunch-meetings, hands-on approach and many impromptu discussions. Mathias, thank you for all the interactions inside and outside the office, was always fun to have you in the office. Ralph, thanks for sharing your positivity and knowledge in noise measurements, I thoroughly enjoyed our collaborative efforts.

Oliver, it was a pleasure to work with you during your master project and thesis. I am very glad that both the projects worked out very well and even happier that you began your doctoral thesis in our group. I am thankful to Wangyang Fu and Cornelia Nef for sharing their graphene knowledge during the start of my project and providing me with the best transition into my thesis. Thanks also goes to Mickael Perrin for all the positivity and many interactions about several topics.

I would like to express my gratitude for the myriad discussions related to CVD graphene and transport with: Andreas Baumgartner, Peter Makk, Simon Zihlmann and Peter Rickhaus, your expertise was certainly helpful.

I would also like to thank all the members of the Nanoelectronics group, who made the group excursions, workshops, Monday-morning meetings enjoyable: Raphaelle Delagrange, Gergö Fülöp, Minkyung Jung, Gulibuistan Abulizi, Arunav Bordoloi, Roy Haller,Clevin Handschin, Cezar Harabula, David Indolese, Christian Jünger, Frederick Thomas, Lujun Wang, Samuel d'Hollosy, Thomas Hasler, Jörg Gramich, Vishal Ranjan, Toni Fröhlich, Axel Fanget and David Marti. No experimental work would be a success without a handy-workshop around. I'd like to thank Sasha Martin and all the workshop staff for all the help in building several items during the work. I am also thankful to our secretaries Barbara Kammermann and Astrid Kalt for all the smooth administrative support throughout.

I am thankful to Sylvia Marelli-Winter for giving me the opportunity to spend my time in Basel at one of the best student residences. I have several fond memories and made many friends during my time at the dorm. It played a pivotal role in helping me unwind and meet many interesting people. I will also be forever thankful to all my red-kitchen members for making me feel at home, always.

I am very grateful and ever thankful to my parents, loving sister and my family members for all their unconditional support I received throughout this time.

I would also like to thank METAS for funding and supporting this project throughout.